DSPACE

https://dspace.org/

Processing, characterization and tribological assessment of novel WC-VC-Co coatings and alloys

Ogunmuyiwa, Enoch Nifise

2014-02-05
http://hdl.handle.net10539/13652

Downloaded from a DSpace repository. https://dspace.org/

PROCESSING, CHARACTERIZATION AND TRIBOLOGICAL ASSESSMENT OF NOVEL WC-VC-Co COATINGS AND ALLOYS

ENOCH NIFISE, OGUNMUYIWA

A thesis submitted to the Faculty of Engineering and the Built Environment, University of the Witwatersrand, Johannesburg, in fulfilment of the requirements for the degree of Doctor of Philosophy in Engineering (Metallurgy and Materials).

October 2013

DECLARATION

I declare that this thesis is my own unaided work. It is being submitted to the degree of Doctor of Philosophy in Engineering to the University of the Witwatersrand, Johannesburg. It has not been submitted before for any degree or examination to any other university.

……...

Enoch Nifise, OGUNMUYIWA

……. day of …….. Year ……

ABSTRACT

This thesis describes a number of novel WC-Co sintered alloys (conventional and spark plasma) and thermal spray coatings, with the addition of 10wt%VC. The VC addition was kept constant for all materials while the Co binder content was varied for the thermal spray coatings (12wt% and 17wt%). The production route of the hardmetal is by powder metallurgy techniques. All the production processes were closely monitored and optimized. The properties of all the materials produced were evaluated using standard hardmetal quality control procedures. The wear performance of the materials was characterized in terms of friction response, sliding wear resistance and slurry erosion resistance.

In general, the addition of 10wt%VC to WC-Co produced a material with a better hardness, comparable toughness and a less dense material for weight saving applications, thus making VC a good substitute for WC. The VC led to WC grain refinement in both coatings and sintered materials. None of the starting VC from the powders remained in the produced materials, as the VC formed the WV_4C_5 phase. The presence of the WV_4C_5 phase resulted in a higher hardness. Despite a poorer wettability of the VC by Co compared to WC, the porosity in the WC-Co-VC materials was minimal. The XRD spectra of the WC-Co-VC materials did not show any eta phase. The wear performance of the materials was generally improved with the addition of the VC with minor exceptions. The wear mechanisms in the sliding wear and slurry erosion wear systems were found to be similar for all three material types. The mechanisms included preferential binder removal, adhesion, smearing, carbide grain cracking, grain pull-out, and formation of thin tribo-films.

DEDICATION

To the loving memory of my late father, Mr Ebenezer Ogunmuyiwa and the entire Ogunmuyiwa family for your support during my years of study.

ACKNOWLEDGMENTS

My profound gratitude goes to the Almighty God, without whom I cease to exist. The list is endless but my sincere thanks go to the following:

- Dr Natasha Sacks, for suggesting, supervising and mentoring this work to completion.
- Prof. Lennart Bergström and Mr Farid Akhtar for their assistance with the SPS work.
- Pilot tools (Pty) SA and Powder Industry (Pty) SA, for supplying the powders and assistance with the production of the conventionally sintered alloys – especially Mr Christopher Freemantle and Mr Andrew Sekgobela.
- CSIR – Mr Clive Oliphant for help with SEM work and Mr Werner Jordan for the XPS work.
- Mintek – Mr Richard Couperthwaite and Mr Mokae Bambo for their assistance with SEM work.
- Prof. David Billings, Ms Natsayi Chiwaye, Mr Wilson Mogodi and Mr Robert Richardson for their assistance with the Rietvled work.
- All the staff and postgraduate students in the School of Chemical and Metallurgical Engineering, Wits for their love, support and friendship.
- The entire Pacesetters generation, my senior friends and colleagues (the Ojos, the Akinlabis, the Adams, the Adeagbos, the Johnsons, the Erinoshos, and the Oladijos) for their love and support.
- The support of the DST/NRF Centre of Excellence in Strong Materials (CoE-SM) and Financial Aid Office of the University of the Witwatersrand, for financial support towards this research is hereby acknowledged.

Last but not the least; my special thanks go to my wife, Grace, and our sons, Joseph and James, who have been forbearing during my years of studies. They provided the lubrications necessary to minimize friction and wear at home.

TABLE OF CONTENT

DECLARATION ii
ABSTRACT iii
DEDICATION iv
ACKNOWLEDGMENTS v
TABLE OF CONTENT vi
LIST OF FIGURES xi
LIST OF TABLES xviii
LIST OF SYMBOLS xx
1. Introduction 1
1.1 Aims and Objectives of the research 3
1.2 Structure of the thesis 4
2. Literature review 5
2.1 Conventionally sintered WC-Co alloys 5
2.1.1 Production of WC-Co alloys 5
2.1.2 Properties of WC-Co alloys 7
2.1.3 Vanadium carbide in sintered WC-Co alloys 11
2.2 Spark plasma sintered alloys 14
2.2.1 Description of SPS process 15
2.2.2 Spark plasma sintered (SPSed) WC-Co alloys 16
2.2.3 Spark plasma sintered WC-Co-VC alloys 19
2.3 High velocity oxy-fuel (HVOF) thermal spray WC-Co coatings 21
2.3.1 HVOF thermal spray process 21
2.3.2 Microstructure development of WC-Co coatings 24
2.3.3 Properties of WC-Co coatings 25
2.3.4 Vanadium carbide in WC-Co thermal spray coatings 29
2.4 Fundamentals of friction 30
2.5 Fundamentals of wear 34
2.5.1 Sliding wear 35

2.5.2 Erosive wear 37
3. Experimental procedures 39
3.1 Introduction 39
3.2 Powders 39
3.2.1 Thermal spray coating powders 39
3.2.2 Sintered alloy powders 40
3.3 Materials processing procedures 41
3.3.1 Thermal spray coating procedure 41
3.3.2 Sintered alloys processing 42
3.4 Materials characterization 44
3.4.1 Sample preparation 44
3.4.2 Microstructure analysis 46
3.4.3 Coating porosity and hardness 46
3.4.4 Sintered alloys characterization 47
3.5 Friction and sliding wear tests 50
3.6 Slurry erosion wear tests 54
3.7 Wear scar analyses 57
4. Results: Thermal Spray Coatings 58
4.1 Introduction 58
4.2 Powder Characterization 58
4.2.2 Particle size and size distribution 59
4.2.3 Phase composition 59
4.3.1 Coating microstructures 61
4.3.2 Phase composition 66
4.3.3 Mean carbides grain sizes 68
4.3.4 Coating hardness 68
4.4 Friction and sliding wear tests 69
4.4.1 Wear mechanisms in sliding wear 74
4.5 Slurry erosion tests 86
4.5.1 Wear mechanisms on eroded coating surfaces 88
5. Results: Conventionally sintered alloys 96
5.1 Introduction 96

5.2 Powder characterization 96
5.2.1 Morphology 96
5.2.2 Particle size and size distribution 97
5.2.3 Phase composition 97
5.3 Alloy characterization 99
5.3.1 Microstructures 99
5.3.2 Phase composition 101
5.3.3 Mechanical properties 102
5.4 Friction and sliding wear tests 103
5.4.1 Wear mechanisms in sliding wear 106
5.5 Slurry erosion tests 109
5.5.1 Wear mechanisms of the eroded alloy surfaces 111
6. Results: Spark plasma sintered alloys 115
6.1 Introduction 115
6.2 Powder characterization 115
6.2.1 Morphology 115
6.2.2 Particle size and size distribution 116
6.2.3 Phase composition 116
6.3 Alloy characterization 117
6.3.1 Microstructures 117
6.3.2 Phase composition 120
6.3.3 Mechanical properties 121
6.4 Friction and sliding wear tests 122
6.4.1 Wear mechanisms in sliding wear 125
6.5 Slurry erosion tests 128
6.5.1 Wear mechanisms of the eroded alloy surfaces 129
7. Discussion 133
7.1 Introduction 133
7.2 HVOF coatings 133
7.2.1 Material characterization 133
7.2.2 Friction and sliding wear response of the coatings 136
7.2.3 Slurry wear response of the coatings 140

7.3 Conventionally sintered alloys 143
7.3.1 Material characterization..... 143
7.3.2 Friction and sliding wear response of the conventionally sintered alloys 144
7.3.3 Slurry wear response of the conventionally sintered alloys..... 146
7.4 Spark plasma sintered alloys 148
7.4.1 Material characterization..... 148
7.4.2 Friction and sliding wear response of the spark plasma sintered alloys 148
7.4.3 Slurry wear response of the spark plasma sintered alloys..... 150
7.5 Conventionally sintered alloys vs. spark plasma sintered alloys 151
7.6 The role of 10wt%VC in the materials..... 154
8. Conclusions..... 155
8.1 General conclusions 155
8.2 Coatings..... 155
8.3 Conventionally sintered alloys 156
8.4 Spark plasma sintered alloys 157
9. Recommendations..... 158
References 159
APPENDICES 174
APPENDIX A: GENERAL DATA 174
Appendix A1: Calculation of the equivalence of weight percent and volume fractions of the starting powders..... 174
Appendix A2: Summary of the properties of the balls used in the friction and sliding wear test as supplied by the manufacturer 176
Appendix A3: Derivation of the formulae for the calculation of wear volume of the samples and the balls used in friction and sliding wear test. 176
APPENDIX B: HVOF THERMAL SPRAY COATINGS 180
Appendix B1: Friction responses..... 180
Appendix B2: SEM images of the wear tracks..... 181
Appendix B3: XPS spectra on the worn tracks after sliding test. 182
Appendix B3A: Against 100Cr steel balls..... 182
Appendix B3B: Against WC-Co balls..... 184

Appendix B4: Slurry erosion wear data 186
Appendix B4A: Average mass loss and erosion rate against time curves... 186
Appendix B4B: High magnification SEM images of the eroded surfaces .. 187
Appendix B5: EDAX mapping and EDX analyses on the eroded surface of WC-17wt%Co-10wt%VC coatings..... 189
APPENDIX C: CONVENTIONALLY SINTERED ALLOYS 191
Appendix C1: Friction responses 191
Appendix C2: SEM images of the wear surface after sliding 191
Appendix C3: Slurry erosion wear data 192
Appendix C3A: Average mass loss and erosion rate against time curves... 192
Appendix C3B: High magnification SEM images of the eroded surfaces..... 193
APPENDIX D: SPARK PLASMA SINTERED ALLOYS..... 194
Appendix D1: Friction responses..... 194
Appendix D2: SEM images of the wear surface after sliding..... 194
Appendix D3: Slurry erosion wear data 195
Appendix D3A: Average mass loss and erosion rate against time curves... 195
Appendix D3B: High magnification SEM images of the eroded surfaces..... 196

LIST OF FIGURES

Figure 2. 1 Typical microstructure of sintered WC-12Co alloy (This study). 7
Figure 2. 2 Fracture toughness against hardness for a range of WC-Co hardmetals with differing grain sizes and binder contents **[32]**..... 9
Figure 2. 3 Relationship between Young's modulus and Co content for samples with a WC grain size of 20 μm **[34]**..... 10
Figure 2. 4 Influence of WC grain size on the transverse rupture strength of WC-6Co hardmetals **[35]**..... 11
Figure 2. 5 Typical microstructure of sintered WC-12Co-10VC alloy (This study). 13
Figure 2. 6 Schematic diagram of a SPS system **[54]**..... 15
Figure 2. 7 Flame temperature-particle velocity combinations of various thermal spray techniques. FS: flame spray; ARC: arc spray; APS/VPS: air/vacuum plasma spraying; DGS: detonation gun spray; HP/HVOF: high pressure, high velocity oxy-fuel spraying **[73]**..... 22
Figure 2. 8 Schematic diagram of HVOF combustion chamber **[79]**. 23
Figure 2. 9 (a) Hardness, (b) fracture toughness, and (c) specific wear rate of 27
Figure 2. 10 The coefficient of friction as a function of sliding distance. (a) A typical S-shaped curve (b) Four hypothetical friction patterns **[112]**. 33
Figure 2. 11 Schematic showing two possibilities of break (1 and 2) during shearing of an interface (the arrow indicates the direction of sliding) **[112]**..... 36
Figure 2. 12 Diagram illustrating the combined influences of load and sliding speed on the sliding wear process [113]. 36
Figure 2. 13 Schematic of a jet of abrasive particles striking a surface at high velocity **[112]**. 37
Figure 2. 14 Variation of erosive wear with impact angle for ductile and brittle materials **[119]**. 38

Figure 3. 1 Sintering profile for WC-12wt%Co SPS alloy. 42
Figure 3. 2 Sintering profile for WC-12wt%Co-10wt%VC SPS alloy..... 43
Figure 3. 3 Malvern Mastersizer 2000 system. 44
Figure 3. 4 Measurement head of the tribometer (A) Applied load, (B) Elastic blade arm, (C) Ball holder, (D) Sample, (E) Disk mandrel. 52
Figure 3. 5 Measurement of the wear track on a WC-12wt%Co sample..... 53
Figure 3. 6 Measurement of the worn area on a 100Cr steel ball. 53
Figure 3. 7 Photograph of the slurry jet impingement rig. 55
Figure 3. 8 Photograph of the impact chamber showing the sample holder (A) and the exit nozzle (B). 55

Figure 4. 1 Morphologies of the (a) WC-12wt%Co, (b) WC-12wt%Co-10wt%VC and (c) WC-17wt%Co-10wt%VC powders. 59
Figure 4. 2 XRD patterns for (a) WC-12wt%Co, (b) WC-12wt%Co-10wt%VC, and (c) WC-17wt%Co-10wt%VC powders. 61
Figure 4. 3 Optical images showing the cross-section of the coating-substrate interface for (a) WC-12wt%Co, (b) WC-12wt%Co-10wt%VC, (c) WC-17wt%Co-10wt%VC (Run 38) and (d) WC-17wt%Co-10wt%VC (Run 39) coatings. 62
Figure 4. 4 BSE image of (a) WC-12wt%Co, (b) WC-12wt%Co-10wt%VC, (c) WC-17wt%Co-10wt%VC (Run 38) and (d) WC-17wt%Co-10wt%VC (Run 39) coatings. WC grains appear as roundish white particles; Co binder phase as a continuous light grey region; and (W,V)C grains as irregularly shaped dark grey regions. The black regions/spots are pores. 63
Figure 4. 5 EDS analysis of the (a) white phase showing WC roundish grains and (b) dark grey regions showing irregularly shaped (W,V)C grains, and (c) continuous matrix. 64
Figure 4. 6 EDAX maps showing the elemental distribution in the WC-12wt%Co-10wt%VC coatings. (a) SEM image (b) Co (c) V and (d) W. 65
Figure 4. 7 EDAX maps showing the elemental distribution in the WC-17wt%Co-10wt%VC (Run 38) coatings. (a) SEM image (b) Co (c) V and (d) W. 65
Figure 4. 8 EDAX maps showing the elemental distribution in the WC-17wt%Co-10wt%VC (Run 39) coatings. (a) SEM image (b) Co (c) V and (d) W. 66
Figure 4. 9 XRD pattern of (a) WC-12wt%Co, (b) WC-12wt%Co-10wt%VC, (c) WC-17wt%Co-10wt%VC (Run 38), and (d) WC-17wt%Co-10wt%VC (Run 39) coatings. 67
Figure 4. 10 Friction behavior against 100Cr ball for (a) WC-12wt%Co, (b) WC-12wt%Co-10wt%VC, (c) WC-17wt%Co-10wt%VC (Run 38), and (d) WC-17wt%Co-10wt%VC (Run 39) coatings. 70
Figure 4. 11 Friction behavior against WC-Co ball for (a) WC-12wt%Co, (b) WC-12wt%Co-10wt%VC, (c) WC-17wt%Co-10wt%VC (Run 38), and (d) WC-17wt%Co-10wt%VC (Run 39) coatings. 71
Figure 4. 12 Friction coefficients for the ball-coating pairs. 72
Figure 4. 13 Wear coefficients comparison for the coatings. 73
Figure 4. 14 Wear coefficients comparison for the balls. 73
Figure 4. 15 SEM images of the wear tracks against 100Cr ball for (a) WC-12wt%Co, (b) WC-12wt%Co-10wt%VC, (c) WC-17wt%Co-10wt%VC (Run 38), and (d) WC-17wt%Co-10wt%VC (Run 39) coatings. 76
Figure 4. 16 SEM images of the wear tracks against WC-Co ball for (a) WC-12wt%Co, (b) WC-12wt%Co-10wt%VC, (c) WC-17wt%Co-10wt%VC (Run 38), and (d) WC-17wt%Co-10wt%VC (Run 39) coatings. 78
Figure 4. 17 SEM image with EDX analysis of the wear tracks on the 100Cr steel ball against (a) WC-12wt%Co, (b) WC-12wt%Co-10wt%VC, (c) WC-17wt%Co-10wt%VC (Run 38), and (d) WC-17wt%Co-10wt%VC (Run 39) coatings. 81

Figure 4. 18 SEM images with EDX analysis of the wear tracks of the WC-Co ball against (a) WC-12wt%Co, (b) WC-12wt%Co-10wt%VC, (c) WC-17wt%Co-10wt%VC (Run 38), and (d) WC-17wt%Co-10wt%VC (Run 39) coatings. 83
Figure 4. 19 Selected XPS spectra against the 100Cr steel ball for the (a) un-worn track (b) WC-12wt%Co, (c) WC-12wt%Co-10wt%VC, and (c) WC-17wt%Co-10wt%VC coatings. 86
Figure 4. 20 Selected XPS spectra against the WC-Co ball for the (a) WC-12wt%Co, and (b) WC-12wt%Co-10wt%VC coatings. 86
Figure 4. 21 Comparison of the average mass loss against time curves of the coatings at 90° impact angle. 87
Figure 4. 22 Comparison of the average erosion rate against impact angles. 88
Figure 4. 23 SEM images of the eroded surface of the WC-12wt%Co at (a) 90°, (b) 75°, (c) 60°, and (d) 45°. 90
Figure 4. 24 SEM images of the eroded surface of the WC-12wt%Co-10wt%VC at (a) 90°, (b) 75°, (c) 60°, and (d) 45°. 91
Figure 4. 25 SEM images of the eroded surface of the WC-17wt%Co-10wt%VC Run 38 at (a) 90°, (b) 75°, (c) 60°, and (d) 45°. 92
Figure 4. 26 SEM images of the eroded surface of the WC-17wt%Co-10wt%VC Run 39 at (a) 90°, (b) 75°, (c) 60°, and (d) 45°. 93
Figure 4. 27 (a) BSE SEM image, (b) EDAX maps overlay and (c) EDX analysis on the eroded surface of the WC-12wt%Co coatings (Brown = C; Blue = Co; Green = O; Yellow = W)..... 94
Figure 4. 28 (a) BSE SEM image, (b) EDAX maps overlay and (c) EDX analysis on the eroded surface of the WC-12wt%Co-10wt%VC coatings (Brown = C; Blue = Co; Green = O; Yellow = W; Purple = V). 95

Figure 5. 1 Morphology and EDX analysis of (a) and (b) WC-12wt%Co powder, (b) and (c) WC-12wt%Co-10wt%VC powder. 97
Figure 5. 2 XRD patterns for (a) WC-12wt%Co and (b) WC-12wt%Co-10wt%VC powders. 98
Figure 5. 3 SEM and optical images of the (a) un-etched WC-12wt%Co, (b) etched WC-12wt%Co, (c) un-etched WC-12wt%Co-10wt%VC, and (d) etched WC-12wt%Co-10wt%VC alloys. WC grains appear as white particles; Co binder phase as continuous region; and (W,V)C grains as irregularly shaped dark grey regions. The black regions/spots are pores. 99
Figure 5. 4 EDS analysis of the (a) white phase showing WC angular grains and (b) dark grey regions showing irregularly shaped (W,V)C grains, and (c) continuous matrix. 100
Figure 5. 5 XRD patterns for (a) WC-12wt%Co and (b) WC-12wt%Co-10wt%VC alloys. 101
Figure 5. 6 Friction behavior against 100Cr ball for (a) WC-12wt%Co and (b) WC-12wt%Co-10wt%VC alloys. 103

Figure 5. 7 Friction coefficients for the alloy-ball pairs sliding against the 100Cr steel balls. 104
Figure 5. 8 Comparison of the wear coefficients of the 100Cr steel ball-alloy sliding pairs. 105
Figure 5. 9 Wear coefficients comparison for the sintered alloys. 106
Figure 5. 10 SEM images with EDX analysis of the wear tracks against 100Cr ball for (a) WC-12wt%Co and (b) WC-12wt%Co-10wt%VC alloys. 108
Figure 5. 11 SEM images of the wear scars on the 100Cr steel ball for (a) WC-12wt%Co and (b) WC-12wt%Co-10wt%VC alloys. 109
Figure 5. 12 Comparison of the average volume loss against time curves of both alloys at 90°. 111
Figure 5. 13 Comparison of the average erosion rate against impact angles. 111
Figure 5 14 SEM images of the eroded surface of the WC-12wt%Co at (a) 90°, (b) 75°, (c) 60°, and (d) 45°. 113
Figure 5. 15 SEM images of the eroded surface of the WC-12wt%Co-10wt%VC at (a) 90°, (b) 75°, (c) 60°, and (d) 45°. 114

Figure 6. 1 Morphology and EDX analysis of (a) and (b) WC-12wt%Co powder, (b) and (c) WC-12wt%Co-10wt%VC powder. 115
Figure 6. 2 XRD patterns for (a) WC-12wt%Co (b) WC-12wt%Co-10wt%VC powders. 117
Figure 6. 3 SEM and optical images of the (a) un-etched WC-12wt%Co, (b) etched WC-12wt%Co, (c) un-etched WC-12wt%Co-10wt%VC, and (d) etched WC-12wt%Co-10wt%VC alloys. WC grains appear as white particles; Co binder phase as continuous region; and (W,V)C grains as irregularly shaped dark grey regions. The black regions/spots are pores. 118
Figure 6. 4 EDS analysis of the (a) white phase showing roundish WC grains and (b & c) light and dark grey regions showing irregularly shaped (W,V)C grains, and (d) continuous matrix. 119
Figure 6. 5 XRD patterns for (a) WC-12wt%Co (b) WC-12wt%Co-10wt%VC alloys. 120
Figure 6. 6 Friction behavior against 100Cr ball for (a) WC-12wt%Co and (b) WC-12wt%Co-10wt%VC alloys. 122
Figure 6. 7 Friction coefficients for the alloy-ball pairs. 123
Figure 6. 8 Comparison of the wear coefficients of the sintered alloys against the 100Cr steel balls. 124
Figure 6. 9 Comparison of the wear coefficients of the 100Cr steel balls sliding pairs against the alloys. 124
Figure 6. 10 SEM images with EDX analysis of the wear tracks against 100Cr ball for (a) WC-12wt%Co and (b) WC-12wt%Co-10wt%VC alloys. 126
Figure 6. 11 SEM images with EDX analysis of the wear tracks against 100Cr ball for (a) WC-12wt%Co and (b) WC-12wt%Co-10wt%VC alloys. 128

Figure 6. 12 Comparison of the average volume loss against time curves of both alloys at 90°. 129
Figure 6. 13 Comparison of the average erosion rate against impact angles. 129
Figure 6. 14 SEM images of the eroded surface of the WC-12wt%Co alloy at (a) 90°, (b) 75°, (c) 60°, and (d) 45°. 131
Figure 6. 15 SEM images of the eroded surface of the WC-12wt%Co-10wt%VC alloy at (a) 90°, (b) 75°, (c) 60°, and (d) 45°. 132

Figure A3. 1 Schematic plan view of the worn track of the samples 177
Figure A3. 2 Sketch showing parameters, a, b, h and R of a spherical segment 178

Figure B1. 1 Friction response against 100Cr steel ball against (a) WC-12wt%Co, (b) WC-12wt%Co-10wt%VC, (c) WC-17wt%Co-10wt%VC (Run 38), and (d) WC-17wt%Co-10wt%VC (Run 39) coatings. 180
Figure B1. 2 Friction response against WC-Co ball against (a) WC-12wt%Co, (b) WC-12wt%Co-10wt%VC, (c) WC-17wt%Co-10wt%VC (Run 38), and (d) WC-17wt%Co-10wt%VC (Run 39) coatings. 181

Figure B2. 1 High magnifications SEM images against the 100Cr steel ball on the wear tracks of (a) WC-12wt%Co, (b) WC-12wt%Co-10wt%VC, (c) WC-17wt%Co-10wt%VC (Run 38), and (d) WC-17wt%Co-10wt%VC (Run 39) coatings. 181
Figure B2. 2 High magnifications SEM images against the 100Cr steel ball on the wear tracks of (a) WC-12wt%Co, (b) WC-12wt%Co-10wt%VC, (c) WC-17wt%Co-10wt%VC (Run 38), and (d) WC-17wt%Co-10wt%VC (Run 39) coatings. 182

Figure B3A. 1 Wide XPS scan of the wear tracks on the (a) WC-12wt%Co, (b) WC-12wt%Co-10wt%VC and (c) WC-17wt%Co-10wt%VC coatings. 182
Figure B3A. 2 Narrow XPS scans of the wear track of the WC-12wt%Co coating showing (a) carbon (b) iron (c) oxygen and (d) tungsten peaks. The inserted tables show the de-convolution of peaks. 182
Figure B3A. 3 Narrow XPS of the worn track of the WC-12wt%Co-10wt%VC coating showing (a) carbon (b) cobalt (c) oxygen (d) vanadium and (e) tungsten peaks. The inserted tables show the de-convolution of peaks. 183
Figure B3A. 4 Narrow XPS of the worn track of the WC-12wt%Co-10wt%VC coating showing (a) carbon (b) cobalt (c) oxygen (d) vanadium and (e) tungsten peaks. The inserted tables show the de-convolution of peaks. 183

Figure B3B. 1 Wide XPS scan of the wear tracks on the (a) WC-12wt%Co, (b) WC-12wt%Co-10wt%10VC and (c) WC-17wt%Co-10wt%VC coatings 184

Figure B3B. 2 Narrow XPS scans of the wear track of the WC-12wt%Co coating showing (a) carbon (b) iron (c) oxygen and (d) tungsten peaks. The inserted tables show the de-convolution of peaks. 184
Figure B3B. 3 Narrow XPS scans of the wear track of the WC-12wt%Co-10wt%VC coating showing (a) carbon (b) iron (c) oxygen and (d) tungsten peaks. The inserted tables show the de-convolution of peaks..... 184
Figure B3B. 4 Narrow XPS scans of the wear track of the WC-17wt%Co-10wt%VC coating showing (a) carbon (b) iron (c) oxygen and (d) tungsten peaks. The inserted tables show the de-convolution of peaks..... 185

Figure B4A. 1 Average mass losses against time curves for (a) 90°, (b) 75°, (c) 60°, and (d) 45°. 186
Figure B4A. 2 Average erosion rate against time curves for (a) 90°, (b) 75°, (c) 60°, and (d) 45°. 186

Figure B4B. 1 SEM images of the eroded surface of (a) WC-12wt%Co, (b) WC-12wt%Co-10wt%VC, (c) WC-17wt%Co-10wt%VC (Run 38), and WC-17wt%Co-10wt%VC (Run 39) coatings at 90°. 187
Figure B4B. 2 SEM images of the eroded surface of (a) WC-12wt%Co, (b) WC-12wt%Co-10wt%VC, (c) WC-17wt%Co-10wt%VC (Run 38), and WC-17wt%Co-10wt%VC (Run 39) coatings at 75°. 187
Figure B4B. 3 SEM images of the eroded surface of (a) WC-12wt%Co, (b) WC-12wt%Co-10wt%VC, (c) WC-17wt%Co-10wt%VC (Run 38), and WC-17wt%Co-10wt%VC (Run 39) coatings at 60°. 188
Figure B4B. 4 SEM images of the eroded surface of (a) WC-12wt%Co, (b) WC-12wt%Co-10wt%VC, (c) WC-17wt%Co-10wt%VC (Run 38), and WC-17wt%Co-10wt%VC (Run 39) coatings at 45°. 188

Figure C1. 1 Friction response against the 100Cr steel ball for (a) WC-12wt%Co, and (b) WC-12wt%Co-10wt%VC alloys..... 191

Figure C2. 1 High magnification SEM images of the wear surfaces after sliding against 100Cr steel ball for (a) WC-12wt%Co, and (b) WC-12wt%Co-10wt%VC alloys. 191

Figure C3A. 1 Average mass losses against time curves for (a) 90°, (b) 75°, (c) 60°, and (d) 45°. 192
Figure C3A. 2 Average erosion rate against time curves for (a) 90°, (b) 75°, (c) 60°, and (d) 45°. 192

Figure C3B. 1 SEM images of the eroded surface of WC-12wt%Co alloy at (a) 90°, (b) 75°, (c) 60°, and (d) 45°. 193

Figure C3B. 2 SEM images of the eroded surface of WC-12wt%Co-10wt%VC alloy at (a) 90°, (b) 75°, (c) 60°, and (d) 45°. 193

Figure D1. 1 Friction response against the 100Cr steel ball for (a) WC-12wt%Co, and (b) WC-12wt%Co-10wt%VC alloys. 194

Figure D2. 1 High magnification SEM images of the wear surfaces after sliding against 100Cr steel ball for (a) WC-12wt%Co, and (b) WC-12wt%Co-10wt%VC alloys. 194

Figure D3A. 1 Average mass losses against time curves for (a) 90°, (b) 75°, (c) 60°, and (d) 45°. 195
Figure D3A. 2 Average mass losses against time curves for (a) 90°, (b) 75°, (c) 60°, and (d) 45°. 195

LIST OF TABLES

Table 2. 1 Comparison of properties of WC and VC [39]. 12

Table 3. 1 Powder compositions in weight percent and volume fraction. 40
Table 3. 2 Characteristics of the starting powders. 40
Table 3. 3 Spray parameters for the WC-12Co and WC-12Co-10VC coatings [70]. 41
Table 3. 4 Spray parameters for the WC-17Co-10VC coatings [120]. 41
Table 3. 5 Grinding and polishing procedure. 45
Table 3. 6 Friction and sliding wear test parameters. 51
Table 3. 7 Friction and sliding wear test parameters. 56

Table 4. 1 Powder particle size and size distributions 59
Table 4. 2 Powder particle size and size distributions 60
Table 4. 3 Porosity levels and coating thicknesses. 62
Table 4. 4 Phase composition of coatings as determined from Rietveld analysis. 67
Table 4. 5 Carbide grain sizes of coatings. 68
Table 4. 6 Hardness values of the coatings. 69
Table 4. 7 Ball penetration depths and wear track width on the coatings. 72
Table 4. 8 XPS results of the worn coating surfaces. 85

Table 5. 1 Powder particle size and size distributions. 97
Table 5. 2 Powder particle size and size distributions. 98
Table 5. 3 Physical properties of the conventionally sintered alloys. 101
Table 5. 4 Phase composition of alloys. 102
Table 5. 5 Mechanical properties of the alloys. 102
Table 5. 6 Ball penetration depths and wear track width on the alloys. 104

Table 6. 1 Powder particle size and size distributions. 116
Table 6. 2 Powder particle size and size distributions. 116
Table 6. 3 Physical properties of the spark plasma sintered alloys. 120
Table 6. 4 Phase composition of alloys. 121
Table 6. 5 Mechanical properties of the alloys. 121
Table 6. 6 Ball penetration depths and wear track width on the alloys. 123

Table 7. 1 Hypothetical friction patterns obtained for the ball-coating sliding pairs. 137
Table 7. 2 Hardness ratios and maximum stress applied during sliding. 138
Table 7. 3 Hardness ratios for the eroded materials. 142

Table 7. 4 Hypothetical friction patterns obtained for the ball-alloy sliding pairs. 144
Table 7. 5 Summary of the E/H ratio, the H_b/H_a ratio and the applied stress for alloys sliding against the 100Cr steel ball. 145
Table 7. 6 Hardness ratios for the eroded materials. 147
Table 7. 7 Hypothetical friction patterns obtained for the ball-alloys sliding pair 149
Table 7. 8 Summary of the E/H ratio, the H_b/H_a ratio and the applied stress for the SPS alloys sliding against the 100Cr steel ball. 149
Table 7. 9 Hardness ratios for the eroded materials. 150
Table 7. 10 Comparison of the properties between the conventionally sintered alloys and the spark plasma sintered alloys. 151

Table A1.1 Relative molecular masses of chemical species 174
Table A1.2 Calculation of volume fractions 176

Table A2. 1 Properties of the balls 176

LIST OF SYMBOLS

SEM – Scanning Electron Microscopy

EDX – Energy Dispersive X-ray Spectroscopy

XRD – X-ray Diffraction

XPS – X-ray Photoelectron Spectroscopy

ICSD – International Centre for Diffraction Data

HVOF – High-Velocity-Oxy-Fuel

SPS – Spark Plasma Sintering

HV – Vickers Hardness

K_{IC} – Fracture toughness

hr(s) – Hours

min(s) – Minute(s)

μm – Micron

wt% - Weight per cent

°C – degrees Celsius

1. Introduction

Cemented carbides were introduced to the market by Fried Krupp of Germany in 1927 under the name Widia (wie Diamant—like diamond) and consisted of tungsten carbide (WC) particles cemented in a 6 wt% cobalt (Co) binder **[1]**. The advent of cemented carbides began with the idea of replacing costly diamond wire drawing dies used for tungsten filaments **[1]**. This group of sintered materials had outstanding properties of high levels of hardness and wear resistance provided by the WC phase while the ductile Co binder contributed a moderate toughness. After this successful application, attention was drawn to better cutting tools and finally to a variety of wear parts and machine components. Today, WC-Co alloys are used in a wide range of applications where wear resistance is very important, such as sand blast/spray nozzles, seals in slurry pumps, drill bit inserts in the mining industry, cutting tools, forming dies, projectiles, rolls, shafts and component parts in the oil industry **[2-4]**.

Schwarzkopf's **[5]** discovery that solid solutions of more than one carbide are superior to individual carbides was the starting point that initiated the development of multicarbide cutting tools for the high speed machining of steel **[1]**. In these materials the composition is modified such that a portion of the WC phase is replaced by transition metal carbides. Metals such as vanadium, niobium, chromium, titanium, tantalum and molybdenum are often added in small quantities to improve the hardmetals properties such as increased hardness by grain refinement, improved corrosion resistance of the binder, and machinability **[5]**. Since their discovery in 1923 **[6]**, these materials have been extensively investigated with the aim of improving their performance. This research project focused on the addition of 10 wt% vanadium carbide (VC) to WC-Co conventionally sintered alloys, spark plasma sintered alloys and thermal spray coatings to improve wear performance and possibly energy conservation.

Energy conservation is promoting the development of lighter components and increasing the need to reduce energy costs during alloy production. In terms of lighter alloys, ceramic compositions are good alternatives but their application is limited when high fracture toughness is required. Therefore, the development of modified WC-Co grades with lower densities would be of technical interest **[7]**. To date research has been conducted on the partial substitution of WC by other non-oxidic compounds, such as Ti(C, N), Mo_2C, Cr_3C_2, TiN, TiC and VC **[8-11]**. Vanadium carbide is generally used in cemented carbide commercial grades in quantities lower than 1 wt% as WC grain growth inhibitors leading to the attainment of higher alloy hardness **[12]**. Limited published research exists on the influence of VC on WC-Co properties and performance when it is added in higher quantities **[13-17]**. VC has a lower density (5.6 g/cm^3 compared to 15.6 g/cm^3 **[18]**) and higher hardness (2800 $HV_{0.05}$ compared to 2000 $HV_{0.05}$ **[18]**) than WC and if added successfully to hardmetals in high quantities could produce lighter and stronger components.

With respect to the reduction of energy costs during alloy production, a recently developed sintering technique, namely spark plasma sintering (SPS), has attracted attention in cemented carbide production due to its rapid heating and rapid sintering at relatively low temperatures and short holding times in comparison with conventional sintering processes **[19-21]**. As consolidation is achieved at a low temperature, grain growth is also minimized. A small grain size results in increased hardness, strength and wear properties of the alloy leading to increased tool efficiencies and lifetimes. To date limited research has been conducted on SPS of cemented carbides therefore the SPS production of cemented carbides with a high VC addition would have scientific merit.

Cemented carbides are also used as wear resistant coatings in a variety of industrial applications. Currently, commercial hardmetal coatings may contain limited amounts of VC. It would therefore be of scientific and commercial interest

to explore the addition of a high amount of VC to hardmetal in order to see if the benefits of VC additions to sintered alloys may be realized in coatings.

In summary, in this research study WC-Co and WC-Co-VC materials were manufactured using three different techniques to produce thermal spray coatings (TSC), conventionally sintered alloys (CSA) and spark plasma sintered alloys (SPSA). The VC addition was kept constant at 10 wt% (and this was meant to show that VC could be used as a partial substitute for WC) for all materials while the Co binder content was varied for the thermal spray coatings. The wear performance of the materials was characterized in terms of friction, sliding wear and slurry erosion. This study using the proposed methodology was expected to give the following contributions to scientific knowledge:

- Provide new information on high content VC thermal spray coatings.
- Provide new information on SPS produced VC alloys.
- Provide new information on the wear mechanisms of cemented carbides.

1.1 Aims and Objectives of the research

The main aim of the research was to improve the wear resistance of WC-Co sintered alloys and thermal spray coatings. A secondary aim was to reduce energy in the production and application of the sintered materials. These aims were achieved through the following objectives:

- Material characterization of novel WC-Co-VC thermal spray coatings;
- Production and material characterization of novel WC-Co-VC alloys using spark plasma sintering;
- Assessment of the wear performance of the materials using friction, sliding wear and slurry erosion tests;

- Comparison of SPS production to conventional production of sintered alloys;
- Comparison of the properties of the WC-Co-VC materials to those of the WC-Co materials to assess the effect of the high VC addition.

1.2 Structure of the thesis

This thesis is structured in the following manner: Chapter 1 explains the significance of the research work. Chapter 2 reviews published literature on the production and properties of WC-Co alloys and coatings as well as some of the fundamentals of friction and wear. Chapter 3 describes the various manufacturing techniques used to produce the materials and describes the instruments and methods used to characterize the materials. The results of the tests described in Chapter 3 are divided into three chapters. The thermal spray coating (TSC) results are presented in Chapter 4. Chapter 5 presents results of the conventionally sintered alloys (CSA) while Chapter 6 focuses on the results of the spark plasma sintered (SPS) alloys. The results are discussed in Chapter 7 while Chapters 8 and 9 provide the conclusions, and recommendations for future work, respectively. Finally a list of references and relevant appendices are provided.

2. Literature review

This review starts by describing the conventional method used to produce cemented carbide alloys and includes a review of the properties of these materials. The addition of VC and its influence on the microstructure and properties is discussed. This is followed by a description of the spark plasma sintering process and a review of the production and properties of WC-Co and WC-Co-VC alloys using this process. A description of the HVOF process used to produce thermal spray coatings is given followed by a review of thermally sprayed WC-Co and WC-Co-VC coatings and their respective properties. The chapter ends with a review on the fundamentals of friction, sliding and erosive wear.

2.1 Conventionally sintered WC-Co alloys

Cemented carbides (hardmetals) are a group of sintered materials essentially made up of tungsten carbide (WC) particles, cemented together by a metal or alloy of the iron group, typically cobalt (Co) **[22]**. In this combination, the carbide phase provides the hardness and the wear resistance while the ductile Co binder contributes the toughness. These hardmetals are used in a wide range of applications where wear resistance is very important, such as sand blast/spray nozzles, seals in slurry pumps, drill bit inserts in the mining industry, cutting tools, forming dies, projectiles, rolls, shafts and component parts in the oil industry **[2-4]**. In this section a description of the conventional production process is given followed by a review of the material properties. The section closes with a review of the influence of vanadium carbide (VC) additions to these alloys.

2.1.1 Production of WC-Co alloys

Cemented carbides are manufactured by powder metallurgy (PM) techniques which involves fabrication using compaction and sintering techniques. The metal powders that form the final product undergo controlled carburization which

produces the various carbides. These carbide powders are ball milled with the metal binder. Ball milling reduces the size of the carbide particles and ensures even coating by the metal binder particles **[23-24]**. Milling is performed in the presence of a milling liquid such as ethanol, heptane or acetone to minimize heating of the powder and to prevent its oxidation. An organic binder such as paraffin wax is added to the powder blend in the final stages of the milling process or later in the blender. The organic binder provides a protective coating for the carbide particles and prevents or greatly reduces oxidation of the powder. The binder also improves the pressing properties of the powder and imparts strength to the pressed or consolidated powder mix (the green body). After milling, the milling liquid is removed by drying. In a spray-drying process commonly used in the cemented carbide industry, a hot inert gas such as nitrogen impinges on a stream of carbide particles. This produces free-flowing spherical powder aggregates **[25]**.

The carbide and cobalt powder mixture is then compacted into billets by hydrostatic means or they are press-compacted into components. Finally, the billets are generally vacuum or hydrogen hip-sintered to produce the final component form **[23-24]**. During the sintering process the microstructure is formed. The carbide phase partially dissolves within the binder and re-precipitates. This process results in the final shape and structure of the carbide grains. In cemented carbides, the solubility of the metallic elements within WC is very low and thus WC forms well defined single crystals, shown in **Figure 2.1**. Cemented carbides are manufactured into different grades by modifying the composition and weight percentage of the carbide/binder as well as the powder particle size **[24]**. The cobalt content is the most important variable when cemented carbides of varying properties are required; cobalt contents up to a maximum of 15-25% mass have the effect of increasing the transverse rupture strength of the cemented carbide significantly **[1]**.

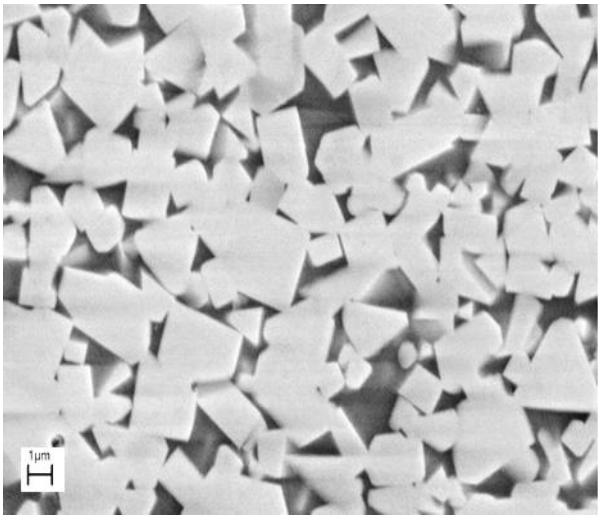


Figure 2. 1 Typical microstructure of sintered WC-12Co alloy (This study).

2.1.2 Properties of WC-Co alloys

Hardness

Cemented carbides are known for their high hardness, which lends itself to high wear resistance **[24]**. The hardness of cemented carbides used for the machining of steel usually ranges between 1100HV to 1600HV, although it can be higher **[26]**. The hardness is not only influenced by the hardmetals' composition but also the carbide grain size, the binder content, the level of porosity and the microstructure **[27]**. These materials are also known to have high hot-hardness qualities which are dependent on the carbide content **[26]**. The hardness of tungsten carbide based hardmetals has been extensively characterized and has been found to increase with decreasing cobalt content and decreasing WC grain size **[27]**.

Fracture toughness

Fracture toughness indicates the resistance of a material to fracture in the presence of a sharp crack. The fracture toughness is measured by the critical stress intensity factor, K_{IC}. The K_{IC} values are calculated from **Equation 2.1 [28]**.

$$K_{IC} = A\sqrt{\frac{HF}{\sum_i a_i}} \qquad 2.1$$

Where

H is the hardness of the material, (HV)

F the indentation load (kg) and

a_i the length of each Palmqvist crack (mm).

A = calibration constant.

All the quantities are expressed in SI units and the constant A is equal to 0.0028 **[28]**.

A plot of the toughness versus hardness exhibits the expected relationship, i.e. the toughness decreases with increasing hardness **(Figure 2.2)**. However for nanostructured hardmetals there is no decrease of the toughness with increasing hardness which implies that different toughening mechanisms are present in conventional and nanostructured materials. The fracture toughness and hardness of hardmetals vary in different ways when the composition and/or microstructure of the material are varied. There is some disagreement in the literature as to what type of relationship exists between these properties **[29-31]**.

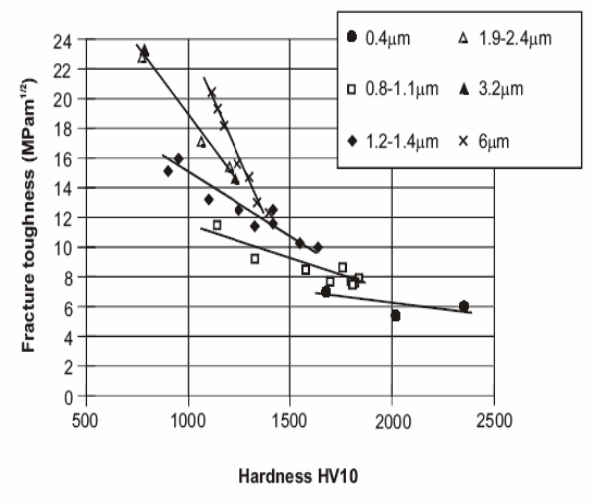


Figure 2. 2 Fracture toughness against hardness for a range of WC-Co hardmetals with differing grain sizes and binder contents **[32]**.

Young's modulus

Young's modulus for WC-Co hardmetals usually lies in the range of 400 to 700 GPa **[12]**. Okamoto *et al.*, **[33]** studied the relationship between Young's modulus and several microstructural parameters in WC-Co hardmetals. Young's modulus of approximately 577 GPa was quoted for samples with a WC grain size ranging from 3 to 20 μm and 523 GPa for samples with a WC grain size of 30 μm. Therefore no clear correlation between the WC grain size and Young's modulus could be established. However, the Young's modulus was found to be inversely proportional to the Co content as shown in **Figure 2.3**. This suggests that the Young's modulus of WC-Co hard metals depends on the ratio of WC to Co.

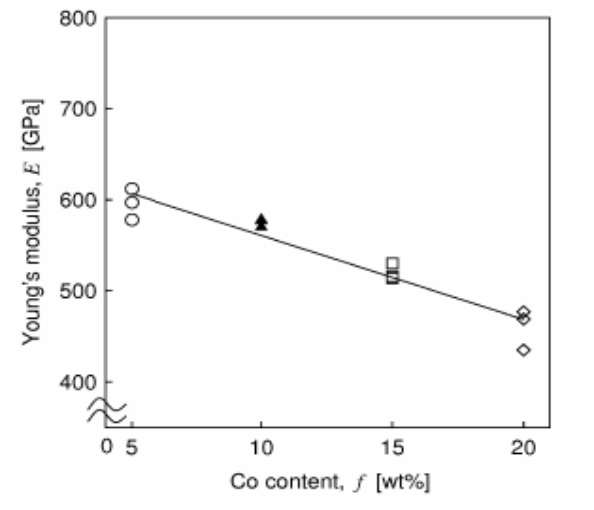


Figure 2. 3 Relationship between Young's modulus and Co content for samples with a WC grain size of 20 μm **[34]**.

Strength properties

Cemented carbides have high compressive strength, much greater than those of most other materials. Typical values of compressive strength range from 3.5 to 7.0 GPa. These materials have low ductility at room temperature so that little difference exists between their yield strength and fracture strength. At higher temperatures the ductility increases slightly. The yield stress decreases monotonically with increasing temperature and the fine-grained carbides tend to lose their yield strength much more rapidly than the coarser grades. However at room temperature the fine-grained carbides exhibit high yield strength **[12]**. The transverse rupture strength (TRS) is a three-point flexure test used to measure the strength of sintered materials and is commonly used in the testing of WC-Co hardmetals. Work by Exner **[35]** showed that the WC grain size has an influence on the TRS of WC-Co hardmetals **(Figure 2.4)**.

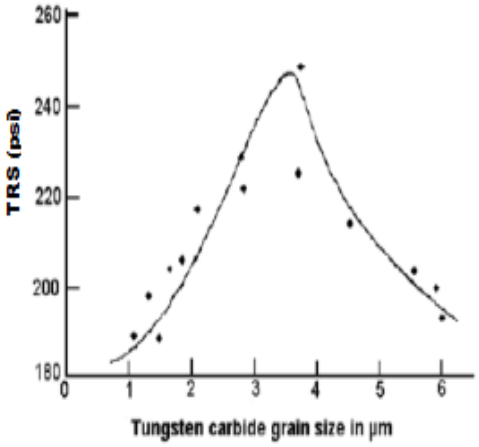


Figure 2. 4 Influence of WC grain size on the transverse rupture strength of WC-6Co hardmetals **[35]**.

Wear behaviour

Bonny *et al.* **[36]** demonstrated that an increase in load and in the sliding velocity causes increased wear rate. The authors noted little similarity between the material microstructures and mechanisms of wear in sintered and thermally sprayed WC-Co hardmetals.

2.1.3 Vanadium carbide in sintered WC-Co alloys

Addition of VC to sintered WC-Co alloys is usually done in small quantities (up to 1 wt%) to inhibit grain growth during sintering **[37-38]**. Higher additions up to 2.5 wt% grant improved hardness and wear resistance during machining operations, but cause embrittlement, an occurrence that appears to have discouraged further research **[37]**. The embrittlement was reported to be as a result of large grains of the carbide phases **[18]**.

In the early 1990's, interest in the addition of higher amounts of VC in sintered WC-Co alloys took a new turn with the aim of optimizing microstructures and processing technique for the new WC-Co-VC alloys **[18]**. The interest was motivated by the fact that there was still room for improved properties such as harder components and weight savings. This is because the room temperature hardness of VC is higher than that of WC and also the density of VC is lower than that of WC. **Table 2.1** shows a comparison of the properties of WC and VC.

Table 2. 1 Comparison of properties of WC and VC **[39]**.

Property	**VC**	**WC**
Density ($g.cm^{-3}$)	5.7	15.7
Microhardness @ 50 g ($kg.\ mm^{-2}$)	2950	2080
Elastic modulus ($kN.mm^{-2}$)	422	696
Thermal expansion coefficient between 24 and 1925°C ($\times 10^{6}$)	7.2	5.0
Solubility in Cobalt (wt%)	6	22
Solubility in Iron (wt)	3	7

The production of sintered WC-Co-VC alloys follows the same powder technology route as that of the WC-Co alloys. The sintered alloys can be made from three types of starting powders namely: V_8C_7, WC and Co; V_2O_5, C, WC and Co; and V, W, C and Co. These powders are ball milled, compacted and sintered either under vacuum or consecutively under vacuum and argon gas **[15,18,40]**. Better properties of the sintered alloys can be obtained by controlling the growth of the VC grains during sintering **[15,18,40]**. This can be achieved by using starting powders having fine carbide grains and by sintering at the lowest possible temperature which can be determined by differential thermal analysis **[40]**.

Microstructure of sintered WC-Co-VC alloys

Microstructures obtained from sintered WC-Co-VC alloys generally consist of three phases namely: WC, Co and (W,V)C. The latter phase is formed due to the solubility of WC in VC **[39]**. Initial detailed analysis of the phase showed it to be of the form $(W_xV_yCo_z)C_7$ **[41]**, where values of x, y and z varied between 4.4 – 4.7; 3.2 – 3.4 and 0.1 – 0.2 respectively. It is possible that the atomic ratios of V and W can vary over a range of values as shown for heated and quenched alloys **[42]**. The contrast of (W,V)C grains on backscattered electron (BSE) micrographs obtained from scanning electron microscope (SEM) depends on the amount of W in solution in VC. It varies from light grey when the amount of W in solution is high to dark grey when the amount is low **[42]**. The formation of $(W,V)C_x$ is predicted in isothermal phase diagrams obtained at the sintering temperatures of the WC-Co-VC alloys **[43]**. However, the three phase field of WC, (W,V)x and Co, suitable for the production of sintered WC-Co-VC alloys, only occurs within a narrow range of compositions, and processing parameters need to be strictly controlled to avoid the formation of either graphite or eta phase. Figure 2.5 shows a typical microstructure obtained from a sintered WC-Co-VC alloy. **Figure 2.5** shows a typical microstructure of WC-Co-VC sintered alloy.

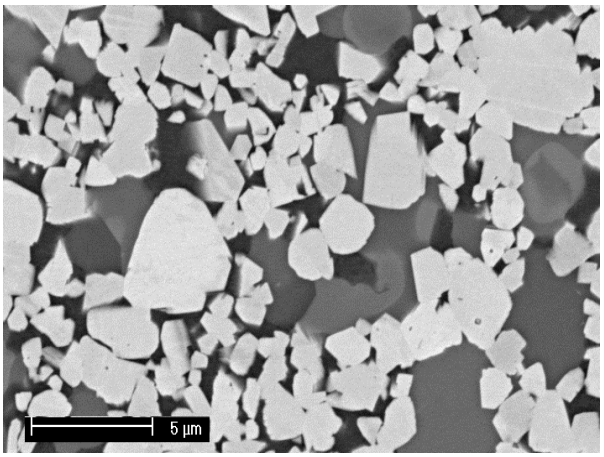


Figure 2. 5 Typical microstructure of sintered WC-12Co-10VC alloy (This study).

Properties of sintered WC-Co-VC alloys

The hardness of sintered WC-Co-VC alloys is higher than that of WC-Co alloys with the same cobalt mass content while the toughness is comparable, and at the same hardness level, the toughness of WC-Co-VC alloys is significantly higher than the toughness of WC-Co alloys, as long as the VC grains are small **[15,41,44]**. Alloys containing VC additions in the range of 20 to 35 wt% have a combined high hardness and rupture strength comparable to WC-Co alloys **[13]**. The improved hardness and toughness has led to improvements in both abrasion and erosion resistance **[40]**. These improvements in properties are achieved at the same time as weight savings are achieved, as the WC-Co-VC alloys are less dense than WC-Co alloys **[18,44]** having the same binder content (in weight per cent).

2.2 Spark plasma sintered alloys

Sintering densification is an important procedure to achieve a dense, hard alloy. It is well known that in conventional hardmetal sintering methods, to achieve a high density, a high sintering temperature, normally located at the liquid-sintering state, and a long holding time, are usually used. As a result, the WC grain size in the densified alloy is prone to increase into the micrometer scale even if the initial sizes of the composite powder particles are smaller than 100 nm **[45]**. The recently developed spark plasma sintering (SPS) technique enables the equivalent density of the conventionally sintered alloy to be achieved is shorter holding times and at lower temperatures **[46-47]**. Moreover, the grain growth during sintering can be effectively inhibited **[45]**. In this section a description of the general SPS process is given followed by a review of WC-Co and WC-Co-VC alloys produced using this method and the resultant properties achieved.

2.2.1 Description of SPS process

SPS uses moderate uni-axial pressures (typically less than 100 MPa) and an on–off DC pulsing current to sinter powders. During this on–off DC pulsing, there are a number of proposed mechanisms to account for the enhanced sintering behaviour. Many, but not all, of these mechanisms assume the presence of a momentarily generated spark plasma between particles and include: spark impact pressure **[38,45]**, plasma cleaning of particle surfaces **[48-49]**, joule heating **[38,48-49]**, local melting and/or evaporation **[45]**, particle surface activation, electromigration **[50-51]** and field assisted diffusion **[49,51-52]**. Of the mechanisms listed above, Joule heating, local melting and evaporation (especially in metallic systems) and electromigration have been relatively well established. The other mechanisms, especially those that invoke the presence of plasma, are highly hypothetical in nature. Other than sintering, SPS technology has been used to join materials, grow crystals, facilitate advanced chemical reactions and even form materials into different shapes **[45,46,53]**.

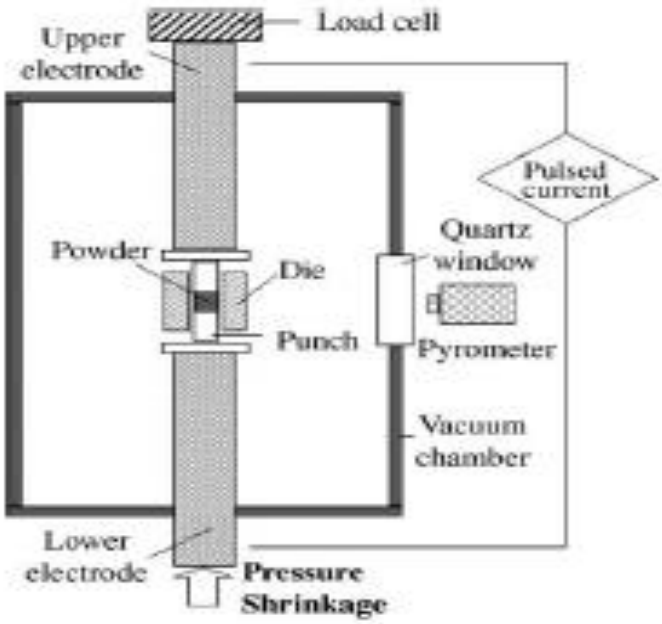


Figure 2. 6 Schematic diagram of a SPS system **[54]**.

Figure 2.6 illustrates a typical SPS system which uses the principle of Joule heating to sinter the material. During each current discharge, metallic material is transported as plasma by the propagation of sparks across the pores of the matrix. When the current is switched off, the matrix undergoes rapid cooling resulting in the condensation of the metallic vapours within the regions where there is mechanical contact between powder grains **[55]**. This condensation of vapour produces necks that consolidate these joints. The material transport in subsequent spark pulses increases due to the greater electric current density in the necks and contacts than inside the body of each powder grain. The rate of material transport is enhanced by the application of an external compressive force **[56]** resulting in the plastic deformation of the powder grains at each interface **[57]** resulting in a flatter joint with lower electrical resistance. This process propagates throughout the matrix and is enhanced by the external pressure which induces the plastic flow of material to form a sintered cermet with a density that is very close the full theoretical density. This process of propagation is similar to that exhibited in the consolidation of matrices by hot isostatic pressing **[57]**.

2.2.2 Spark plasma sintered (SPSed) WC-Co alloys

Jia *et. al* **[58]**, conducted studies on the effect of powder particle size on the densification and properties of WC-Co alloy produced by SPS. Nanometer scale and conventional WC–Co powders were densified for 5 min under a pressure of 25 MPa, with the heating rate maintained at 200 ^{o}C/min, and the sintering temperature varied between 900 ^{o}C and 1100 ^{o}C maximum, which was then quickly reduced to 600 ^{o}C. The authors concluded that the density as well as the hardness of the sintered WC–Co carbides increased with the sintering temperature for both powders and also reported a better property from the Nanoscale powder.

Huang *et. al.* **[19]**, investigated the influence of starting powder on the microstructure of WC–Co hardmetals obtained by SPS using three types of starting powders (multi-directionally mixed WC–Co (PA), commercial available attritor-milled WC–Co obtained by the spray conversion process (PB), and chemically synthesized composite WC–Co powders, (PC)). Powders PA and PB were sintered for 2 min at 1240 °C, while powder PC was consolidated for 2 min at 1280 °C under a maximum pressure of 60 MPa, with a heating rate of 100 K/min and cooling rate of around 200 K/min. The applied pressure was adjusted within 0.5 min from 6 to 30 MPa at 1050 °C and from 30 to 60 MPa within 1 min at the sintering temperatures. The authors reported between 97-98% theoretical densities and good mechanical properties from the sintering condition. They also noted that the PA powder resulted in a graded microstructure composed of a WC-rich edge and Co-enriched core, as well as elongated Co segregations in the core. They concluded that the powders PB and PC resulted in hardmetals with homogeneous microstructures and mechanical properties.

Zhao *et. al.* **[59]**, studied the effect of WC particle size on the densification and properties of an SPSed WC-10wt%Co alloy. The WC–Co alloys were prepared with different WC mean particle sizes (0.2, 0.8 and 1.5 μm) while the Co powder size was 1.0 μm. At a heating rate of 70 ^{o}C/min, the powders were sintered at 1180^{o}C for 10 min under a pressure of 60 MPa. At the sintered temperature, a nearly full density was obtained with good mechanical properties and an optimized WC and Co particle-size combination. The authors concluded that in spite of a weak effect of WC particle size on the SPS densification stages, the WC particle size played a significant role in the homogeneity of the alloy microstructure and also the scale combination of WC and Co particles affected the strength of the SPSed alloy by means of the WC grain size and the Co distribution state in the matrix.

Liu *et. al.* **[45]** proposed a novel rapid route for synthesizing WC-6wt%Co. The route integrated the synthesis of the composite powder (6wt%Co and WC average grain size of about 650 nm) by *in situ* reactions and subsequent consolidation in the SPS system. The WC–Co was prepared by SPS at 1250 ^{o}C for 5 min at a heating rate of 70 °C/min with a maximum pressure of 60 MPa. The resultant alloy had a homogeneous fine-grained microstructure and good combined mechanical properties (Rockwell hardness of 93.2 HRA and the fracture toughness of 10.1 MPa.m$^{0.5}$).

Picas *et. al.* **[60]**, investigated the microstructure and wear resistance of WC–Co by three consolidation processing techniques (HVOF and LENS WC–Co coatings, and SPS WC–Co alloy). The SPS alloy was sintered at 1100 °C with a heating rate of 150 °C/min for 10 min and a pressure of 50 MPa. An experiment using a tribometer (ball on disk configuration) under dry conditions was performed in order to evaluate the friction and wear properties of the different systems. The authors recorded that dense coatings and alloys without any cracks were produced from microstructured WC–Co-Cr and nanostructured WC–Co powders by using the three processes. The SPS bulk sample presented a higher porosity than the HVOF and LENS coatings, due to the short sintering time and relatively low sintering temperature, yet maintained the nanocrystalline characteristics of the feedstock powder. The SPS sample also presented a higher universal hardness and Young's modulus in comparison to the HVOF and LENS coatings, which was directly correlated to the finer WC grains and cobalt distribution. The authors concluded that the SPS sample showed similar tribological properties to the HVOF coating and both samples showed better wear resistance than the LENS coating under the same sliding conditions and attributed the good performance of SPS alloy to its homogenous microstructure and larger microhardness.

To the author's knowledge there is currently no published literature on the slurry erosion performance of SPSed WC-Co alloys.

2.2.3 Spark plasma sintered WC-Co-VC alloys

Sivaprahasam *et. al.* **[61]** studied the microstructure and mechanical properties of a nanocrystalline WC-12Co alloy consolidated by SPS, using powders with different amounts of VC and (VC + Cr_3C_2). The alloy properties were then compared to that obtained from liquid phase sintering. The SPS experiments were done in the temperature range 1000 – 1100 °C for 3 – 10 min under a pressure of 50 MPa. The heating rate for all SPS experiments was maintained at around 150 °C/min, and the natural cooling rate down to 800 °C was 100 – 150 °C/min. The sintering cycle adopted for the liquid phase sintering included the following steps: heating to 900 °C at 10 °C/min, holding for 30 min, heating to 1300 °C at 5 °C/min followed by heating to final sintering temperature (1400 and 1450 °C) at the rate of 20 °C/min. The holding time at the sintering temperature was 30 – 45 min. The authors reported an acceptable density level with good mechanical properties for all the SPSed alloys produced compared to that from liquid phase sintering. They concluded that the addition of VC decreased the grain growth in both sintering methods, and while inhibiting grain growth, the addition decreased the sintered density significantly in SPS alloys and also improved the hardness greatly for the SPS alloys for the same composition.

Huang *et. al.* **[62]** studied the influence of sintering condition and VC concentration on the densification, grain growth and mechanical properties of WC-12wt%Co using Pulsed electric current sintering (PECS) and spark plasma sintering (SPS). The WC-12Co powder was mixed with varying amounts of VC additions (0, 0.45 and 0.9 wt%) and sintered at 1080 – 1240^{o}C for 2 min under a maximum pressure of 60 MPa, with a heating rate of 200 ^{o}C/min up to 1050^{o}C and subsequently at 100 ^{o}C/min up to the sintering temperatures. The initial cooling rate was 200 ^{o}C/min. The applied pressure was adjusted within 0.5 min from 16 to 30 MPa at 1050 ^{o}C and from 30 to 60 MPa upon reaching the sintering temperature. The authors recorded a nearly full density at 1240^{o}C after 2 minutes

and obtained a homogenous and comparable hardness for the WC-12Co grades. They noted that the densification behaviour of the WC–Co alloys was strongly influenced by the VC concentration. They also noted that the fracture toughness was better with the grade having the lowest VC-doping. The authors concluded that VC addition proved to be effective to inhibit WC grain growth during SPS with an optimal hardness/toughness combination.

Bonache *et. al.***[63]** studied the effect of VC and/or Cr_3C_2 on densification, microstructural control and mechanical behaviour of WC–12wt%Co ultrafine and nanocrystalline mixtures consolidated by SPS. The alloys were sintered at 1100 ^oC, applying a pressure of 80 MPa in combination with a heating rate of 100 ^oC/min. The authors recorded a high density for the nanocrystalline mixtures and that only the mixture without the inhibitor (N) presented full densification. The density values achieved were compared with that obtained by other authors **[64-66]** and were much higher. It was also recorded that the materials obtained from the N mixture had excellent hardness accompanied by a loss of fracture toughness. The authors concluded that the addition of inhibitors, especially VC, is more efficient in the control of grain growth in the solid state and on the improvement of the mechanical properties of the alloys.

Sun, *et. al.***[67]** investigated the influence of varying the amount of VC addition (0.3, 0.5 and 0.7 wt% VC) on the density, microstructure and mechanical properties of a WC–Cr_3C_2–11Co alloy. The alloys were prepared at a temperature of 1200 °C in 5 min under a pressure of 40 MPa and a heating rate was maintained at 100 °C/min. They recorded good densification and mechanical properties. They concluded that Cr_3C_2 and VC are effective at limiting grain growth of WC and promoting the hardness and the fracture toughness of the samples under a certain range, but excessive addition cannot inhibit the grain growth and improve the properties.

To the author's knowledge at the time of this review, there was no published work on the friction and sliding wear behaviour, and the slurry erosion behaviour of SPSed WC-Co-VC alloys.

2.3 High velocity oxy-fuel (HVOF) thermal spray WC-Co coatings

WC-Co thermal spray coatings were initially produced for use in the aerospace industry **[68]**, but applications have since expanded to include use in pulp and paper mills **[68]**, steel rolling mills **[69]**, textile mills **[70]**, and the mining industry **[71]**. The use of these coatings in wear applications is mainly due to their high hardness and the good bond strength between the different phases. Control of the coating properties is complex because the properties are derived from the interaction of various factors such as the properties of the feedstock powders, type of spraying technique employed and the spraying process parameters. In this section a brief description of the HVOF process and the role of feedstock powders are given. Microstructural development and wear properties of WC-Co coatings with and without the addition of VC are reviewed.

2.3.1 HVOF thermal spray process

Spraying techniques for depositing WC-Co coatings are classified as either plasma or fuel combustion spraying, each with several other sub-classifications **[72]**. All the techniques impart both thermal and kinetic energy to the powder particle being sprayed, but to varying degrees, because each technique has a unique velocity-temperature combination **(Figure 2.7) [73]**. As a result of these differences, coatings deposited by different techniques have different microstructures and phases and also different responses to e.g. wear. Among the techniques, high velocity oxy-fuel, HVOF, processes produce coatings with good microstructure more easily than plasma related techniques **[74-76]**. This is

because the HVOF process is characterized by low flame temperatures and high particle velocities.

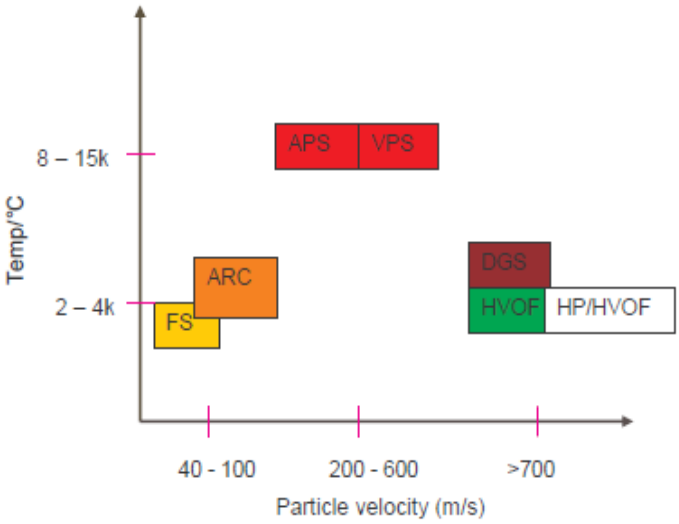


Figure 2. 7 Flame temperature-particle velocity combinations of various thermal spray techniques. FS: flame spray; ARC: arc spray; APS/VPS: air/vacuum plasma spraying; DGS: detonation gun spray; HP/HVOF: high pressure, high velocity oxy-fuel spraying **[73]**.

HVOF is a thermal spray system utilising the combustion of gases, such as hydrogen or a liquid fuel such as kerosene **[77]**. Fuel and oxygen mix and atomise within the combustion area under conditions that monitor the correct combustion mode and pressure. The process creates a very high velocity which is used to propel the particles at near supersonic speeds before impact onto the substrate. One of the basic rules of spraying is that high combustion pressure equals high gas velocity, high particle velocity and resulting high coating quality. One of the key benefits of this system's high velocity is the extremely high coating density and low oxide content. The low oxides are due partly to the speed of the particles spending less time within the heat source and partly due to the lower flame temperature (around 3000 °C) of the heat source compared with alternative

processes **[78]**. **Figure 2.8** gives a schematic diagram of the combustion chamber of a HVOF system.

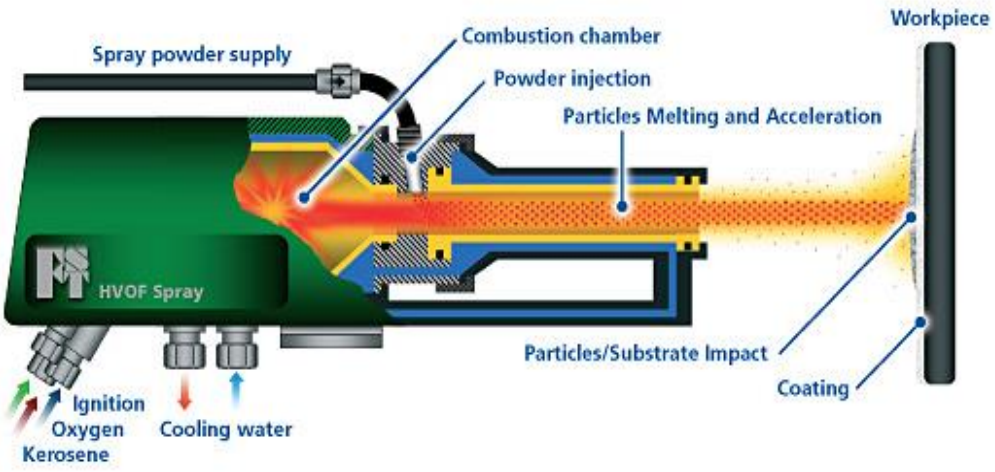


Figure 2. 8 Schematic diagram of HVOF combustion chamber **[79]**.

Influence of feedstock powders

The feedstock powders used in thermal spraying may be produced via several processing techniques including fusing and sintering, sintering and crushing, agglomeration and sintering, and agglomeration and plasma densifying **[78]**. The processing route determines the morphology and phase composition of the powder. Powder particle shape, size and size distribution influence the microstructural integrity **[63,73,80-81],** the phases in the coatings (due to the differences in heat-up rates during spraying between small and large particles which affect surface reactions such as decarburisation) **[34,82-88]** and the flowability of the particles during spraying **[80]**. Poor powder processing may result in poor or uneven coating deposition rates **[81]** which can cause porosity in the deposited coating. Due to their higher heat-up rates during deposition, small powder particles are prone to evaporation **[82]** which reduces deposition efficiency and increases porosity **[63]**. For thermal spraying, agglomerated and

sintered powders are preferred because of their spherical morphology which makes them flow easily and provide better coating properties **[34,89]**.

2.3.2 Microstructure development of WC-Co coatings

HVOF coatings are not pore-free but porosity is generally low because of the high particle velocities **[86]** during spraying. Depending on the deposition parameters, the microstructures can have visible splats (layers deposited per pass of deposition) **[90-91]**. The microstructures are also characterized by variations in grey level contrast of the binder phase in BSE micrographs, a result of variations in compositions **[90]**. Powders sprayed by HVOF techniques produce phase changes because spraying is done in the presence of oxygen. Little or no phase changes occur when oxygen is replaced by air, as is done in the high velocity air-fuel processes (HVAF) **[92]**. The most common phase changes in coatings produced by HVOF processes are: WC decarburization to W_2C; amorphous binder phase as compared to crystalline in powders **[90]**, and the formation of eta phase of the form M_nC, where n is either 6 or 12 and M includes W and Co **[75]**.

Decarburization reduces the amount of WC originally present in the powders. The amount of carbon and free cobalt also decrease after deposition, the latter due to vaporization in the spraying flame **[75,88,90]**. The amount of decarburization in HVOF processes depends on parameter settings and becomes appreciable with settings that lead to higher flame temperatures. In published literature, there does not seem to be a universally accepted mechanism for WC decarburization as researchers postulate mechanisms based on the phases found in the coatings **[34,74,86]**. A decarburization mechanism that would most likely occur in thermal spray processes is the following **[88,93]**:

$$4WC + O_2 \rightarrow 2W_2C + 2CO \qquad (Stage\ 1)$$

$$2W_2C + O_2 \rightarrow 4W + 2CO \qquad (Stage\ 2)$$

$$2WC + O_2 \rightarrow 2W + 2CO \qquad (Stage\ 3)$$

Stage 3 in the mechanism occurs only in very high thermal energy spraying processes, including HVOF processes **[89]**. Eta phase in powders has been found to increase the amount of W_2C in coatings **[34,86-87]**, while the occurrence of W_2C in powders favours stage 2, and leads to the occurrence of W in coatings. The amorphous nature of the binder after spraying is thought to be caused by the dissolution of W and C **[94]** and W_2C **[90]** in the binder. The solutes fail to precipitate out of solution because of the fast cooling rates during and immediately after deposition. This dissolution phenomenon has been observed by transmission electron microscopy (TEM) analysis, which showed the occurrence of nanocrystalline WC and W_2C phases in the binder **[91,93,95]**. HVOF processes lead to a reduction in the WC grain size in the coatings compared to the starting powders **[88]**. However, documentation of quantitative analysis of the change in grain size is rare.

2.3.3 Properties of WC-Co coatings

Hardness

The higher the amount of retained WC the higher the hardness in any thermal spray WC-Co coatings deposited by any technique **[34,87,93]**. Hardness is lowered with high amounts of porosity **[96]**. The amount of retained WC depends on the level of decarburization. Complete decarburization of WC to W reduces the amount of retained WC and hence lowers the hardness **[34,87]**, while partial decarburization to W_2C increases hardness **[89,94]**. The hardness of most WC-Co thermal spray coatings in literature is done using micro-hardness obtained with a test load of 300 g **[89-90,97-98]**. The scatter in the micro-hardness values reported by the authors **[99]** is however very large and this was attributed to the difficulty

in reproducing indents. Macro-hardness values are rarely quoted **[92]**. Hardness also increases with a decrease in the WC grain size.

Sliding wear

Rajinikanth and Venkateswarlu, **[100]**, investigated the sliding wear behaviour of HVOF WC-12wt%Co thermal spray coating. Dry sliding wear tests were performed on specimens of mild steel (MS) and WC coated mild steel (MSC) specimens against a hardened EN32 steel (EN32) and a WC coated EN32 steel (EN32C) discs. Four different combinations of specimen and counter surface were tested under dry sliding conditions. The authors reported that wear mechanisms differ depending on the combination of materials under sliding contact and concluded that under the same sliding conditions, when slid against EN32 disc the MSC specimen gained weight, signifying the transfer of worn particles due to severe cutting of the counter surface.

Yang et al., **[101]** examined the effect of carbide grain size on microstructure and sliding wear behavior of HVOF-sprayed WC-12wt%Co coatings. Dry sliding friction and wear test were conducted against sintered alumina (Al_2O_3) as the mating material. The authors reported that binder extrusion followed by carbide removal or carbide fracture is the dominant material removal mechanisms. **Figure 2.9** shows the effect of WC grain size on the hardness, fracture toughness and sliding wear rate of WC-12wt%Co HVOF coating **[101]**.

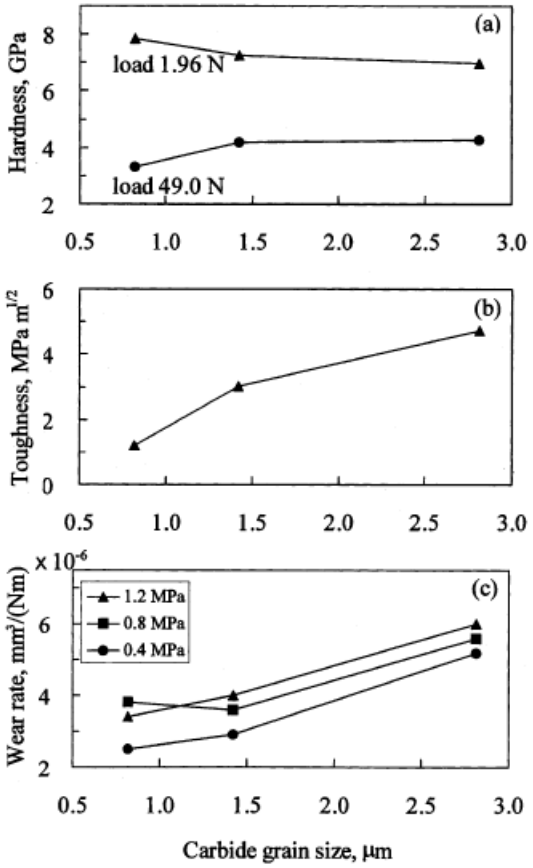


Figure 2. 9 (a) Hardness, (b) fracture toughness, and (c) specific wear rate of WC–Co coatings as a function of carbide grain size. **[101]**.

Shipway *et. al*. **[102]**, examined the performance of conventional and nanostructured WC-12wt%Co coatings deposited by HVOF thermal spraying. The coatings were deposited using both conventional and nanostructured powders. High level of decomposition was reported for the nanostructured coating. The performance of the coatings were examined under sliding wear conditions against an alumina ball and compared with the behaviour of a conventional sintered WC–Co hardmetal. Microstructural examination on the worn coatings showed wear dominated by the loss of ductility in the Co-rich binder phase and the generation of wear debris.

Sudaprasert *et. al.* **[103]**, investigated the sliding wear behaviour of WC–Co coatings HVOF sprayed with both liquid-fuelled (HVOLF) and gas-fuelled (HVOGF) systems. The authors demonstrated that with a dense powder feedstock, the HVOGF deposited coating is superior to the HVOLF deposited coating. The poorer performance of the HVOLF-sprayed coating was attributed with mechanical damage to the WC–Co powder particles as they impact with the substrate resulting in carbide cracking and a reduction in the integrity of the bond between the carbide particles and the matrix phase.

Yang et. al. **[104]**, investigated the sliding wear behaviour of WC–12mass%Co coatings using sintered alumina (Al_2O_3) as the mating material at elevated temperatures (200 - 400 °C) with different carbide grain size distributions. In their work, the authors reported increase in the specific wear rate of the coatings with increasing carbide grain size at a given testing temperature and decreased with increasing the temperature for a given carbide grain size. Microscopic analyses of the worn tracks showed formation of tribofilm and that the tribofilm formed at higher temperature is denser and more adhesive to the underlying surface, thus providing more surface protection against wear. They concluded that the formation of dense and adhered tribofilms plays an important role on the low sliding wear rate of the coatings at elevated temperatures.

Erosive wear

Generally, the erosion resistance is better with higher amounts of retained WC **[89,94]**, but is impaired by decarburization **[97]**. The effect of WC grain size on erosion is not clear. Some researchers find better resistance with finer grains **[94,104]**, while others find the opposite to be true **[65]**. The angle of incidence of the erodent jet relative to the eroding surface appears to determine the role of WC grain size. At lower angles of impingement, better resistance was obtained for coatings with coarser WC grains **[65]**.

Erosion mechanisms are determined by the properties of the inter-splat boundaries where crack initiation occurs **[66,97,105]**. Cracks initiate easily when porosity at the inter-splat boundaries is high and/or when the inter-splat bond strength is low. When the inter-splat bond strength is high, erosion occurs by preferential binder removal followed by WC grains pull-out **[106]**, a mechanism similar to that of sintered alloys. In general, the angle of incidence at which maximum mass loss occurs helps to distinguish between ductile and brittle wear mechanisms, which is important when deciding where to use the material, especially in pipe layouts in process industries **[107]**. Materials eroding by a ductile mechanism have erosion rate curves which go through the maximum at acute angles, while the maximum for materials with a brittle mechanism occurs at angles close to 90°. It is possible that a material behaves in both ways, depending on the test conditions **[108]**.

2.3.4 Vanadium carbide in WC-Co thermal spray coatings

The first attempt at introducing VC in WC-Co thermal spray coatings **[98,109]** was aimed at determining whether the high hardness and wear resistance observed in sintered WC-Co-VC alloys **[15,18,40-41,44]** compared to WC-Co alloys, could be obtained in coatings. For example the addition of VC to a sintered cemented carbide results in a decreased carbide grain size as it acts as a grain growth inhibitor **[110]**. It has been shown **[98,109]** that when VC is added in 18-22 vol% the micro-hardness of WC-Co-VC coatings is statistically the same as for WC-Co coatings; an occurrence that contradicted the observation made for sintered components. This could be attributed to the quality of the powders and/or the spray parameters used.

Wear testing showed that the dry erosion resistance of 63vol.%WC-(15-19)vol%Co-(18-22)vol%VC coatings was better than the dry erosion of 63vol.%WC-(18-22)vol.%Co coatings at low angles of incidence of the eroding

jet. However, the dry erosion resistance of the VC-coatings at high angles of incidence and the abrasion resistance in dry sand rubber wheel tests was lower than the wear resistance of the WC-Co coatings **[98,109]**. This was attributed to the large size of the VC grains as well as their heterogeneous distribution which showed segregation in some areas.

In work done by Machio et. al., **[111]** 10wt%VC was added to WC-Co coatings and the hardness of the VC-containing coatings was reported to be lower than that of the non-VC coatings. An improvement in dry and slurry abrasion conditions was observed with the VC addition, although the erosion response of the non-VC coatings was better. No explanations for the wear behaviour were provided other than speculation that the hard VC grains were better able to withstand abrasion compared to impact during erosion. The authors did report high levels of porosity and eta phase which may have influenced the results.

In the current study the thermal spray conditions have been optimized in an attempt to reduce the porosity and eta phase and to assess if an improvement in both hardness and slurry erosion is possible. The friction and sliding wear properties were also assessed as there is currently no published work in this area for high content VC-coatings.

2.4 Fundamentals of friction

Friction is the resistance to motion during sliding or rolling that is experienced when one solid body moves tangentially over another with which it is in contact **[112]**. It is usually described or compared using a ratio known as the coefficient of friction, μ. This coefficient of friction indicates the relationship between the frictional force experienced, F (N), and the normal load on the object, W (N), according to **[23,113-114]**:

$$\mu = \frac{F}{W} \qquad 2.2$$

It is unitless and its value usually lies between 0.1 and 1 for most common materials sliding in air **[113]**. In other to accurately describe a system experiencing friction, there are two types of coefficients of friction that are required namely: the static coefficient of friction, μ_s, and the dynamic coefficient of friction, μ_k. The μ_s, describes a system wherein an object remains stationary though a force is exerted on it, while the μ_k, describe a system when an object is in motion under an applied force. It is common knowledge that μ_s is usually larger than μ_k as the force required to initiate motion is larger than the force required to maintain motion **[113-114]**.

Friction is not a material property but rather a system response **[112]**. Various factors influence the friction properties of materials, e.g. oxide films, composition, microstructure, environmental conditions and the applied loads **[113]**. Temperature has a significant effect on friction with metal. Increase in the temperature of a metal affects the mechanical properties and the rate of oxidation and also the possibility of phase transformations **[113]**. Although no accurate relationship which produces realistic result has yet been defined **[23]**, friction plays a contributory role to the rate of wear within a given system. Sliding velocity does not usually affect friction but affect the frictional energy dissipation which in turn affects the temperature at the sliding interface **[113]**.

Changes in the sliding behaviour of materials can be monitored by measuring the CoF during a wear test. These changes often correspond to changes in the wear behaviour and as well as the resulting wear mechanism(s) **[113]**. For sliding friction, the total intrinsic frictional force consists of two components namely: the adhesive and ploughing components. The adhesive friction component is the force required to shear the asperities while that required to supplying the energy of deformation is called the ploughing component. For brittle materials, the fracture

of adhesive contacts and brittle deformation must needs to be considered thus making fracture toughness as important **[112]**.

Typically, friction response during dry sliding wear is presented in an S-shaped curve as shown in **Figure 2.10(a) [112]**. The shapes of these curves are influenced by the interface materials as well as the operating conditions. During sliding, changes occur between surfaces in contact and within material's surface which affect the friction and wear properties. During sliding, the initial sliding period where the frictional forces stabilize is often referred to as the "run-in", "break-in", or "wearing-in" period and thereafter the friction stabilizes into the "steady-state" period. During run-in, high asperities may be worn down, surfaces may mate better, initial surface films may be removed, new films may be formed or structural changes may occur within the material. These changes can cause the initial value of friction to either increase or decrease. During the steady-state period, new changes such as roughening and/or the presence of trapped wear particles which may lead to an increase in the friction level or cause it to increase to a new steady state plateau, may occur at the interfaces of two sliding bodies **[112]**.

During sliding wear test, friction transitions can generally be grouped into four hypothetical patterns namely: I, II, III and IV as illustrated in **Figure 2.10(b) [112]**. Pattern I shows that friction stays at an initial steady state level for a period of time and then slowly increases to another steady state value. This pattern is often associated with identical metals sliding against each other and such response is a result of ploughing due to roughening of the surface and entrapped wear particles. For smooth surfaces involving elastic deformation with a dominant adhesive component of friction an increase in the friction level is associated with the smoothing of the surfaces resulting in a larger component of adhesive friction **[112]**.

Pattern II indicates friction staying at an initial steady state level for a period of time and then increases to a higher level after which it decreases slightly and then levels off. This decrease is attributed to the smoothing of two hard surfaces experiencing plastic deformation which results in a decrease in the ploughing component. If the surfaces experience elastic contact where the adhesive component is dominant then a decrease in the adhesive component of the friction would be due to the decreased real contact area as a result of ploughing which is due to roughening and wear debris **[112]**.

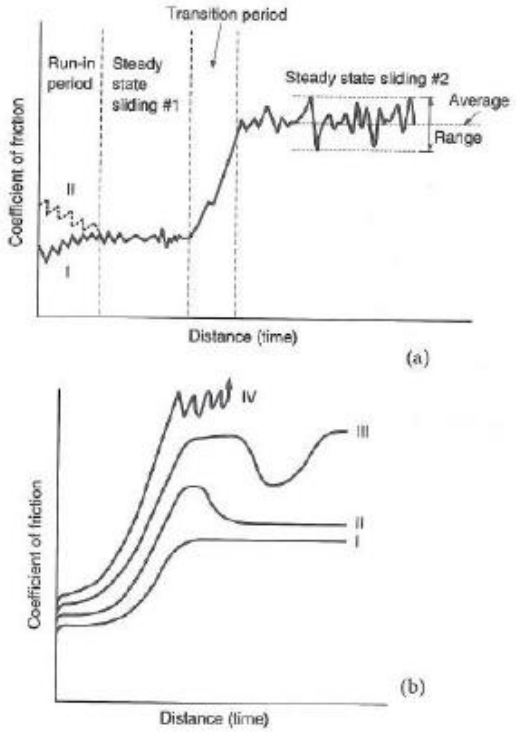


Figure 2. 10 The coefficient of friction as a function of sliding distance. (a) A typical S-shaped curve (b) Four hypothetical friction patterns **[112]**.

Pattern III showed that friction increases to a high value at which it remains for a period of time and then decreases to a lower value. Shortly afterward it increases

again to a high level. This pattern can often be repetitive. The decrease in the friction level during plastic contact is thought to be due to the ejection of wear particles from the contact surfaces and then subsequently the formation of new wear particles contributes to the increase in the friction levels **[112]**.

Pattern IV is similar to pattern III however the high and low levels are not repetitive but rather unpredictable. The sharp rise in friction level and its erratic behaviour is usually associated with incompatible material pairing **[112]**.

2.5 Fundamentals of wear

Wear is the surface damage or removal of material from one or both of two solid surfaces in sliding, rolling, or impact motion relative to one another **[112]**. In most cases, it occurs through surface interactions at the asperities. During relative motion, first, material on the contacting surface may be displaced so that properties of the solid body are altered with little or no material lost. Later, material may be removed and may result in the transfer to the mating surface or may break loose as a wear particle. Wear damage precedes actual loss of material, and it may also occur independently. The definition of wear is generally based on loss of material, but it should be emphasized that damage may be due to material displacement on a given body (observed using microscopy), with no net change in weight or volume, also constitutes wear **[112]**.

Wear is usually measured either by removing a material at intervals and weighing or measuring it or by continuously measuring its position with an electrical or mechanical transducer and deducing the wear from its change in dimensions **[113]**.Wear, as friction, is not a material property; it is a system response and is influenced by the operating conditions **[112]**. Wear can be classified into different types of mechanisms based on the manner in which material is removed.

In the current study sliding and erosion wear testing will be conducted hence these two types of wear will be briefly reviewed.

2.5.1 Sliding wear

Sliding wear occurs when one body slides over another **[113]**. It results in surface deformation of materials due to the breakdown of lubrication. At high speed this breakdown is often called scuffing. During un-lubricated conditions at low sliding speeds, severe sliding wear which results in severely roughened surfaces and transfer or displacement of large fragment of materials, due to localized welding, is called galling. **[113]**.

Plastic deformation has been shown to be the main cause of sliding wear amongst the several mechanisms that was proposed to explain how sliding wear operates, though the specific details of material removal differs **[113]**. One of the mechanisms involves shearing of the asperities on the interface either with no wear occurring (path 1) or with the irregular shaped sheared particles adhering to the opposite surface (path 2) as shown in **Figure 2.11 [112]**. Another mechanism attributes wear to the plastic shearing of successive layers of an asperity with complete detachment of the wedge shaped fragment. The plastic shearing occurs in conjunction with a shear crack which occurs along a slip line field along which the fragment can be detached. This fragment then becomes attached to the opposite surface due to adhesion **[112]**. These two mechanisms can be repetitive and can result in fragments finally being released as wear particles which may be of roughly equal size in each dimension **[112]**.

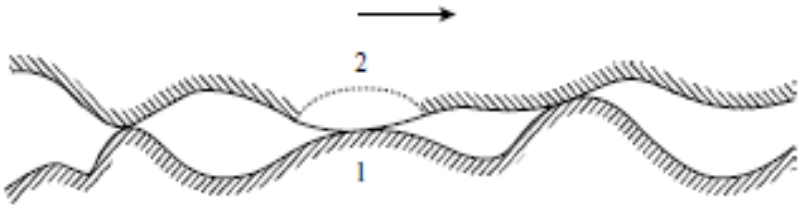


Figure 2. 11 Schematic showing two possibilities of break (1 and 2) during shearing of an interface (the arrow indicates the direction of sliding) **[112]**.

During sliding wear no singular mechanism operates at a given time but rather a combination of mechanisms. These mechanisms are affected by certain dominating factors and can change as these factors are changed. Factors such as contact stresses, thermal conditions, sliding speeds and chemical environment are all vital in all wear tests **[113]**. These factors are interrelated and are influenced by changes in the sliding parameters such as the normal load, sliding velocity and often the sliding time or distance as illustrated in **Figure 2.12 [113]**.

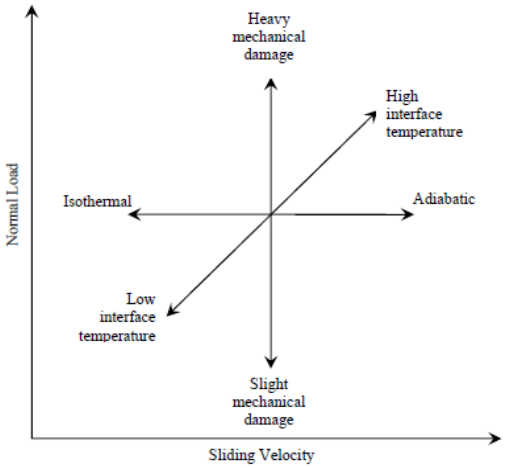


Figure 2. 12 Diagram illustrating the combined influences of load and sliding speed on the sliding wear process **[113]**.

2.5.2 Erosive wear

Erosive wear takes place when hard solid particles impact on a surface (See **Figure 2.13)** and material loss is measured as the ratio of the mass/volume of removed material with respect to the mass of erosive particles **[113,115-117]**. Erosion can occur by jets and streams of solid particles, liquid droplets, and implosion of bubbles formed in the fluid **[112]**. Solid particle erosion occurs when discrete solid particles strike a surface and several forces of different origin may act on the eroding particles in contact with the solid surface. In erosive wear, neighboring particles may exert contact forces and the presence a fluid will cause drag and under some conditions, gravity may be vital. The contact force exerted by the surface is however, the dominant force on an erosive particle, which is mainly responsible for decelerating it from its initial impact velocity **[113]**. The erosion processes and erosive wear depend on the impact angle, impact velocity and relative hardness of the materials and incident particles **[118]**. It also depends on the number and mass of individual particles striking the surface as well as the erodent geometry **[113]**.

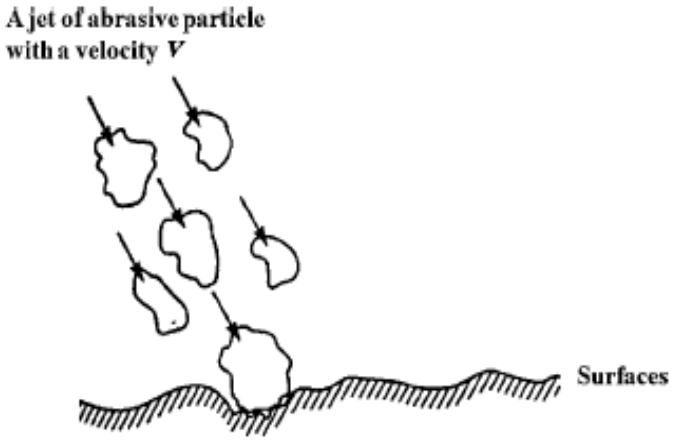


Figure 2. 13 Schematic of a jet of abrasive particles striking a surface at high velocity **[112]**.

Mechanisms of erosive wear can involve both plastic deformation and brittle fracture. Erosion of ductile materials usually involves plastic flow, whereas that of brittle materials may wear predominantly either by flow or by fracture depending on the impact conditions **[113]**. Plastic deformation mechanisms involve material removal by displacing or cutting action of the eroded particle while brittle fracture involves the formation and intersection of cracks that radiate out from the point of impact of the eroded particle **[107]**.

Figure 2.14 illustrates the variation of the erosion rate with the impact angle for materials which would have ductile and brittle responses to erosion. Ductile materials present maximum erosion rates at low impact angles and show a good erosion resistance for impacts normal to the surface. They also present extensive plastic flow of the surface around the points of impact. Brittle materials on the other hand, show more severe damage under normal impacts and have very good resistance at low impact angles. The impact of hard particles on brittle materials produces the propagation of cracks which lead to material removal from the surface **[119]**.

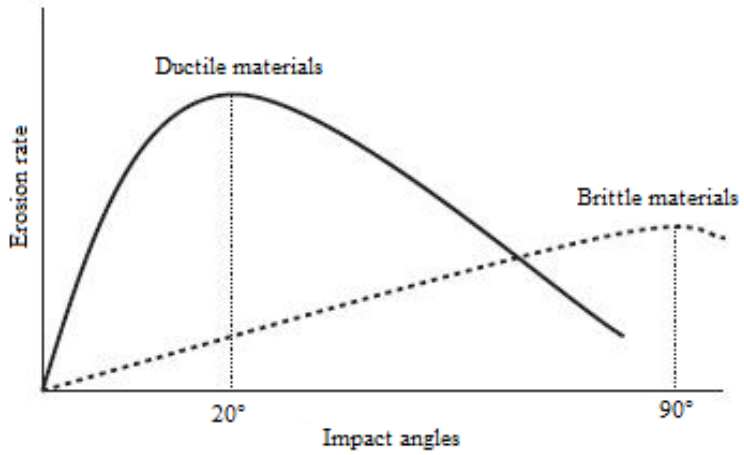


Figure 2. 14 Variation of erosive wear with impact angle for ductile and brittle materials **[119]**.

3. Experimental procedures

3.1 Introduction

This chapter describes the experimental procedures that were followed to produce and evaluate the friction, sliding wear and slurry erosion properties of HVOF thermal spray coatings (TSC), conventionally sintered alloys (CSA), and spark plasma sintered alloys, (SPSA).

3.2 Powders

The powders used in this project comprised of tungsten carbide (WC), cobalt (Co) and vanadium carbide (VC). Different types of powders are required for thermal spraying and for sintering and a description of each powder type is given below.

3.2.1 Thermal spray coating powders

Three groups of feedstock powder materials supplied by H.C Starck from Germany were used for this investigation. The powders, namely WC-12wt%Co, WC-12wt%Co-10wt%VC and WC-17wt%Co-10wt%VC were used for spraying. The powders, agglomerated and sintered, were received with a nominal size distribution of (-45 + 15) µm and was sprayed in this form. **Table 3.1** gives the nominal compositions in weight percent and volume fraction percent. The equivalent volume fraction of the powders was approximated as VC was found to have dissolved WC to form (W,V)C. Assumptions were made to find the amount of WC that went into solution of VC. The calculation of the volume fraction is shown in **Appendix A1**. Characterization of the powders was done using the techniques described in **section 3.4.2.**

Table 3. 1 Powder compositions in weight percent and volume fraction.

	Weight (%)			Volume fraction (%)		
Powders	WC	Co	VC	WC	Co	(W,V)C
WC-12wt%Co	88	12	-	80.6	19.4	-
WC-12wt%Co-10wt%VC	78	12	10	55.5	16.8	27.7
WC-17wt%Co-10wt%VC	73	17	10	50.0	23.1	26.9

3.2.2 Sintered alloy powders

WC and Co powders were supplied by Pilot Tools, South Africa while VC powder was purchased from Element Six, South Africa. The properties of the powders and the mixing ratio are summarized in **Table 3.2**.

Table 3. 2 Characteristics of the starting powders.

Powder	Size (μm)	Weight (%)
WC	4	78
Co	1	12
VC	0.6	10

The powders were used in the production of both the conventional sintered alloys and the spark plasma sintered alloys. The as-received powders were mixed and then milled for 12.5 hours using WC balls as the milling media and a ball to powder ratio of 4:1. The milled powders were characterized using the analytical techniques described in **section 3.4.2**.

3.3 Materials processing procedures

3.3.1 Thermal spray coating procedure

Four HVOF coatings were produced for this study using mild steel plates (100 x 75 x 5) mm as the substrates. Two coatings namely, WC-12wt%Co and WC-12wt%Co-10wt%VC were deposited using the spray parameters shown in **Table 3.3** with the procedure described elsewhere **[70]**. The WC-17wt%Co-10wt%VC powder was used to produce two coatings by varying the spray parameters which will be designated as – Run 38 and Run 39 respectively. The spray parameters are shown in **Table 3.4** and the procedure described elsewhere **[120]**.

Table 3. 3 Spray parameters for the WC-12Co and WC-12Co-10VC coatings **[70]**.

Spray parameter	**Value**	
	WC-12wt%Co	WC-12wt%Co-10wt%VC
Gun barrel (mm)	102	102
Spraying distance (mm)	380	330
Kerosene flow rate (m^3/hr)	0.0227	0.0254
Oxygen flow rate (Sm^3/hr)	56.6	62.3
Miller powder feeder (rev/min)	3	4
Argon flow rate	25	25

Table 3. 4 Spray parameters for the WC-17Co-10VC coatings **[120]**.

Spray parameter	**Value**	
	Run 38	Run 39
Hydrogen flow rate (l/min)	788	640
Oxygen flow rate (l/min)	274	241
Oxygen stoichiometry (%)	75	75
Chamber size (mm)	22	22
Carrier gas flow rate (l/min)	17	17
Nozzle length (mm)	120	120
Standoff distance (mm)	250	200
Powder feed rate (g/min)	50.9	50.8

3.3.2 Sintered alloys processing

3.3.2.1 Conventional sintering

The milled powders were cold pressed to form green compacts. 45.5 g of each powder was compacted uniaxially with a pressure of 0.34 MPa for 5 seconds, using an industrial hydraulic press. The alloys were then sintered at a final temperature of 1430 °C using standard commercial production conditions.

3.3.2.2 Spark plasma sintering

The powders were sintered under a pressure of 50 MPa for 5 minutes. The WC-12wt%Co alloys were sintered at 1130 °C with a heating rate of 200 ^{o}C/min while the WC-12wt%Co-10wt%VC alloys were sintered at 1100 °C with a heating rate of 100 ^{o}C/min to avoid partial melting. Several sintering trials were performed to determine the optimum sintering temperatures and heating rates. **Figures 3.1** and **3.2** show the sintering profiles for the different alloys.

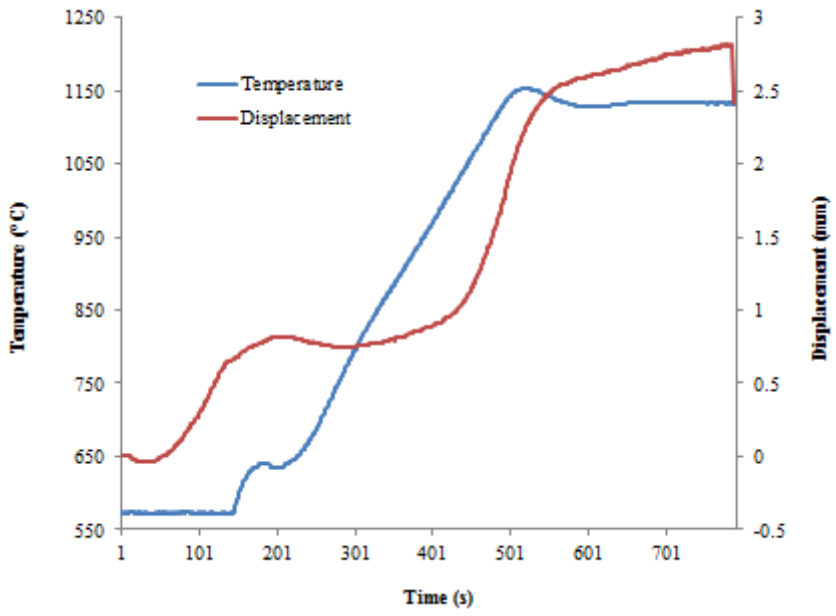


Figure 3. 1 Sintering profile for WC-12wt%Co SPS alloy.

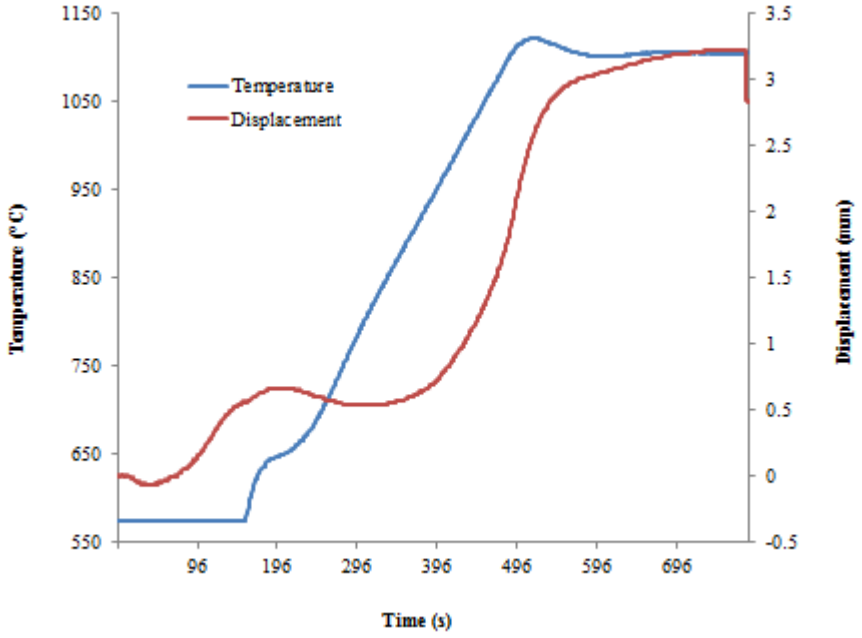


Figure 3. 2 Sintering profile for WC-12wt%Co-10wt%VC SPS alloy.

During the consolidation process, the dimensional changes of powders were monitored by measuring the position of lower punch in **Figure 2.6**, which plays a role of electrode to produce high pulsed current within the powder compact and, at the same time, press to apply. The consolidation mechanism, i.e. liquid phase sintering or solid state sintering, is determined by the dimensional changes according to processing temperature as shown in **Figures 3.1 and 3.2** respectively. When the liquid phase is formed during the SPS, the volume of sintered body slightly increased due to the larger volume of liquid Co compared to that of solid. If liquid phase is not formed during the sintering process, the dimension of powder compact decreases continuously by densification **[46,47]**. The initial decrease in the profiles shown in **Figures 3.1** and **3.2** could be as a result of the thermal expansion of the graphite dies and/or liquid phase sintering stages. The positive sign of displacement indicates the shrinkage of specimen during the SPS. It could be concluded that the initial sintering started at about 850 °C and 750 °C for WC-12wt%Co and WC-12wt%Co-10wt%VC alloys while the peak sintering occurred around 900 °C and 800 °C for WC-12wt%Co and WC-12wt%Co-10wt%VC alloys respectively. The continuous increase in the

displacement after the sintering process could be that there is a possibility of reaction product(s), phase transformation(s) and/or thermal expansion of the graphite dies.

3.4 Materials characterization

3.4.1 Sample preparation

3.4.1.1 Powder particle size distribution

The Malvern Mastersizer 2000 particle size analyzer was used to determine the particle size distribution of the milled powders. The Mastersizer 2000 was designed to measure the distribution of different sizes within a sample. The Mastersizer combines the principles of the Fraunhofer model and the Mei theory and works backward from the above theories by using the optical unit to capture the actual scattering pattern from a field of particles. It then uses the theory to calculate the size of the particles that created the pattern. **Figure 3.3** shows the Malvern Mastersizer 2000 particle size analyzer.



Figure 3. 3 Malvern Mastersizer 2000 system.

Particle size determination

In order to obtain an average particle size with narrow particle size distribution, tests were conducted using water as dispersant. The powders were dispersed in 0.5 wt% by liquid mass using external ultrasound for 1 minute. About 14 g of powder was prepared and put in a 4 L beaker for the size distribution tests. Obscuration was less than 16%. Particles added to the beaker were homogenized using a stirrer at a pump speed of 2000 rpm. A refractive index of 1.33 was used to determine the size distribution of the milled powder.

3.4.1.2 Sample preparation

Prior to testing, cross-sections of each representative sample used in this study (the coatings and the sintered alloys) were mounted in PolyFast resin, ground and polished to a surface finish of 1 µm using a Leco Spectrum System 2000 automatic polishing machine. After each polishing step, the samples were cleaned ultrasonically in water for 5 minutes. **Table 3.5** shows the grinding and polishing routine.

Table 3. 5 Grinding and polishing procedure.

Process	**Steps**	**Time (min)**	**Speed (rpm)**	**Pressure (N)**	**Abrasive disc**	**Coolant/ Lubricant**
Grinding	1	5	300	20	Piano 220	Water
	2	3	300	20	Piano 1200	Water
Polishing	1	4	150	15	Largo 9 µm	9 µm diamond suspension and lubricant
	2	4	150	15	Largo 6 µm	6 µm diamond suspension and lubricant
	3	4	150	15	Dac 3µ m	3 µm diamond suspension and lubricant
	4	20	150	10	Nap 1 µm	1 µm diamond suspension and lubricant

3.4.2 Microstructure analysis

The samples were etched using a solution of Murakami's Reagent (10 g KOH, 100 ml Water, 10 g $K_3Fe(CN)_6$) for 2 minutes. The samples were rinsed under running water followed by ethanol and then dried. The etched surfaces were initially studied using a Leica DM6000M microscope at a magnification of 1000X. Images were taken and in the microstructure were characterized.

Detailed analysis of the microstructures was done using a Zeiss Axiotech® reflected light microscope and a FEI NOVANANO SEM200 scanning electron microscope (SEM) fitted with the Everhard-Thornley Detector (ETD) using SE and BSE modes. Elemental X-ray dot maps of photographed locations were acquired to help identify the grains. The mean grain sizes of the WC and VC grains were obtained by lineal analysis. Phase analysis was done on all materials using a BRUKER D2 X-ray diffractometer fitted with a copper anode and set at 30 kV and 10 mA. Phase identification was done using Phillips Analytical X'Pert HighScore® Software with an in-built database. The percentage compositions of the phases present were determined by Rietveld refinement, utilizing a Pearson VII peak shape function **[121-128]**.

3.4.3 Coating porosity and hardness

Porosity levels were obtained by dot counting **[129]** on optical micrographs obtained from coating cross-sections. The hardness was obtained using a Vickers micro-hardness tester with a load of 500 g and dwell time of 15 s. Indents were made on coating cross-sections with ten measurements made for each coating and the average hardness value determined. The effect of the proximity of substrate on hardness was avoided by ensuring that indents were made in the middle of the coating cross-section.

3.4.4 Sintered alloys characterization

In addition to the microstructure analysis described in **section 3.4.3** the physical and mechanical properties of the sintered alloys described below were also characterized.

3.4.4.1 Density and porosity

The density was determined using the Archimedes principle. Two samples were used for each alloy and the average values were recorded. The specimens were first weighed in air, then again while suspended in water. The density was calculated using **Equation 3.1,** while the percentage porosity for each sample was calculated using **Equation 3.2**. Five density measurements were made per sample.

$$\rho_s = \rho_w \times \frac{M_a}{M_{wt} - M_w} \qquad 3.1$$

$$\%\ Porosity = \frac{M_{wt} - M_a}{M_{wt} - M_w} \times 100 \qquad 3.2$$

Where

ρ_s = Density of the sintered alloy (g/cm^3)

ρ_w = Density of water (g/cm^3)

M_a = Mass of sintered alloy in air (g)

M_{wt} = Wet mass of sintered alloy (g)

M_w = Mass of sintered alloy in water (g).

3.4.4.2 Hardness and fracture toughness

Vickers hardness was determined using a Leco V-100-A2 Vickers hardness machine in accordance with ISO 3878, using an indenting load of 30 kg for 30 s. Five indentations were made per sample. The hardness was calculated using **Equation 3.3**.

$$H_V = \frac{1854.4P}{d^2} \qquad 3.3$$

Where

P = Load (kg)

d = Average diameter of the diagonals (mm)

To obtain the fracture toughness the Palmqvist technique **[120]** was used, wherein the cracks radiating from the corners of the Vickers hardness indentation were measured and used to calculate the toughness. **Equation 3.4** developed by Shetty et al **[28]** and considered most suitable for WC-Co hardmetals was used.

$$K_{IC} = \beta \left(\frac{E}{H}\right)^{\frac{1}{2}} \left(\frac{P}{c^{\frac{3}{2}}}\right) \qquad 3.4$$

Where

K_{IC} = Fracture toughness ($MPa.m^{0.5}$)

E = Young's modulus (GPa)

H = Hardness (GPa)

P = Applied load (kg)

c = Average crack length (m)

β = Constant

The constant β is calculated from **Equation 3.5**

$$\beta = \frac{1}{3(1 - v^2)\left(\sqrt{2\pi}.\tan\psi\right)^{\frac{1}{3}}} \qquad 3.5$$

Where

ν = Poisson's ratio

$\Psi = 68°$

3.4.4.3 Coercivity and magnetic saturation

The coercivity of the samples was measured using an Institute Dr Forster Reutlingen Koerzimeter according to ISO 3326. A test piece was placed in the Koerzimeter and magnetized to saturation. The sample was then removed from the magnetic field, and the field strength required to de-magnetize the sample was recorded. The unit used is kA/m. Factors such as composition and grain size may influence coercivity. Coercivity decreases with an increase in cobalt content and with an increase in tungsten carbide grain size **[1]**. The amount of magnetic cobalt present was determined from magnetic saturation tests. A sample was placed on a weighing scale connected to a LDJ Inc. Saturation Induction Measuring System Model SM 8100 and the amount of magnetic cobalt present, in percentages, was recorded.

3.4.4.4 Poisson's ratio and moduli

The Poisson's ratio and moduli (Young's, bulk and shear) of each alloy was determined using speed of sound measurements (longitudinal and transverse speed of sound). The test was conducted using the Pulse Echo Ultrasonic method with a Krautkramer USIP 12 machine with a longitudinal probe frequency of 50 Hz and a transverse probe frequency of 20 Hz. To calculate the speed of sound in the materials **Equation 3.6** was used. **Equation 3.7** was used to determine Poisson's ratio and **Equations 3.8** to **3.10** were used to compute the moduli.

$$Speed\ of\ sound, c\ (m/s) = \frac{Sample\ thickness}{Average\ time\ on\ way} \times 1000 \qquad 3.6$$

$$Poisson's\ ratio, v = \frac{1 - 2\left(\frac{C_T}{C_L}\right)^2}{2\left(1 - \left(\frac{C_T}{C_L}\right)^2\right)} \quad 3.7$$

$$Young's\ modulus, E = 2G(1 + v) \quad 3.8$$

$$Shear\ modulus, G = \frac{\rho c_T^2}{10^6} \quad 3.9$$

$$Bulk\ modulus, B = \frac{E}{3(1 - 2v)} \quad 3.10$$

Where

C_T = Transverse speed of sound (m/s)

C_L = Longitudinal speed of sound (m/s)

ν = Poisson ratio

E = Young's modulus (GPa)

B = Bulk modulus (GPa)

G = Shear modulus (GPa)

ρ = Density (g/cm^3)

3.5 Friction and sliding wear tests

The friction and sliding wear tests were performed using a CSM tribometer with a ball-on-disk configuration at room temperature under unlubricated conditions. The test parameters are listed in **Table 3.6**. For the coatings, two different balls (6 mm diameter) were used namely 100Cr steel balls and WC-Co balls, while only the 100Cr steel balls were used for the sintered alloys. The properties of the balls are given in **Appendix A2**. The carbide samples were polished to a 1 µm surface

finish prior to wear testing. All samples were cleaned ultrasonically with ethanol for 5 minutes and dried before and after testing. Two tests per ball-sample pair were conducted.

Table 3. 6 Friction and sliding wear test parameters.

Test conditions	**Value**
Acquisition radius	4.09 mm
Linear speed	0.26 m/s
Normal Load	10.00 N
Sliding distance	200.00 m
Acquisition rate	30 Hz
Temperature	$(25 \pm 3)^{o}C$

The test set-up is illustrated in **Figure 3.4**. The tribometer has an elastic blade (B) which serves as an arm to keep the ball holder (C) fixed in one position and to hold the applied load (A). There is a disk-holder mandrel (E) to which the test sample (D) is fixed. During testing the mandrel rotates while the ball holder remains stationary. The speed of rotation is set by the user on the tribometer's parameter input page in the software program. The tribometer uses CSM TriboX software for online measurement.

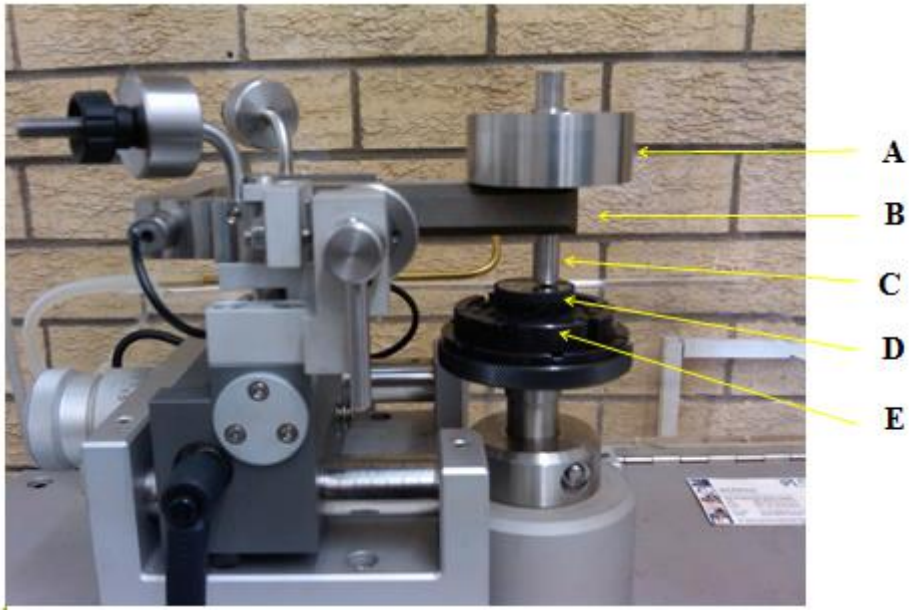


Figure 3. 4 Measurement head of the tribometer (A) Applied load, (B) Elastic blade arm, (C) Ball holder, (D) Sample, (E) Disk mandrel.

Prior to each test the ball and the sample were each fitted into their correct positions in the tribometer. Once the selected load was applied the computer software was initiated to commence a test. The input parameters **(Table 3.6)** and the data sampling parameters were first verified in the input sheet. These factors were the frequency at which measurements would be taken, the linear speed, the sliding distance, the applied load and the wear track radius. Once these were confirmed the test was initiated.

After each test, the balls and samples were examined using a Motic stereo microscope. The wear tracks on the samples and the worn area on the balls were measured. **Figures 3.5** and **3.6** illustrate the typical wear scars for the samples and balls respectively. These measurements were used to calculate the volume of material lost.

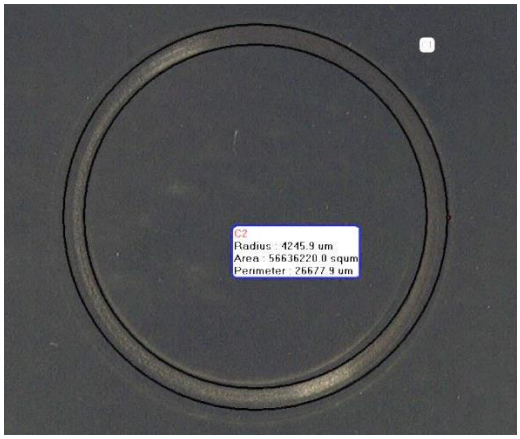


Figure 3. 5 Measurement of the wear track on a WC-12wt%Co sample.

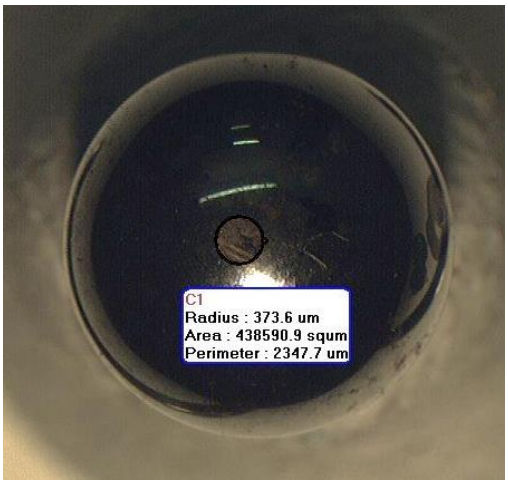


Figure 3. 6 Measurement of the worn area on a 100Cr steel ball.

To obtain the worn volume of the samples it was assumed that the wear track followed an elliptical shape due to the elliptical Hertzian pressure profile **[112,131]** that the sphere shaped end of the ball exerts onto the sample. The important parameters when calculating the worn volume of the carbide sample were the area of the wear track, which was obtained by measuring the outer and inner area of the wear track, (R_2 and R_1) and the penetration depth of the ball into the carbide surface, Pd. Thus the worn volume, V_s, for a given wear track of maximum penetration depth, Pd_{max}, was calculated as follows:

$$V_s = \pi \times (R_2^2 - R_1^1) \times Pd_{max} \qquad 3.11$$

To obtain the worn volume of the ball, the worn area, A_b, was measured. The important parameters when calculating the worn volume on the ball were the worn ball height, h, and the ball radius, R_b. The worn ball height, h, was calculated using the worn area diameter, d, which is calculated from A_b. Thus the worn volume, V_b, for a given ball was calculated as follows:

$$V_b = \frac{1}{3} \times \pi \times h^2 \times (3 \times R_b - h) \qquad 3.12$$

The volume losses, V_s and V_b were used to determine the wear rates (k) of the carbide samples and balls using **Equation 3.13** developed by Lancaster **[117]**.

$$k = \frac{V}{WS} \qquad 3.13$$

Where

k = Wear rate (mm^3/Nm)

V = Volume of material lost (mm^3)

W = Normal applied load (N)

S = sliding distance (m)

3.6 Slurry erosion wear tests

The slurry jet impingement erosion rig was designed and built by Wentzel **[132]**, based on the original rig devised by Zu et. al.**[133]**. **Figure 3.7** is a photograph of the slurry erosion rig while **Figure 3.8** shows the impact chamber where the sample is placed during testing.



Figure 3. 7 Photograph of the slurry jet impingement rig.

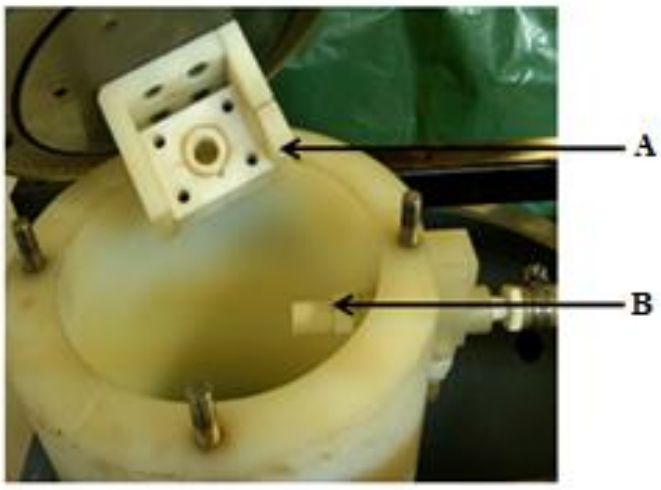


Figure 3. 8 Photograph of the impact chamber showing the sample holder (A) and the exit nozzle (B).

Table 3.7 lists the slurry wear erosion test parameters employed in this study.

Table 3. 7 Friction and sliding wear test parameters.

Operating parameter	**Value**
Erodent	2 kg of 500µm silica sand
Carrier fluid	Tap water
Operating temperature	25 ± 3 ^{o}C
Erodent concentration of slurry	16 wt%
Impact velocity	6.4 ms^{-1}
Impact angles	45^{o}, 60^{o}, 75^{o}, & 90°
Test time	60 minutes

The silica erodent was washed in water prior to testing to remove dust. In order to avoid problems of erodent degradation, fresh silica was used for each test. The nozzle of the ejector was monitored to ensure that there was no variation in the slurry velocity. Before the tests were carried out, the rig was calibrated by measuring the flow rate of the slurry. The effective concentration of the slurry out of the nozzle was found to be 16 wt% of the erodent and the slurry jet was 6.4 m/s. The erodent concentration and the impact velocity of the slurry were determined using **Equations 3.14** and **3.15** respectively.

$$Erodent\ concentration = \frac{weight\ of\ dried\ sand}{weight\ of\ known\ mass\ of\ slurry} \qquad 3.14$$

$$Impact\ velocity = \frac{slurry\ flowrate}{Area\ of\ the\ exit\ nozzle} \qquad 3.15$$

Once calibration was completed the rig was ready for testing. The holding tank of the slurry rig was filled with 200l of tap water, while 2 kg of sieved, washed silica erodent was placed in the funnel shaped container. The carbide specimens, polished to a 1 µm surface finish, were cleaned ultrasonically in ethanol for 5 min before each erosion test. In order to avoid the effect of moisture, the samples were dried for 5 min before weighing. Each sample was positioned in the specimen holder with the right orientation. The specimen holder was set to the required impact angle and secured to the top of the impact chamber, positioning the specimen 30 mm from the output nozzle, directly in the path of the slurry jet. The

impingement angle was varied to establish at which angle the maximum erosion rate would occur.

The sample was then subjected to the action of the slurry jet for a pre-determined time, during which the temperature of the carrier fluid was monitored. The sample was then removed from the holder, cleaned ultrasonically in alcohol, dried, cooled and weighed. All samples were tested for a total time period of 60 min with the mass loss measured at 5 min intervals. At each impact angle two samples per carbide grade were tested and the average mass loss obtained. Mass loss measurements were converted to volume loss data. The erosion rate of each carbide sample was determined as volume loss of the carbides per mass of erodent particles to facilitate comparison between the carbide grades.

3.7 Wear scar analyses

The wear scars generated during the sliding and erosion wear tests were studied using SEM in order to determine the wear mechanisms. XRD and Energy Dispersive Spectroscopy (EDS) were performed on selected areas to identify if there was any material transfer during sliding wear. EDS was performed using an EDAX system for X-ray analysis together with a Backscattered Secondary Electron Detector (BSED) for backscattered SE imaging. EDAX mapping was performed on the eroded surfaces to assist in the identification of the wear mechanisms.

X-ray Photoelectron Spectroscopy (XPS) was performed on the wear tracks of the coating samples to verify the presence of oxides, if any. XPS was performed using a Physical Electronics Quantum 2000 machine (X-rays: Al Kα (1486eV), X-ray power 20W, beam diameter of 100 μm, pass energy (wide) 117.4 eV, (narrow) 29.35 eV.

4. Results: Thermal Spray Coatings

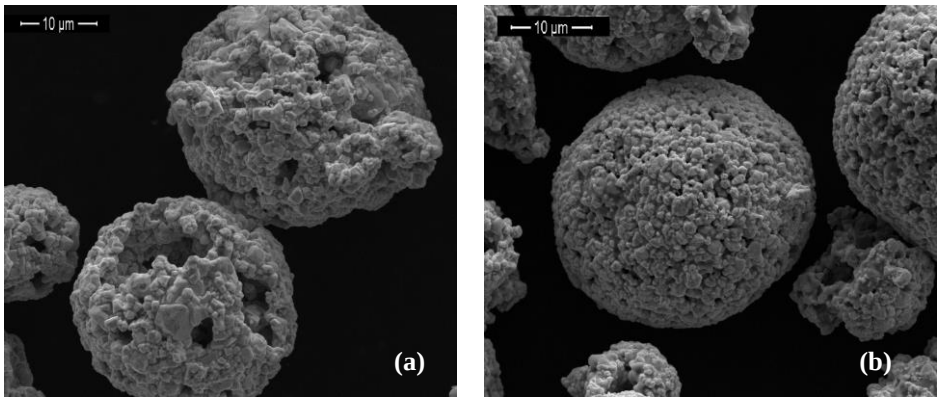
4.1 Introduction

This chapter presents the results from the characterization and testing of the HVOF-thermal spray coatings. It explains the properties of the coatings based on the properties of the powders and the coating deposition parameters, and compares the performances of the coatings based on the tests performed.

4.2 Powder Characterization

4.2.1 Morphology

The powder particles were predominantly spherical with smooth but porous surface textures. The microstructures showed angular carbide grains cemented by the Co binder **(Figure 4.1(a – c))**. The spherical shapes and porosity of the powder particles are characteristics typical of powders produced by spray drying **[89,134]** and the porosity is reportedly caused by a low green density after agglomeration **[73]**.



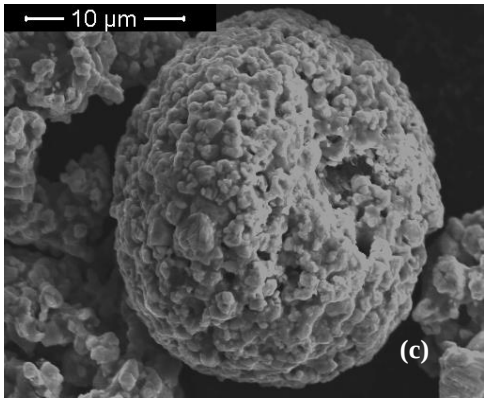


Figure 4. 1 Morphologies of the (a) WC-12wt%Co, (b) WC-12wt%Co-10wt%VC and (c) WC-17wt%Co-10wt%VC powders.

4.2.2 Particle size and size distribution

Table 4.1 gives the average particle sizes and size distributions obtained from the Malvern laser diffraction technique. All particle sizes and size distributions were within the range of those required for thermal spray powders (between 10 and 60 µm) **[135]** that allow for homogeneous powder particle heat up rates during spraying **[73]**.

Table 4. 1 Powder particle size and size distributions

HVOF Coatings	**Sizes (µm)**			
	$d_{0.1}$ (1)	**$d_{0.5}$ (2)**	**$d_{0.9}$ (3)**	**Mean**
WC-12wt%Co	21.57	33.37	51.93	35.63
WC-12wt%Co-10wt%VC	15.57	26.45	44.87	28.96
WC-17wt%Co-10wt%VC	17.82	30.84	56.68	35.11

[1] Equivalent volume mean diameter at 1st percentile; [2] Equivalent volume mean diameter at 5th percentile; [3] Equivalent volume mean diameter at 9th percentile. (equivalent volume mean diameter = the average diameter measured at each percentile)

4.2.3 Phase composition

Table 4.2 and **Figure 4.3** respectively show the phases and their approximate mass fractions and the XRD patterns obtained for the powders.

Table 4. 2 Powder particle size and size distributions

HVOF Coatings	**Phase composition in mass fraction (%)** [a]			
	WC	**Co**	**$VC_{0.94}$**	**$VC_{0.845}$**
WC-12wt%Co	83.17	16.83	-	-
WC-12wt%Co-10wt%VC	78.99	12.91	8.10	-
WC-17wt%Co-10wt%VC	55.46	17.82	-	26.72

[a] Phase mass composition determined by Rietveld analysis

The phases observed in the powders were consistently the WC, Co and VC phases. The stoichiometric chemistry of the powders i.e. non-occurrence of secondary phases such as eta phase and W_2C, was an indication that the powder processing route was optimized. Secondary phases in thermal spray powders are undesirable because if transferred to the coatings they may lower the wear resistance **[80]**. The occurrence of stoichiometric chemistries is, apart from a spherical morphology **(Figures 4.1)**, another characteristic of agglomerated and sintered powders **[89]**.

The d-values of WC in all the powders were lower than those given in the XRD reference cards. The d-values of WC in the WC-12wt%Co-10wt%VC powders were larger than those of the WC-12wt%Co powder. The lower d-values of WC in the WC-12wt%Co powder indicated that the WC grains were under higher compressive stresses **[136]** because at the same cobalt weight content, the volume fraction of the binder in the WC-12wt%Co powders was higher than in the WC-12wt%Co-10wt%VC powders **(Table 3.1)**. The d-values of WC in the 17wt%Co powder were however lower compared to the 12wt%Co powders. This could be a result of the higher amount of Co binder in the powder.

For all the powders, the d-values of the binder phase were larger than those in the XRD reference card. This may have been caused by the presence of W and V

atoms in solution in the binder (as was shown by EDS analysis; **see Figure 4.5(c)**), as well as tensile stresses. The binder in two powders (WC-12wt%Co and WC-17wt%Co-10wt%VC), had an FCC structure. The Co in the WC-12wt%Co-10wt%VC powder had the HCP structure; its occurrence in the other powders could not be ruled out. VC in the powders occurred as VC_x, where x ranged between 0.845 and 0.94.

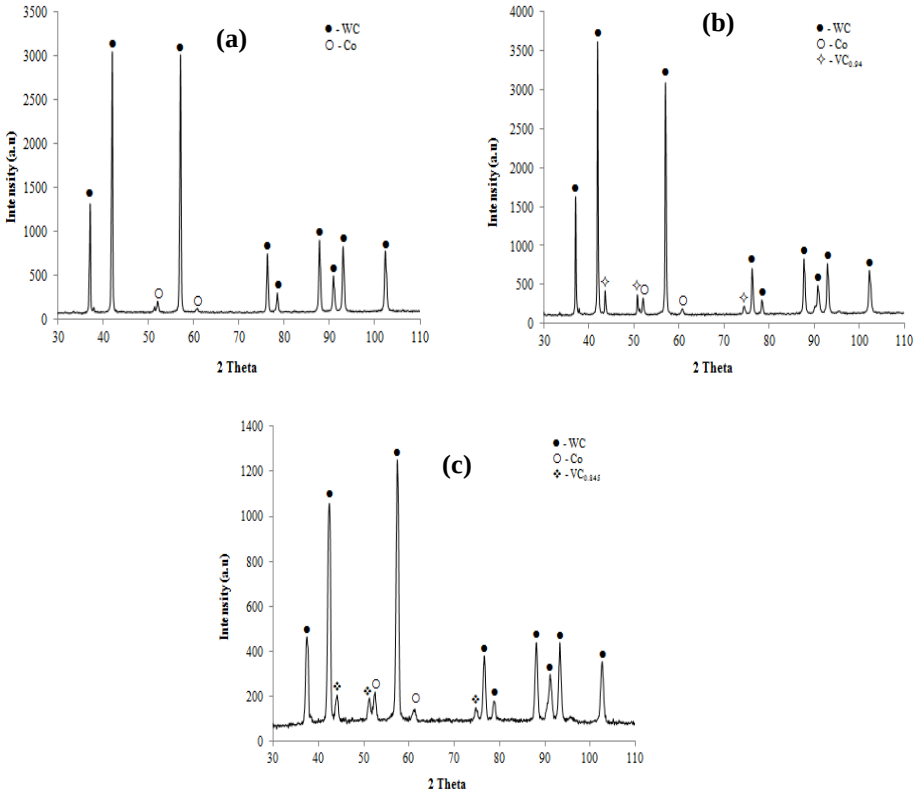


Figure 4. 2 XRD patterns for (a) WC-12wt%Co, (b) WC-12wt%Co-10wt%VC, and (c) WC-17wt%Co-10wt%VC powders.

4.3.1 Coating microstructures

Optical micrographs of the un-etched cross-sections of all the coatings **(Figure 4.4 (a-d))** showed that the coating-substrate interfaces were generally without any deleterious (e.g. inclusions from surface preparations prior to spraying) materials. All the coatings were porous. A comparison showed that the porosity levels

obtained in this study were better than those obtained by Machio **[70],** this could be attributed to improved spraying parameters. The level of porosity is affected by the spraying parameters. **Table 4.3** shows the porosity levels and the thickness of the coatings. The cracks observed were either the result of the coating deposition process or due to sample preparation procedure.

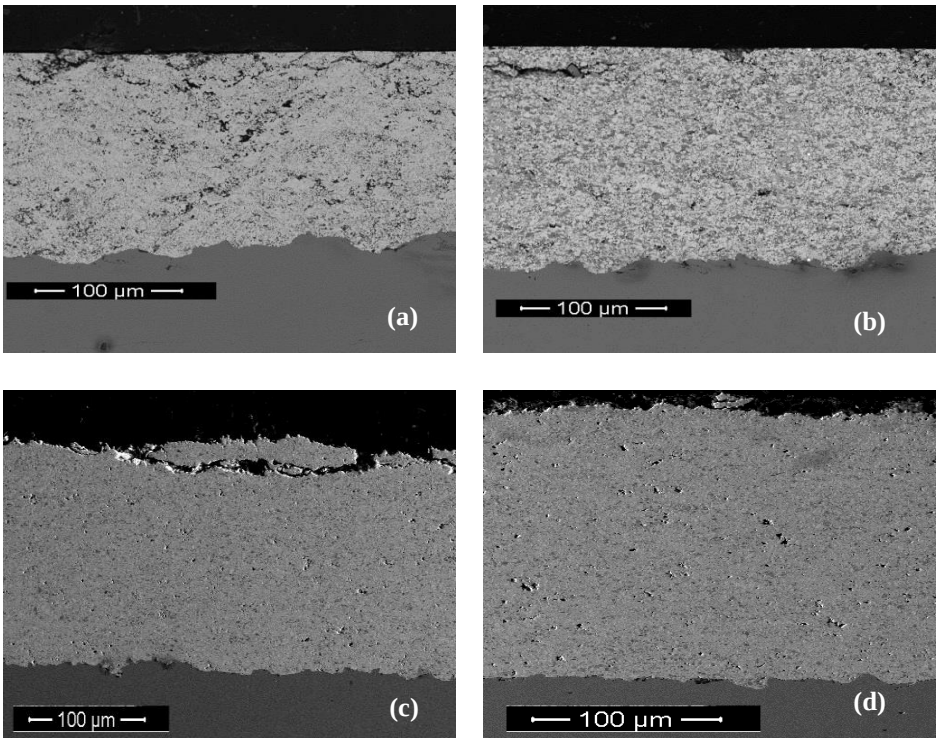


Figure 4. 3 Optical images showing the cross-section of the coating-substrate interface for (a) WC-12wt%Co, (b) WC-12wt%Co-10wt%VC, (c) WC-17wt%Co-10wt%VC (Run 38) and (d) WC-17wt%Co-10wt%VC (Run 39) coatings.

Table 4. 3 Porosity levels and coating thicknesses.

HVOF Coatings	**Porosity (%)**	**Thickness (µm)**
WC-12wt%Co	1.7 ± 0.2	250 ± 2.3
WC-12wt%Co-10wt%VC	2.1 ± 0.6	250 ± 2.7
WC-17wt%Co-10wt%VC (Run 38)	2.0 ± 0.4	234 ± 3.8
WC-17wt%Co-10wt%VC (Run 39)	1.9 ± 0.4	266 ± 3.6

SEM studies showed that all the coatings had a splat-like structure **(Figure 4.4)**. This is typical of thermal spraying where coatings are built up from the deposition of thin layers, called splats, one over the other **[77]**. The WC grains were rounded, compared to being prismatic as seen in the powders, an indication that dissolution occurred during spraying. The binder phase appeared as a continuous matrix interspersed with carbide grains. The (W,V)C grains appeared as dark grey irregularly shaped regions. EDS **(Figure 4.5)** revealed that the (W,V)C grains contained some Co, but due to the poor spatial resolution of the EDS system, it is possible that the Co detected was from the adjacent binder phase.

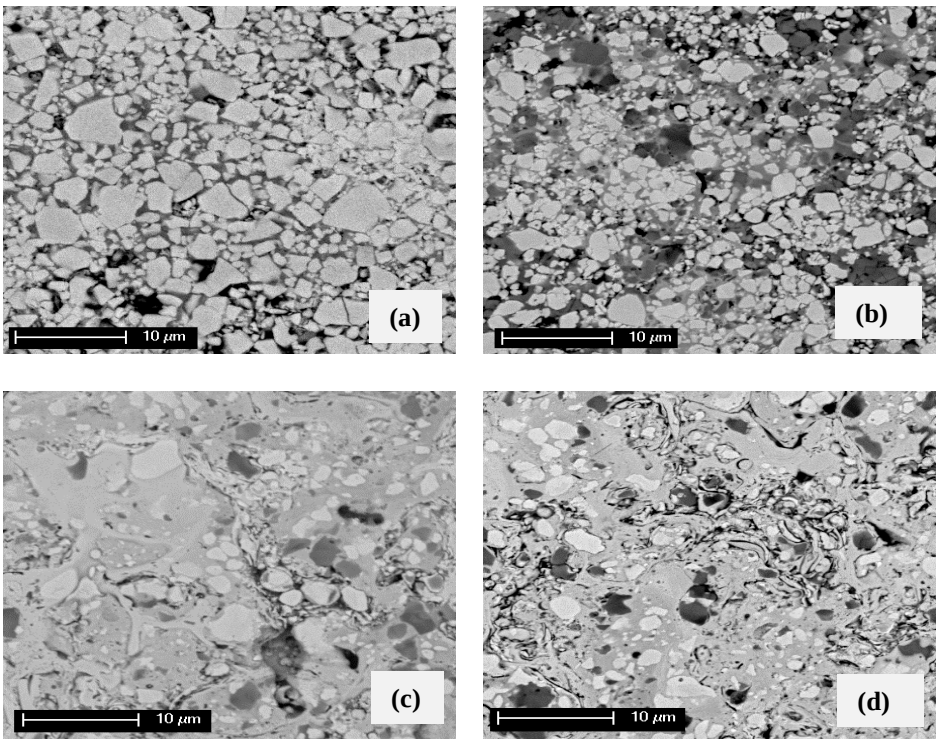


Figure 4. 4 BSE image of (a) WC-12wt%Co, (b) WC-12wt%Co-10wt%VC, (c) WC-17wt%Co-10wt%VC (Run 38) and (d) WC-17wt%Co-10wt%VC (Run 39) coatings. WC grains appear as roundish white particles; Co binder phase as a continuous light grey region; and (W,V)C grains as irregularly shaped dark grey regions. The black regions/spots are pores.

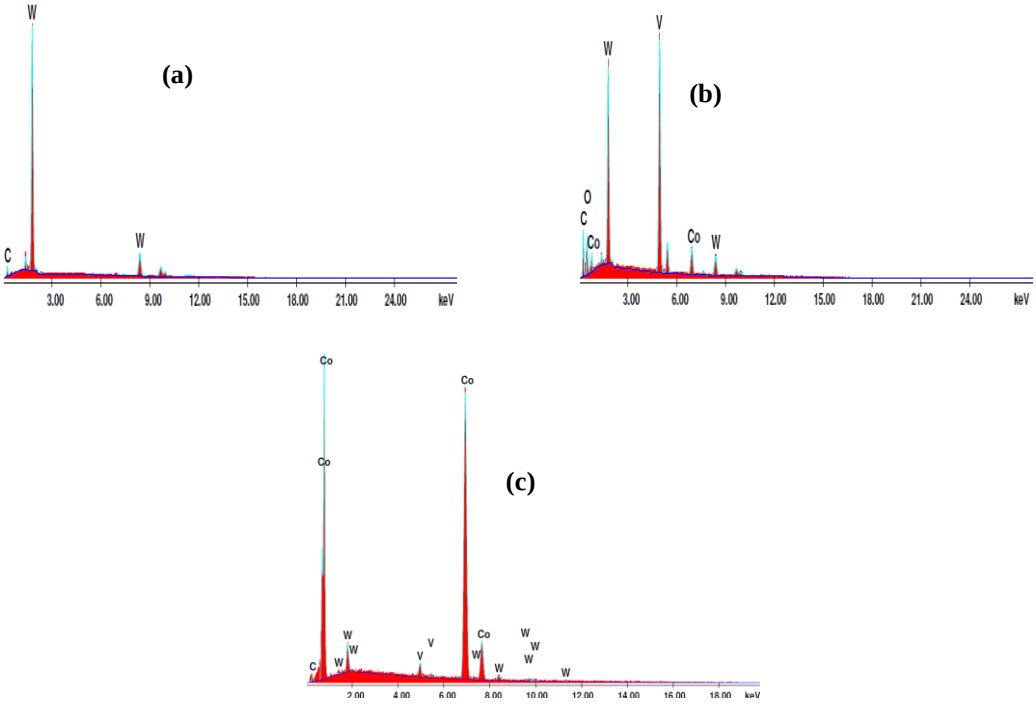
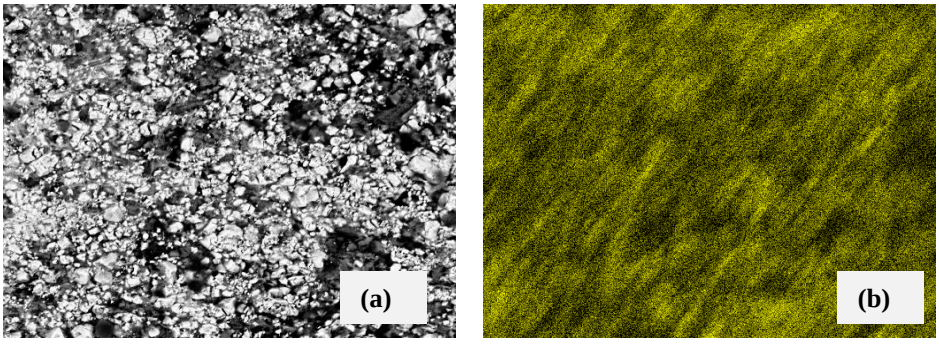


Figure 4. 5 EDS analysis of the (a) white phase showing WC roundish grains and (b) dark grey regions showing irregularly shaped (W,V)C grains, and (c) continuous matrix.

Figures 4.6 to **4.8** show the characteristic EDAX maps used to determine the homogeneity of the elemental distribution in the VC-addition coatings. The distribution of (W,V)C grains appeared to be homogenous.



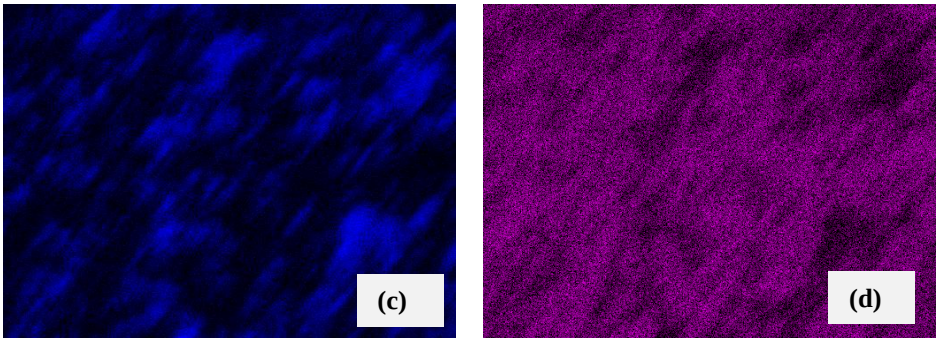


Figure 4. 6 EDAX maps showing the elemental distribution in the WC-12wt%Co-10wt%VC coatings. (a) SEM image (b) Co (c) V and (d) W.

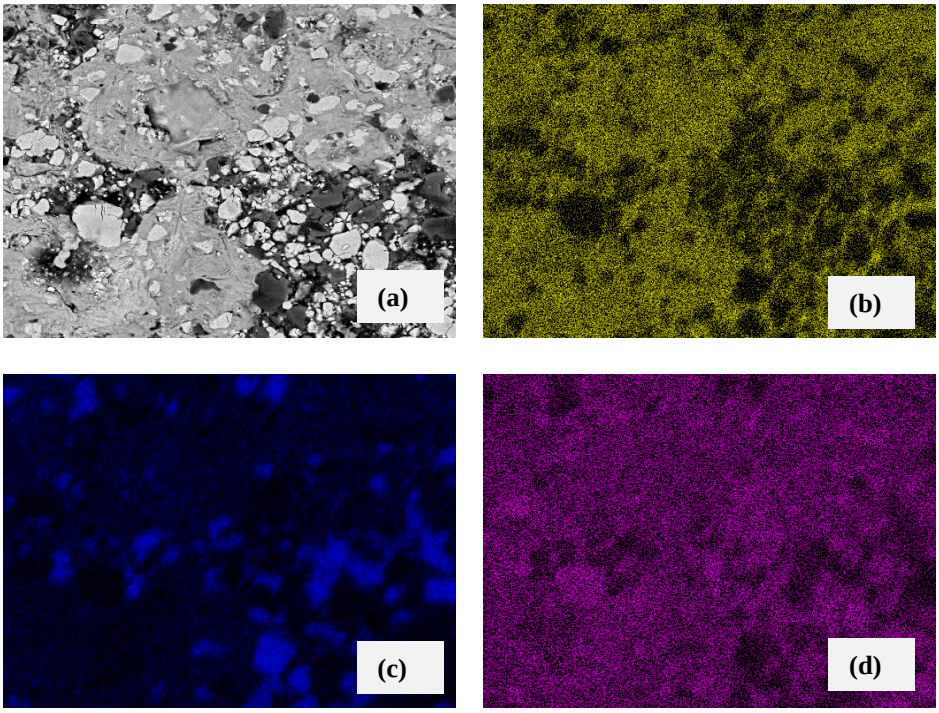
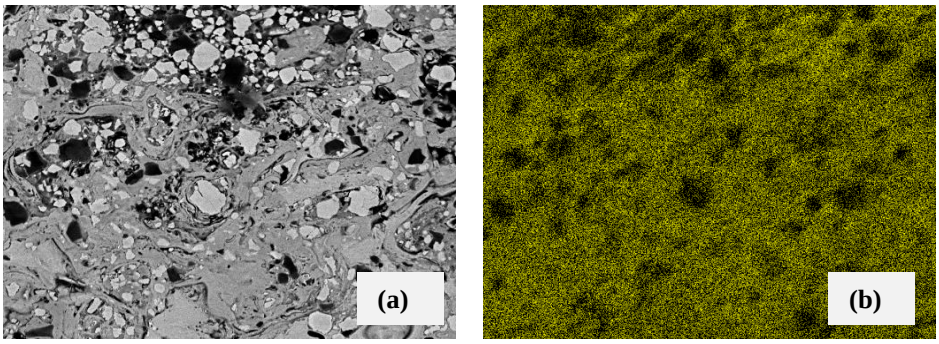


Figure 4. 7 EDAX maps showing the elemental distribution in the WC-17wt%Co-10wt%VC (Run 38) coatings. (a) SEM image (b) Co (c) V and (d) W.



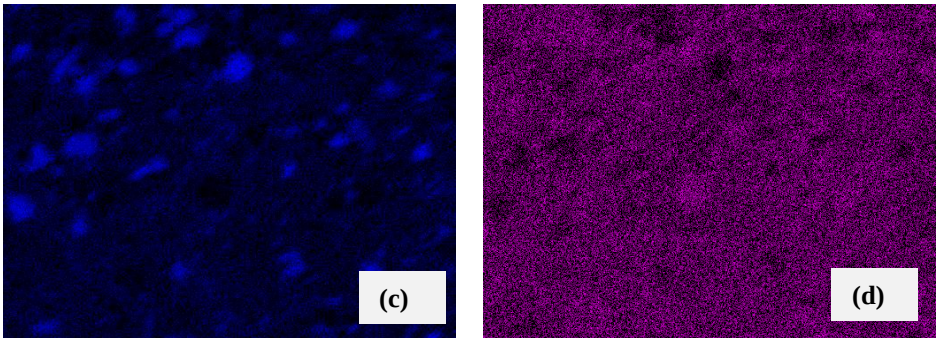


Figure 4. 8 EDAX maps showing the elemental distribution in the WC-17wt%Co-10wt%VC (Run 39) coatings. (a) SEM image (b) Co (c) V and (d) W.

4.3.2 Phase composition

The phases in the coatings are indicated by the XRD patterns in **Figure 4.9** with the approximate mass fractions listed in **Table 4.4**. The mass fractions were determined using Rietveld analysis and the values are only approximate because the amount of amorphous Co could not be determined because its peaks were not present in the XRD patterns. The most prominent phase on the XRD patterns of all the coatings was WC. The d-values of WC in all the coatings were larger than those of the starting powders. Co peaks, seen for the powders **(Figure 4.2)**, were missing in all the coatings. This may be due to the pure phase being present in amounts below the detection limit of the XRD technique.

For the 17wt%Co coatings amorphous regions were found **(Figure 4.9 (c)** and **(d))** where the Co peaks are typically found. These regions indicate that the Co became amorphous probably due to high cooling rates during coating deposition or because the high cooling rates prevented solute atoms in the Co from precipitating out of solution **[74,95]**. In the WC-12Co coatings, the eta-phase (Co_6W_6C) appeared which may have been facilitated by slow decreases in temperatures between spraying passes **[94]**. The (W,V)C phase, as seen in the powders, also appeared in the coatings. The occurrence of the (W,V)C phase in the VC-coatings could be the result of the WC dissolving in the VC during

deposition and/or as a carry-over of the (W,V)C phase from the powder. In addition, the di-tungsten carbide phase (W_2C) was observed in the WC-17wt%Co-10wt%VC coatings. W_2C is formed by the decarburization of WC during thermal spraying **[75,89,93,95,98]** when oxygen is used as the fuel gas.

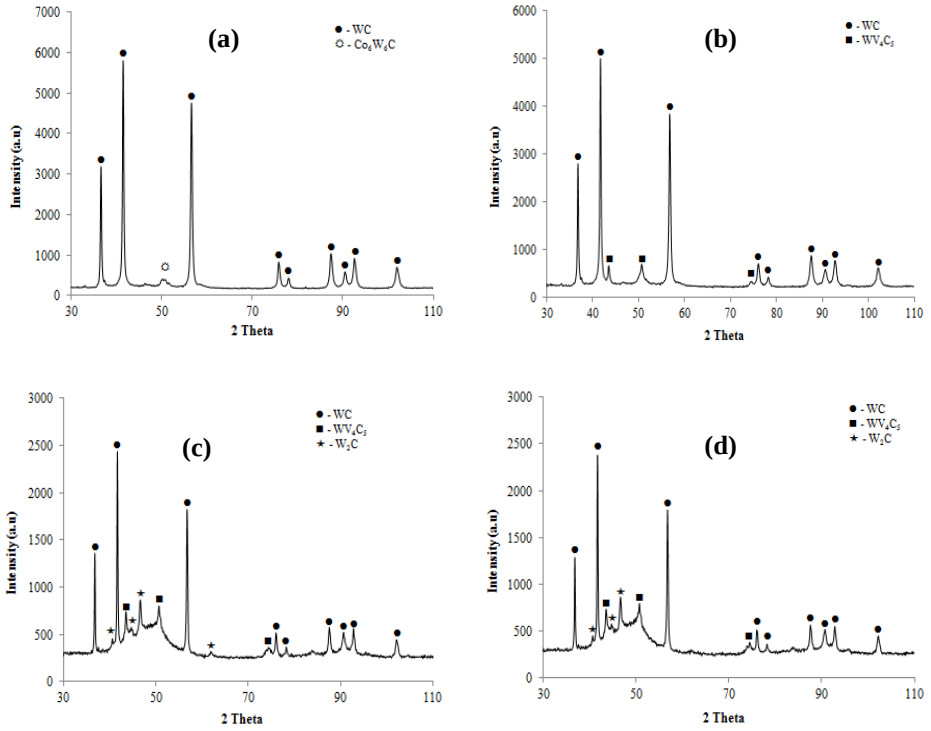


Figure 4. 9 XRD pattern of (a) WC-12wt%Co, (b) WC-12wt%Co-10wt%VC, (c) WC-17wt%Co-10wt%VC (Run 38), and (d) WC-17wt%Co-10wt%VC (Run 39) coatings.

Table 4. 4 Phase composition of coatings as determined from Rietveld analysis.

HVOF Coatings	**Phases and their mass fraction (%)**				
	WC	**Co_6W_6C**	**W_2C**	**WV_4C_5**	**Co**
WC-12wt%Co	99.94	0.06	-	-	ND*
WC-12wt%Co-10wt%VC	73.81	-	-	26.19	ND*
WC-17wt%Co-10wt%VC (Run 38)	43.55	-	18.81	37.64	ND*
WC-17wt%Co-10wt%VC (Run 39)	43.10	-	21.66	35.24	ND*

*ND = not determined because the Co was amorphous.

4.3.3 Mean carbides grain sizes

The mean carbide (WC and (W,V)C) grain sizes in the coatings, as determined by lineal analysis, are summarized in **Table 4.5**. The WC mean grain sizes were smaller in the VC-containing coatings compared to WC-12wt%Co coating. This is due to the grain refinement properties of the VC **[137]**. The WC and (W,V)C mean grain sizes in the 17wt%Co coatings were smaller than that of the 12wt%Co coatings. The WC-17wt%Co-10wt%VC coatings (Run 38 and Run 39), have the same mean WC grain size while the (W,V)C grain sizes are different.

Table 4. 5 Carbide grain sizes of coatings.

HVOF Coatings	**Carbide grain sizes (µm) ***	
	WC	WV_4C_5
WC-12wt%Co	0.6 ± 0.2	-
WC-12wt%Co-10wt%VC	0.4 ± 0.1	1.0 ± 0.4
WC-17wt%Co-10wt%VC (Run 38)	0.3 ± 0.1	0.9 ± 0.2
WC-17wt%Co-10wt%VC (Run 39)	0.3 ± 0.1	0.7 ± 0.2

* = mean grains sizes.

4.3.4 Coating hardness

Table 4.6 lists the hardness values of the coatings. The hardness values align with the carbide grain sizes **(Table 4.5)** in that the hardness increased as the carbide grain size decreased. The higher hardness of the 17wt%Co coatings is attributed to a combination of the fine carbide grain size and the hard W_2C phase, only detected in these two coatings. W_2C is known to increase coating hardness **[74,89]**. The average indentation size for the coatings range between 28 and 35 and this indicates that the hardness values measured were not on the carbide grains but across the entire coating.

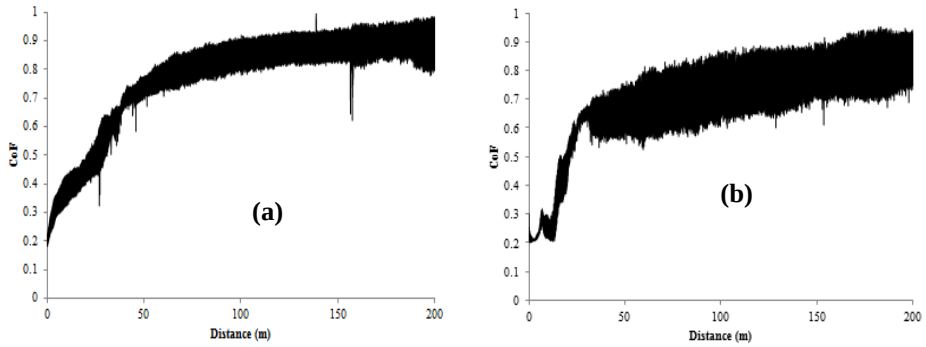
Table 4. 6 Hardness values of the coatings.

HVOF Coatings	**Hardness, $HV_{0.5}$**
WC-12wt%Co	796 ± 53
WC-12wt%Co-10wt%VC	868 ± 60
WC-17wt%Co-10wt%VC (Run 38)	1164 ± 90
WC-17wt%Co-10wt%VC (Run 39)	1161 ± 51

4.4 Friction and sliding wear tests

The friction behavior of each coating sliding against the balls (100Cr steel and WC-Co) as a function of sliding distance for the test condition stated in **Table 3.6** is illustrated in **Figures 4.10** and **4.11**. The coefficients of friction (CoF) of the coating-100Cr steel ball sliding pairs are higher than the CoFs of the coating-WC-Co ball sliding pairs. The friction behaviour for all the sliding pairs typically showed two distinct regions namely a running-in phase and a steady-state region.

In general, the running-in phase for the coating-100Cr steel ball sliding pairs occurred within the first 50 m of sliding during which the CoF increased almost linearly from 0.2 up to 0.6. An exception to this trend was observed for the Run 38 **(Figure 4.10(c))** which did not show a distinct running-in phase; rather the CoF increased sharply from 0.2 to 0.6 within the first 2 m of sliding. The steady state kinetic CoF for all these coatings ranged from 0.6 to 0.9.



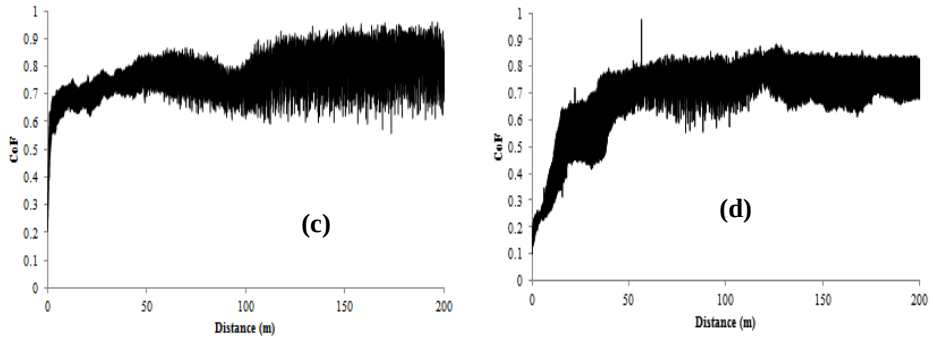


Figure 4. 10 Friction behavior against 100Cr ball for (a) WC-12wt%Co, (b) WC-12wt%Co-10wt%VC, (c) WC-17wt%Co-10wt%VC (Run 38), and (d) WC-17wt%Co-10wt%VC (Run 39) coatings.

The running-in phases of the coating-WC-Co ball sliding pairs **(Figure 4.11)** were distinctly different to those of the coating-100Cr steel ball sliding pairs. Differences amongst the WC-Co ball sliding pairs were also notable. The CoF of the WC-12wt%Co coating initiated at approximately 0.25, slightly decreased for a few meters and then appeared to level off for 30 m after which it gradually increased for 60 m reaching a CoF of 0.34 and then remained steady for the remainder of the test. The CoF of the WC-12wt%Co-10wt%VC coating initiated at 0.2 and remained steady for approximately 10 m and then showed a gradual linear increase for approximately 140 m reaching a CoF of 0.26. After this a very short increase in the CoF occurred up to about 0.28 and then a further gradual increase up to approximately 0.33. The CoF behavior of the two 17wt%Co coatings was similar. The CoF increased sharply within the first few meters of sliding and then remained constant for the duration of the test ranging from 0.24 to 0.5.

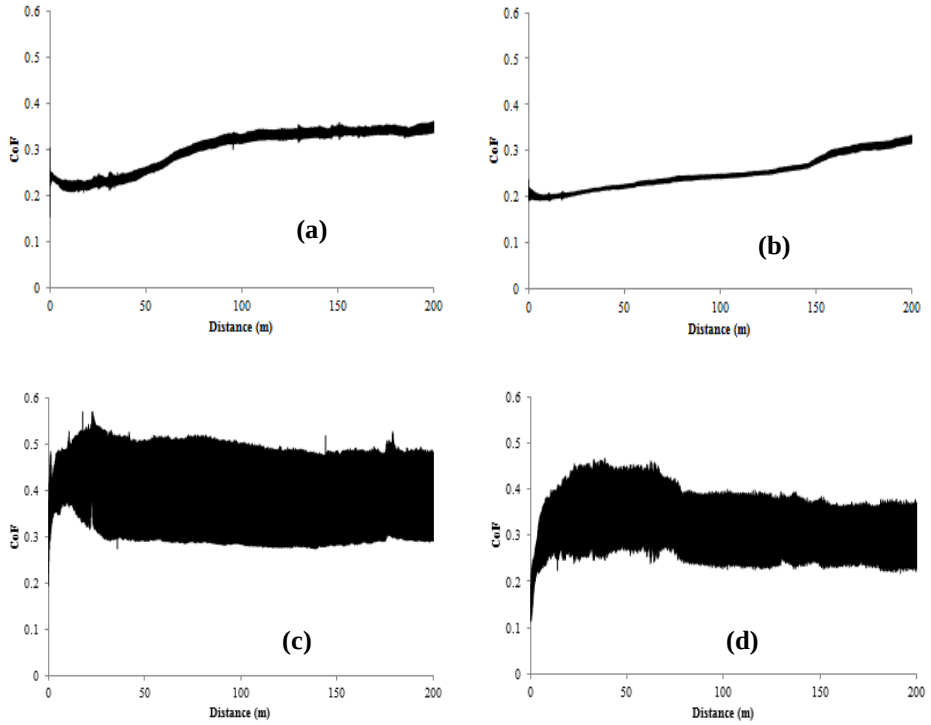


Figure 4. 11 Friction behavior against WC-Co ball for (a) WC-12wt%Co, (b) WC-12wt%Co-10wt%VC, (c) WC-17wt%Co-10wt%VC (Run 38), and (d) WC-17wt%Co-10wt%VC (Run 39) coatings.

Figure 4.12 shows the static and dynamic CoF for each ball-coating pair after 200 m of sliding while **Table 4.7** lists the penetration depths of the balls into the coatings as well as the wear track widths made on the coatings. From **Figure 4.12**, the coating-100Cr steel ball generated a higher friction than the coating-WC-Co ball. Observation from **Table 4.7** showed that the penetration depths and the wear track widths of the coating-ball pairs for the 100Cr steel ball were higher than those of the coating-WC-Co ball. With the 100Cr ball, the penetration depths of the 10wt%VC coatings were lower compared to the WC-12wt%Co coating. The 12wt%Co-10wt%VC coating had the highest wear track width against the 100Cr steel ball while the 17wt%Co-10wt%VC Run 39 had the smallest.

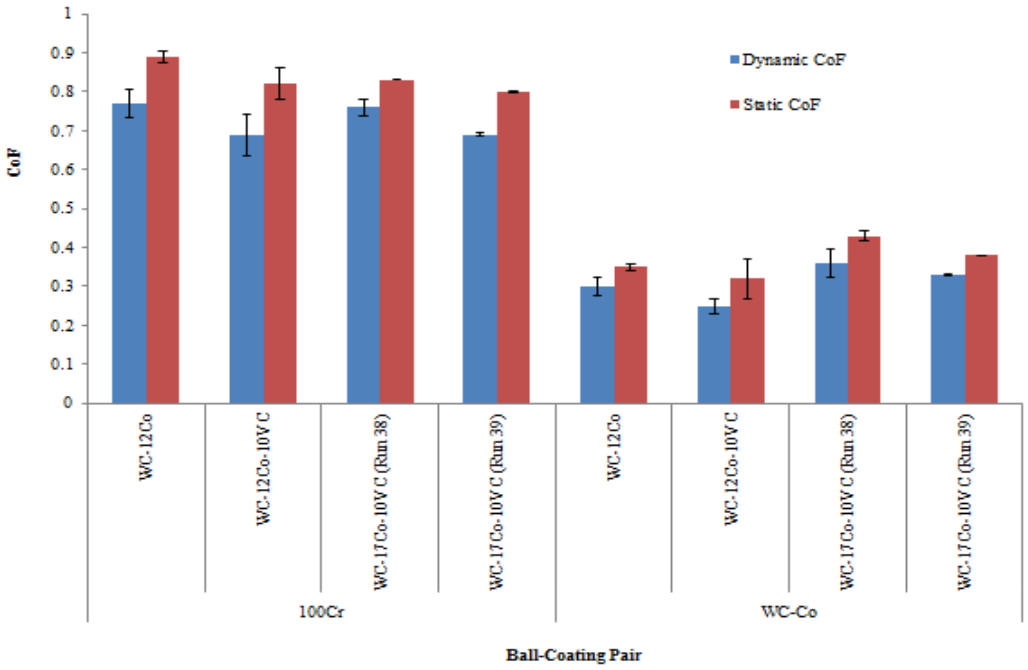


Figure 4. 12 Friction coefficients for the ball-coating pairs.

Table 4. 7 Ball penetration depths and wear track width on the coatings.

HVOF Coatings	100Cr ball		WC-Co ball	
	Wear track width (µm)	Penetration depth (µm)	Wear track width (µm)	Penetration depth (µm)
WC-12wt%Co	642 ± 72	2.74 ± 0.3	290 ± 07	0.34 ± 0.4
WC-12wt%Co-10wt%VC	673 ± 58	2.05 ± 0.8	255 ± 14	0.57 ± 0.7
WC-17wt%Co-10wt%VC (Run 38)	601 ± 72	1.47 ± 1.8	408 ± 00	0.32 ± 0.2
WC-17wt%Co-10wt%VC (Run 39)	357 ± 15	0.79 ± 1.1	296 ± 43	0.82 ± 0.2

Figures 4.13 compares the wear coefficients of the coating against the balls while **Figure 4.14** compares those of the balls on the coatings. The wear coefficients for all the coatings were generally higher against the 100Cr ball and lower against the WC-Co ball. The coatings with VC additions showed a better wear resistance compared to the WC-12wt%Co coating. The 17wt%Co coatings showed a superior wear rate against the 100Cr ball compared to the 12wt%Co coatings. Against the WC-Co balls, a reverse trend was observed. The trends showed

sliding pairs with high friction values having high wear coefficients which translate into high wear rates.

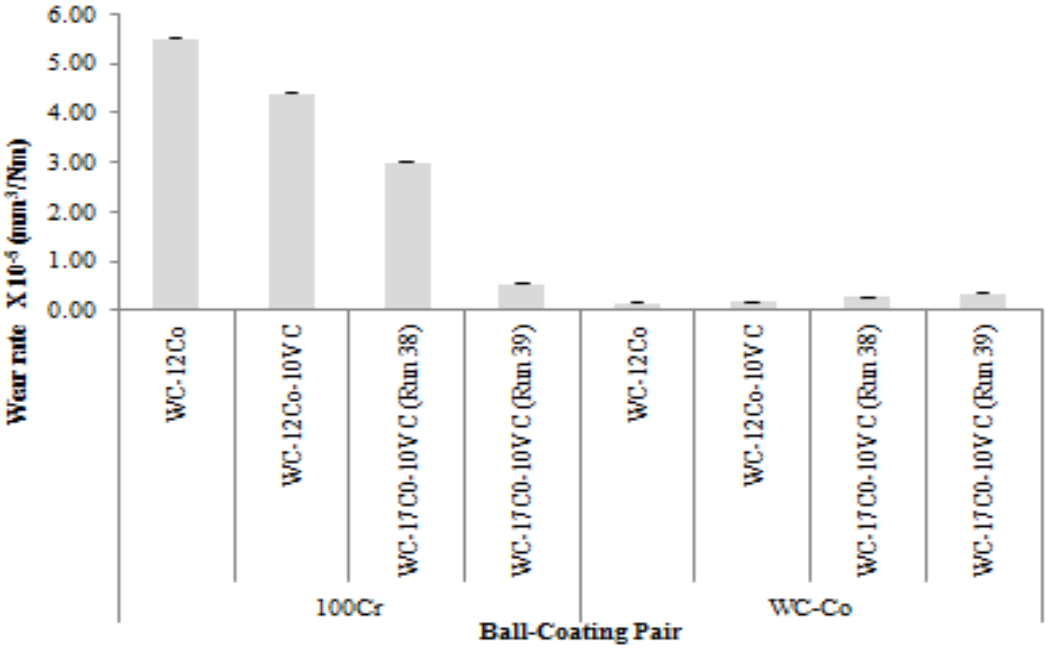


Figure 4. 13 Wear coefficients comparison for the coatings.

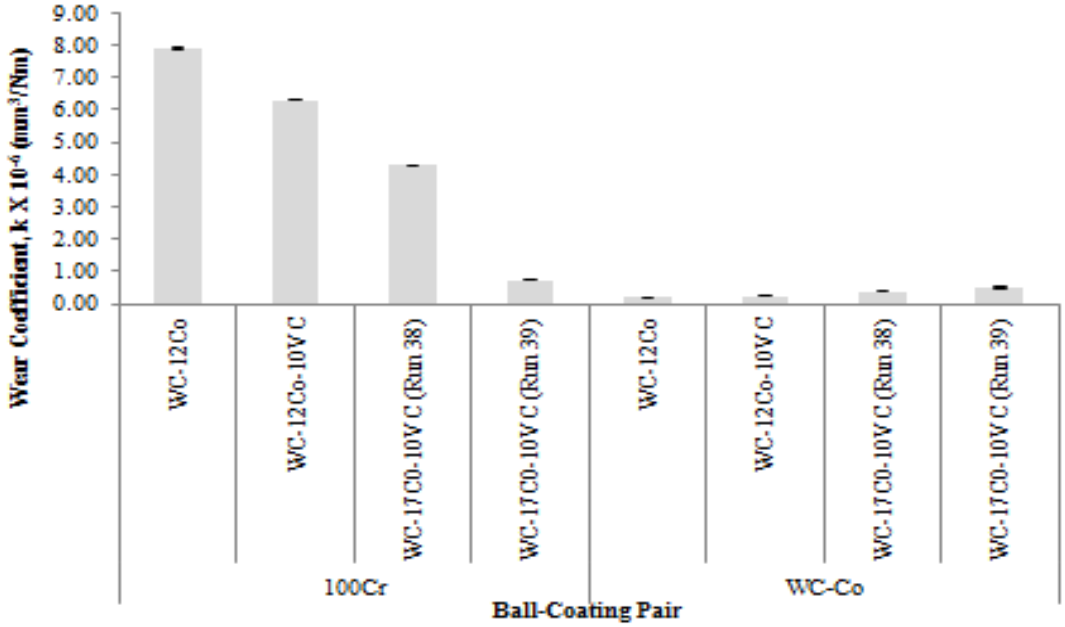
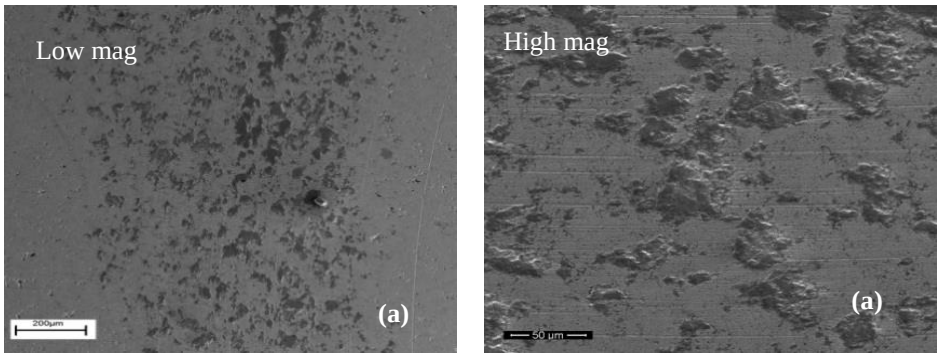


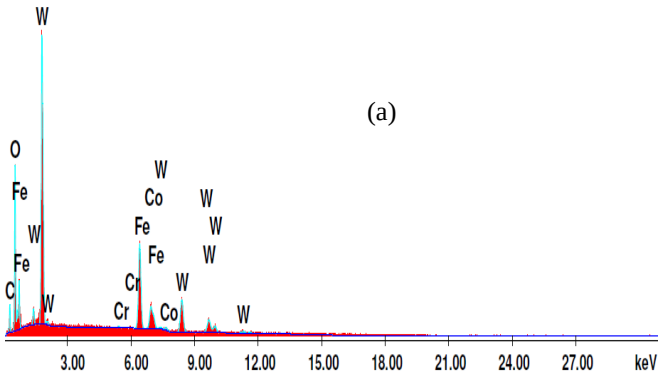
Figure 4. 14 Wear coefficients comparison for the balls.

4.4.1 Wear mechanisms in sliding wear

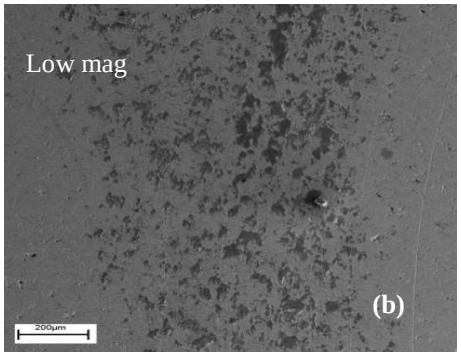
The wear scars from the sliding wear tests on the coatings were examined using SEM with EDX, and XPS in order to determine the wear mechanisms. Some selected SEM images are presented to provide a summary of the wear mechanisms observed. In many instances similar wear mechanisms were observed when tested against both balls.

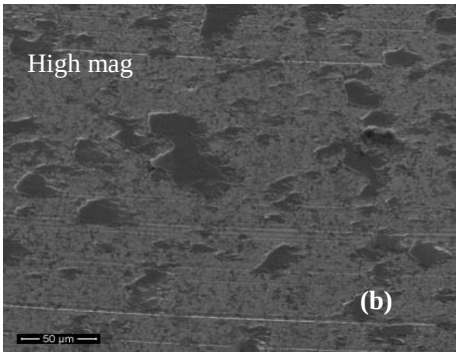
Figures 4.15 and **4.16** illustrate the typical wear tracks on the coatings under the test conditions with the EDX analyses on the wear track. These images provide a general impression of the variation in wear track widths achieved with the different balls on the operating condition.

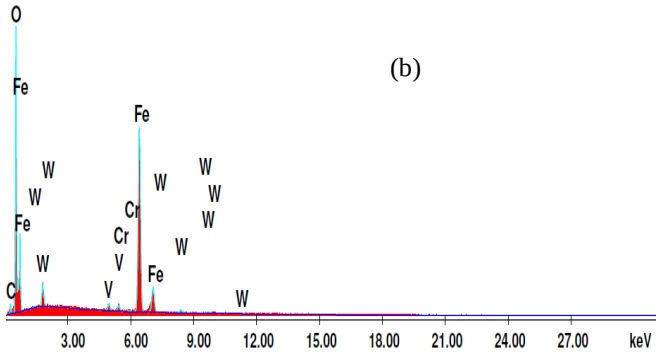




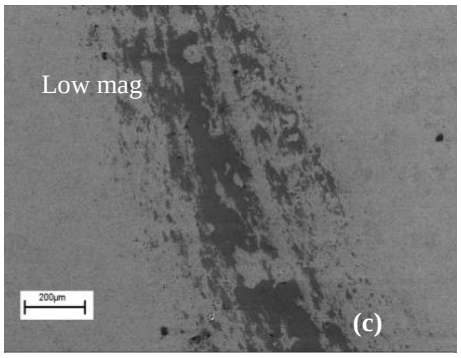
(a)

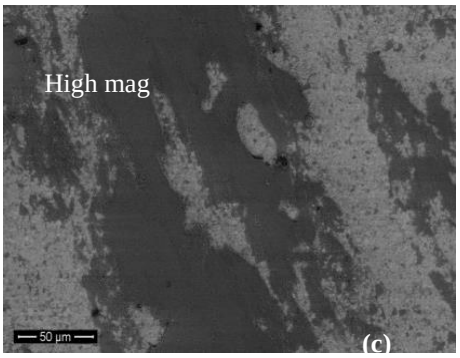

Low mag
(b)

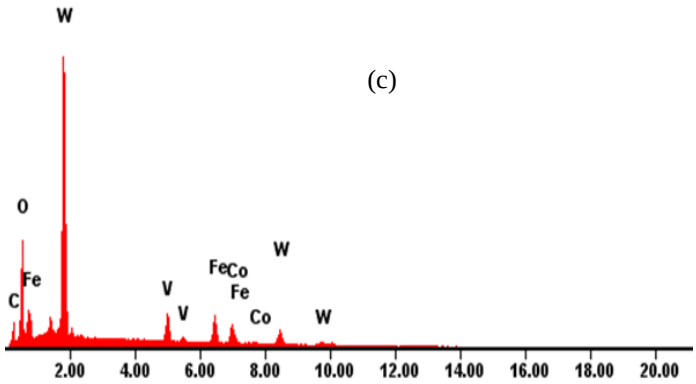

High mag
(b)


O
Fe
W
W
Fe
W
C
Cr
V
V
Fe
Fe
W
W
W
W
W
3.00
6.00
9.00
12.00
15.00
18.00
21.00
24.00
27.00
keV

(b)


Low mag
(c)


High mag
(c)


W
O
Fe
C
V
V
Fe
Co
Fe
Co
W
W
2.00
4.00
6.00
8.00
10.00
12.00
14.00
16.00
18.00
20.00

(c)

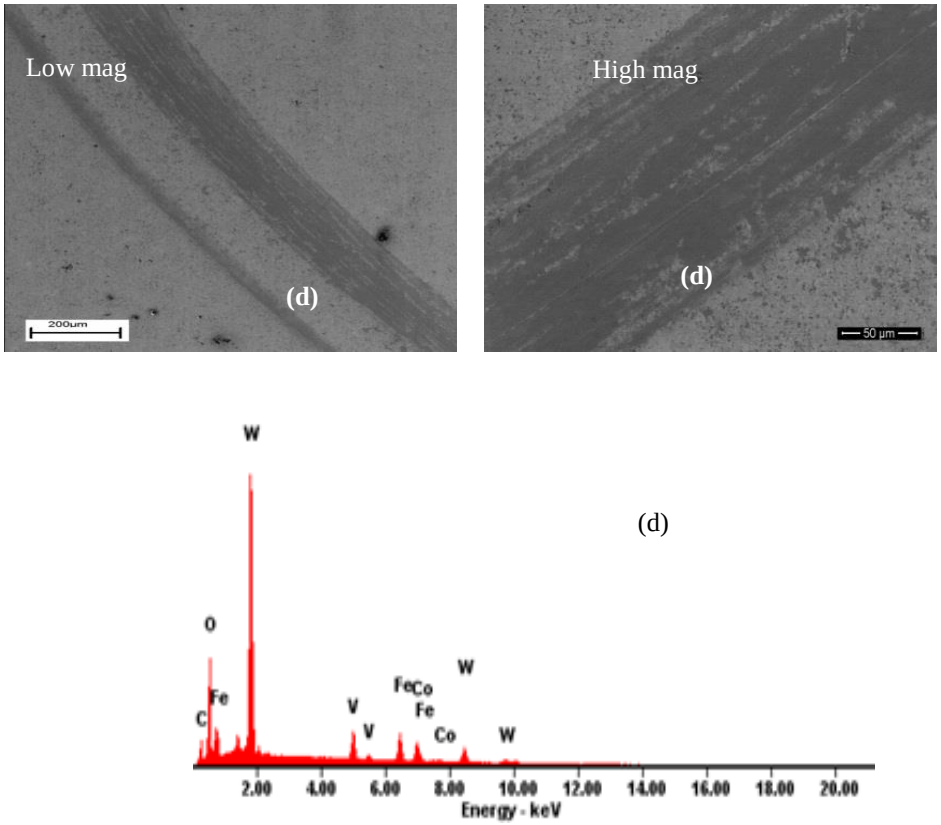
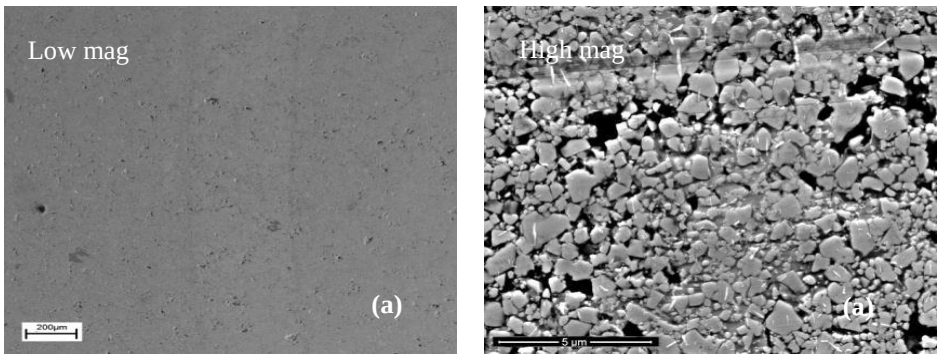
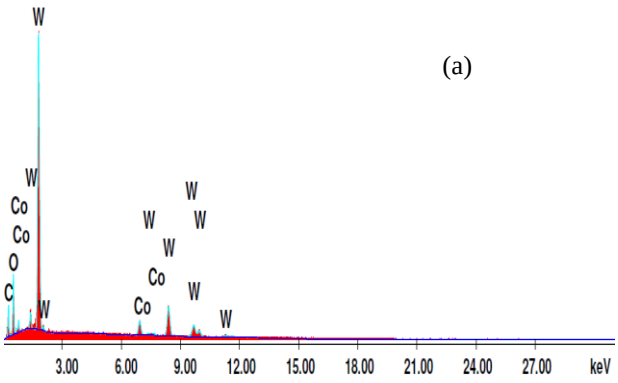
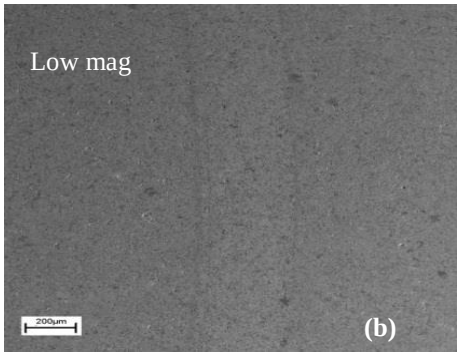


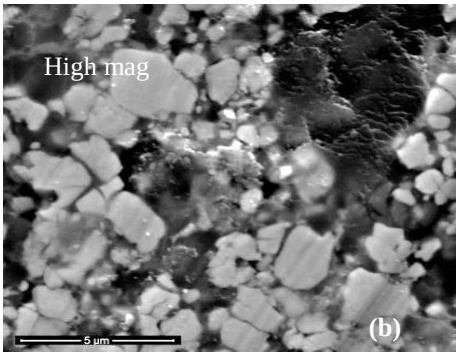
Figure 4. 15 SEM images of the wear tracks against 100Cr ball for (a) WC-12wt%Co, (b) WC-12wt%Co-10wt%VC, (c) WC-17wt%Co-10wt%VC (Run 38), and (d) WC-17wt%Co-10wt%VC (Run 39) coatings.



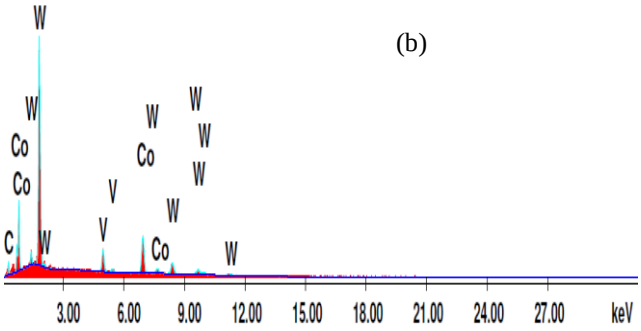
(a)

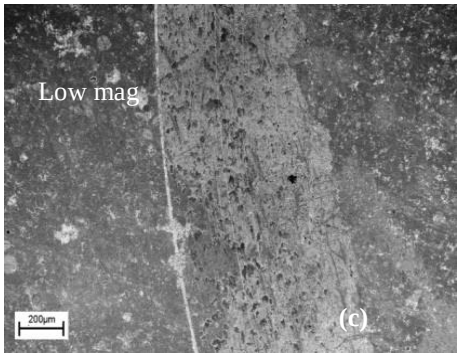

W
W
Co
Co
O
C
W
Co
W
W
W
W
Co
W
W
3.00
6.00
9.00
12.00
15.00
18.00
21.00
24.00
27.00
keV

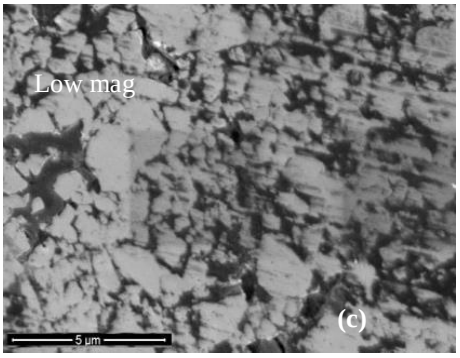

Low mag
200µm
(b)


High mag
5 µm
(b)

(b)


W
W
Co
Co
C
W
V
V
W
Co
W
W
W
W
Co
W
3.00
6.00
9.00
12.00
15.00
18.00
21.00
24.00
27.00
keV


Low mag
200µm
(c)


Low mag
5 µm
(c)

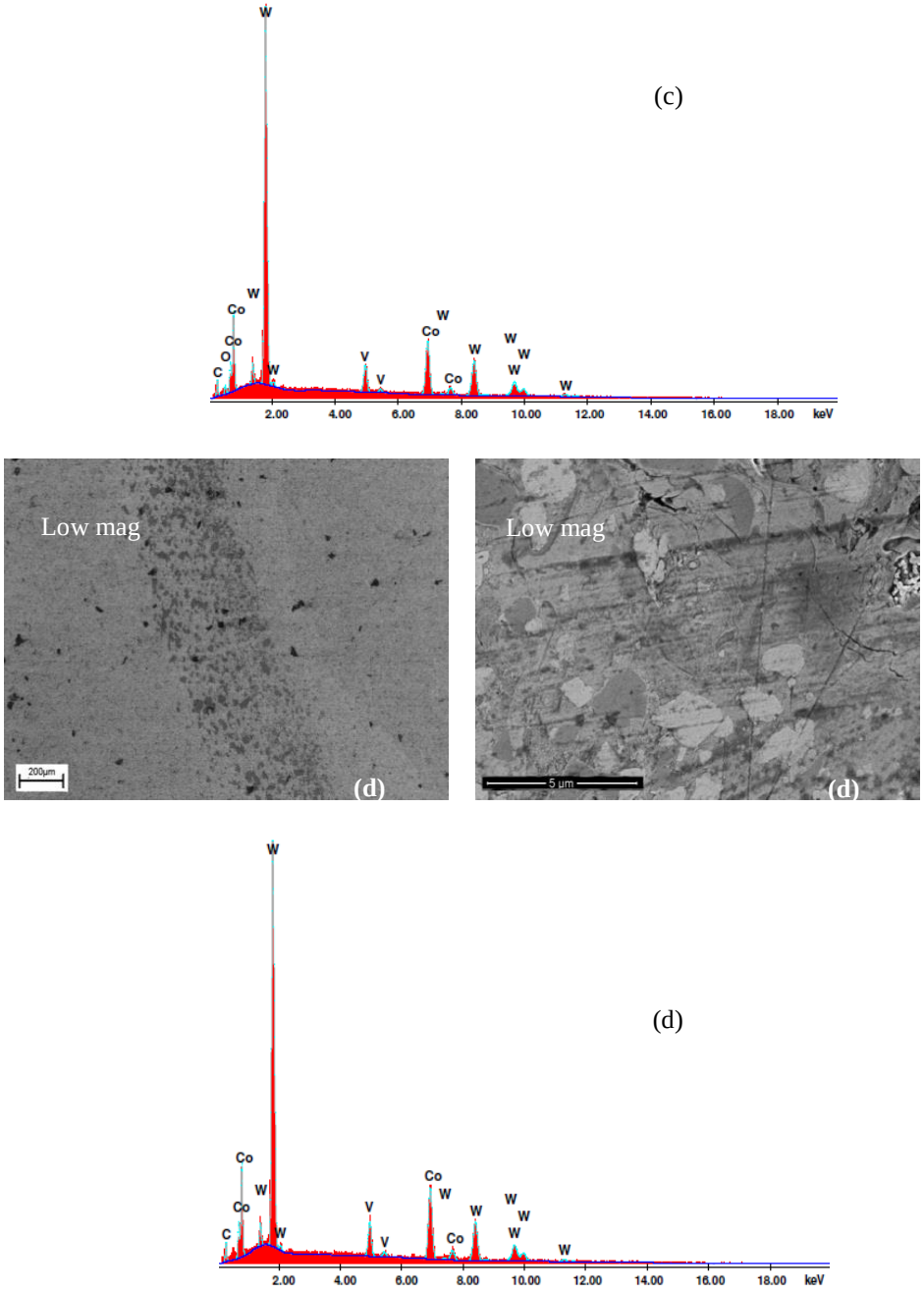
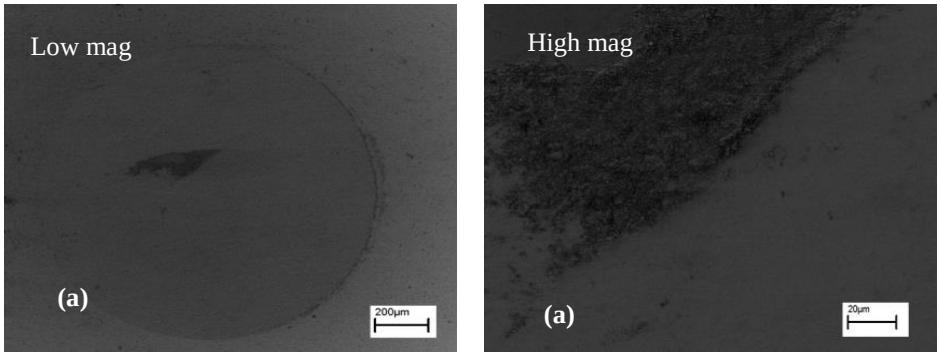


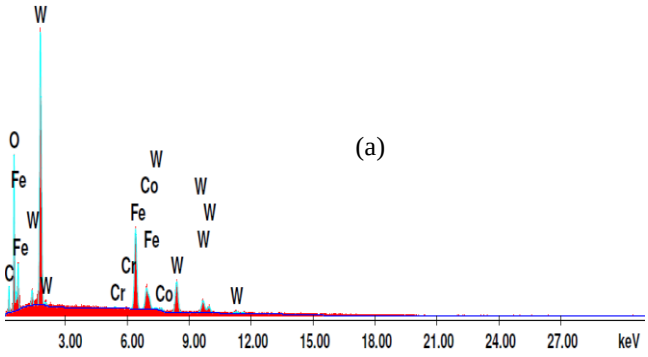
Figure 4. 16 SEM images of the wear tracks against WC-Co ball for (a) WC-12wt%Co, (b) WC-12wt%Co-10wt%VC, (c) WC-17wt%Co-10wt%VC (Run 38), and (d) WC-17wt%Co-10wt%VC (Run 39) coatings.

The wear mechanisms for all the coatings against the balls were found to be very similar. Smearing of worn particles **(Figure 4.15),** ploughing of wear particles, which had contributed to groove formation **(Figure 4.16)**. Preferential binder

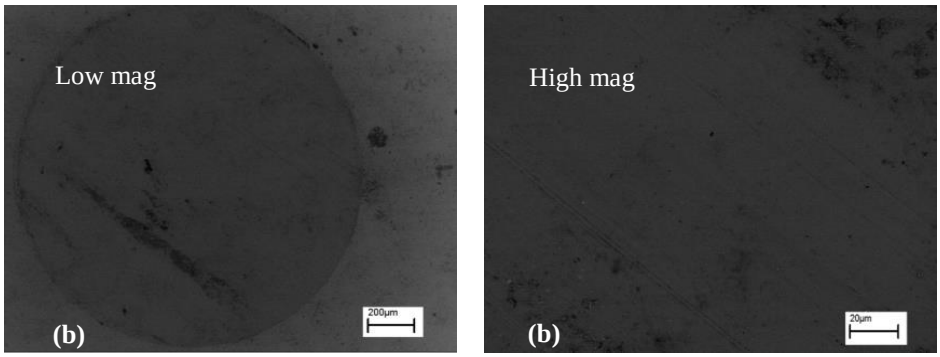
removal, carbide grain cracking and fragmentations, grain pull-out, adhesion and formation of thin tribo-layer oxides during wear. It is believed that the binder removal occurs first, followed by subsequent carbide grain cracking and carbide grain pull-out. The grooves formed can be seen to be parallel with the sliding direction. Extensive smearing occurred in the 10wt%VC coatings compared to the WC-12wt%Co coating while higher magnification images **(Appendix B2)** showed that the WC-12wt%Co coating had severe grain pull-out compared to the 10wt%VC coatings, when tested against the 100Cr steel ball **(Figure 4.15)**. The 17wt%Co coatings showed less wear debris and less wear tracks on their surfaces compared to those of the 12wt%Co coatings, which correlates with their decreased wear coefficients experienced against the 100Cr steel balls. EDX results on the wear track of the coatings against the 100Cr balls as presented in **Figure 4.15** show the presence of Fe and Cr. This confirms the transfer of materials from the ball to the surface of the coatings during wear. EDX analysis on all the surface of the coatings showed materials' transfer from the balls to the coatings. Against the WC-Co ball, the 10wt%VC coatings showed a reverse trend as they worn more compare to the WC-12wt%Co coating.

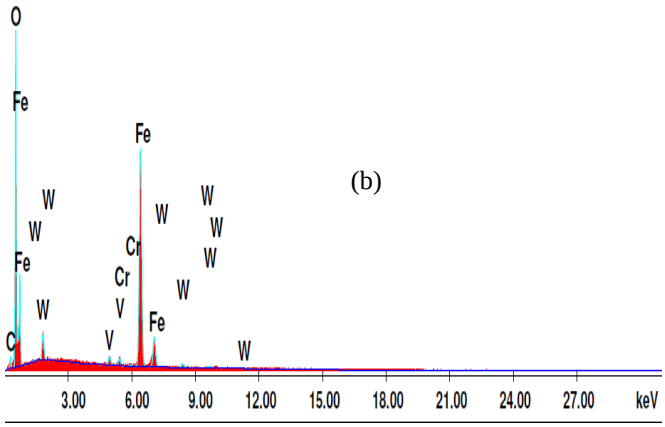
Typical wear scars on the 100Cr steel and the WC-Co balls against the coatings are shown in **Figures 4.17** and **4.18**, with their respective EDX analyses. The images contain both lower and higher magnifications. **Figure 4.17** shows the wear scar on the ball that produced the wear track on the coatings shown in **Figure 4.15**, while **Figure 4.18** represents that from **Figure 4.16**. The presence of W on the wear scars on the 100Cr steel ball against the coatings gave evidence of materials' transfer. There was no evidence of materials transfer on the wear scar on the WC-Co ball against 10wt%VC coatings from the EDX analyses.


Low mag
(a)
200µm
High mag
(a)
20µm


O
Fe
W
Fe
C
W
Cr
W
Co
Fe
Cr
Co
W
Fe
W
W
W
3.00
6.00
9.00
12.00
15.00
18.00
21.00
24.00
27.00
keV

(a)


Low mag
(b)
200µm
High mag
(b)
20µm


O
Fe
W
W
Fe
C
W
Fe
Cr
Cr
V
V
W
Fe
W
W
W
W
3.00
6.00
9.00
12.00
15.00
18.00
21.00
24.00
27.00
keV

(b)

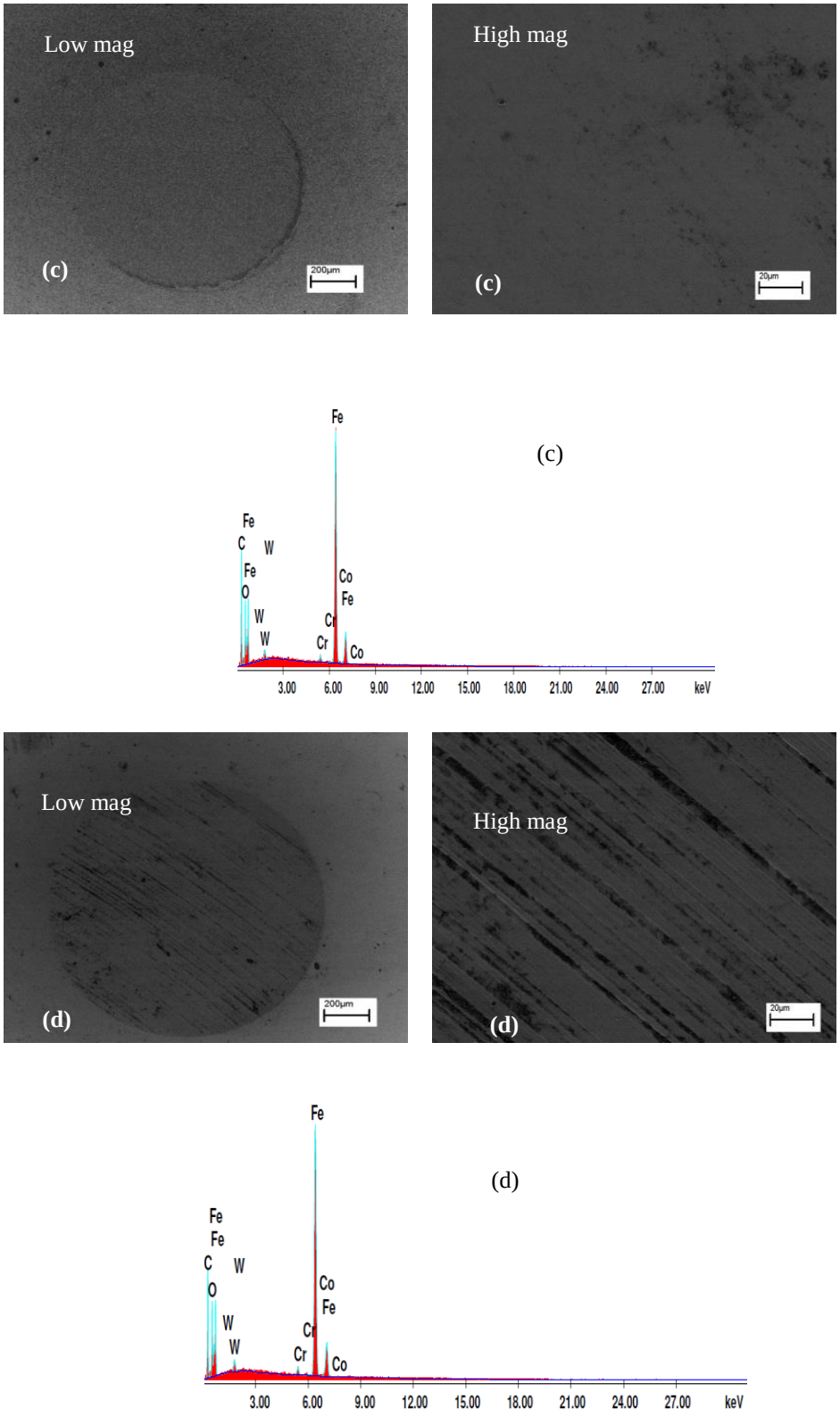
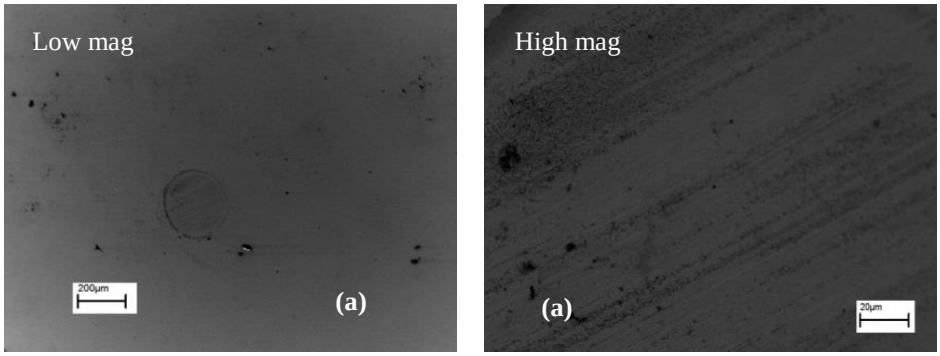
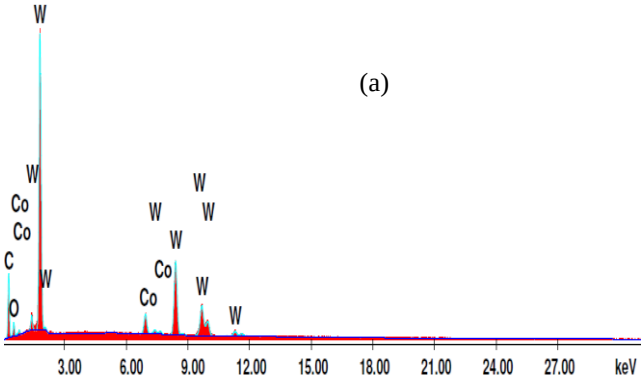
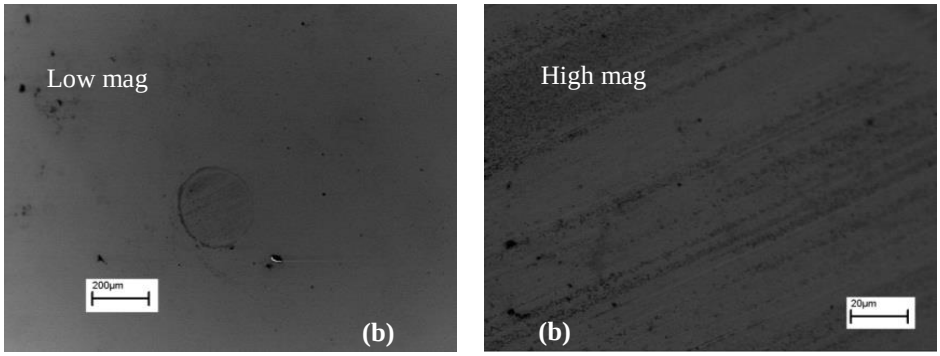


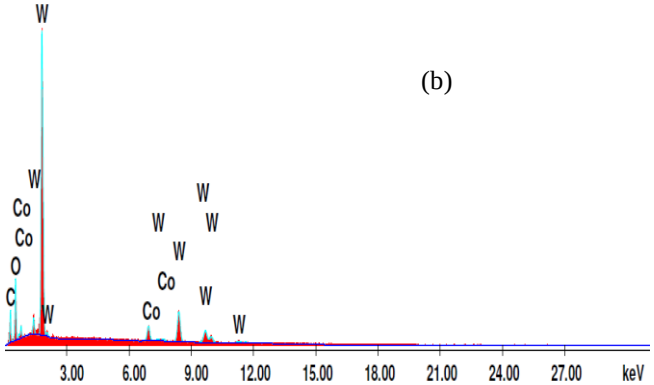
Figure 4. 17 SEM image with EDX analysis of the wear tracks on the 100Cr steel ball against (a) WC-12wt%Co, (b) WC-12wt%Co-10wt%VC, (c) WC-17wt%Co-10wt%VC (Run 38), and (d) WC-17wt%Co-10wt%VC (Run 39) coatings.


Low mag
200µm
(a)
High mag
(a)
20µm


W
W
Co
Co
C
O
W
Co
Co
W
W
W
W
W
W
3.00
6.00
9.00
12.00
15.00
18.00
21.00
24.00
27.00
keV

(a)


Low mag
200µm
(b)
High mag
(b)
20µm


W
W
Co
Co
O
C
W
Co
Co
W
W
W
W
W
W
3.00
6.00
9.00
12.00
15.00
18.00
21.00
24.00
27.00
keV

(b)

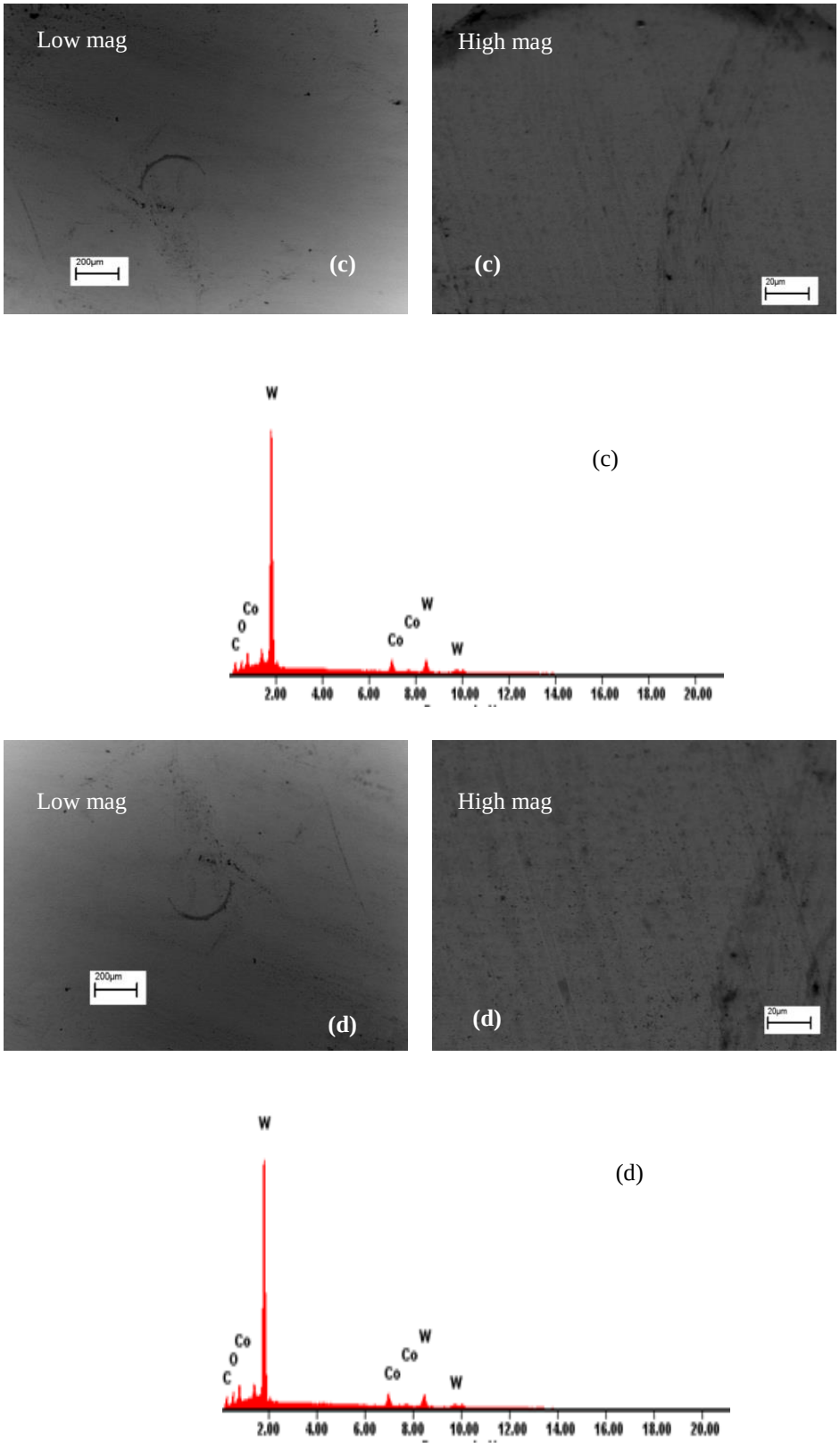


Figure 4. 18 SEM images with EDX analysis of the wear tracks of the WC-Co ball against (a) WC-12wt%Co, (b) WC-12wt%Co-10wt%VC, (c) WC-17wt%Co-10wt%VC (Run 38), and (d) WC-17wt%Co-10wt%VC (Run 39) coatings.

Table 4.8 summarizes the atomic concentration of the elements and the probable compounds found on the worn surfaces of the coatings using XPS analyses.

For all the coatings, XPS spectra (**Figures 4.19** and **4.20**) on the un-worn and worn tracks showed prominent loss of the binder phase. Selected spectra for WC-12wt%Co, WC-12wt%Co-10wt%VC and WC-17wt%Co-10wt%VC coatings are illustrated in **Figures 4.19** and **4.20** respectively. The compounds present on the surfaces of the 10wt%VC coatings were found to be very similar across the different sliding pairs, while that of the WC-12wt%Co were different for the sliding pair under the test condition. Iron oxide tends to be more prevalent under test with 100Cr ball for WC-12wt%Co and 17wt%Co coatings, except for the WC-12wt%Co-10wt%VC coating. The occurrence of the compound WO_3 was observed to be present on the surface of the 17wt%Co coatings when tested against both the 100Cr steel and the WC-Co ball, while the occurrence of V_2O_5 was observed for the 10wt%VC coating under all test condition. The presence of WO_3 and V_2O_5 indicates oxidation of the 10wt%VC coatings' surfaces during sliding while that of Iron oxide indicates materials' transfer from the 100Cr ball. WO_3 was also observed on the worn surface of the WC-12wt%Co-WC-Co ball pair **(see Table 4.8)**. **Appendix B3** shows the wide and narrow XPS scans on the wear tracks of the coatings.

Table 4. 8 XPS results of the worn coating surfaces.

Ball	**HVOF Coatings**	**Element**	**Atomic concentration (%)**	**Probable compounds**
100Cr steel	WC-12wt%Co	C Fe O W	48.2 11.4 19.5 20.9	WC, FeO, CoO, Cr_2O_3, $CoFe_2O_4$
	WC-12wt%Co-10wt%VC	C Co O V W	45.0 12.0 10.0 6.6 26.5	WC, V_2O_3, $Co(OH)_2$
	WC-17wt%Co-10wt%VC	C Fe O V W	33.5 20.9 29.6 2.3 13.6	WC, FeO, V_2O_3, WO_3
WC-Co	WC-12wt%Co	C Co O W	48.0 8.3 7.4 36.2	WC, WO_3
	WC-12wt%Co-10wt%VC	C Co O V W	47.3 11.1 8.2 5.8 27.6	WC, V_2O_3
	WC-17wt%Co-10wt%VC	C Co O V W	36.6 11.5 14.9 5.8 31.2	WC, V_2O_3, WO_3

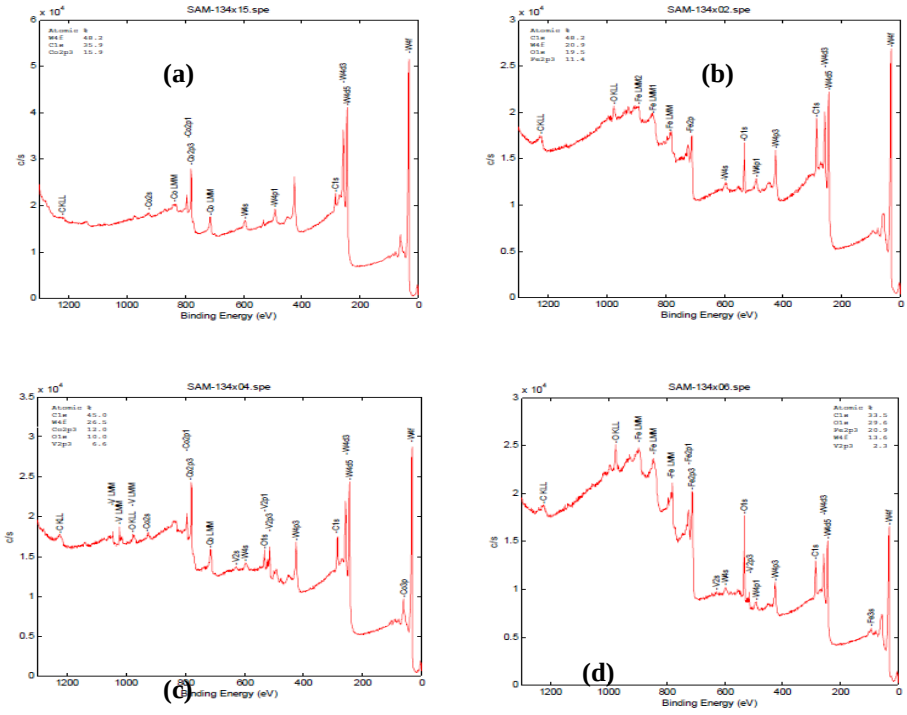


Figure 4. 19 Selected XPS spectra against the 100Cr steel ball for the (a) un-worn track (b) WC-12wt%Co, (c) WC-12wt%Co-10wt%VC, and (c) WC-17wt%Co-10wt%VC coatings.

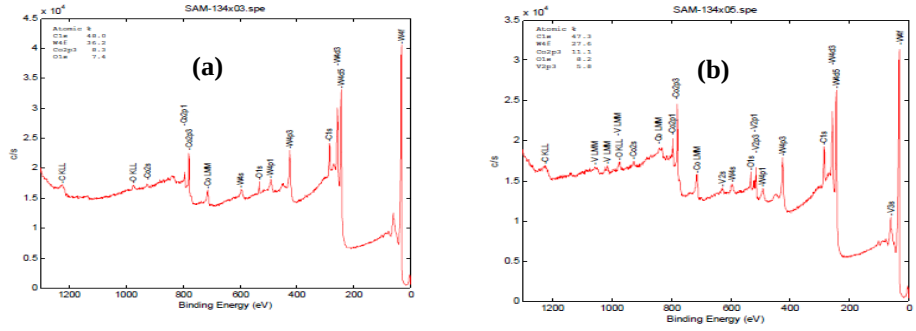


Figure 4. 20 Selected XPS spectra against the WC-Co ball for the (a) WC-12wt%Co, and (b) WC-12wt%Co-10wt%VC coatings.

4.5 Slurry erosion tests

The average mass loss against time and the erosion rate against time curves of the polished surfaces of the coatings at the four different test angles are shown in

Appendix B4. **Figure 4.21** compare the average mass loss of the coatings against time at 90°. The erosion rate was obtained as the quotient of the cumulative mass loss and the erodent mass **[117]**. At all the test angles, the average mass loss increases with test time and the mass losses for the 10wt%VC coatings were generally lower compared to the WC-12wt%Co coating, which translates to a better wear resistance. The average mass losses for all the coatings decreases as the impact angle decreased. At angle 45°, the average mass losses from all the coatings were very low and erratic in nature. At higher impact angles, (90° and 75°), the 17wt%Co-10wt%VC coatings had a lower average mass loss compared to the 12wt%Co-10wt%VC coating. This could be a result of the optimized processing parameter, which could have resulted in higher inter-splat strength of the 17wt%Co coatings. The 12wt%Co-10wt%VC coating showed better erosion resistance at 60° compared to the 17wt%Co-10wt%VC coatings. **Figure 4.22** compares the average slurry erosion rate against the impact angles for the coatings. The 12wt%Co coatings showed a maximum erosion rate at 90°. The erosion rate of the WC-17wt%Co-10wt%VC Run 39 peaks at 75° while that of the Run 38 had two peaks (60° and 90°). In general, all the coatings showed a behaviour that is consistent with that of brittle materials **[108]**.

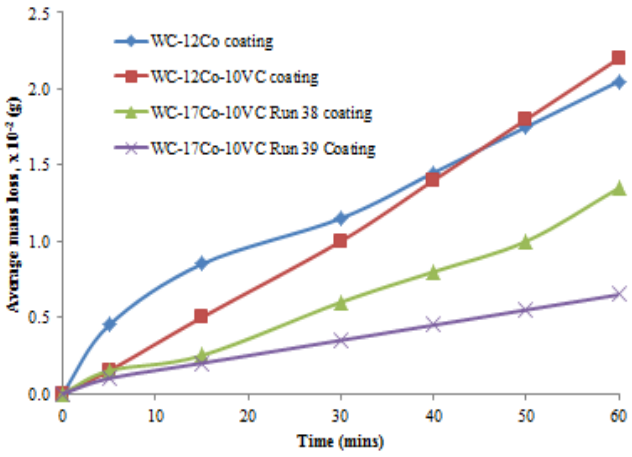


Figure 4. 21 Comparison of the average mass loss against time curves of the coatings at 90° impact angle.

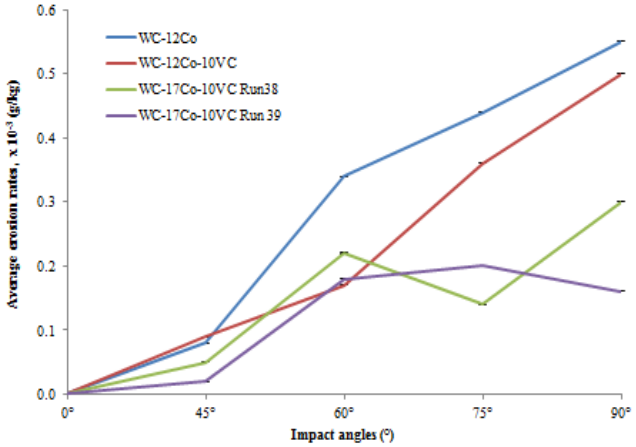


Figure 4. 22 Comparison of the average erosion rate against impact angles.

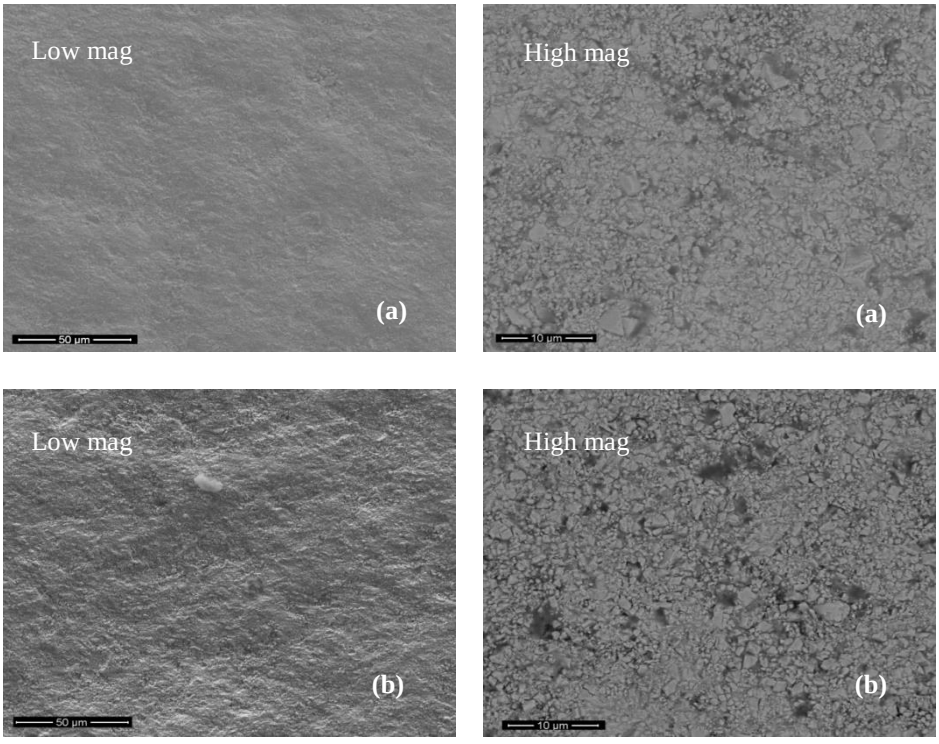
4.5.1 Wear mechanisms on eroded coating surfaces

Figure 4.23 to **4.26** shows the SEM image at low and high magnifications of eroded surface of the coatings. The predominant erosion mechanism for the coatings in this study appeared to have been loss of the binder phase and as a consequence of this, the carbide grains (both WC and WV_4C_5) were exposed to erosion action which resulted into cracking, fragmentations and subsequent fall-outs. The occurrence of carbide grains fall-out in the coatings were not really evident but could not be over-ruled since such occurrences could have been obliterated by subsequent impacts. No evidence of grooving occurred.

SEM examination of the eroded surface of the coatings reveals that the slurry impact caused plastic deformation of the surface (depressions and ridges). The eroded surfaces exhibited depressions due to ploughing action of the eroding particles. The surface degradation in all the coatings appeared similar at all the test angles but the damages were, to a lesser degree as the impact angles decreased. At lower impact angles, ploughing mechanism seems to be more dominant apart from the plastic deformation at higher impact angles, an indication that the force during impact at lower angle had a component parallel to the surface hence causing more sliding than impacting. The difference in impact angle

appeared not to have changed the wear mechanisms in the coatings, but only changing the amount of materials lost.

The appearances of the eroded surfaces of the 10wt%VC coatings were different to the non-VC coating. The eroded surfaces of the 10wt%VC coatings were characterized by low frequency of surface depressions compared to that of the non-VC coating **(see Figures 4.23** to **4.26)**. The 10wt%VC coatings' surfaces were characterized by small WC grain sizes while the non-VC coating by large WC grain size. It could be that the wear mechanisms of the WC grain for the coatings were influenced by their size **(Table 4.5)**. The WC grains in the 12wt%Co coating eroded by a combination of plastic deformation, chipping and fragment fall-out, while those in the 10wt%VC coatings wore generally by chipping. Erosion mechanisms for the (W.V)C grains appeared to be predominantly by chipping and fragment fall-out.



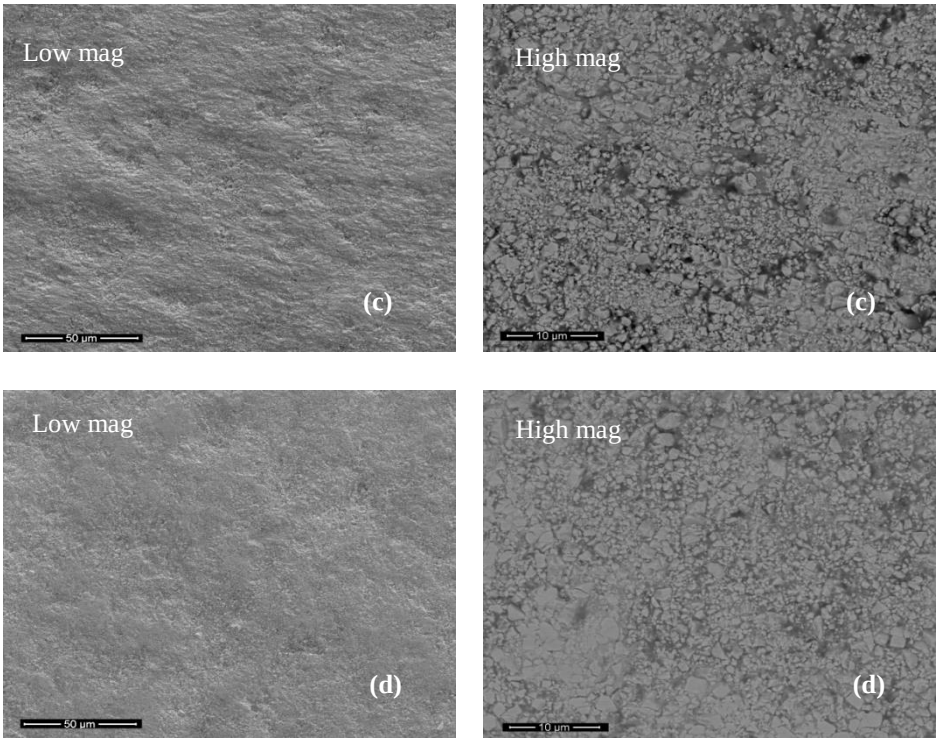
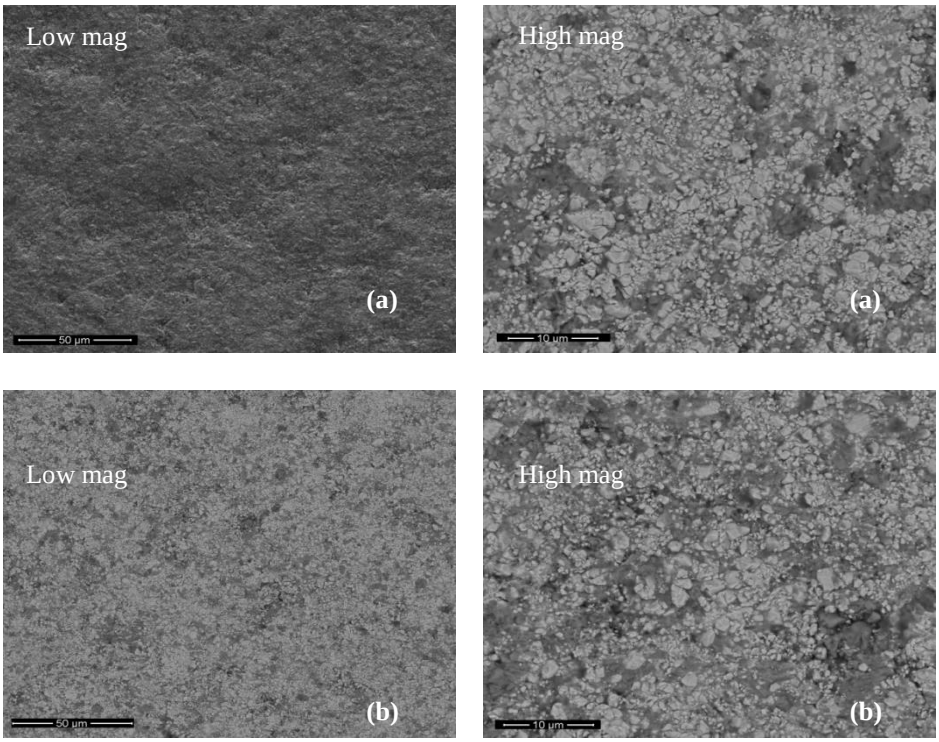


Figure 4. 23 SEM images of the eroded surface of the WC-12wt%Co at (a) 90°, (b) 75°, (c) 60°, and (d) 45°.



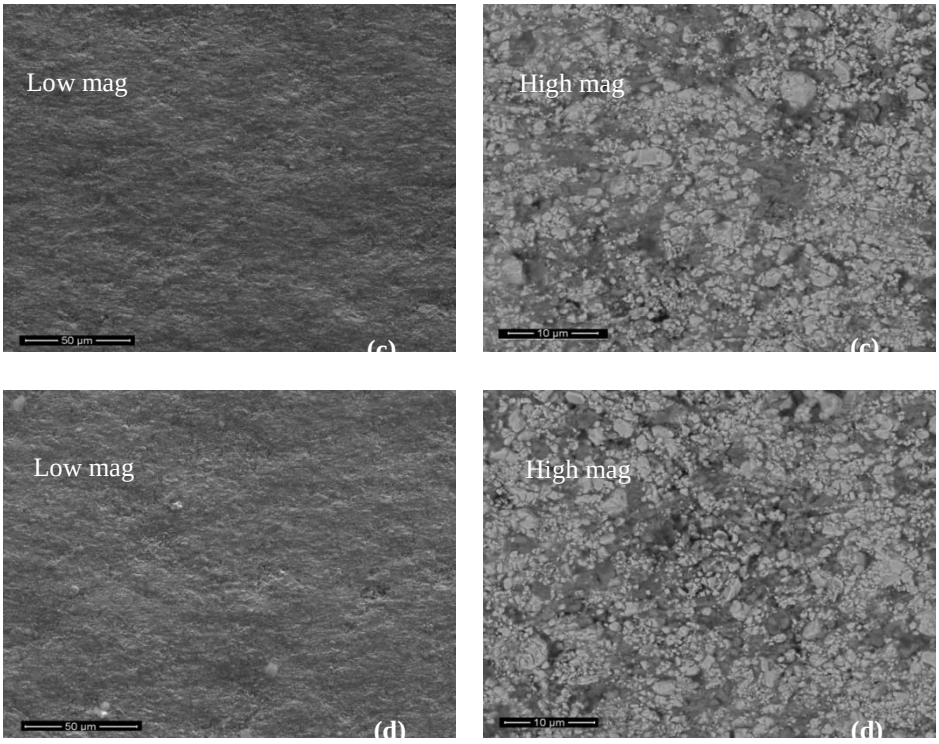
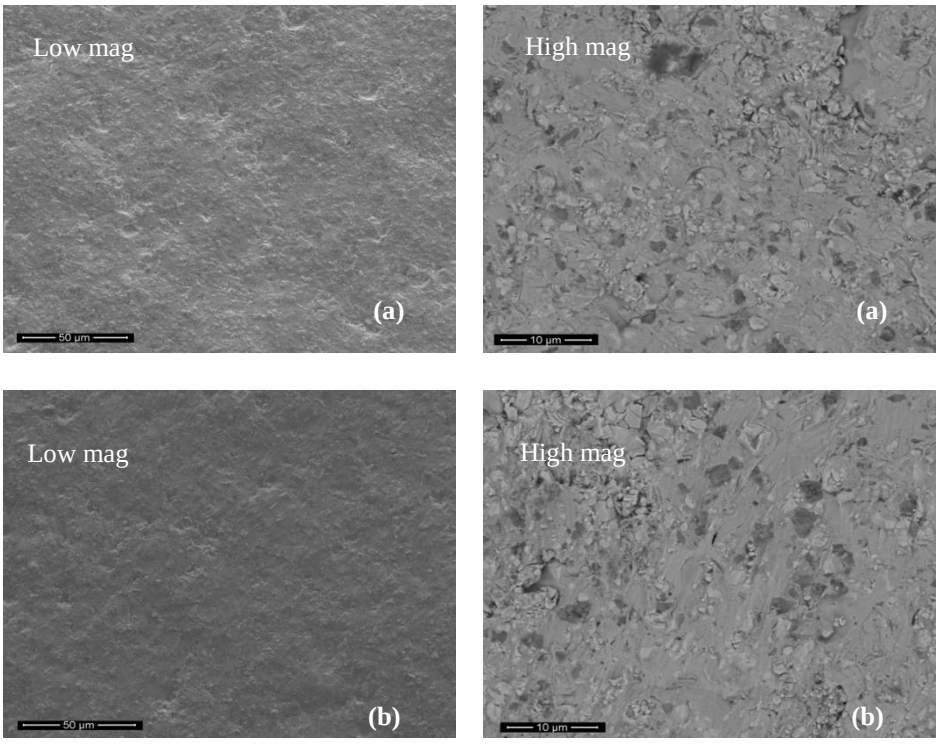


Figure 4. 24 SEM images of the eroded surface of the WC-12wt%Co-10wt%VC at (a) 90°, (b) 75°, (c) 60°, and (d) 45°.



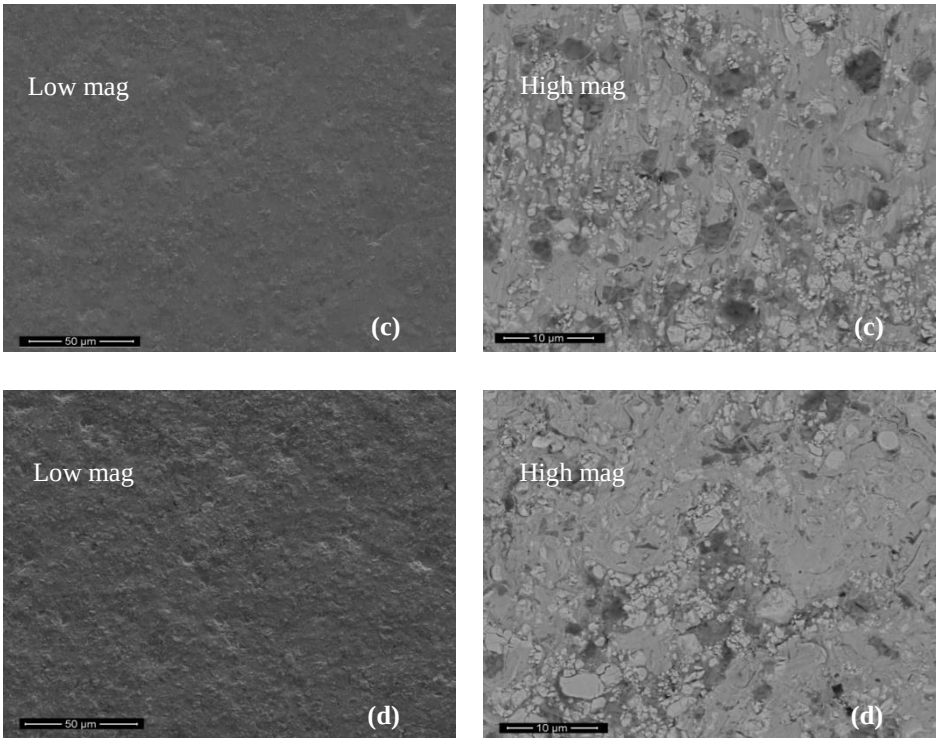
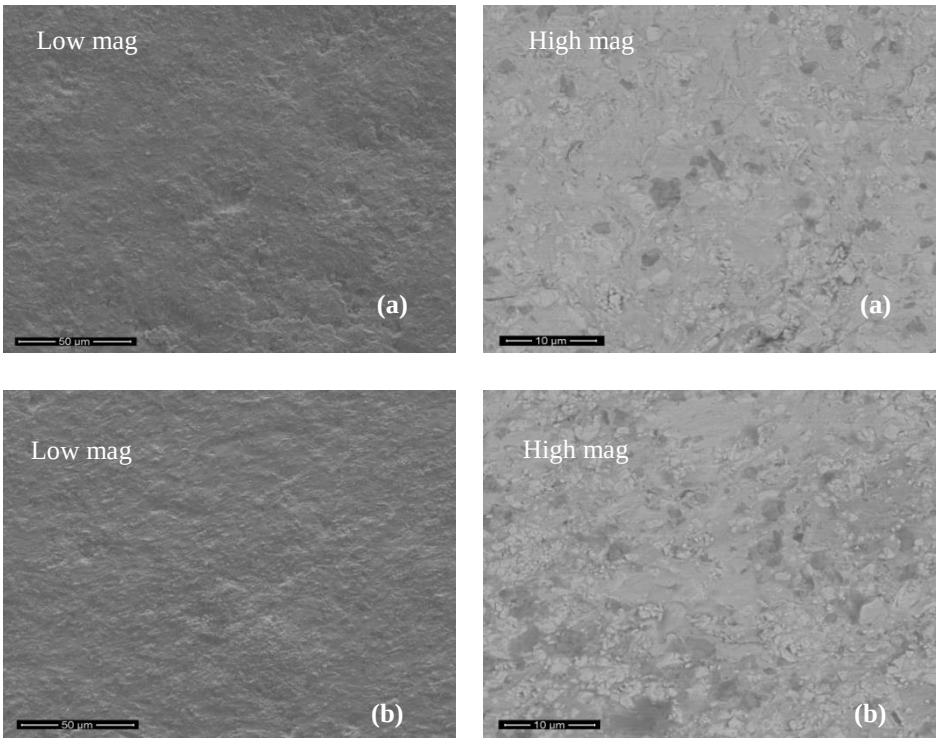


Figure 4. 25 SEM images of the eroded surface of the WC-17wt%Co-10wt%VC Run 38 at (a) 90°, (b) 75°, (c) 60°, and (d) 45°.



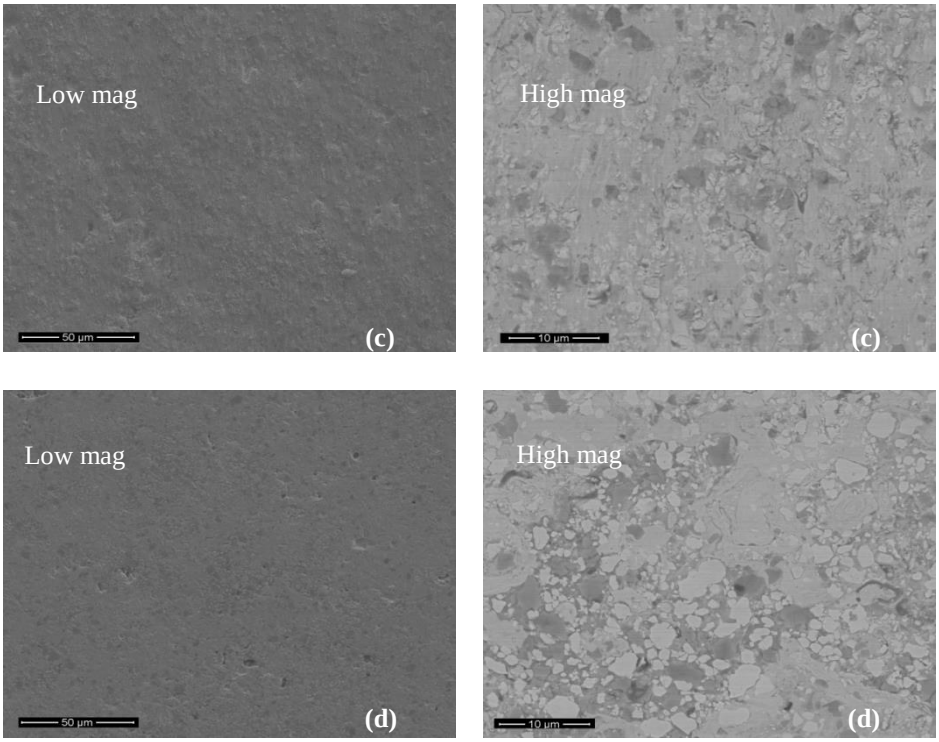


Figure 4. 26 SEM images of the eroded surface of the WC-17wt%Co-10wt%VC Run 39 at (a) 90°, (b) 75°, (c) 60°, and (d) 45°.

EDAX mappings performed on the eroded surfaces of the coatings were used to identify possible transfer of material between the erodent and the coatings. The mapping shows the presence of oxygen which could have been from water and/or the SiO_2 used. **Figure 4.27** and **4.28** shows selected EDAX mapping with EDX analysis on the eroded surfaces of WC-12wt%Co and WC-12wt%Co-10wt%VC coatings. The EDAX mapping and EDX analysis of the WC-17wt%Co-10wt%VC coatings are presented in **Appendix B5**. EDX analysis on the worn surface of the coatings does not show any evidence of Si from the erodent but its occurrence could not be rule out. Also, the inability of the EDX analysis to identify Si could be a result of the close characteristic X-ray energy between W and Si (1.774 and 1.734 keV).

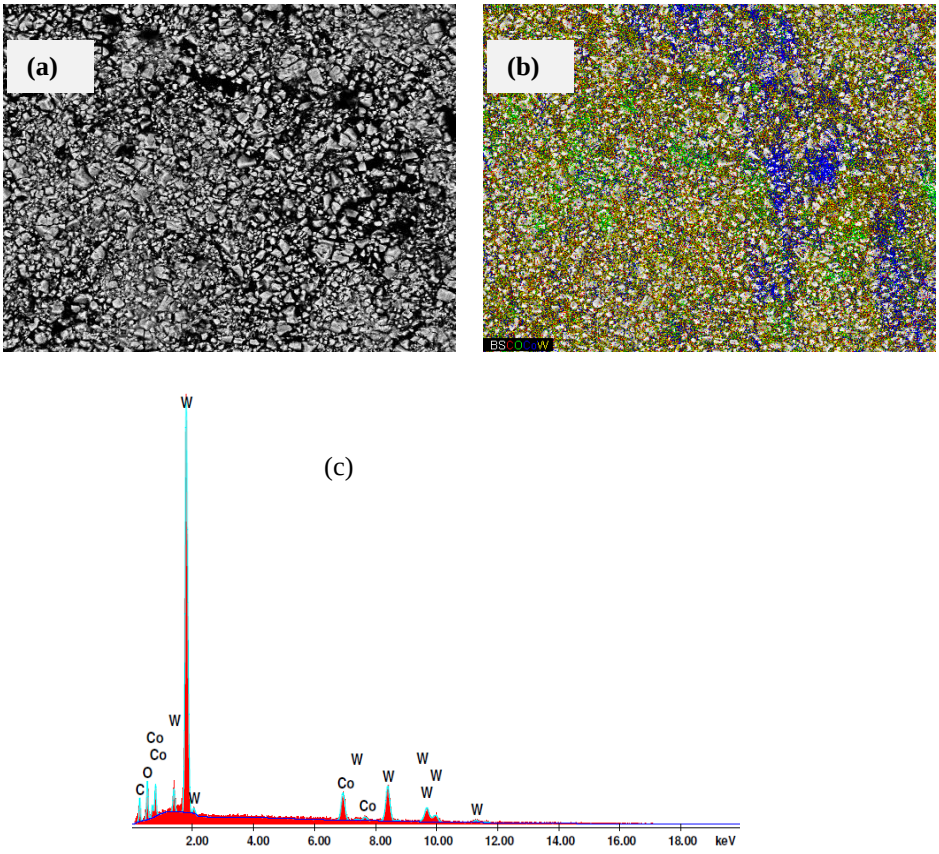
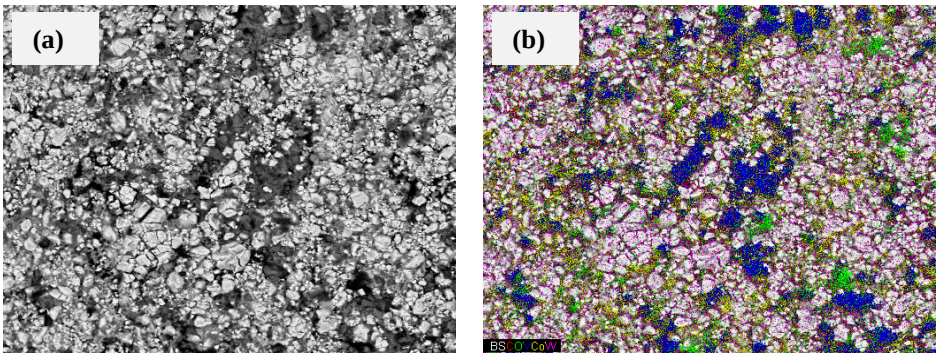


Figure 4. 27 (a) BSE SEM image, (b) EDAX maps overlay and (c) EDX analysis on the eroded surface of the WC-12wt%Co coatings (Brown = C; Blue = Co; Green = O; Yellow = W).



(c)

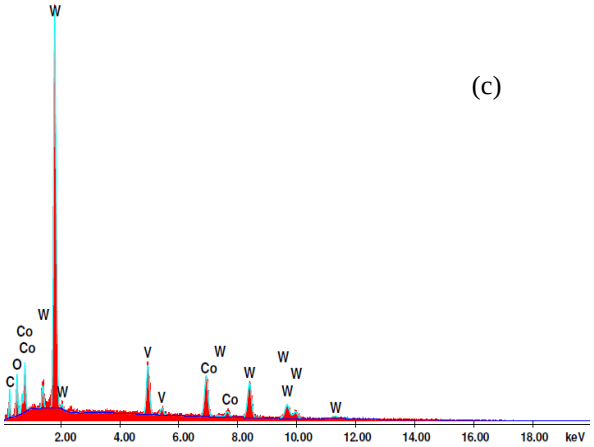


Figure 4. 28 (a) BSE SEM image, (b) EDAX maps overlay and (c) EDX analysis on the eroded surface of the WC-12wt%Co-10wt%VC coatings (Brown = C; Blue = Co; Green = O; Yellow = W; Purple = V).

5. Results: Conventionally sintered alloys

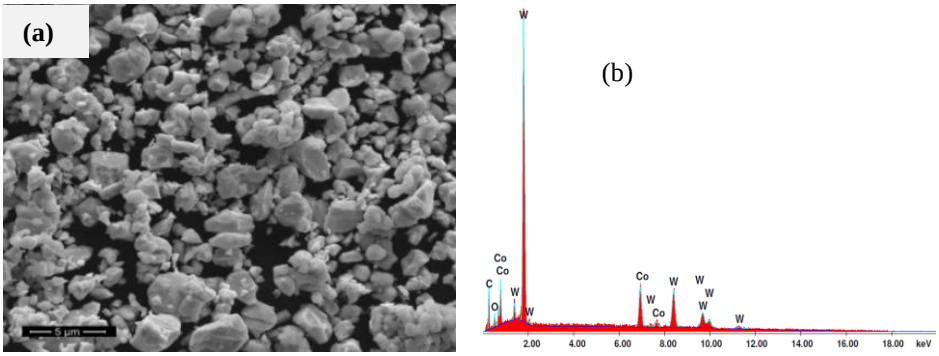
5.1 Introduction

This chapter presents the results from the characterization and testing of the conventionally sintered alloys. It explains the properties of the alloys based on the properties of the powders and the sintering process, and compares the performance of the alloys based on the tests conducted.

5.2 Powder characterization

5.2.1 Morphology

Figure 5.1 shows the SEM and EDX analysis of the two powders used to produce the WC-12wt%Co and WC-10wt%VC-12wt%Co alloys. The particles of both powders were predominantly granular with some agglomerated grains. The EDX analyses on the powders confirmed no evidence of inclusion elements was present.



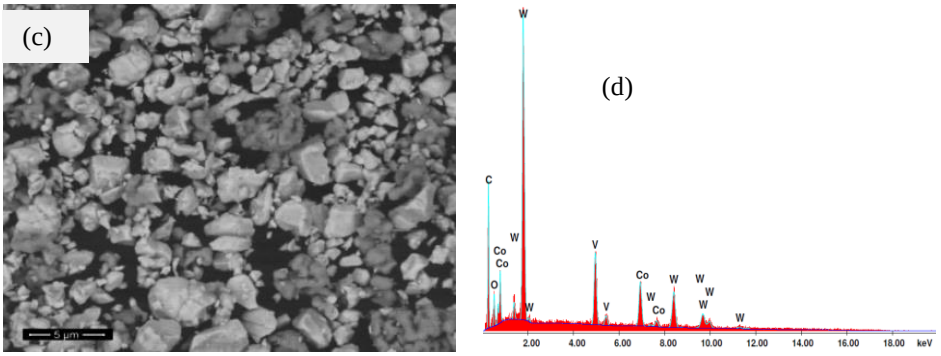


Figure 5. 1 Morphology and EDX analysis of (a) and (b) WC-12wt%Co powder, (b) and (c) WC-12wt%Co-10wt%VC powder.

5.2.2 Particle size and size distribution

Table 5.1 gives the average particle sizes and size distributions obtained from the Malvern laser diffraction technique. At equal cobalt content, after the 5th percentile, the mean particle size of the WC-12wt%Co-10wt%VC powder was lower than that of the WC-12wt%Co powder.

Table 5. 1 Powder particle size and size distributions.

Conventionally Sintered alloys	**Sizes (µm)**			
	$d_{0.1}$ (1)	**$d_{0.5}$ (2)**	**$d_{0.9}$ (3)**	**Mean**
WC-12wt%Co	0.66	2.17	4.42	2.43
WC-12wt%Co-10wt%VC	0.68	2.20	4.19	2.35

[1] Equivalent volume mean diameter at 1st percentile; [2] Equivalent volume mean diameter at 5th percentile; [3] Equivalent volume mean diameter at 9th percentile.

5.2.3 Phase composition

Table 5.2 lists the phases and their mass fractions while **Figure 5.2** shows the XRD patterns obtained for the powders. The phases observed in the powders were consistently the WC, Co and VC phases. No evidence of secondary or deleterious phases was observed confirming the EDX analysis shown in **Figure 5.1**.

Table 5. 2 Powder particle size and size distributions.

Conventionally Sintered alloys	**Phase composition in mass fraction (%)** [a]		
	WC	**Co**	**$VC_{0.75}$**
WC-12wt%Co	97.64	2.36	-
WC-12wt%Co-10wt%VC	79.42	8.28	12.29

[a] Phase mass composition determined by Rietveld analysis

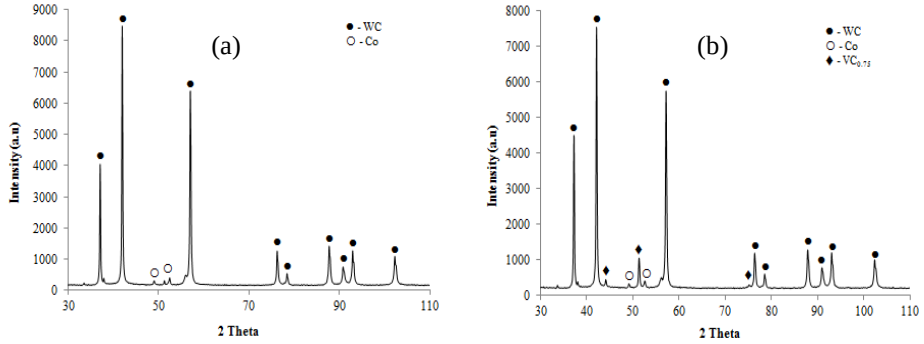


Figure 5. 2 XRD patterns for (a) WC-12wt%Co and (b) WC-12wt%Co-10wt%VC powders.

The d-values of WC in both powders were lower than those given in the XRD reference cards. The WC d-values in the WC-12wt%Co-10wt%VC powders were lower than that in the WC-12wt%Co powder. These lower d-values indicate that the WC grains in the WC-12wt%Co-10wt%VC powders were under higher compressive stresses **[136]**, because at the same cobalt weight content, the volume fraction of the binder in the WC-12wt%Co powder was lower than in the WC-12wt%Co-10wt%VC powders **(Table 3.1)**. For both powders, the d-values of the binder phase were larger than those in the XRD reference cards. This may have been caused by the presence of W and V atoms in solution in the binder (as was shown by EDS analysis; refer to **Figure 5.4**), as well as tensile stresses. The binder in both powders had an HCP structure. VC in the WC-12wt%Co-10wt%VC powder occurred as $VC_{0.75}$. The VC d-values in the WC-12wt%Co-10wt%VC powder were lower than that from the XRD reference cards.

5.3 Alloy characterization

5.3.1 Microstructures

Figure 5.3 illustrates the microstructure (un-etched and etched) of the sintered WC-12wt%Co and the WC-12wt%Co-10wt%VC alloys. The angular carbide grain structure typical of cemented carbides is clearly visible in both alloys. The average WC grain size in the WC-12wt%Co alloy was about 2.96 µm **(Table 5.3)**, while that in the WC-12wt%Co-10wt%VC alloy had an average size of 2.09 µm **(Table 5.3)**. This clearly indicates a small reduction in the WC grain size by the addition of VC. The double carbide phase (WV_4C_5) in the WC-12wt%Co-10wt%VC alloy had larger grain sizes compared to the WC grains **(Table 5.3**). Etched surfaces of both alloys revealed a homogenous microstructure.

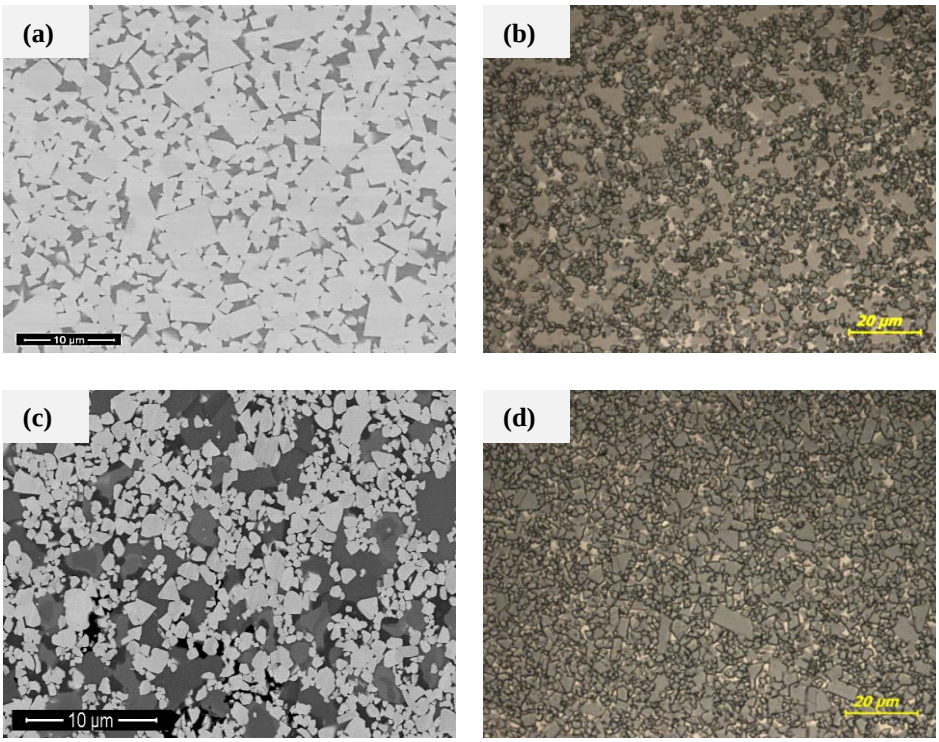


Figure 5. 3 SEM and optical images of the (a) un-etched WC-12wt%Co, (b) etched WC-12wt%Co, (c) un-etched WC-12wt%Co-10wt%VC, and (d) etched WC-12wt%Co-10wt%VC alloys. WC grains appear as white particles; Co binder phase as continuous region; and (W,V)C grains as irregularly shaped dark grey regions. The black regions/spots are pores.

EDX analyses on the individual phases are shown in **Figure 5.4**. The EDX analyses on the alloys confirmed no evidence of inclusion elements.

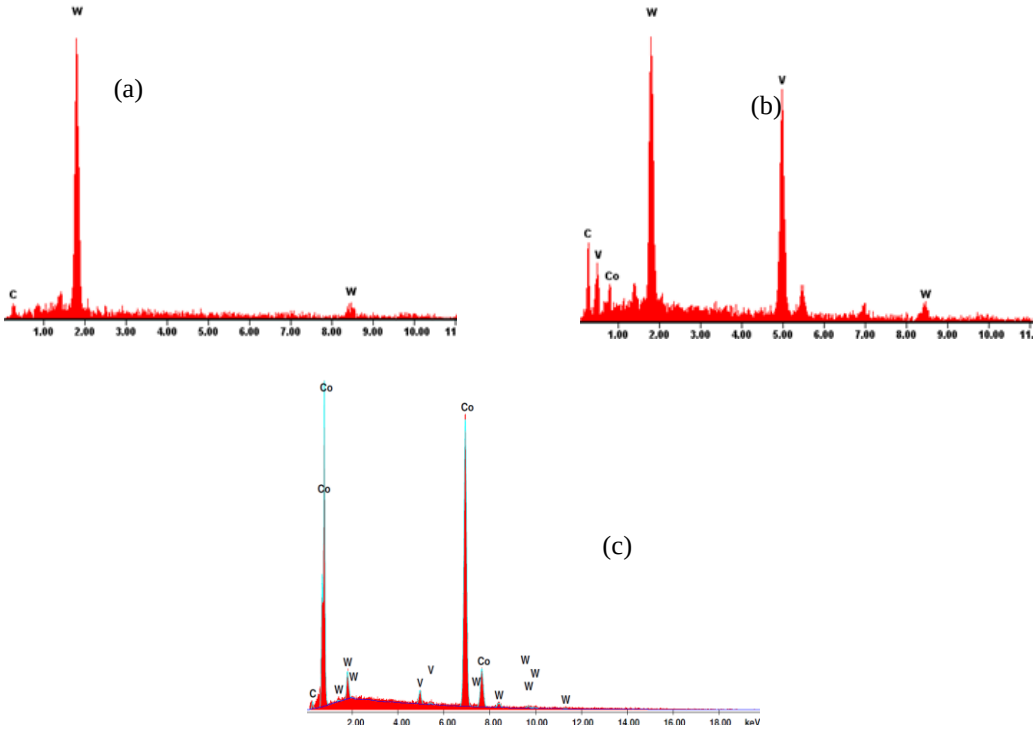


Figure 5. 4 EDS analysis of the (a) white phase showing WC angular grains and (b) dark grey regions showing irregularly shaped (W,V)C grains, and (c) continuous matrix.

Table 5.3 provides a comparison of the physical properties of the two alloys. The density of the WC-12wt%Co-10wt%VC alloy was 14% lower than that of the WC-12wt%Co alloy, which could be beneficial for producing lighter alloys. The low levels of porosity are an indication of good densification of the alloys during the sintering process although the VC-alloy had a higher porosity. The coercivity of the WC-12wt%Co alloy is less than that of the WC-12wt%Co-10wt%VC alloy. A higher coercivity value generally indicates a finer carbide grain size which is confirmed when the WC grain size values in both alloys are compared.

Table 5. 3 Physical properties of the conventionally sintered alloys.

Conventionally Sintered alloys	Density (g/cm^3)	Porosity (%)	Coercivity (kA/m)	WC mean size (µm)	(W,V)C mean size (µm)
WC-12wt%Co	14.3 ± 0.06	0.03 ± 0.01	7.33	2.96 ± 0.05	-
WC-12wt%Co-10wt%VC	12.3 ± 0.10	0.06 ± 0.01	9.00	2.09 ± 0.04	6.64 ± 0.54

5.3.2 Phase composition

Figure 5.5 shows the phases of the alloys identified using XRD. The most prominent phase on the XRD pattern of both alloys was WC. No deleterious phases were found. For the WC-12wt%Co alloy, the Co peaks, seen in the powders **(Figure 5.2)**, were still found in the alloy but the peak intensity was smaller and broader in the latter. In the WC-12wt%Co-10wt%VC alloy, the $VC_{0.75}$ peaks found in the powder were replaced with the double carbide phase, WV_4C_5. The occurrence of the WV_4C_5 phase could be a result of the WC dissolving in VC.

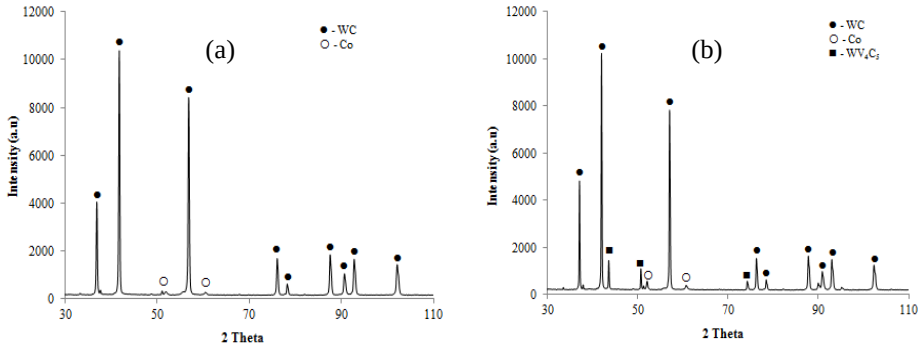


Figure 5. 5 XRD patterns for (a) WC-12wt%Co and (b) WC-12wt%Co-10wt%VC alloys.

The approximate mass fraction of the phases in the alloys is shown in **Table 5.4**, as determined by Rietveld analysis. The d-values of WC in all the alloys were larger than those of the starting powders.

Table 5. 4 Phase composition of alloys.

Conventionally Sintered alloys	**Phases and their mass fraction (%)**		
	WC	**Co**	**WV_4C_5**
WC-12wt%Co	94.31	5.69	-
WC-12wt%Co-10wt%VC	63.25	15.14	21.61

5.3.3 Mechanical properties

Table 5.5 summarizes the mechanical properties of the alloys.

Table 5. 5 Mechanical properties of the alloys.

Conventionally Sintered alloys	**HV_{30}**	**K_{IC} ($MPa.m^{0.5}$)**	**Y (GPa)**	**ν**
WC-12wt%Co	1280 ± 2.1	12.8 ± 1.0	682	0.22
WC-12wt%Co-10wt%VC	1390 ± 7.8	11.3 ± 0.5	570	0.23

The WC-12wt%Co-10wt%VC alloy had a 9% higher hardness than the WC-12wt%Co alloy, which could be beneficial for improved wear properties. This increased hardness is probably the combined result of the finer WC carbide grain size and the presence of the harder double carbide phase (WV_4C_5). The fracture toughness of the WC-12wt%Co-10wt%VC alloy decreased by 13% but is still considered moderate. These results are aligned with the coercivity values **(Table 5.3)** and the microstructure images shown earlier **(Figure 5.3)**. The Young's modulus of the WC-12wt%Co alloy was found to be within the expected range for 12wt%Co cemented carbides while the addition of VC lowered the Young's modulus by 16%. The Poisson's ratio calculated was similar for both alloys.

5.4 Friction and sliding wear tests

The friction behavior of each alloy sliding against the 100Cr ball as a function of distance for the test condition stated in **Table 3.6** is illustrated in **Figure 5.6**. The friction behaviour for the different alloy-ball pairs showed two distinct regions namely a running-in phase and a steady-state region.

For the WC-12wt%Co alloy **(Figure 5.6(a))**, the running-in period occurred during the first 20 m of sliding where the CoF linearly increased from 0.17 to 0.7. After this the CoF showed a small sharp decrease which was followed by a gradual linear increase reaching approximately 0.8 after 200 m of sliding. For the WC-12wt%Co-10wt%VC alloy **(Figure 5.6(b))** the running-in phase begins with a short gradual increase in friction for the first 10 m of sliding reaching a CoF of 0.24 after which a sharp increase in friction is observed for a few meters followed by a more gradual increase until the steady state is reached with the CoF ranging from 0.6 to 0.8.

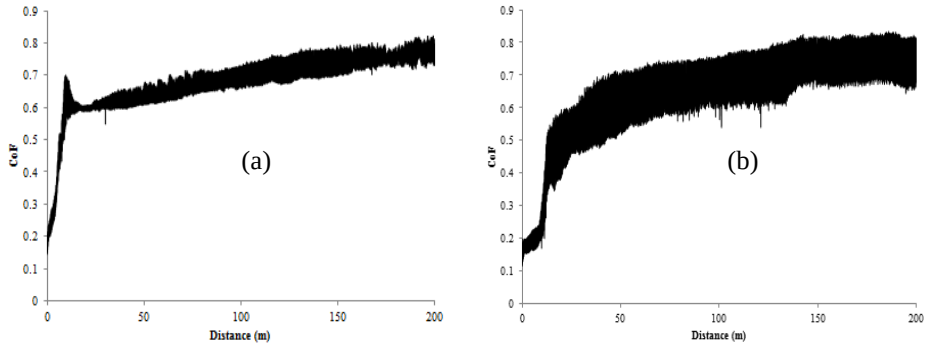


Figure 5. 6 Friction behavior against 100Cr ball for (a) WC-12wt%Co and (b) WC-12wt%Co-10wt%VC alloys.

Figure 5.7 shows the static and dynamic CoFs for each alloy-ball pair after 200 m of sliding. As expected the static CoF was higher than the dynamic CoF. The static and dynamic CoF for the WC-12wt%Co-10wt%VC alloys were lower than those of the WC-12wt%Co alloys.

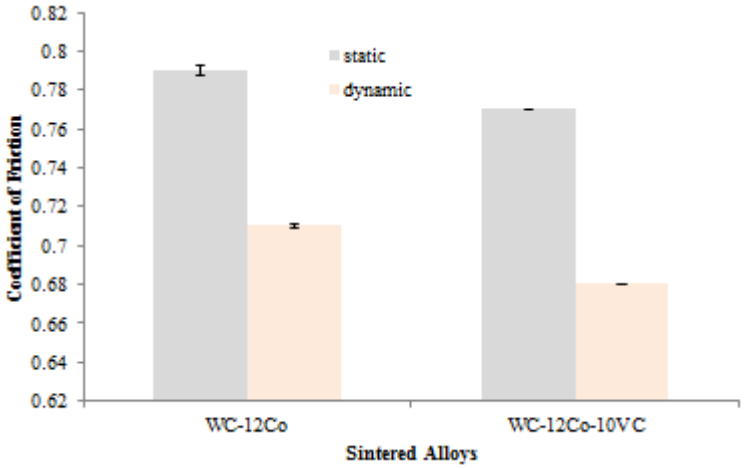


Figure 5. 7 Friction coefficients for the alloy-ball pairs sliding against the 100Cr steel balls.

Table 5.6 lists the penetration depths of the balls into the alloys as well as the wear track widths made on the alloys. Observation from **Table 5.6** showed that the penetration depth and the wear track widths of the WC-12wt%Co-10wt%VC alloy was lower compared to the WC-12wt%Co alloy.

Table 5. 6 Ball penetration depths and wear track width on the alloys.

Conventionally Sintered alloys	**100Cr ball**	
	Wear track width (µm)	**Penetration depth (µm)**
WC-12wt%Co	215 ± 25	2.38 ± 0.3
WC-12wt%Co-10wt%VC	229 ± 26	2.62 ± 0.2

Figures 5.8 compare the wear coefficients of the alloys against the balls while **Figure 5.9** compares those of the balls on the alloys. The wear coefficients of the WC-12wt%Co-10wt%VC alloy was higher compared to that of the WC-12wt%Co alloy. An indication that the WC-12wt%Co had a better wear resistance compared to the WC-12wt%Co-10wt%VC alloy. It could be expected that the pair with the higher CoF should wear more, but this was not the case here, as the WC-12wt%Co/ball pair generated a higher CoF and a lower wear rate compared to the WC-12wt%Co-10wt%VC/ball pair with a lower CoF and a higher wear rate. The reason for the higher wear rate in the WC-12wt%Co-10wt%VC alloy could be a result of the higher penetration depth and the wider worn track width as observed from **Table 5.6**.

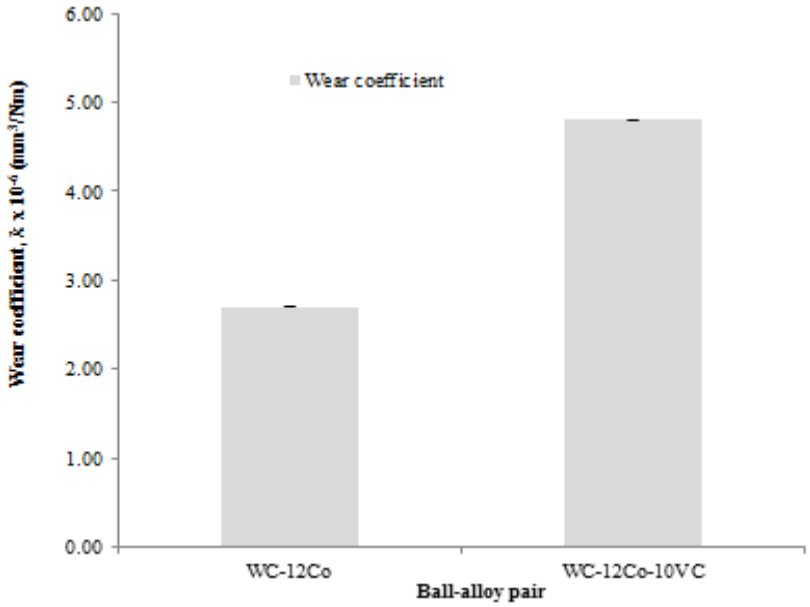


Figure 5. 8 Comparison of the wear coefficients of the 100Cr steel ball-alloy sliding pairs.

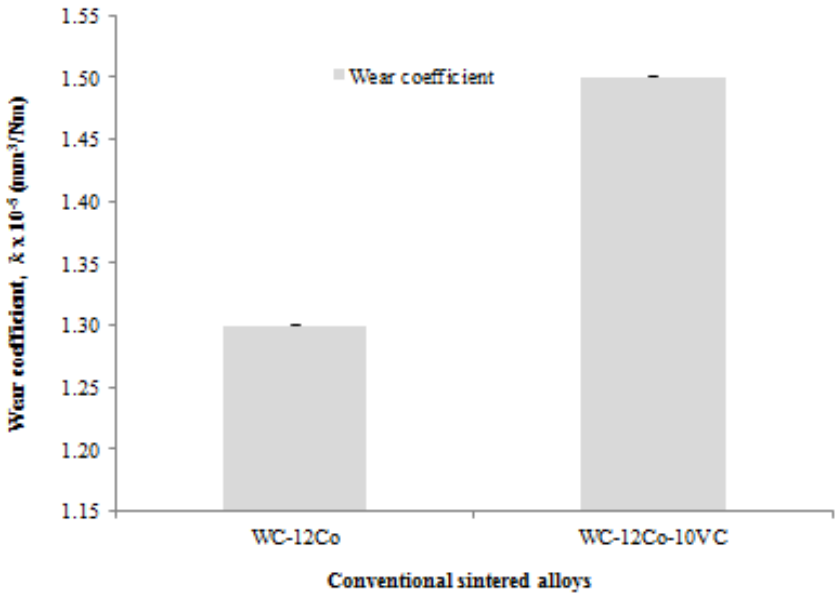


Figure 5. 9 Wear coefficients comparison for the sintered alloys.

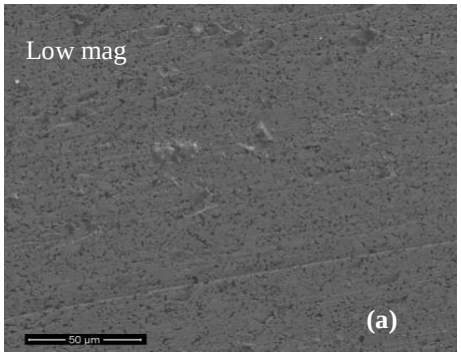
5.4.1 Wear mechanisms in sliding wear

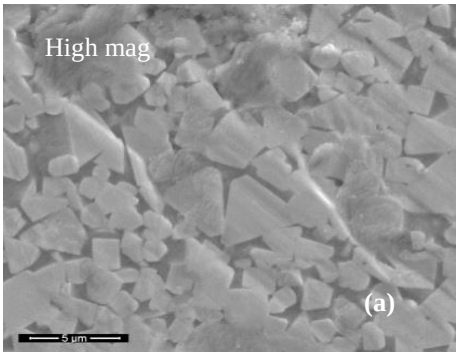
The wear scars from the sliding wear tests on the alloys were examined using SEM with EDX, in order to determine the wear mechanisms. Selected SEM images are presented to provide a summary of the wear mechanisms observed.

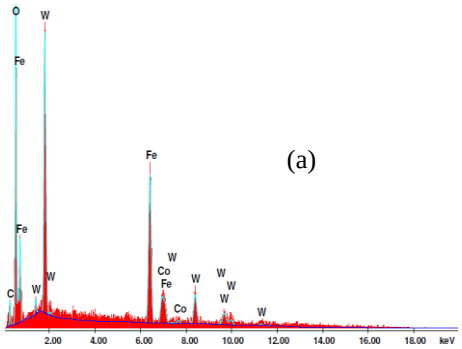
Figure 5.10 illustrates the typical wear tracks on the alloys under the test conditions with their respective EDX analysis. These images provide a general impression of the variation in wear track widths achieved with the 100Cr steel ball at the operating condition. The wear mechanisms for all the alloys were found to be very similar. Ploughing of wear particles, which had contributed to groove formation **(Figure 5.10)** were observed. The grooves formed are parallel with the sliding direction. Higher magnifications on the wear track showed evidence of particle smearing on the worn surfaces of the alloys. Plastic deformation of the carbide grains is also evident **(Figure 5.10(c))**. Binder removal was also evident in both alloys. No evidence of WC carbide grain pull out was observed in both alloys. Formation of thin films on the wear surfaces suggests the occurrence of

tribo-layers oxides. The WC-12wt%Co alloy showed less smearing debris on the wear track compared to that of the WC-12wt%Co-10wt%VC alloy, which correlates with the decreased wear rate **(Figure 5.8)**. Evidence of WC grain cracking observed in the WC-12wt%Co-10wt%VC alloy was missing in the WC-12wt%Co but such occurrence could not be completely ruled out. EDX analysis on the wear track of the alloys, against the 100Cr balls indicates the presence of Fe and Cr. This confirms the transfer of material from the ball to the surface of the alloys during wear.

In general, the wear mechanisms for all the alloys were found to be the same portraying plastic deformation, preferential binder removal, carbide grain cracking and fragmentations, adhesion and formation of thin tribo-layer oxides during wear. It is believed that the binder removal occurs first, followed by subsequent carbide grain cracking.







(a)

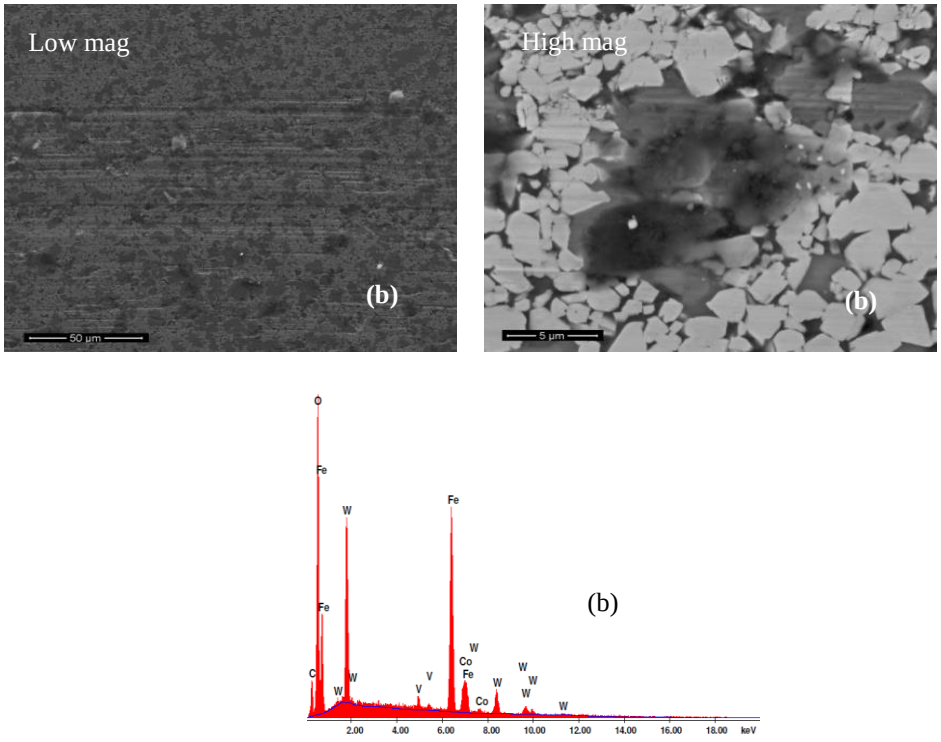
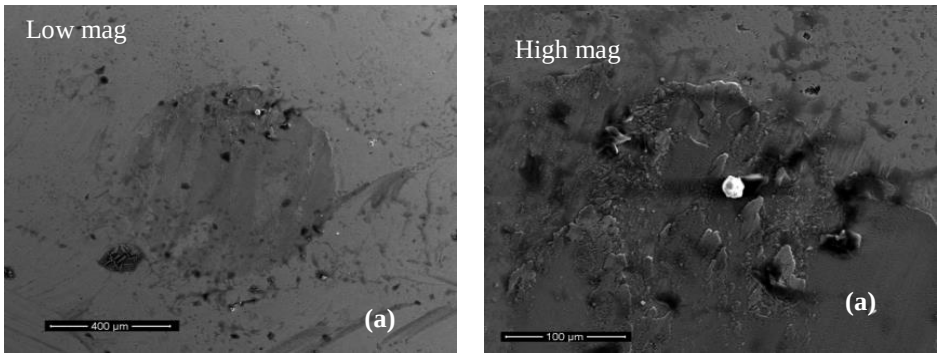


Figure 5. 10 SEM images with EDX analysis of the wear tracks against 100Cr ball for (a) WC-12wt%Co and (b) WC-12wt%Co-10wt%VC alloys.

Figure 5.11 shows typical wear scars on the 100Cr steel ball against the alloy, with the respective EDX analyses. Both the lower and higher magnifications are represented. **Figure 5.11** is the ball that produced the wear track shown in **Figure 5.10**. The presence of W on the wear scars on the 100Cr steel ball against the alloys gave evidence of materials' transfer.



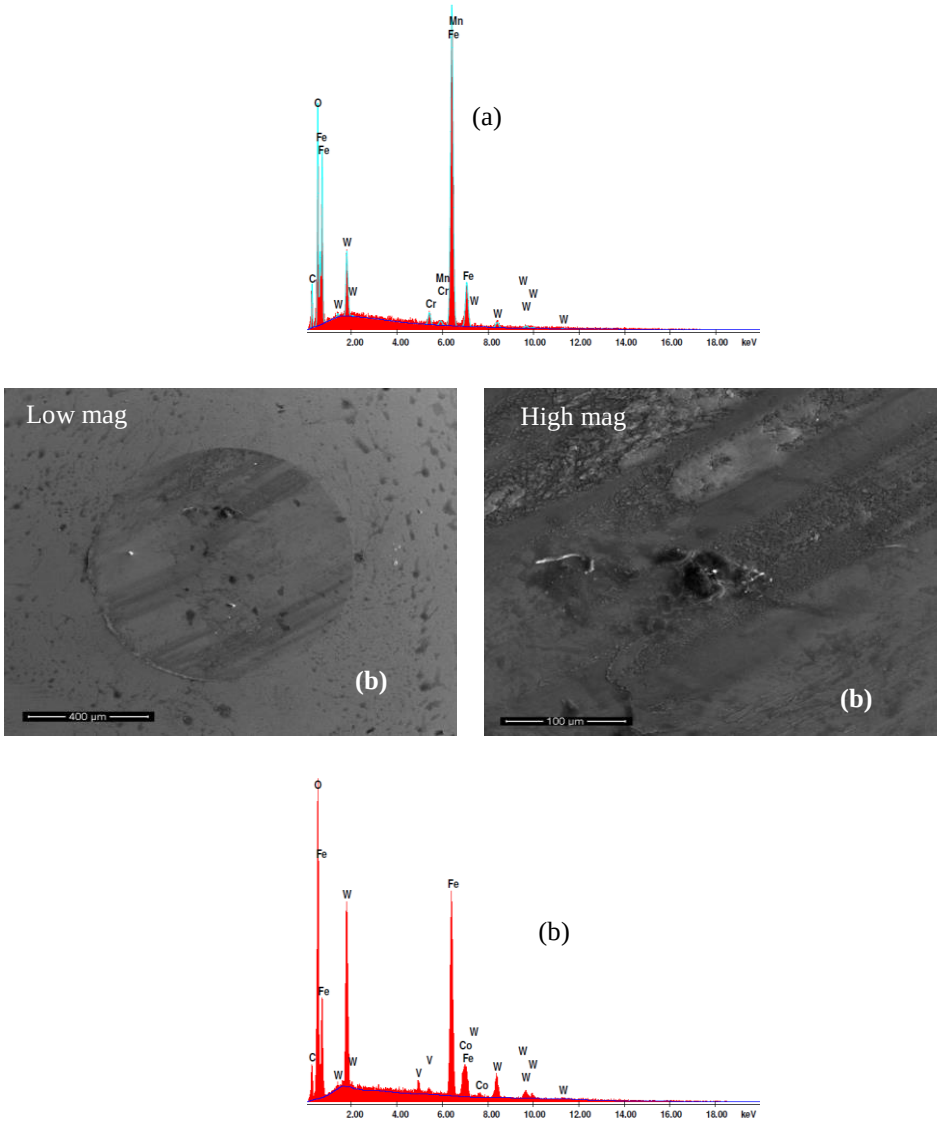


Figure 5. 11 SEM images of the wear scars on the 100Cr steel ball for (a) WC-12wt%Co and (b) WC-12wt%Co-10wt%VC alloys.

5.5 Slurry erosion tests

The average mass losses of the alloys were converted into average volume loss using the densities of the alloys. The average volume loss against time and the erosion rate against time curves of the polished surfaces of the alloys at the different test angles are shown in **Appendix C3A**. **Figure 5.12** compares the average volume losses of both alloys against time when tested at 90°. At all the test angles, the average volume loss increases with test time. The average volume

losses for both alloys decreases as the impact angle decreased. At angle 45°, the average mass losses from all the coatings were very low and erratic in nature.

Figure 5.13 compares the average slurry erosion rate against the impact angles for the alloys. Both alloys showed a maximum erosion rate at 90°, a behaviour that is consistent with that of brittle materials **[108]**. Observations from the erosion rate curves showed that at higher test angles (90° and 75°), the erosion rate of the WC-12wt%Co alloy was higher than that of the WC-12wt%Co-10wt%VC alloy, which indicates that the slurry erosion resistance of the WC-12wt%Co-10wt%VC is superior to that of the WC-12wt%Co alloy. It could be that at higher impact angles, the larger WV_4C_5 grains protect the smaller WC grain in the alloy. However, at low test angles (60° and 45°), the slurry erosion resistance of the WC-12wt%Co alloy is better than that of the WC-12wt%Co-10wt%VC alloy; this translates to better slurry erosion resistance of the WC-12wt%Co alloy. The reason here could be that the larger WC grain in the WC-12wt%Co alloy resist erosion better than the finer grains in the WC-12wt%Co-10wt%VC alloy. Finer grains could easily fell out sooner after the removal of the cementing binder and/or carried away with the binder.

At the same binder contents, the erosion resistance for both alloys follows a particular trend: at high impact angles the erosion resistance of the WC-12wt%Co-10wt%VC alloy was better while that of the WC-12wt%Co was better at lower impact angles.

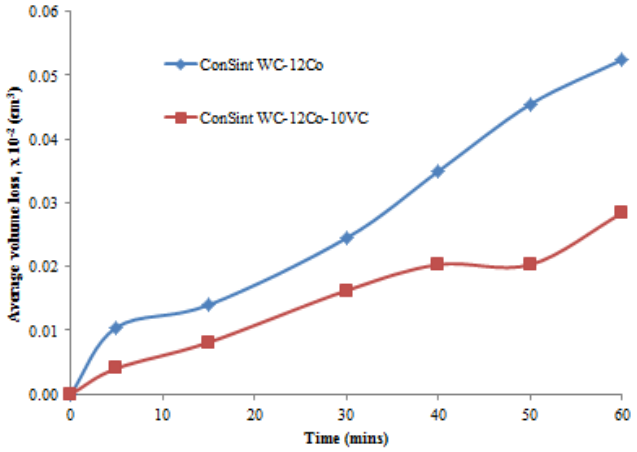


Figure 5. 12 Comparison of the average volume loss against time curves of both alloys at 90°.

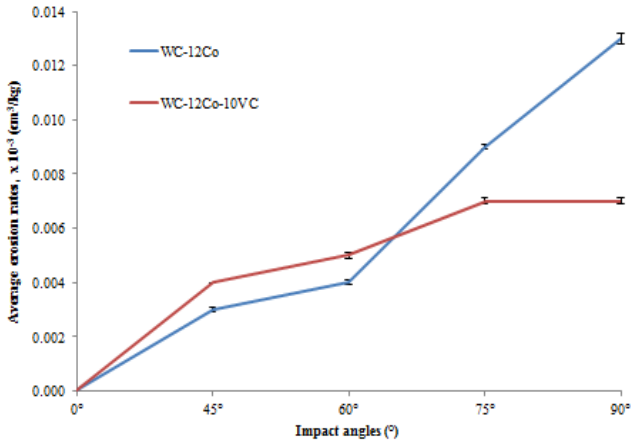


Figure 5. 13 Comparison of the average erosion rate against impact angles.

5.5.1 Wear mechanisms of the eroded alloy surfaces

SEM examination of the eroded surface of both alloys reveals that the slurry impact caused some plastic deformation of the surface. The eroded surfaces exhibited depressions due to ploughing action of the eroding particles. The surface degradation in both alloys appeared similar at all the test angles but the damages were, to a lesser degree as the impact angles decreased. At higher impact angles, plastic deformation of the carbide grain were more dominant compared to lower

impact angles, an indication that the force during impact at higher angle had a component perpendicular to the surface. The difference in impact angle appeared does not change the wear mechanisms in both alloys, but only changed the amount of materials lost.

The predominant erosion mechanism for the alloys in this study appeared to have been loss of the binder phase and as a consequence of this, the carbide grains (both WC and (WV_4C_5) were exposed to further erosion action which resulted into cracking, fragmentations and possible fall-outs. The appearances of the eroded surfaces of the VC and the non-VC alloys were not very different. The WC grains in the WC-12wt%Co alloy eroded by a combination of plastic deformation, chipping and fragment fall-out, while those in the VC alloy wore generally by chipping. Erosion mechanisms for the WV_4C_5 grains appeared to be predominantly by plastic deformation, cracking, chipping and fragment fall-out. The mechanism of erosion does not seem to change with the change in impact angles of testing.

Figures 5.14 and **5.15** show the SEM images with EDX analyses of the eroded surfaces of the WC-12wt%Co and WC-12wt%Co-10wt%VC alloys respectively at all the test angles. EDX analyses performed on the eroded surfaces of the coatings were used to identify possible transfer of material between the erodent and the coatings. The analyses shows the presence of oxygen which could have been from water and/or the SiO_2 used. It could also show the possibility of the formation of oxide. The analysis on the worn surface of the alloys does not show any evidence of Si from the erodent but its occurrence could not be ruled out. Also, the inability of the EDX analysis to identify Si could be a result of the close characteristic X-ray energy between W and Si (1.774 and 1.734 keV).

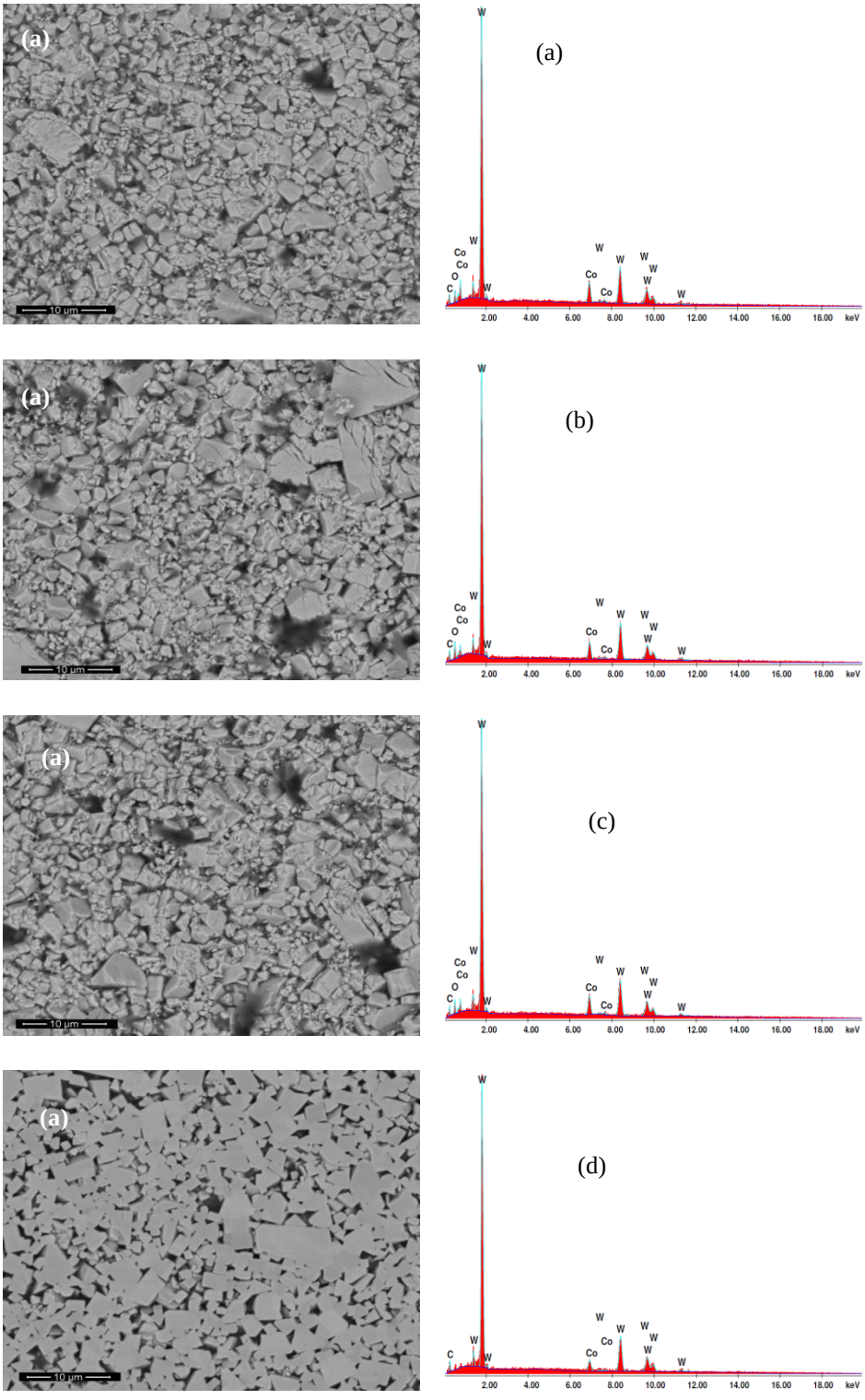


Figure 5 14 SEM images of the eroded surface of the WC-12wt%Co at (a) 90°, (b) 75°, (c) 60°, and (d) 45°.

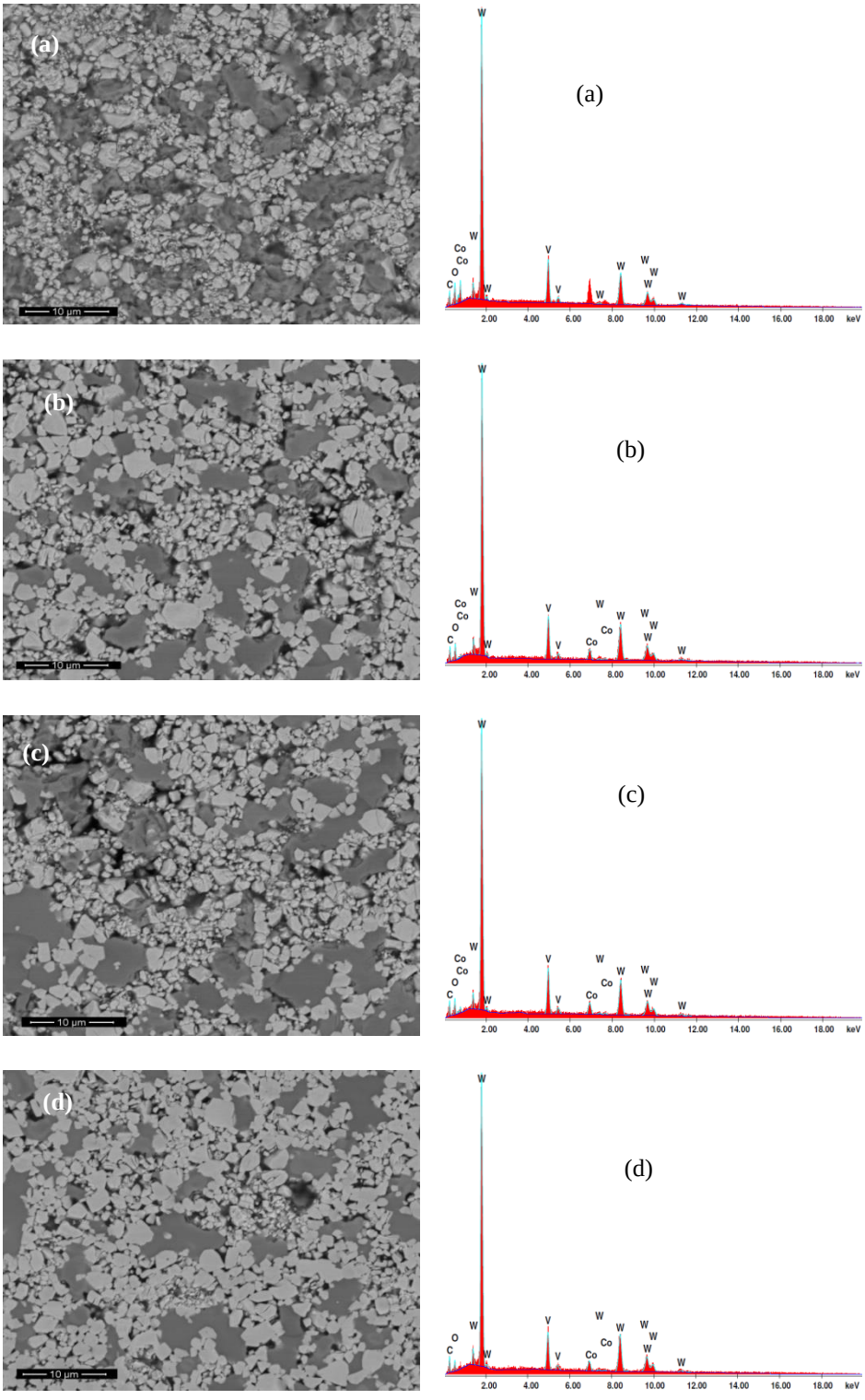


Figure 5. 15 SEM images of the eroded surface of the WC-12wt%Co-10wt%VC at (a) 90°, (b) 75°, (c) 60°, and (d) 45°.

6. Results: Spark plasma sintered alloys

6.1 Introduction

This chapter presents the results from the characterization and testing of the spark plasma sintered alloys. It explains the properties of the alloys based on the properties of the powders, and the sintering process and compares the performances of the alloys based on the tests conducted.

6.2 Powder characterization

6.2.1 Morphology

Figure 6.1 shows the SEM and EDX analysis of the two powders used to produce the WC-12wt%Co and WC-10wt%VC-12wt%Co alloys. The particles of both powders were predominantly granular with some agglomerated grains. The EDX analyses on the powders confirmed no evidence of deleterious elements.

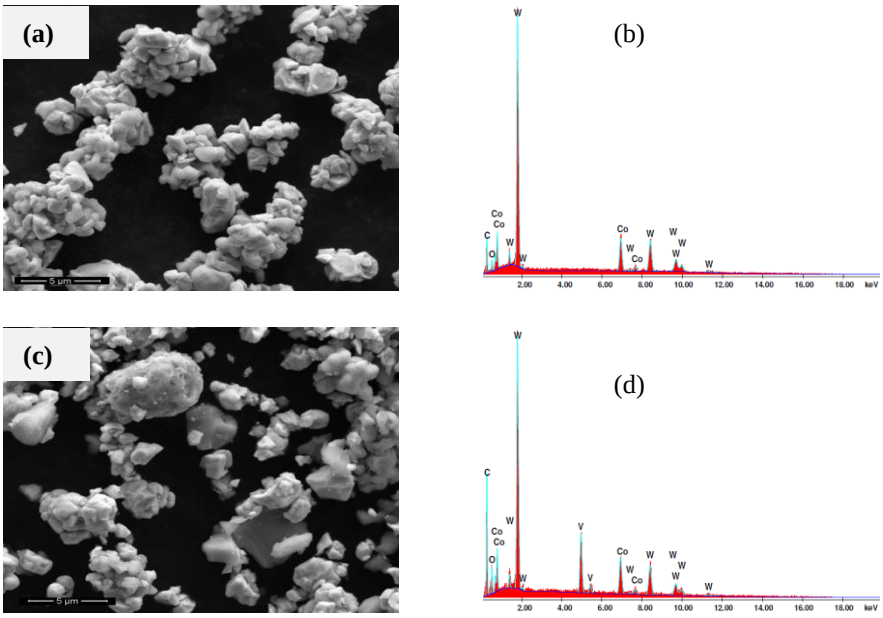


Figure 6. 1 Morphology and EDX analysis of (a) and (b) WC-12wt%Co powder, (b) and (c) WC-12wt%Co-10wt%VC powder.

6.2.2 Particle size and size distribution

Table 6.1 gives the average particle sizes and size distributions obtained from the Malvern laser diffraction technique. At equal cobalt content, after the 5th percentile, the mean particle size of the WC-12wt%Co-10wt%VC powder was lower than that of the WC-12wt%Co powder.

Table 6. 1 Powder particle size and size distributions.

Spark plasma sintered alloys	**Sizes (µm)**			
	$d_{0.1}$ (1)	**$d_{0.5}$ (2)**	**$d_{0.9}$ (3)**	**Mean**
WC-12wt%Co	0.66	2.10	4.36	2.37
WC-12wt%Co-10wt%VC	0.65	2.12	4.12	2.30

1 Equivalent volume mean diameter at 1st percentile; 2 Equivalent volume mean diameter at 5th percentile; 3 Equivalent volume mean diameter at 9th percentile.

6.2.3 Phase composition

Table 6.2 lists the phases and their mass fractions while **Figure 6.2** shows the XRD patterns obtained for the powders. The phases observed in the powders were consistently the WC, Co and VC phases. No evidence of secondary or deleterious phases was observed confirming the EDX analysis shown in **Figure 6.1**.

Table 6. 2 Powder particle size and size distributions.

Spark plasma sintered alloys	**Phase composition in mass fraction (%)[a]**		
	WC	**Co**	**VC**
WC-12wt%Co	97.47	2.53	-
WC-12wt%Co-10wt%VC	87.99	3.03	8.98

[a] Phase mass composition determined by Rietveld analysis

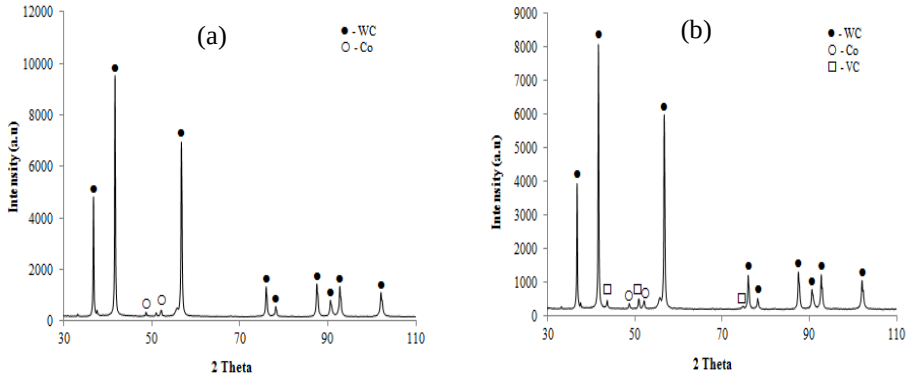


Figure 6. 2 XRD patterns for (a) WC-12wt%Co (b) WC-12wt%Co-10wt%VC powders.

The d-values of WC in both powders were higher than those given in the XRD reference cards. The WC d-values in the WC-12wt%Co-10wt%VC powders were lower than that in the WC-12wt%Co powder. The reason could be the same as that given in **section 5.2.3**. For both powders, the d-values of the binder phase were larger than those in the reference cards. The reason for this has already been given in **section 5.2.3**. The binder in both powder occurred as HCP structure. The VC in the WC-12wt%Co-10wt%VC powder occurred as VC.

6.3 Alloy characterization

6.3.1 Microstructures

Figure 6.3 illustrates the microstructure (un-etched and etched) of the sintered WC-12wt%Co and the WC-12wt%Co-10wt%VC alloys. The WC grains in both alloys were rounded at the edges, at low magnifications, compared to that obtained with the conventional sintering. The WC grain size in both alloys could not be measured from linear intercept method because, at higher magnifications, agglomeration of the WC grain was observed. Hence, the WC grain sizes in both alloys were calculated from the equation 6.1 given by the authors in **[138]**.

$$d = \frac{235(Co\ wt\%)^{-1.2}}{H_C - 3.3} \qquad \ldots 6.1$$

Where

d = Crabide grain size (μm)

Hc = Magnetic coercivity (kA/m)

Co wt% = Cobalt weight per cent.

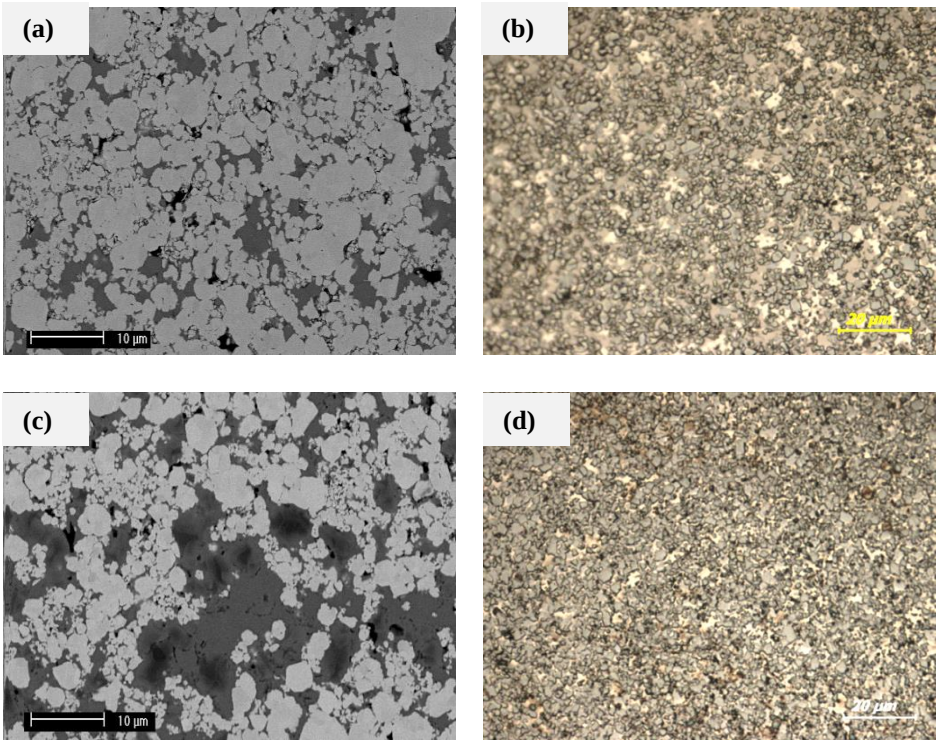


Figure 6. 3 SEM and optical images of the (a) un-etched WC-12wt%Co, (b) etched WC-12wt%Co, (c) un-etched WC-12wt%Co-10wt%VC, and (d) etched WC-12wt%Co-10wt%VC alloys. WC grains appear as white particles; Co binder phase as continuous region; and (W,V)C grains as irregularly shaped dark grey regions. The black regions/spots are pores.

EDX analyses on the individual phases are shown in **Figure 6.4**. The EDX analyses on the alloys confirmed no evidence of inclusion elements.

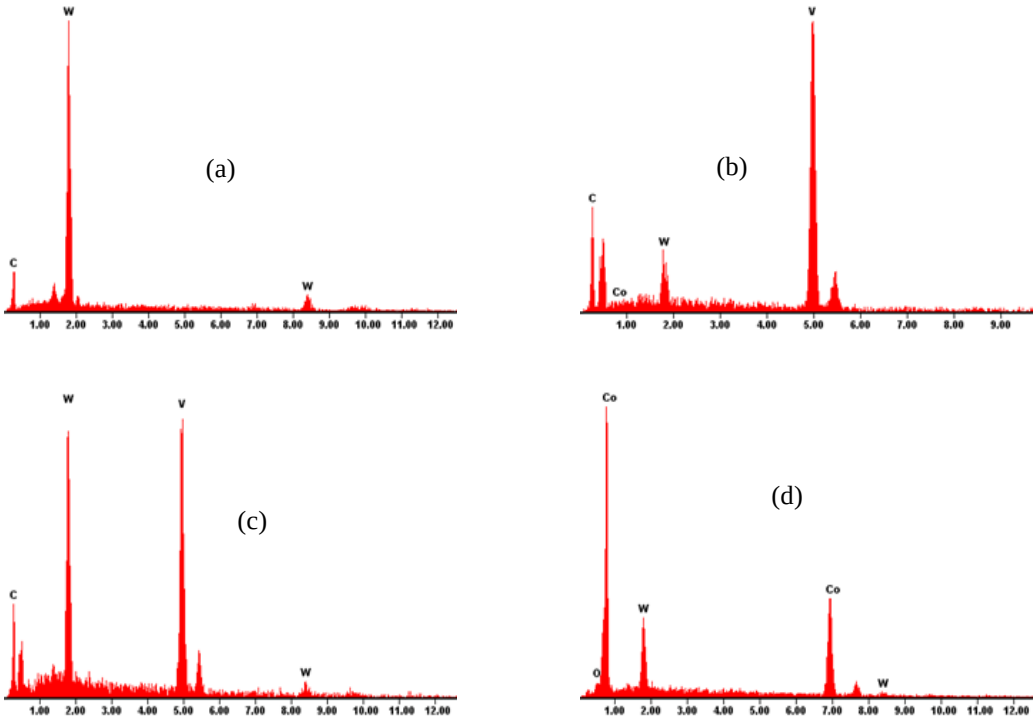


Figure 6. 4 EDS analysis of the (a) white phase showing roundish WC grains and (b & c) light and dark grey regions showing irregularly shaped (W,V)C grains, and (d) continuous matrix.

Table 6.3 provides a comparison of the physical properties of the two alloys. The density of the WC-12wt%Co-10wt%VC alloy was 12.3% lower than that of the WC-12wt%Co alloy, which could be beneficial for producing lighter alloys. The higher porosity level in the WC-12wt%Co alloy is an indication of incomplete densification during the sintering process, which could be due to the short sintering time and/or low sintering temperature of the alloy. The coercivity values of both alloys are comparable. A high coercivity value generally indicates a finer carbide grain size and in some cases, it also indicates the presence of eta phase or high levels of porosity. The WC grain size in the WC-12wt%Co-10wt%VC alloy is lower compared to that of the WC-12wt%Co alloy, and at such the coercivity value of WC-12wt%Co-10wt%VC alloy is expected to be lower. No eta phase was detected in both alloys, as reflected by the XRD patterns in **Figures 6.5,** but the higher porosity level in the WC-12wt%Co alloy could have been responsible for the comparable coercivity value.

Table 6. 3 Physical properties of the spark plasma sintered alloys.

Spark plasma sintered alloys	Density (g/cm^3)	Porosity (%)	Coercivity (kA/m)	WC mean size (µm)[a]	(W,V)C mean size (µm)
WC-12wt%Co	13.8 ± 0.1	1.4 ± 1.9	9.21	2.22	ND
WC-12wt%Co-10wt%VC	12.1 ± 0.0	0.6 ± 0.8	9.78	1.94	ND

[a] Values calculated from **[127]**; * ND - (Not determined) due to irregularity in the shape of the phase.

6.3.2 Phase composition

Figure 6.5 shows the phases of the alloys identified using XRD. The most prominent phase on the XRD pattern of both alloys was WC. No deleterious phases were found. For the WC-12wt%Co alloy, the Co peaks, seen in the powders **(Figure 6.2)**, were still found in the alloy but the peak intensity was smaller and broader in the latter. In the WC-12wt%Co-10wt%VC alloy, the VC peaks found in the powder were replaced with the double carbide phase, WV_4C_5. The reason for this has been given in **section 5.3.2**.

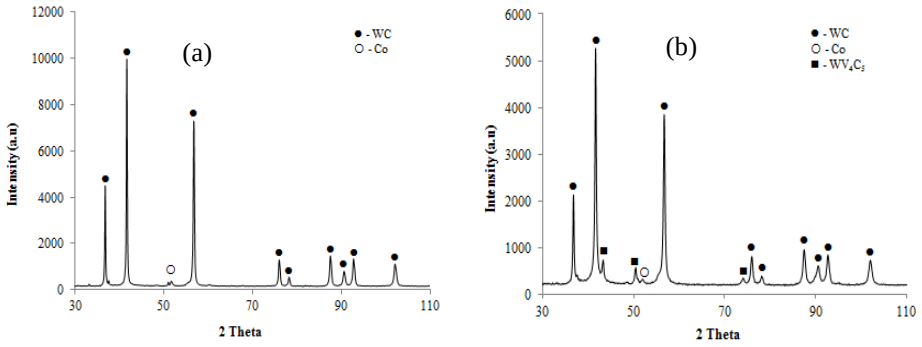


Figure 6. 5 XRD patterns for (a) WC-12wt%Co (b) WC-12wt%Co-10wt%VC alloys.

The approximate mass fraction of the phases in the alloys is shown in **Table 6.4**, as determined by Rietveld analysis. The d-values of WC in all the alloys were larger than those of the starting powders.

Table 6. 4 Phase composition of alloys.

Spark plasma sintered alloys	**Phases and their mass fraction (%)**		
	WC	**Co**	**WV_4C_5**
WC-12wt%Co	95.23	4.77	-
WC-12wt%Co-10wt%VC	86.47	0.77	12.77

6.3.3 Mechanical properties

Table 6.5 summarizes the mechanical properties of the alloys.

Table 6. 5 Mechanical properties of the alloys.

Spark plasma sintered alloys	**HV30**	**K_{IC} ($MPa.m^{0.5}$)**	**Y (GPa)**	**ν**
WC-12wt%Co	1319 ± 8	14.6 ± 0.8	664	0.18
WC-12wt%Co-10wt%VC	1461 ± 9	9.6 ± 0.2	648	0.26

The WC-12wt%Co-10wt%VC alloy had a 10% higher hardness than the WC-12wt%Co alloy, which could be beneficial for improved wear properties. This increased hardness is probably the combined result of the finer WC carbide grain size and the presence of the harder double carbide phase (WV_4C_5). The fracture toughness of the WC-12wt%Co-10wt%VC alloy decreased by 34% but is still considered moderate. These results are aligned with the coercivity values **(Table 6.3)** and the microstructure images shown earlier **(Figure 6.3)**. The Young's modulus of the WC-12wt%Co alloy was found to be within the expected range for 12wt%Co cemented carbides while the addition of VC lowered the Young's modulus by 2%. The Poisson's ratio calculated was higher in the WC-12wt%Co-10wt%VC alloy compared with the WC-12wt%Co alloys.

6.4 Friction and sliding wear tests

The friction behavior of each alloy sliding against the 100Cr ball as a function of distance for the test condition stated in **Table 3.6** is illustrated in **Figure 6.6**. The friction behaviour for the different alloy-ball pairs showed two distinct regions namely a running-in phase and a steady-state region.

For the WC-12wt%Co alloy **(Figure 6.6(a))**, the running-in period occurred during the first 20 m of sliding where the CoF linearly increased from 0.19 to 0.23. After this the CoF showed a small sharp decrease dropped to about 0.2 and which was followed by a linear increase reaching approximately 0.8 after 200 m of sliding. For the WC-12wt%Co-10wt%VC alloy **(Figure 6.6(b))** the running-in phase begins with a short sharp increase in friction for the first 35 m of sliding reaching a CoF of 0.7 and quickly attained the steady state with the CoF ranging from 0.6 to 0.8.

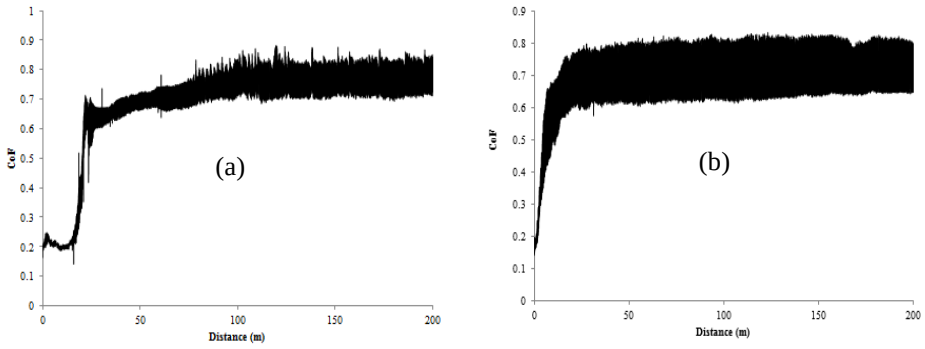


Figure 6. 6 Friction behavior against 100Cr ball for (a) WC-12wt%Co and (b) WC-12wt%Co-10wt%VC alloys.

Figure 6.7 shows the static and dynamic CoFs for each alloy-ball pair after 200 m of sliding. As expected the static CoF was higher than the dynamic CoF. The static and dynamic CoF for the alloys were comparable.

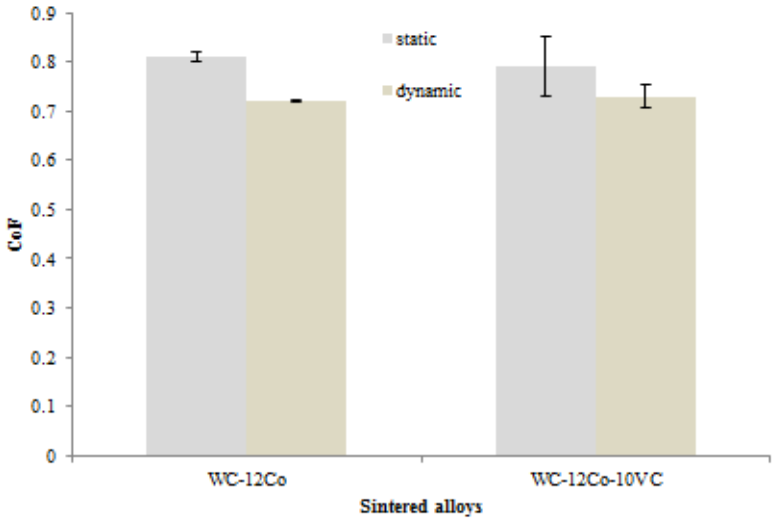


Figure 6. 7 Friction coefficients for the alloy-ball pairs.

Table 6.6 lists the penetration depths of the balls into the alloys as well as the wear track widths made on the alloys. Observation from **Table 6.6** showed that while the penetration depth of the WC-12wt%Co-10wt%VC alloy was lower, the wear track widths was larger compared to the WC-12wt%Co alloy.

Table 6. 6 Ball penetration depths and wear track width on the alloys.

Spark plasma sintered alloys	**100Cr ball**	
	Wear track width (μm)	**Penetration depth (μm)**
WC-12wt%Co	391 ± 72	2.81 ± 0.1
WC-12wt%Co-10wt%VC	518 ± 36	1.97 ± 0.7

Figures 6.8 compare the wear coefficients of the alloys against the balls while **Figure 6.9** compares those of the balls on the alloys. The wear coefficients of the

WC-12wt%Co-10wt%VC alloy was lower compared to that of the WC-12wt%Co alloy, an indication that the WC-12wt%Co-10wt%VC had a better wear resistance compared to the WC-12wt%Co. **Figure 6.9** showed that the ball worn more with the WC-12wt%Co-10wt%VC alloy compared to the WC-12wt%Co alloy.

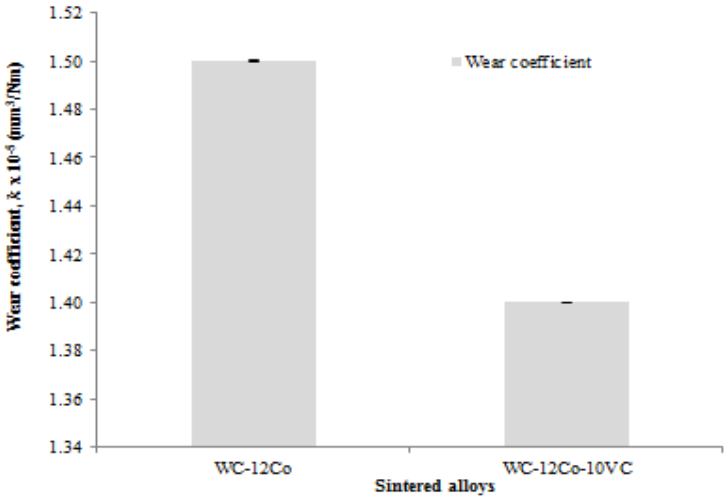


Figure 6. 8 Comparison of the wear coefficients of the sintered alloys against the 100Cr steel balls.

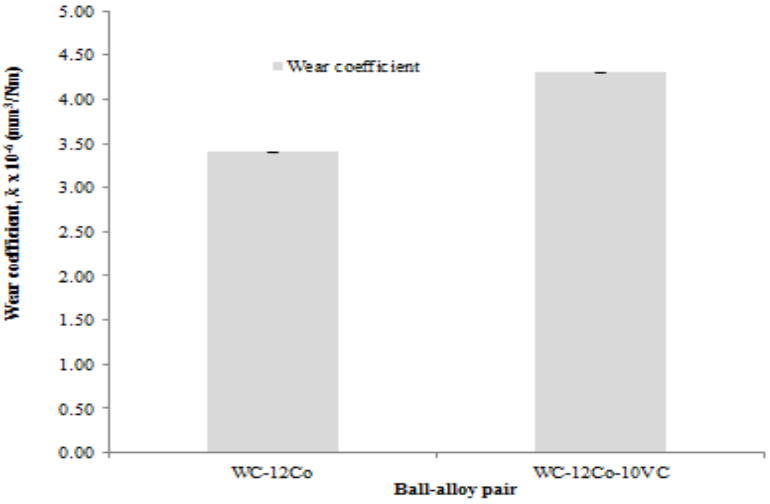


Figure 6. 9 Comparison of the wear coefficients of the 100Cr steel balls sliding pairs against the alloys.

6.4.1 Wear mechanisms in sliding wear

The wear scars from the sliding wear tests on the alloys were examined using SEM with EDX, in order to determine the wear mechanisms. Selected SEM images are presented to provide a summary of the wear mechanisms observed. **Figure 6.10** illustrates the typical wear tracks on the alloys under the test conditions with their respective EDX analysis. These images provide a general impression of the variation in wear track widths achieved with the 100Cr steel ball at the operating condition. The wear mechanisms for all the alloys were found to be very similar. Ploughing of wear particles, which had contributed to groove formation **(Figure 6.10)** were observed. The grooves formed are parallel with the sliding direction. Higher magnifications on the wear track showed evidence of particle smearing on the worn surfaces of the alloys. The groove formed is more pronounced on the wear track of the WC-12wt%Co alloy compared to the WC-12wt%Co-10wt%VC alloy, hence an evidence of more wear **(Figure 6.8)**.

Some plastic deformations of the carbide grains are also evident. Binder removal was also evident in both alloys. No evidence of WC carbide grain pull out was observed in both alloys, but the occurrence cannot be completely ruled out. The formation of thin films on the wear surfaces suggests the occurrence of tribo-layers oxides. Less smearing was observed on the wear track of the WC-12wt%Co alloy compared to that of the WC-12wt%Co-10wt%VC alloy, which correlates with the increased wear coefficient of the 100Cr ball **(Figure 6.9)**. Evidence of WC grain cracking observed in the WC-12wt%Co alloy was missing in the WC-12wt%Co-10wt%VC alloy but such occurrence could not be completely ruled out. EDX analysis on the wear track of the alloys against the balls indicates the presence of Fe and Cr. This confirms the transfer of material from the ball to the surface of the alloys during wear. In general, the wear mechanisms for all the alloys were found to be the same portraying plastic deformation, preferential binder removal, carbide grain cracking and fragmentations, adhesion and formation of thin tribo-layer oxides during wear. It

is believed that the binder removal occurs first, followed by subsequent carbide grain cracking.

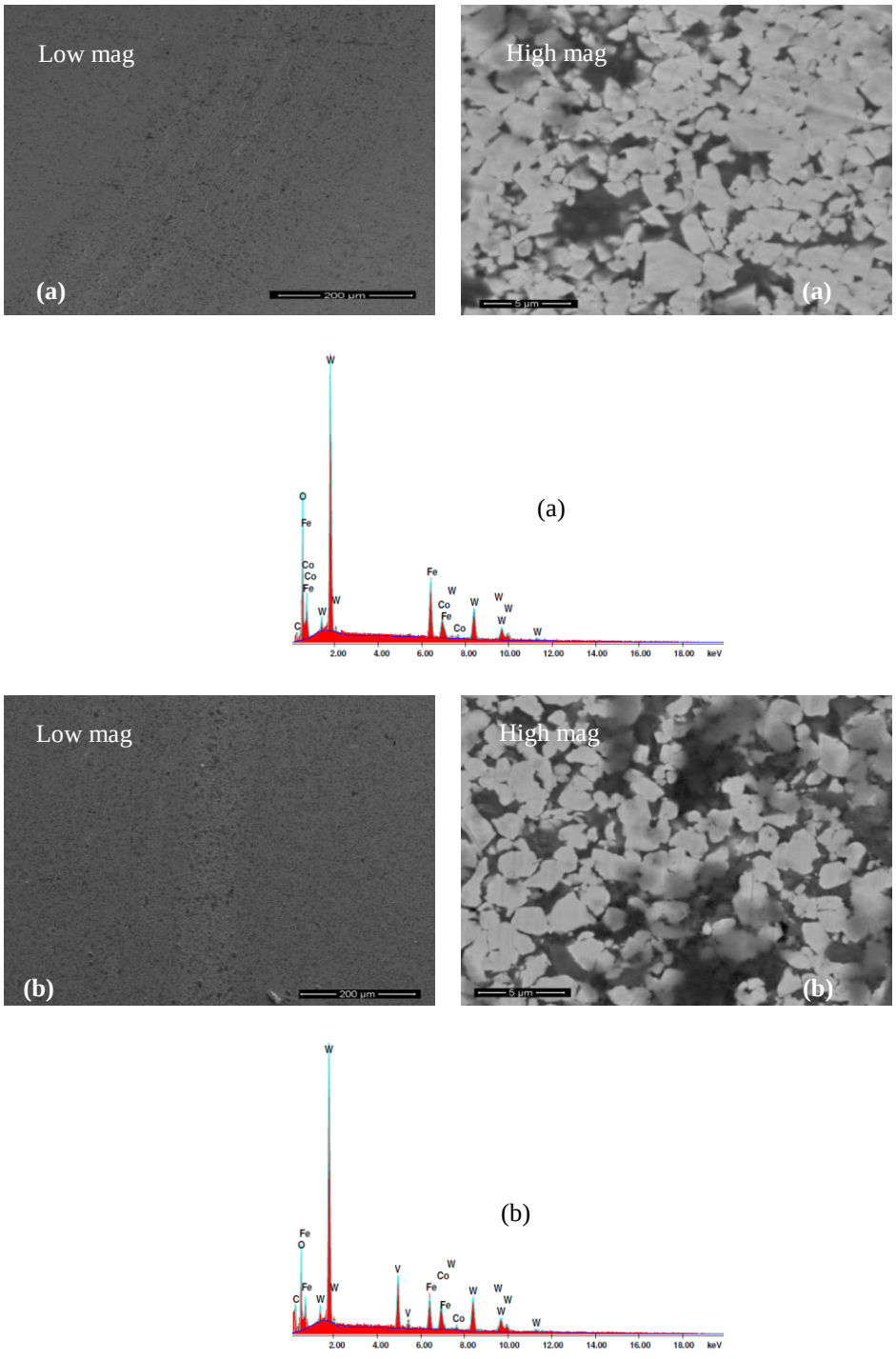
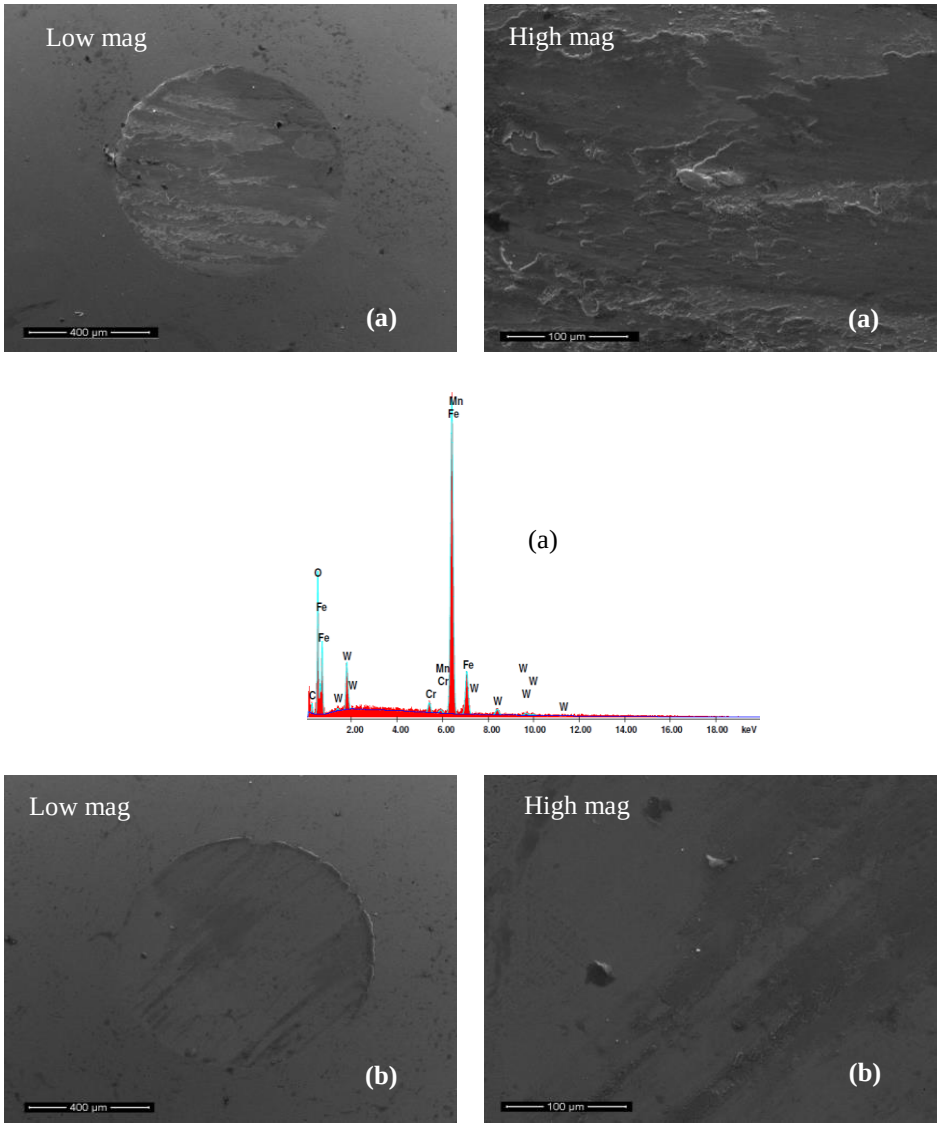


Figure 6. 10 SEM images with EDX analysis of the wear tracks against 100Cr ball for (a) WC-12wt%Co and (b) WC-12wt%Co-10wt%VC alloys.

Figure 6.11 shows typical wear scars on the 100Cr steel ball against the alloy, with the respective EDX analyses. Both the lower and higher magnifications are represented. **Figure 6.11** is the ball that produced the wear track shown in **Figure 6.10**. The presence of W on the wear scars on the 100Cr steel ball against the alloys gave evidence of materials' transfer.



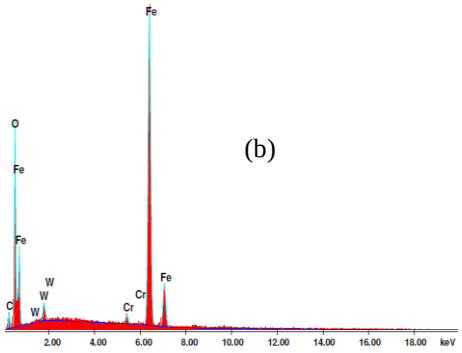


Figure 6. 11 SEM images with EDX analysis of the wear tracks against 100Cr ball for (a) WC-12wt%Co and (b) WC-12wt%Co-10wt%VC alloys.

6.5 Slurry erosion tests

The average mass losses of the alloys were converted into average volume loss using the densities of the alloys. The average volume loss against time and the erosion rate against time curves of the polished surfaces of the alloys at the different test angles are shown in **Appendix D3A**. **Figure 6.12** compares the average volume losses of both alloys against time when tested at 90°. At all the test angles, the average volume loss increases with test time. The average volume losses for both alloys decreases as the impact angle decreased. At angle 45°, the average mass losses from all the coatings were very low and erratic in nature.

Figure 6.13 compares the average slurry erosion rate against the impact angles for the alloys. Both alloys showed a maximum erosion rate at 90°, a behaviour that is consistent with that of brittle materials **[108]**. Observations from the erosion rate curves showed that at all test angles, the erosion rate of the WC-12wt%Co alloy was lower than that of the WC-12wt%Co-10wt%VC alloy, which indicates that the slurry erosion resistance of the WC-12wt%Co alloy is superior to that of the WC-12wt%Co-10wt%VC alloy. The reason here could be that the larger WC grain in the WC-12wt%Co alloy resist erosion better than the finer grains in the WC-12wt%Co-10wt%VC alloy. Finer grains could easily fell out sooner after the removal of the cementing binder and/or carried away with the binder. The

possibility could also be a result of the short sintering time and/or low sintering temperature.

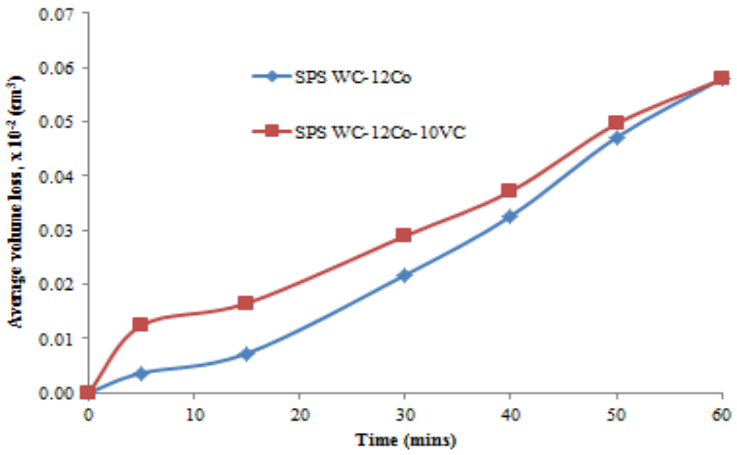


Figure 6. 12 Comparison of the average volume loss against time curves of both alloys at 90°.

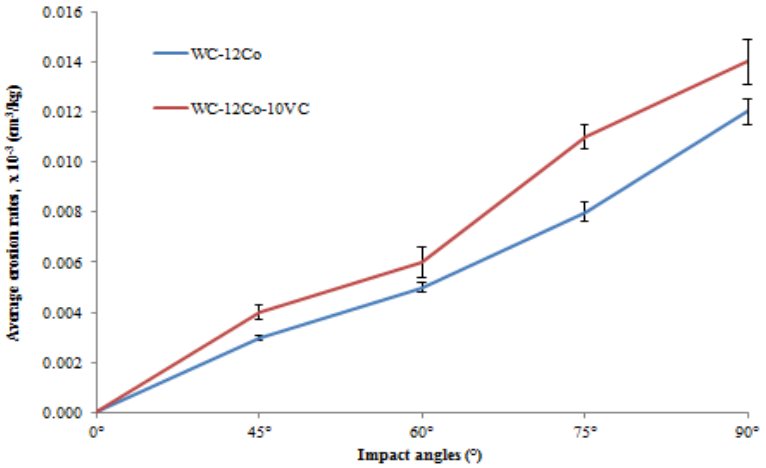


Figure 6. 13 Comparison of the average erosion rate against impact angles.

6.5.1 Wear mechanisms of the eroded alloy surfaces

SEM examination of the eroded surface of both alloys reveals that the slurry impact caused some plastic deformation of the surface. The eroded surfaces exhibited depressions due to ploughing action of the eroding particles. The surface degradation in both alloys appeared similar at all the test angles but the damages

were, to a lesser degree as the impact angles decreased. At higher impact angles, plastic deformation of the carbide grain were more dominant compared to lower impact angles, an indication that the force during impact at higher angle had a component perpendicular to the surface. The difference in impact angle appeared does not change the wear mechanisms in both alloys, but only changed the amount of materials lost.

The predominant erosion mechanism for the alloys in this study appeared to have been loss of the binder phase and as a consequence of this, the carbide grains (both WC and (WV_4C_5) were exposed to further erosion action which resulted into cracking, fragmentations and possible fall-outs. The appearances of the eroded surfaces of the VC and the non-VC alloys were not very different. The WC grains in the WC-12wt%Co alloy eroded by a combination of plastic deformation, chipping and fragment fall-out, while those in the VC alloy wore generally by chipping. Erosion mechanisms for the WV_4C_5 grains appeared to be predominantly by plastic deformation, cracking, chipping and fragment fall-out. The mechanism of erosion does not seem to change with the change in impact angles of testing.

Figures 6.14 and 6**.15** show some selected SEM images with EDX analyses of the eroded surfaces of the WC-12wt%Co and the WC-12wt%Co-10wt%VC alloys respectively at all the test angles. EDX analyses performed on the eroded surfaces of the alloys were used to identify possible transfer of material between the erodent and the alloys. The analyses shows the presence of oxygen which could have been from water and/or the SiO_2 used. It could also show the possibility of the formation of oxide. The analysis on the worn surface of the alloys does not show any evidence of Si from the erodent but its occurrence could not be ruled out. Also, the inability of the EDX analysis to identify Si could be a result of the close characteristic X-ray energy between W and Si (1.774 and 1.734 keV).

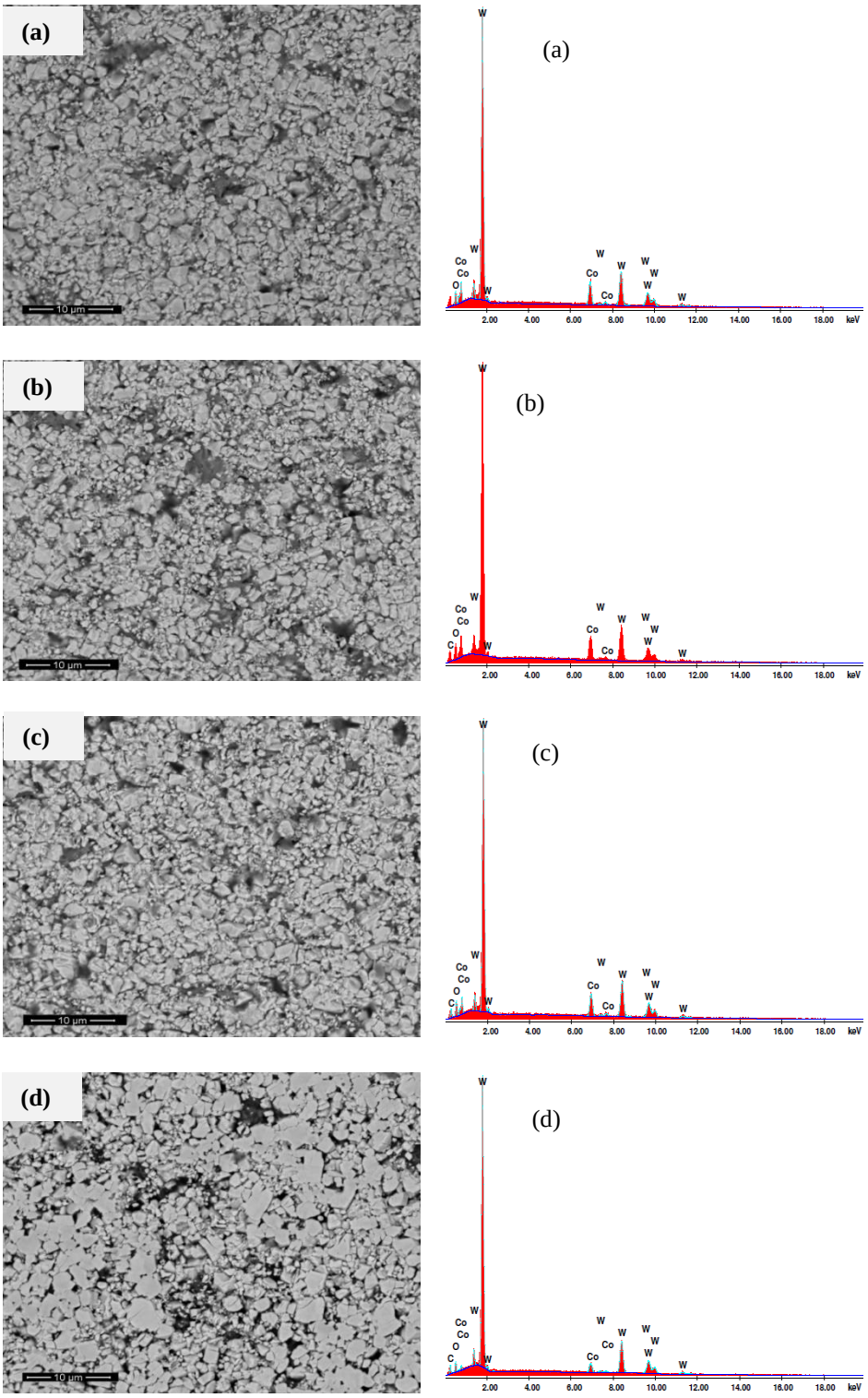


Figure 6. 14 SEM images of the eroded surface of the WC-12wt%Co alloy at (a) 90°, (b) 75°, (c) 60°, and (d) 45°.

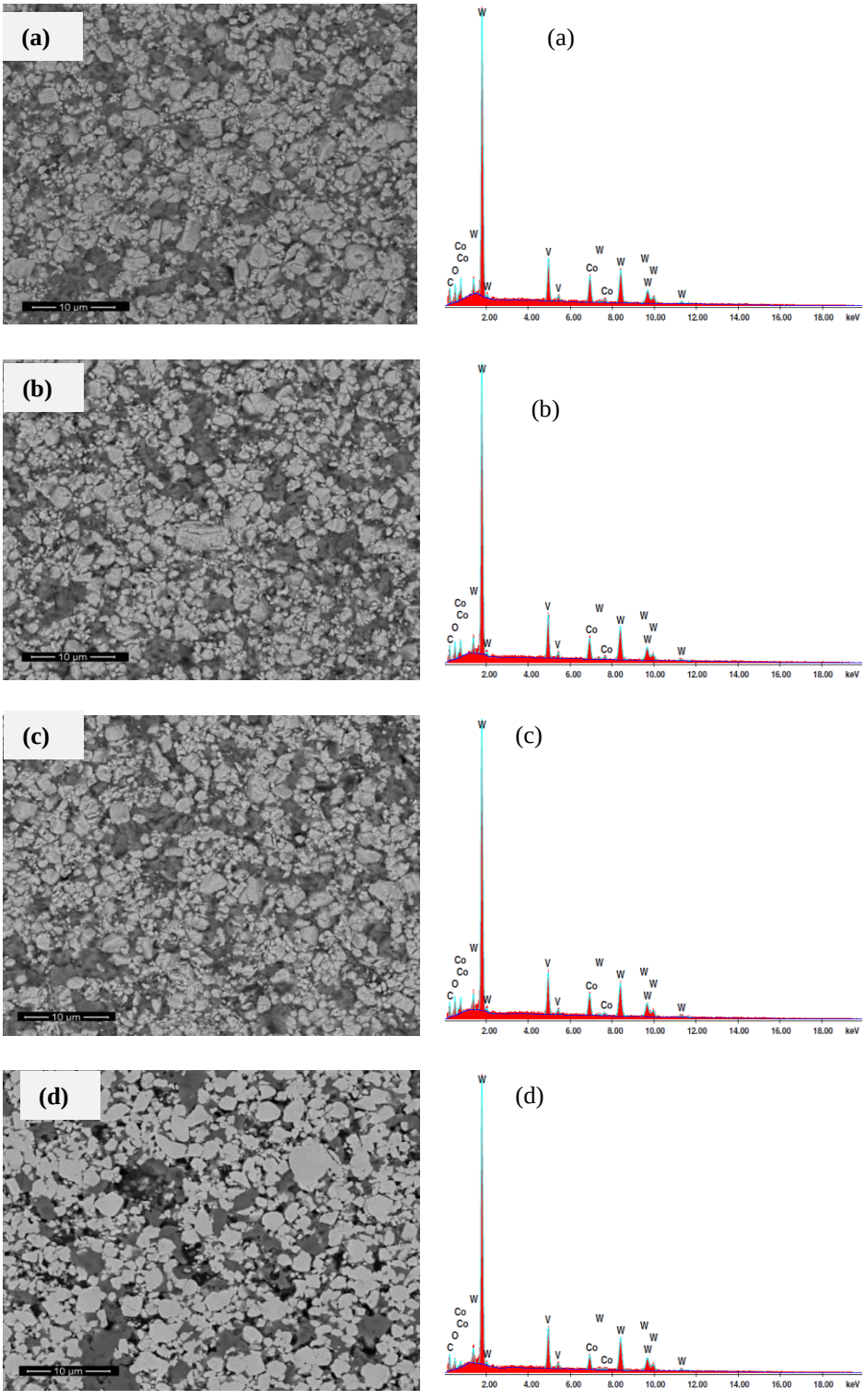


Figure 6. 15 SEM images of the eroded surface of the WC-12wt%Co-10wt%VC alloy at (a) 90°, (b) 75°, (c) 60°, and (d) 45°.

7. Discussion

7.1 Introduction

This chapter presents a general discussion on all the materials studied. It discusses the interaction between the powder properties and the various manufacturing techniques and compares the materials based on the observations made through the investigations.

7.2 HVOF coatings

7.2.1 Material characterization

All the coatings investigated in this study had a splat-like microstructure, a characteristic of thermal spraying where coatings are built up from the deposition of thin layers, called splats, one over the other. The splat-like structure creates a challenge since the coatings should be homogeneous; an ideal microstructure would be like that of sintered components. The homogeneity has been reported **[70]** to be required at two levels namely a macro-level (at which the coatings are required to appear continuous with the substrate) and micro-level (splat level). Acceptable homogeneity is obtained by ensuring coating-substrate and inter-splat adhesion. The wear response of the coatings indicates that good bond strength exists within the coating microstructure.

The observed coatings' porosities in this study agree with that from thermal sprayed coatings **[76,97,135]**. The higher porosity in the 10wt%VC-coatings compared to that of the non VC-coating could be due to the differences in the powder particle sizes prior to the deposition process. Particle characterizations of the powders showed that the VC-coating starting powders were finer and less dense than the non-VC coating powders **(Table 4.1)**. Finer powders are prone to evaporation as a result of higher heat up rates and less dense powders decelerate

faster than more dense particles **[70,77]**. This occurrence reduces the rate of particles arriving at the substrate, and thus increases porosity in the resulting coating. The lower porosity obtained for the 17wt%Co-10wt%VC-coatings compared to the 12wt%Co-10wt%VC coatings, could be a result of optimized spraying parameters.

The differences in the phase compositions between the powders and the coatings were caused by the deposition process. Phase changes are a typical occurrence for WC-based coatings sprayed in the presence of oxygen **[70,77]**. Decarburization is facilitated by high heat input to powder particles and/or coating deposition in an oxidizing environment and thus reduces the amount of WC. The decarburization of WC to W_2C was more pronounced in the 17wt%Co coatings than the 12wt%Co coatings. The formation of W_2C in the 17wt%Co coatings could have been encouraged by the heat input to the powder particles being sprayed and/or the deposition parameter. The change in the morphology and grain size of the WC grains in all the coatings relative to the powders was a result of the failure of the WC grains to re-precipitate after dissolving in the binder phase during heating in the spray gun due to the high cooling rate. The change in morphology of the WC grains (from angular-particles in the powders to rounded-particles in the coatings) was due to the fact that dissolution starts from the edges of the grains.

The reduction in the WC grain sizes were more pronounced in the 10wt%VC coatings as compared to the WC-12wt%Co coating. This occurrence cannot be explained in terms of the grain refinement processes (which occurs in the sintered alloys when VC is added), because there was hardly any evidence of re-precipitation of the WC grains. The high degree of amorphocity as shown by the XRD analysis (Figure 4.9 (c) & (d)) in the 17wt%Co-10wt%VC coatings could be due to the high amount of the binder phase in the starting powders. The larger d-values of WC grains in all the coatings compared to the powders gave evidence of changes in the residual thermal stress distribution on the WC grains. This change

in stress could be attributed to the binder phase changing from crystalline in the powders to amorphous in the coatings, as indicated by XRD analysis.

At the same binder content, the WC-12wt%Co and WC-12wt%Co-10wt%VC coatings did not differ much in their hardness values. This could be that the addition of VC in a large quantity does not impact much on the hardness of the coating and/or as a result of the differences in the spraying parameters. The lack of effect of the VC addition on the hardness could also have been caused by the influence of microstructure and phase composition of the coatings. The hardness values of all the 17wt%Co-10wt%VC coatings were better than those of the 12wt%Co coatings. This is attributed to the presence of the harder WV_4C_5 and W_2C phases **(Table 4.4)** and the finer WC grains in the coatings **(Table 4.5)**. The hardness of any WC-Co coating is a function of the amount of retained WC, porosity and the level of decarburization **[34,74,89,93]**. A low volume fraction of WC leads to a low hardness value when the decarburization product is metallic tungsten **[1]** and in the event that the decarburization product being W_2C, (as observed in this study), the hardness increases because W_2C is harder than WC **[1]**. The effect of porosity is to reduce hardness regardless of the amount of retained WC and/or W_2C present in a coating. Since porosity, decarburization and the amount of retained WC are all functions of the spraying parameters, the interaction of these properties make it difficult to determine the exclusive role of VC on the hardness.

The microstructural characteristics obtained for the coatings in this study agree with those from other authors **[34,70,75,76,86,88-89,94,97,135]**. Due to optimized processing parameters better properties such as lower porosities, absence of eta phase from the VC-added coatings, and homogenous distribution of phases were obtained in this study.

7.2.2 Friction and sliding wear response of the coatings

Friction is not a material property but rather a system response **[113]**. It is influenced by properties of the materials in contact as well as the operating environment. Friction in a sliding system is generally described in terms of the static and kinetic coefficients of friction and it is known that μ_s is usually higher than μ_k as reviewed in **section 2.4**. In this study, this trend was observed for all the ball-coating sliding pairs under the tested conditions.

Frictional force is proportional to applied load and independent of sliding velocity **[23,112-113]**. Sliding velocity affects the frictional energy dissipation which in turn affects the temperature at the sliding interface **[113]**. The friction tests were conducted at a constant sliding velocity of 0.26 m/s, and this velocity is considered too low to cause a significant increase in the interface temperature. Any heat generated at this speed at the interface is expected to be rapidly conducted away. Random temperature measurements taken during tests confirm that the test area remained at room temperature. Although the friction tests were conducted at room temperature, oxides were detected on several coating surfaces using XPS. It is possible that flash temperatures occurred, leading to the formation of the oxides detected on the coatings when sliding against the balls. The occurrence of hot spots during sliding wear is well known **[113]**, and unfortunately the current test system does not permit the measurement of flash temperatures.

Table 7.1 shows the friction pattern followed by the ball-coatings sliding pairs. The patterns can be aligned with one or more of the four hypothetical S-shaped patterns defined by **[112]** and reviewed in **section 2.4 (see Figure 2.16)**.

Table 7. 1 Hypothetical friction patterns obtained for the ball-coating sliding pairs.

HVOF Coatings	**Balls**	
	100Cr steel	**WC-Co**
WC-12wt%Co	I	1
WC-12wt%Co-10wt%VC	III/IV	I
WC-17wt%Co-10wt%VC (Run 38)	III	II
WC-17wt%Co-10wt%VC (Run 39)	I	II

From **Table 7.1**, sliding against the 100Cr steel balls, the WC-12wt%Co and the WC-17wt%Co-10wt%VC (Run 39) coatings followed pattern I. This pattern is the result of ploughing due to roughening of the surface and entrapped wear particles. The increase in the friction level is associated with the smoothing of the surfaces resulting in a larger component of adhesive friction **[112]**. The WC-12wt%Co-10wt%VC and the WC-17wt%Co-10wt%VC (Run 38) coatings sliding against the 100Cr steel ball followed pattern III, which is thought to be due to the ejection of wear particles from the contact surfaces and the subsequent formation of new wear particles which contribute to increases in the friction levels **[112]**. In addition, the WC-12wt%Co-10wt%VC coatings also displayed characteristics of pattern IV which is associated with incompatible materials pairing **[112]**. With respect to the WC-Co balls, two major friction patterns were observed namely patterns I and II. The 12wt%Co coatings followed pattern I while the 17wt%Co coatings followed pattern II.

The wear rates of the materials were defined by the dimensional wear coefficient, ***k***, which is based on the volume of material lost during wear, the applied load and the material hardness. Sliding pairs which displayed high friction values were found to have high wear coefficients which translated into high wear rates. The sliding wear rates of the 10wt%VC coatings in the sliding wear test were lower than those of the WC-12wt%Co coatings at the same Co content. The wear rate is generally considered to be a function of the hardness of the sliding surfaces with harder surfaces having lower wear rates than softer surfaces. In this study the

average hardness of the WC-12wt%Co-10wt%VC coating was slightly higher than that of the WC-12wt%Co coating and therefore this would contribute to the differences noted in the wear rates. However due to the minor difference in the hardness, the wear rate differences cannot be explained by the coating hardness alone. The properties of the balls (such as hardness, compressive strength, toughness and Young's modulus) and the interaction between the balls and the coatings play an important role in the material removal process. One method to characterize this interaction was defined by Hutchings **[113]** as the H_b/H_c ratio where H_b is the hardness of the ball and H_c the hardness of the coating. The higher the H_b/H_c ratio, the higher the degree of indentation which leads to higher wear rates. Typically an H_b/H_c ratio of 1.2 signifies the boundary condition between mild and severe wear as defined by Hutchings **[113]**. **Table 7.2** lists the ratios for each of the sliding pairs as well as the maximum stress experienced during sliding. This stress was calculated using the applied force and the geometry of the wear scar generated on the ball.

Table 7. 2 Hardness ratios and maximum stress applied during sliding.

HVOF coatings	**Hardness ratio**		**Applied Stress (MPa)**	
	100Cr	**WC-Co**	**100Cr**	**WC-Co**
WC-12wt%Co	1.01	1.76	4.5 ± 0.15	98 ± 2.17
WC-12wt%Co-10wt%VC	0.92	1.61	4.9 ± 0.17	120 ± 3.58
WC-17wt%Co-10wt%VC (Run 38)	0.69	-	9.8 ± 1.04	-
WC-17wt%Co-10wt%VC (Run 39)	0.69	-	12 ± 0.03	-

The H_b/H_c ratios for the 100Cr steel balls sliding pairs do not exceed the 1.2 boundary condition and therefore these sliding systems can be termed 'mild wear'. For the WC-Co ball sliding pairs, the H_b/H_c ratios were greater than the boundary condition; hence these systems are termed 'severe wear'. In terms of applied stress the VC coatings showed higher values than the non-VC coatings which would normally be used to predict higher mechanical damage and higher

wear rates. However these coatings had lower wear rates than the non-VC coatings. The higher stress is due to the smaller contact area between the sliding surfaces.

Several mechanisms have been proposed to explain how sliding wear operates. Although the detail of material removal differs for each sliding system, plastic deformation has been shown to be the main mechanism of wear **[113]**. Shearing of the asperities on the interfaces and possible subsequent adhesion of the fragments onto one or both of the surfaces as well as ploughing and smearing of the interfaces are primary mechanisms by which plastic deformation occurs during sliding wear **[113,139]**. For all the sliding pairs in this study combinations of these mechanisms were observed.

The wear mechanisms for the sliding pairs were predominantly smearing and groove formation caused by ploughing of the wear particles. Grooving is initially caused by the initial deformation of asperities on the contact surfaces. Subsequent grooving is caused by abrasive wear from particles of wear debris. Low and high magnification SEM images of the wear tracks revealed surfaces with significant amounts of adhered wear debris **(Figure 4.15)** as well as scratches and grooves **(Figure 4.16)**. The predominant wear mechanisms for the coatings were preferential binder removal, followed by carbide grain cracking and carbide grain pull-out, similar to that found by other authors **[139,140]**. The initial increase in the friction which was observed in all the wear tests provides the energy required to initiate the binder removal and micro-cracking **[140]**. Occasional grooving observed on the coatings is believed to be caused by hard carbide grains which have been extracted from the coatings and which subsequently act as abrasive particles as sliding continued. The XPS results indicated the presence of oxides present on the worn surfaces of the coatings. These oxides provide low shear strength at the sliding interface thereby reducing friction due to limited metallic contact consequently reducing wear.

The sliding wear test results on the coatings in this study could not be directly compared to those from other authors **[70,64,103]**, because the test parameters were different. However, the wear mechanisms were found to be similar.

7.2.3 Slurry wear response of the coatings

A comparison of the slurry erosion resistance of the coatings showed that the addition of the VC led to an improvement in the slurry erosion resistance at all impact angles tested. When the Co content of the VC-coatings was increased from 12wt% to 17wt% a further improvement in erosion resistance was noted at impact angles greater than 60° which is attributed to the optimized processing parameters used for the 17wt%Co coatings which resulted in better properties for these coatings such as a higher inter-splat strength which is better able to resist impact. The 10wt%VC coatings had finer WC grain sizes **(Table 4.3),** higher volume fractions of the hard phases **(Table 3.1)** and higher hardnesses **(Table 4.5)** than the non-VC coating.

The slurry erosion resistance is a function of the integrity of the coating microstructure and the relative resistance of the WC and (W,V)C grains to impact wear **[70]**. The harder WV_4C_5 grains are better able to withstand impact than the WC grains and thus improved the erosion resistance. At a given cobalt mass content, the porosity was higher in the 10wt%VC coatings than the WC-12wt%Co coatings which could have led to an increase in mass losses in these materials. However due to the better erosion resistance of the VC coatings the role of porosity is probably minor. At higher impact angles, the WC grains on the eroded surface of the WC-12wt%Co coating exhibited severe fragmentation which could assist in more material being removed during erosion compared to the WC-12wt%Co-10wt%VC alloy **(Figure 4.23 – 4.24)**.

From the wear scar analyses of all the coatings, the erosion mechanisms were similar, namely, preferential removal of binder, followed by wear of the carbide grains leading to fragmentation and grain fall-out. The binder removal results from extrusion between the carbide grains as a result of grains moving towards each other in the direction of the erodent particles due to friction **[70]**. In addition, the presence of an aqueous environment could enable the removal of the binder via corrosion, and the two processes of extrusion and corrosion could lead to faster rates of binder removal. This in turn would facilitate higher incidences of carbide grain fall-out.

For all the coatings the highest erosion rate was recorded at an impact angle of 90° and the lowest erosion rate at 45°. At all impact angles the erosion rates of the WC-12wt%Co coating was higher than those of the 10wt%VC coatings. The erosion behaviour of all the coatings is aligned with Hutchings **[113]** definition of a material having a brittle response to erosion when the maximum wear is recorded at high impact angles. This means that the material is more prone to cracking and fracture at higher impact angles than at lower impact angles. Confirmation of this can be seen from the SEM micrographs of the worn surfaces. The degree of carbide grain cracking, fragmentation, crushing and displacement increased as the impact angle increased. It was noted that the VC grains did not show the same severe extent of fracture as the WC grains. This explains why the 10wt%VC coatings had a lower erosion rate than the WC-12wt%Co coating. At all impact angles the extrusion and preferential removal of the Co binder phase was visible. Once the binder was removed it was easier for single unsupported carbide grains to become dislodged by repeated impact. At the lower impact angles crack initiation and fracture of the hard carbide grains is known to be was limited **[70]** and therefore the predominant wear mechanism was the removal of the softer Co binder phase.

The relationship between the hardness of the silica (H_S, - 1200 HV **[141]**) erodent and the hardness of the alloys (H_1, H_2, H_3, H_4) and the individual phases (H_{WC}, - 2000 HV **[18]**; H_{VC}, - 2800 HV **[18]**; H_{Co}, - 106 HV **[142]**) play a role in the erosion response of the materials. These ratios are listed in **Table 7.3** with H_1, H_2, H_3, and H_4 representing the hardness of WC-12wt%Co, WC-12wt%Co-10wt%VC, WC-17wt%Co-10wt%VC (Run 38), and WC-17wt%Co-10wt%VC (Run 39) coatings respectively.

Table 7. 3 Hardness ratios for the eroded materials.

H_S/H_1	H_S/H_2	H_S/H_3	H_S/H_4	H_S/H_{WC}	H_S/H_{VC}	H_S/H_{Co}
1.41	1.29	0.96	0.96	0.56	0.40	10.6

At the ratio below 1 it is more difficult for the silica erodent to initiate cracks and fracture the material. Based on the ratios of the individual phases the VC is better able to withstand attack from the silica erodent than the WC while the Co phase is extremely susceptible to attack which explains its selective removal. The silica erodent initially subjects the WC and VC grains to a low cycle micro-fatigue action until crack initiation begins. With subsequent repeated impacts, fracture and crushing of the grains becomes progressively easier. This effect is more pronounced at higher impact angles than at lower impact angles as was observed in the SEM images where the carbide grains were largely intact at 45°.

The impact stress at higher impact angles is greater than at lower impact angles which causes a higher degree of crack propagation and crack intersection which leads to increased rates of material removal. This is aided by the increase in kinetic energy of the erodents as the impact angle increases. This indicates that fracture toughness of the material should play a role in determining the erosion response of a material. However the effect of this could not be confirmed because at the applied load of 500 g, no cracks were obtained from all the coatings.

The results obtained in this study could not be directly compared with that from that of Machio **[70]**, because the test parameters (such as erodent impact velocity, and slurry concentrations) were different. Machio's slurry speed and concentration were 12.5 m/s and 5wt% **[70]** while those of this study were 6.4 m/s and 16wt% respectively **[Table 3.7]**. These parameters will have influence on the amount of materials' removal, thus making the comparison a bit challenging. However, the wear mechanisms were found to be similar.

7.3 Conventionally sintered alloys

7.3.1 Material characterization

The WC-12wt%Co-10wt%VC alloy sintered successfully at 1430 °C, in a standard commercial production sintering cycle and despite the VC being less wettable by Co compared to WC, the porosity in the WC-12wt%Co-10wt%VC alloy was minimal. The major problem during sintering was grain growth of the WV_4C_5 phase. This growth occurs by solution of VC and WC into the cobalt during liquid phase sintering. On cooling, the WV_4C_5 forms by re-precipitation from Co, while the VC assists in keeping the WC grain sizes to a minimum. In addition the higher solubility and diffusivity of VC in Co increases the restriction of WC grain growth, thus inhibiting the driving force for WC grain growth (for which the mechanism is dissolution and re-precipitation) **[143]**. This problem could be solved by starting from (W,V)C powders and not separate WC and VC powders (as used in this study), because only one carbide would go into solid-solution in the cobalt rather than both WC and VC **[144]**. No inhomogeneities were found in both alloys, an indication of good and effective milling and mixing conditions.

The double carbide (WV_4C_5) has a lower density than WC; hence the lower density of the WC-12wt%Co-10wt%VC alloy. This lower density may be useful in weight saving in components. Together with the weight saving, there is a higher hardness and comparable fracture toughness of the WC-12wt%Co-10wt%VC alloy compared to the WC-12wt%Co alloy of the same cobalt content. The higher hardness is attributed to the WV_4C_5 phase and the grain refining effect of the VC on the WC grains present in the structure.

The XRD spectra for the alloys (Figures 5.5 and 6.5) did not show eta phase. None of the starting VC remained in the sintered alloys, as seen from the shift from lower to higher values in the VC d-spacing (0.416 to 0.420), which is due to the formation of the WV_4C_5 phase. The crystal structure of this phase is the same as that of the VC, but with larger lattice parameters. The microstructural characteristics obtained for the alloys in this study agree with those from other authors **[15,41,44,145]** and the properties comparable with that of the conventionally sintered alloys **[12,26]**.

7.3.2 Friction and sliding wear response of the conventionally sintered alloys

Table 7.4 shows the friction patterns followed by the ball-alloy sliding pairs during testing. Sliding against the 100Cr steel balls, the WC-12wt%Co alloy followed pattern II while the WC-12wt%Co-10wt%VC alloy followed pattern III/IV (see discussion in **section 7.2.2**).

Table 7. 4 Hypothetical friction patterns obtained for the ball-alloy sliding pairs.

Conventionally sintered alloys	**100Cr steel balls**
WC-12wt%Co	II
WC-12wt%Co-10wt%VC	III/IV

Sliding pairs with high friction values did not display high wear coefficients; an indication that high friction does not necessarily translate into high wear rates. The sliding wear resistance of the WC-12wt%Co alloy was better than that of the WC-12wt%Co-10wt%VC alloy which was surprising as the VC alloy had the higher hardness. This indicates that hardness cannot be used to infer wear resistance under these test conditions.

The hardness and the elastic/plastic properties of a material play a complimentary role in the material removal process **[113].** The role of these properties can be assessed in terms of two ratios namely the material's E/H ratio, where E is the modulus of elasticity and H is the hardness, and the H_b/H_a ratio defined in **section 7.2.2**. Low E/H ratios indicate that materials will wear by a cutting mode while high E/H ratios indicate wear by a ploughing mode. The cutting mode results in higher material removal rates than the ploughing mode, because plastic deformation is greater under ploughing conditions. The higher the H_b/H_a ratio, the higher the wear rates **[113]**. **Table 7.5** lists the respective ratios for each ball-alloy sliding pair and the maximum stresses experienced during sliding.

Table 7. 5 Summary of the E/H ratio, the H_b/H_a ratio and the applied stress for alloys sliding against the 100Cr steel ball.

Conventionally sintered alloys	**E/H**	**H_b/H_a**	**Applied stress (MPa)**
WC-12wt%Co	0.53	0.63	22
WC-12wt%Co-10wt%VC	0.41	0.58	17

Based on the applied stress and H_b/H_a ratios presented in **Table 7.5** it was expected that the WC-12wt%Co alloy would experience more wear than the WC-12wt%Co-10wt%VC alloy. However, the WC-12wt%Co-10wt%VC alloy experienced more wear than the WC-12wt%Co alloy **(Figure 5.8)**. The average penetration depths of the balls into the VC alloy were deeper than those on the non-VC alloy, which led to higher material removal rates. The reason for this is

attributed to the lower Young's Modulus of the VC alloy. This is supported by the lower E/H ratio for this alloy which indicates more cutting and less plastic deformation than the non-VC alloy which ultimately leads to higher material removal rates. Therefore, based on this evidence, the E/H ratio is a better indicator of the wear response of alloys for the present sliding system than the H_b/H_a ratio.

In general, the wear mechanisms for both alloys were found to be the same namely preferential binder removal, carbide grain cracking and fragmentation, adhesion and formation of thin tribo-layer oxides **(see Table 4.8)** during wear. The sliding wear tests of the alloys in this study could not be directly compared with those from other authors **[36,110,139]**, because the test parameters and material compositions were different.

7.3.3 Slurry wear response of the conventionally sintered alloys

For both alloys the highest erosion rate was recorded at an impact angle of 90° and the lowest erosion rate at 45°. Below an impact angle of 65° the erosion rates of the alloys were similar. Above 65° the erosion rate of the WC-12wt%Co alloy was higher than that of the WC-12wt%Co-10wt%VC alloy and at 90° was approximately 50% higher. The erosion behaviour of both alloys is aligned with Hutchings **[113]** definition of a material having a brittle response to erosion when the maximum wear is recorded at high impact angles. This means that the material is more prone to cracking and fracture at higher impact angles than at lower impact angles. Confirmation of this can be seen from the SEM micrographs of the worn surfaces. The degree of carbide grain cracking, fragmentation, crushing and displacement increased as the impact angle increased. It was noted that the VC grains did not show the same severe extent of fracture as the WC grains. Even at an impact angle of 75° relatively few VC grains were fractured or crushed. This explains why the WC-12wt%Co-10wt%VC alloy had a lower erosion rate than the WC-12wt%Co alloy. At all impact angles the extrusion and preferential

removal of the Co binder phase was visible. Once the binder was removed it was easier for single unsupported carbide grains to become dislodged by repeated impact. At the lower impact angles crack initiation and fracture of the hard carbide grains was limited and the predominant wear mechanism was the removal of the softer Co binder phase.

The relationship between the hardness of the silica (H_S) erodent and the hardness of the alloys (H_1, H_2) and the individual phases (H_{WC}, H_{VC}, H_{Co}) play a role in the erosion response of the materials. These ratios are listed in **Table 7.6** with H_1 and H_2 representing the hardness of WC-12wt%Co and WC-12wt%Co-10wt%VC alloys respectively. As the ratio decreases below 1 it is more difficult for the silica erodent to initiate cracks and fracture the material. Based on the ratios of the individual phases the VC is better able to withstand attack from the silica erodent than the WC while the Co phase is extremely susceptible to attack which explains its selective removal. The silica erodent initially subjects the WC and VC grains to a low cycle micro-fatigue action until crack initiation begins. With subsequent repeated impacts, fracture and crushing of the grains becomes progressively easier. This effect is more pronounced at higher impact angles than at lower impact angles as was observed in the SEM images where the carbide grains were largely intact at 45°.

Table 7. 6 Hardness ratios for the eroded materials.

H_S/H_1	H_S/H_2	H_S/H_{WC}	H_S/H_{VC}	H_S/H_{Co}
0.88	0.81	0.56	0.40	10.6

The impact stress at higher impact angles is greater than at lower impact angles which causes a higher degree of crack propagation and crack intersection which leads to increased rates of material removal. This is aided by the increase in kinetic energy of the erodents as the impact angle increases. This indicates that

fracture toughness of the material should play a role in determining the erosion response of a material. However the WC-12wt%Co-10wt%VC alloy had a lower fracture toughness than the WC-12wt%Co alloy and yet had a better resistance against erosion. This is because once the tough Co binder has been removed from the material the ability of the material to withstand further erosive wear is more dependent on the ability of the individual carbide grains to withstand individual fracture.

7.4 Spark plasma sintered alloys

7.4.1 Material characterization

The WC-12wt%Co-10wt%VC alloy was successfully sintered at 1100 °C with minimal porosity. No inhomogeneities were found in both alloys; an indication of good and effective milling and mixing conditions. The major problem during sintering was grain growth of the WV_4C_5 phase (see discussion in **section 7.3.1**). The XRD spectra for the alloys **(Figures 6.5)** did not show eta phase and none of the starting VC remained in the sintered alloy. The microstructural characteristics obtained for the alloys in this study agree with those from other authors **[19,45,58-62,67]**. The properties could not be quantitatively compared because the processing parameters as well as some of the compositions were different. The addition of the VC to the SPS alloys led to an improvement in the properties of the alloys in a similar manner to that shown in the conventionally sintered alloys. A higher hardness, lower density and comparable fracture toughness was achieved. The reasons for these improvements are also based on the grain refining properties of the VC.

7.4.2 Friction and sliding wear response of the spark plasma sintered alloys

Table 7.7 shows the friction patterns followed by the ball-alloy sliding pairs during testing. Sliding against the 100Cr steel balls, the WC-12wt%Co alloy

followed patterns II and III while the WC-12wt%Co-10wt%VC alloy followed pattern I (see discussion in **section 7.2.2**).

Table 7. 7 Hypothetical friction patterns obtained for the ball-alloys sliding pair

Spark plasma sintered alloys	**100Cr steel balls**
WC-12wt%Co	II/III
WC-12wt%Co-10wt%VC	I

The coefficients of friction for both alloys were comparable and as such it may be assumed that their sliding wear resistances would be similar. However the sliding wear resistance of the WC-12wt%Co-10wt%VC alloy was better than that of the WC-12wt%Co alloy. This is mainly attributed to the higher hardness of the VC alloy as well as the interaction between the alloys and the ball during sliding.

Table 7.8 lists the respective material property ratios for each ball-alloy sliding pair and the maximum stress experienced during sliding.

Table 7. 8 Summary of the E/H ratio, the H_b/H_a ratio and the applied stress for the SPS alloys sliding against the 100Cr steel ball.

Spark plasma sintered alloys	**E/H**	**H_b/H_a**	**Applied stress (MPa)**
WC-12wt%Co	0.50	0.61	20
WC-12wt%Co-10wt%VC	0.44	0.44	18

From **Table 7.8**, based on the applied stress during sliding and the H_b/H_a ratio, it is expected that the WC-12wt%Co alloy should experience more wear than the WC-12wt%Co-10wt%VC alloy. **Figure 6.10** supports this expectation. However the E/H ratios predict that the WC-12wt%Co-10wt%VC alloy should wear by more cutting than ploughing compared to the non-VC alloy and hence have a

higher wear rate. SEM analysis of the worn surfaces **(Figure 6.10)** did not support this. Therefore in the present sliding system, based on this evidence the H_b/H_a ratio is more reliable than the E/H ratio to predict wear performance.

The wear mechanisms were found to be similar to those observed for the conventionally sintered alloys (see **section 7.3.2**).

7.4.3 Slurry wear response of the spark plasma sintered alloys

For both alloys, the highest erosion rate was recorded at the normal impact angle (90°) and the lowest erosion rate was at 45°. Similar occurrence observed from the conventionally sintered alloys was also observed with the spark plasma sintered alloys. Although the VC grains did not show severe damage compared to the WC grains, however, the erosion rate of the WC-12wt%Co alloy was lower than that of the WC-12wt%Co-10wt%VC alloy at all tested angles. The reason here could be that the larger WC grain in the WC-12wt%Co alloy resist erosion better than the finer grains in the WC-12wt%Co-10wt%VC alloy. Finer grains could easily fell out sooner after the removal of the cementing binder and/or carried away with the binder. The possibility could also be a result of the short sintering time and/or low sintering temperature.

The relationship between the hardness of the silica (H_S) erodent and the hardness of the alloys (H_1, H_2) and the individual phases (H_{WC}, H_{VC}, H_{Co}) are listed in **Table 7.9**, with H_1 and H_2 representing the hardness of WC-12wt%Co and WC-10wt%VC-12wt%Co alloys respectively.

Table 7. 9 Hardness ratios for the eroded materials.

H_S/H_1	H_S/H_2	H_S/H_{WC}	H_S/H_{VC}	H_S/H_{Co}
0.85	0.77	0.56	0.40	10.6

As discussed in **section 7.3.2**, and based on the ratios of the individual phases the VC is better able to withstand attack from the silica erodent than the WC and the Co phase. The ratios from **Table 7.9** also suggested that the WC-12wt%Co alloy suffer more wear compared to the WC-12wt%Co-10wtVC alloy however this was not the case. As the impact angle increases, the kinetic energy of the erodent also increases which in turn increases the impact stress. This leads to a higher degree of crack propagation and crack intersection, hence an increase in material removal. This indicates that fracture toughness of the material should play a role in determining the erosion response of a material. The fracture toughness of the WC-12wt%Co alloy is better than that of the WC-12wt%Co-10wt%VC alloy (14.6 compared to 9.6 $MPa.m^{0.5}$, see **Table 6.5**), hence this explains why the erosion response of the WC-12wt%Co was superior to that of the WC-12wt%Co-10wt%VC alloy.

7.5 Conventionally sintered alloys vs. spark plasma sintered alloys

A comparison of the alloys manufactured by the two different sintering techniques is provided based on the result obtained during this study. **Table 7.10** is a comparison of the material properties for the conventionally sintered alloys and the spark plasma sintered alloys.

Table 7. 10 Comparison of the properties between the conventionally sintered alloys and the spark plasma sintered alloys.

Properties	**Conventionally sintered alloys**		**Spark plasma sintered alloys**	
	WC-12wt%Co	WC-12wt%Co-10wt%VC	WC-12wt%Co	WC-12wt%Co-10wt%VC
Density (g/cm^3)	14.3 ± 0.06	12.3 ± 0.10	13.8 ± 0.1	12.1 ± 0.0
Porosity (%)	0.03 ± 0.01	0.06 ± 0.01	1.4 ± 1.9	0.6 ± 0.8
Hardness (HV30)	1280 ± 2.1	1390 ± 7.8	1319 ± 8	1461 ± 9

Fracture toughness ($MPa.m^{0.5}$)	12.8 ± 1.0	11.3 ± 0.5	14.6 ± 0.8	9.6 ± 0.2
Coercivity (kA/m)	7.33	9.00	9.21	9.78
WC grain size (μm)	2.96	2.09	2.22	1.94
Young's modulus (GPa)	682	570	664	648
Poisson ratio	0.22	0.23	0.18	0.26

The densities of the alloys from the conventional sintering were 2-3% higher than those from the spark plasma sintering. The reason for the increased density in the conventionally sintered alloy is due to the longer processing time which is approximately 12 - 14 hours while in spark plasma sintering the sintering time is extremely short; only about 20 min. The lower SPS density could be seen as a weight saving as well as an energy saving application. However the effect of the low density on material performance should be considered. The sintering times also led to lower porosities in the conventionally sintered alloys.

Despite the lower densities and higher porosity levels the spark plasma sintered alloys produced a better hardness than the conventionally sintered alloys, with an increase of 3% in the WC-12wt%Co alloy and an increase of 5% in the WC-12wt%Co-10wt%VC alloy. The better hardness from the spark plasma sintered alloys could be a result of the reduction in the carbide grain size and the amount of retained carbide grains (see **Tables 5.5** and **6.5**), which are all a function of the processing parameters. Due to the short sintering time in the spark plasma sintering technique, there was no/less time for the grain growth in the WC-12wt%Co alloy and the addition of the VC also helps to minimize grain growth in the WC-12wt%Co-10wt%VC alloy.

The fracture toughness of the alloys from the two sintering techniques did not show consistent results. The spark plasma sintered WC-12wt%Co alloy had a far better toughness compared to the conventionally sintered alloy (an increase of

12%), while the toughness of the conventionally sintered WC-12wt%Co-10wt%VC alloy was better (15%) than that of the spark plasma sintered alloy. Fracture toughness of WC-Co alloys increase as binder phase volume fraction, mean carbide grain size, and binder phase mean free path are increased, while increased carbide contiguity causes a decrease in the fracture toughness **[146]**. The interaction of these parameters with the sintering conditions could have resulted in the differences observed between the fracture toughness from the two techniques. The increase in toughness for these alloys could also be due to the lower modulus of elasticity **[147]**.

Comparing the Young's modulus of the alloys from the two techniques, the conventionally sintered WC-12wt%Co alloy had a higher modulus compared to the spark plasma sintered alloy (an increase of 3%). The Young's modulus of the spark plasma sintered WC-12wt%Co-10wt%VC was 12% higher than that of the conventionally sintered alloy. The role of residual stresses in cemented carbide, irrespective of microscopic or macroscopic origin, is very important in deformation. Microscopic residual stresses are present as a result of differences in the coefficient of thermal expansion between the phases. After cooling from the sintering temperature, the WC phase is under a state of compression **[1]**. Hence, the reason for these differences could be a result of the residual stress in the alloys, as a result of the differences in the sintering techniques.

Under the sliding wear examinations, the conventionally sintered WC-12wt%Co alloy performed better than that of the spark plasma sintered WC-12wt%Co alloy with an increase in sliding wear resistance of about 13%, whereas, the spark plasma sintered WC-12wt%Co-10w%VC alloy showed an increase of about 7% lower compared to the conventionally sintered WC-12wt%Co-10wt%VC alloy. The reason for these occurrences had been given in **sections 7.3.2** and **7.4.2**. The erosion response of the conventionally sintered WC-12wt%Co alloy was found to be toughness controlled mechanism.

The slurry wear response of the conventionally sintered WC-12wt%Co alloy increased by 7% compared to that of the spark plasma sintered WC-12wt%Co alloy. The wear response of the spark plasma sintered WC-12wt%Co-10wt%VC alloy is superior at higher angle to that of the conventionally sintered alloy (about 50%). The reason for this could be found in **sections 7.3.3** and **7.4.3**.

From the properties above, the choice of which technique is better will best be answered based on the application of the alloy. If the manufacturer is interested in weight saving application and energy saving and could afford to compromise some properties, then the spark plasma is an option. This could also be due to the lower density and higher porosity of the VC alloy which makes it more susceptible to impact damage and hence higher material removal rates.

7.6 The role of 10wt%VC in the materials

It was evident that the presence of VC played different roles in the materials (coatings and sintered alloys) in this study including improving the hardness, lowering the density and generally improving the wear resistance. The addition of VC to WC-Co materials is usually done in small quantities (up to 1 wt%) to inhibit grain growth during sintering **[37-38]**, and higher additions up to 2.5 wt% have been reported to cause embrittlement **[37]**. In this study it has been shown that an addition of 10wt%VC to WC-Co materials can prevent WC grain growth and serve as a partial replacement for the expensive WC. The VC does all this in addition to having a weight saving attribute due its lower density.

8. Conclusions

8.1 General conclusions

The conclusions that can be drawn from the present investigation are based on the result obtained. In general, the addition of 10wt%VC to WC-Co produced a material with a better hardness, comparable toughness and a less dense material for weight saving applications, thus making VC a good substitute for WC. The VC led to WC grain refinement in both coatings and sintered materials. None of the starting VC from the powders remained in the produced materials, as the VC formed the WV_4C_5 phase. The presence of the WV_4C_5 phase resulted in a higher hardness. Despite a poorer wettability of the VC by Co compared to WC, the porosity in the WC-Co-VC materials was minimal. The XRD spectra of the WC-Co-VC materials did not show any eta phase. The wear performance of the materials was generally improved with the addition of the VC with minor exceptions. The wear mechanisms in the sliding wear and slurry erosion wear systems were found to be similar for all three material types. The mechanisms included binder removal, adhesion, smearing, carbide grain cracking, grain pull-out, and formation of thin tribo-films. There were however, certain differences in the materials produced in this study and the main aspects are concluded in the following sections.

8.2 Coatings

The addition of VC to the WC-12wt%Co coatings did not have much impact on the hardness of the coating. However the addition of VC to the 17wt%Co coatings caused an increase in the hardness of these coatings. The reason for the different responses is probably due to the optimized conditions used for the 17wt%Co coatings.

The friction response was dependent on the ball-coating pair. The 100Cr steel balls produced higher coating wear rates than the WC-Co balls. The wear response of the VC-coatings varied in that the addition of VC improved the wear resistance when sliding against the 100Cr steel balls, but did not improve the wear resistance when sliding against the WC-Co balls. Therefore the addition of VC to WC-Co coatings in order to improve sliding wear resistance appears to be system dependent.

Under slurry erosion conditions the VC addition improved the erosion response, while a further improvement was observed at higher impact angles when the Co content was increased from 12wt% to 17wt%. The ability of the carbide phases to resist impact appeared to be the erosion rate controlling mechanism once the Co binder had been selectively removed.

8.3 Conventionally sintered alloys

Although the addition of VC to WC-12wt%Co produced a better hardness in this alloy, the sliding wear response of the WC-12wt%Co alloy was superior. This was due to the lower Young's modulus of the VC alloy which allowed greater penetration during sliding leading to higher material removal rates. An additional reason may be due to the fact that both materials were sintered using the same sintering conditions, namely the commercial one used for the WC-12wt%Co alloy. This sintering condition may not be optimum for the VC alloy.

Under slurry erosion conditions the wear response of the alloys followed two trends. The WC-12wt%Co alloy performed marginally better at low impact angles while the WC-12wt%Co-10wt%VC performed better at high impact angles. At higher impact angles, the WC grains were subjected to more severe fragmentation

than the VC carbides based on the hardness differences between erodent and carbide phase. This led to higher material removal rates for the non-VC alloy.

8.4 Spark plasma sintered alloys

The addition of VC to the WC-12wt%Co alloy produced a better hardness and moderate fracture toughness and this resulted in a superior sliding wear response of the WC-12wt%Co-10wt%VC alloy compared to the WC-12wt%Co alloy. However under slurry erosion conditions the WC-12wt%Co alloy showed a better wear response. This is likely due to the lower density and higher porosity of the VC alloy which makes it more susceptible to impact damage and hence higher material removal rates.

9. Recommendations

In view of the conclusions from the present investigations, the following future work is hereby recommended

- The WC and VC starting powders should be replaced with (W,V)C powder and the result compared.
- This study limits the VC content to 10wt%, this amount should be varied say from 0wt% to about 12.5wt% to find the best composition with optimum properties of VC content that can replace WC, without compromising the properties.
- Corrosion experiments should be performed on the new materials, by varying the corrosive environment.
- Further study using TEM should be performed on the new materials.
- The new materials need to be tested under other wear situations, for example three body abrasion, so as to verify if there is an improved wear resistance.
- Further optimization work needs to be done in areas where the wear resistance of the new materials is lacking.

References

1. G.S. Upadhyaya. Cemented Tungsten Carbides - Production, Properties, and Testing. Noyes Publications, Westwood, New Jersey, USA 1998.
2. H. Engqvist, G.A. Botton, S. Ederyd, M. Phanuel, J. Fondelius, and N. Axên. Wear phenomena on WC-based face seal rings, International Journal of Refractory Metals and Hard Materials, 18, (2000), 39 – 46.
3. R. Edwards. Cutting Tools. Institute of Materials, (1993), 200.
4. S.Z.D. Luyckx. Nucleation and propagation of fracture in WC-Co alloys. PhD Thesis. (1967). University of the Witwatersrand, Johannesburg.
5. P. Schwarzkopf. Deutsche Edelstahl Werke AG, German Patent 720502 (Patented 1929, issued 1942).
6. K. Schroter. – German Patent – No. 420, (1923) 689.
7. F.J. Arenas, A. Matos, M. Cabezas, C. Di Rauso, and C. Grigorescu. Densification, mechanical properties and wear behavior of WC-VC-Co-Al hardmetals. International Journal of Refractory Metals and Hard Materials, 19, (2001)381 – 387.
8. S.K., Bhaumik, G.S. Upadhyaya and M.L. Vaidya. Microstructure and mechanical properties of WC-TiN-10Co and WC-TiN-Mo2C-Co(Ni) cemented carbides. Ceramics International, 18, (1992) 327 – 336.
9. T. Viatte, S. Bolognini, T. Cutard, G. Feusier, D. Mari and W. Benoit. Investigation into the potential of a composite combining toughness and plastic deformation resistance. International Journal of Refractory Metals and Hard Materials, 17, (1999) 79 – 89.
10. H. Suzuki and H. Matsubara. Some properties of Ti(C,N)-WC-Ni alloy. Journal of Japan Society of Powder Metallurgy, 33(4), (1986) 199 – 203.
11. P. Lindhal, T. Mainert, H. Jonnson and H.O. Andren. Microstructure and mechanical properties of a (TiC, Ta, Mo) (CN)-(Co, Ni)-type cermet. Journal of. Hard Materials, 4, (1993) 187 – 204.
12. K.J.A. Brookes (Ed.). Hardmetals and other hard materials. 6th edition (1997) UK: International Carbide Data.
13. S.A. Cho, A. Hernandez, J. Ochoa and J. Lira. Phase relations, microstructure and mechanical properties of VC substituted WC-10Co

cemented carbide alloys. International Journal of Refractory Metals and Hard Materials, 15, (1997) 205 – 214.

14. F. Arenas, I.B de Arenas, J. Ochoa, and S.A Cho. Influence of VC on the microstructure and mechanical properties of WC-Co sintered cemented carbides. International Journal of Refractory Metals and Hard. Materials, 17, (1999) 91 – 97.
15. S. Luyckx, C. Osborne, L.A. Cornish and D. Whitefield. Fine grained WC-VC-Co hardmetal. Powder Metallurgy, 39 (3), (1996) 210 – 212.
16. F. Arenas, G. Darias, I.B de Arenas, J. Ochoa, and S.A Cho. Anatypical microstructure in WC-Co cemented carbides. In: Proceedings of the Powder Metallurgy & Particulate Materials (PM2 Tec 99) Vancouver, Canada: MPIF eds. No. 10, (1999) 169 – 177.
17. C. Osborne, L. Cornish and S. Luyckx. On the preparation of fine V_8C_7-WC and V_4C_3-WC powders. International Journal of Refractory Metals and Hard Materials, 15, (1997) 163 – 168.
18. S. Luyckx. Vanadium carbide in hardmetals. XVth CMMI Congress, Johannesburg, SAIMM, 2, (1994) 11 – 13.
19. S.G. Huang, K. Vanmeensel, L. Li, O. Van der Biest and J. Vleugels. Influence of starting powder on the microstructure of WC-Co hardmetals obtained by spark plasma sintering. Materials Science and Engineering, 475, (2008) 87 – 91.
20. L. Sun, C. Jia, C. Lin and R. Cao. VC Addition Prepared Ultrafine WC-11Co Composites by Spark Plasma Sintering. Proceedings of Sino-Swedish Structural Materials Symposium, (2007) 85 – 89.
21. D.M. Hulbert, D.J. Jiang, D.V. Dudina and A.K. Mukherjee. The synthesis and consolidation of hard materials by spark plasma sintering. International Journal of Refractory Metals and Hard Materials, 27, (2009) 367 – 375.
22. Cobalt monograph – Ed. By Centre d‟Information du Cobalt, Brusseles (1960).

23. K.G. Budinski, M.K. Budinski. Engineering Materials, Properties and Selection, 7th Edition, Prentice Hall, (2002), Upper Saddle River, New Jersey Columbus, Ohio.
24. A. Mortensen. Concise Encyclopaedia of Composite Materials – 2nd Edition, Elsevier, (2007), Oxford, UK.
25. A.T. Santhanam, P. Tierney and J.L. Hunt. Metal's Handbook, 10th Edition 2 (1990), 950 – 977.
26. E. Isakov. Cutting data for turning of steel. Industrial Press Inc., (2009) New York, USA.
27. H.C. Lee and J. Gurland. Hardness and deformation of cemented tungsten carbide. Materials Science and Engineering 33, (1978) 125 – 133.
28. D.K. Shetty, I.G. Wright, P.N. Mincer and A.H. Clauer. Indentation fracture of WC-Co cermets. Journal of Materials Science 20, (1985) 1873 – 1882.
29. V. Richter and M.V. Ruthendorf. Hardness and toughness of ultrafine and nanocrystalline hard materials. International Journal of Refractory Metals and Hard Materials 17, (1999) 141 – 152.
30. J.L. Chermant and F. Osterstck. Fracture toughness and fracture of WC-Co composites. Journal of Material Science 11, (1976) 1939 – 1951.
31. R. Warren and B., Johannesson. The Fracture Toughness of Hardmetals. International Journal of Refractory Metals and Hard Materials 3, (1984) 187 – 191.
32. D.G.F. O'Quigley, S. Luyckx, M.N. James. New results on the relationship between hardness and fracture toughness of WC-Co hardmetal. Materials Science and Engineering A209, (1996) 228 – 230.
33. S. Okamoto, Y. Nakazono, K. Otsuka, Y. Shimoitani and J. Takada. Mechanical properties of WC-Co cemented carbide with larger WC grain size. Materials Characterization 55, (1995) 281 – 287.
34. M.S.A. Khan and T.W. Clyne. Microstructure and abrasion resistance of plasma sprayed cermet coatings. In: Thermal Spray: Practical solutions for Engineering Problems, C.C Berndt (Ed), ASM Int. (Pub) Materials Park, Ohio-USA, (1996) 113 – 122.

35. H.E Exner and J.A Gurland. A review of parameters influencing some mechanical properties of tungsten carbide cobalt alloys. Powder Metallurgy 13, (1970) 13 – 31.
36. K. Bonny, P. De Baets, Y. Perez, J. Vleugels, and B. Lauwers. Friction and wear characteristics of WC-Co cemented carbides in dry reciprocating sliding contact. Wear, 268 (2010), 1504 – 1517.
37. W. Mader, R. Kieffer, H. Nowotny and P. Ettmayer. The pseudo-quaternary system WC-TaC-TiC-VC and VC containing cemented carbides. International Journal of Powder Metallurgy and Powder Technology, 13(1), (1977) 41 – 49.
38. G.E. Spriggs. A history of fine grained Hardmetals. International Journal of Refractory Metals and Hard Materials, 13 (1995) 241 – 255.
39. D.J. Whitefield. The optimisation and evaluation of WC-VC-Co Hardmetals. PhD Thesis, (2011), University of the Witwatersrand Johannesburg.
40. S. Luyckx. (V,W)C-based hardmetal and its resistance to wear and erosion, proceed. Powder Metallurgy World Congress, Paris. Vol. 1, (1994) 169 – 171.
41. D.J. Whitefield, S. Luyckx,, M.J Witcomb, L.A. Cornish. Microstructure and properties of fine grained WC-VC-Co hardmetal with cobalt content ranging from 10 to 15 wt%. Proceedings of the 14th International Plansee Seminar, G Kneringer, P Rodhammer and P Wilharitz (Eds.) Plansee AG, Reutte, 2, (1997) 477 – 484.
42. J. Zinyana. An investigation of the C-Co-V-W phase diagram. MSc dissertation, (2000) University of the Witwatersrand, Johannesburg.
43. E.G. Obbard, S. Luyckx, S. Hamar-Thibault and C.H. Allibert. Determination of the composition range suitable to the formation of WC-(V,W)C_x-Co materials. International Journal of Refractory Metals and Hard Materials, 19, (2001) 349 – 357.
44. D. du Randt, S. Luyckx, D. Markoulides, I.T. Northrop, D.J. Whitefield. A comparison between ultrafine WC-Co and fine WC-VC-Co alloys.

International Journal of Materials and Product Technology, 15(3/4/5), (2000) 270 – 274.

45. W. Liu, X. Song, K. Wang, J. Zhang, G. Zhang, and X. Liu. A novel rapid route for synthesizing WC-Co bulk by in situ reactions in spark plasma sintering. Materials Science and Engineering A 499, (2009) 476 – 481.
46. S.I. Cha, S.H. Hong, B.K. Kim. Spark plasma sintering behavior of nanocrystalline WC-10Co cemented carbide powders. Materials Science and Engineering A351, (2003) 31 – 38.
47. R. Chaim. Densification mechanisms in spark plasma sintering of nanocrystalline ceramics. Materials Science and Engineering A 443, (2007) 25 – 32.
48. P. Arato, L. Bartha, R. Porat, S. Berger, A. Rosen. Solid or liquid phase sintering of nanocrystalline WC/Co hardmetals. Nanostructure Materials 10, (1998) 245 – 255.
49. C. Jia, L. Sun, H. Tang, X. Qu. Hot pressing of nanometer WC-Co powder. International Journal of Refractory Metals and Hard Materials, 25, (2007) 53 – 56.
50. L.J. Prakash. Application of fine grained tungsten carbide based cemented carbide. International Journal of Refractory Metals and Hard Materials, 13, (1995) 257 – 264.
51. I. Azcona, A. Ordonez, J.M. Sanchez, F. Castro. Hot isostatic pressing of ultrafine tungsten carbide-cobalt hardmetals. Journal of Materials Science, 37, (2002) 4189 – 4195.
52. H.C. Kim, I.J. Shon, J.K. Yoon, J.M. Doh. Consolidation of ultrafine WC and WC-Co hard materials by pulsed current activated sintering and its mechanical properties. International Journal of Refractory Metals and Hard Materials, 25, (2007) 46 – 52.
53. H.C. Kim, I.J. Shon, and Z.A. Munir. Rapid sintering of ultra-fine WC–10wt%Co by high-frequency induction heating. Journal of Materials Science, 40, (2005) 2849 – 2854.
54. B. Huang, L.D. Chen, S.Q. Bai. Bulk ultrafine binderless WC prepared by spark plasma sintering. Scripta Materialia 54, (2006) 441 – 445.

55. M. Rosinski, E. Fortuna, A. Michalski, Z. Pakiela, K.J. Kurzydlowski. W/Cu composites produced by pulse plasma sintering technique (PPS). Fusion and Engineering Design, 82, (2007) 2621 – 2626.

56. J. Zhang, L. Wang, W. Jiang and L. Chen. Effect of TiC content on the microstructure and properties of Ti_3SiC_2-TiC composites in situ fabricated by spark plasma sintering. Materials Science and Engineering A 487, (2008) 137 – 143.

57. H.V. Atkinson and S. Davies. Fundamental aspects of hot isostatic pressing: An overview. Metallurgical and Materials Transaction A 31, (2000) 2981 – 3000.

58. C. Jia, H. Tang, X. Mei, F. Yin, and X. Qu. Spark plasma sintering on nanometer scale WC–Co powder. Materials Letters 59, (2005) 2566 – 2569.

59. S. Zhao, X. Song, C. Wei, L. Zhang, X. Liu, and J. Zhang. Effects of WC particle size on densification and properties of spark plasma sintered WC–Co cermet. International Journal of Refractory Metals and Hard Materials, 27, (2009) 1014 – 1018.

60. J.A. Picas, Y. Xiong, M. Punset, L. Ajdelsztajn, A. Forn, and J.M. Schoenung. Microstructure and wear resistance of WC–Co by three consolidation processing techniques. International Journal of Refractory Metals and Hard Materials, 27, (2009) 344 – 349.

61. D. Sivaprahasam, S.B. Chandrasekar, R. Sundaresan. Microstructure and Mechanical Properties of Nanocrystalline WC-12Co Consolidated by Spark Plasma Sintering. International Journal of Refractory Metals and Hard Materials, 25, (2007) 144 – 152.

62. S.G. Huang, K. Vanmeensel, L. Li, O. Van der Biest, J. Vleugels. Tailored sintering of VC-doped WC-Co cemented carbides by pulsed electric current sintering. International Journal of Refractory Metals and Hard Materials, 26, (2008) 256–262.

63. M.H. Poech, S. Isfahani and H. Opielka. Size distribution analysis of powders used for thermal spraying. Powder Metallurgy Industry, 25(5), (1993) 233 – 237.

64. V. Rajinikanth, K. Venkateswarlu. An investigation of sliding wear behaviour of WC–Co coating. Tribology International, 44 (2011), 1711 – 1719.

65. A. Karimi and Ch. Verdon. Hydro-abrasive wear behaviour of high velocity oxy-fuel thermally sprayed WC-M coatings, Surface Coatings Technology, 62, (1993) 493 – 498.

66. H.J. Kim, Y.G. Kweon and R.W. Chang. Wear and erosion behaviour of plasma sprayed WC-Co coatings. Journal of Thermal Spray Technology, 3(2), (1994) 169 – 178.

67. L. Sun, T. Yang, C. Jia, and J. Xiong. VC, Cr_3C_2 doped ultrafine WC–Co cemented carbides prepared by spark plasma sintering. International Journal of Refractory Metals and Hard Materials, 29, (2011) 147 – 152.

68. J.M. Perry, T. Hodgkiess, and A. Neville. Some aspects of the erosion and corrosion behaviour of a WC-Co-Cr HVOF sprayed coating. In: Thermal Spray: Surface Eng. Via applied research, Proc. 1st ITSC, Montreal, Canada, 8 – 11 May, CC Berndt (Ed.), ASM Int. (Pub.) (2000) 1033 – 1038.

69. M. Dorfman, J. DeFalcon and J. Karthikeyan. Tungsten carbide-cobalt coatings for industrial applications. In: Thermal Spray: Surface Eng. Via applied research, Proc. 1st ITSC, Montreal, Canada, 8 – 11 May 2000, CC Berndt (Ed.), ASM Int. (Pub.) pp. 471 – 478.

70. C.N. Machio. Preparation, characterization and testing of WC-VC-Co HP/HVOF thermal spray coatings. PhD Thesis, (2005), University of the Witwatersrand, Johannesburg.

71. H.J. Howse and P. van Wyk. The application of thermal spray coatings for combating slurry erosion in centrifugal pumps. 6th International Tribology Conference of South African Institute of Tribology, SAIT (1998) 27 – 33.

72. Stan Grainger (Ed.). Engineering coatings – design and application. Abington Publishing (Pub.) (1989) Woodhead Publishing Ltd.

73. L.M. Berger, W. Hermel, P. Vuoristo, T. Mantyla, W. Lengauer and P. Ettmayer. Structure, properties and potentials of WC-Co, Cr_3C_2-NiCr and TiC-Ni-based hardmetal-like coatings. In Thermal Spray: Practical

Solutions for Engineering Problems, CC Berndt (Ed.) ASM Int. (Pub) Materials Park, Ohio-USA, (1996) 89 – 96.

74. M.E. Vinayo, F. Kassabji, J. Guyonnet, and P. Fauchais. Plasma sprayed WC-Co coatings: Influence of spray conditions (atmospheric and low pressure plasma spraying) on the crystal structure, porosity and hardness, Journal of Vacuum Science Technology, A3(6), (1985) 2483 – 2489.
75. T.P. Slavin and J. Nerz. Material characteristics and performance of WC-Co wear resistant coatings. In: Thermal spray research and applications, Proc. 3rd National Thermal Spray Conf. Long Beach, CA USA, 20 – 25 May, (1990) 159 – 164.
76. H. Kreye, R. Schwetzke, and S. Zimmermann. High velocity oxy-fuel flame spraying process and coating characteristics. In: Thermal Spray: Practical solution for engineering Problems, CC Berndt (Ed), AST Int. (Pub) Materials Park, Ohio-USA, (1996) 451 – 456.
77. L. Pawlowski. The science and engineering of thermal spray coatings. John Wiley & Sons, 2nd Edition, (2008) England.
78. K.E. Schneider, V. Belashchenko, M. Dratwinski, S. Siegmann and A. Zarorski. Thermal spray for power generation components. Wilecy-VCH Verlag GmbH & Co., KGaA, Weinheim 2006.
79. http://www.fst.nl/hvof-high-velocity-oxygen-fuel/. – accessed 15/10/2012.
80. L.M. Berger, P. Vuoristo, T. Mantyla, W. Kunert, W. Lengauer, P. Ettmayer. Microstructure and properties of WC-Co-Cr coatings. In: Thermal Spray: Practical Solutions for Engineering Problems, CC Berndt (Ed.) ASM Int. (Pub) Materials Park, Ohio-USA, (1996) 97 – 106.
81. S.Y. Hwang, B.G. Seong and M.C. Kim. Characterization of WC-Co coatings using HP/HVOF process. In: Thermal Spray: Practical Solutions for Engineering Problems, CC Berndt (Ed.) ASM Int. (Pub) Materials Park, Ohio-USA, (1996) 107 – 112.
82. D.J. Varacalle Jnr., G.R. Smolik, G.C. Wilson, G. Irons and J.A. Walter in Protective Coatings. Processing and Characterization, R.M Yazici (Ed.), MMM Soc. (1990) 121 – 133.

83. V. Ramnath and N. Jayaraman. Characterization and wear performance of plasma sprayed coatings, Journal of Materials Science and Technology, 5, (1989) 382 – 388.

84. B. Schultrich, L.M. Berger, J. Henke and A. Oswald. Influence of carbide powder composition on decarburization during APS. Proc. 2nd Plasma – Technik – Symposium, Sulzer Metco AG, Rigackerstrasse 16, CH -5610 Wohlen, Switzerland (Pub.), 2, (1990) 363 – 371.

85. H.L. de Villiers-Lovelock, J. Kinds and P.M. Young. Characterization of WC-12Co thermal spray powders and HP/HVOF wear resistant coatings. Journal of Powder Metallurgy, 41(4), (1998) 292 – 299.

86. C.J. Li, A. Ohmori and Y. Harada. Effect of powder structure on the structure of thermally sprayed WC-Co coatings. Journal of Materials Science, 31, (1996) 785 – 794.

87. Y. Arata, A. Ohmori and E. Gofuku. WC-Co high energy thermal spray coatings – structures and mechanical properties. Trans. JWRI, 14(2), (1985) 267 – 273.

88. M.R. Dorfman, B.A. Kushner, J. Nerz and A.J. Rotolico. A technical assessment of high velocity oxygen-fuel versus high energy plasma tungsten carbide-cobalt coatings for wear resistance. Proc. 12th Int. Thermal Spray Conf., London, I.A. Bucklow (Ed.) (1998) P108 1 – 12.

89. P. Vuoristo, K. Niemi, T. Mantyla, L.M. Berger, and M. Nebelung. Comparison of different hard metal like coatings sprayed by plasma and detonation gun processes. Proc. 8th National Thermal Spray Conf., Houston, Texas, (1995) 309 – 315.

90. K. Korpiola and P. Vuoristo. Effect of HVOF gas velocity and fuel to oxygen ratio on the wear properties of tungsten carbide coating. In Thermal Spray: Practical solution for engineering Problems, CC Berndt (Ed), AST Int. (Pub) Materials Park, Ohio-USA, (1996) 177 – 184.

91. D.A. Stewart, P.H. Shipway and D.G. McCartney. Microstructure evolution in thermally sprayed WC-Co coatings: Comparison between nanocomposite and conventional starting powders, Acta Mater. 48, (2000) 1593 – 1604.

92. L. Jacobs, M. Hyland and M. de Bonte. Wear behaviour of HVOF and HVAF sprayed WC-cermet coatings. Proc. 15th Int. Thermal Spray Conf. 25 – 29 May Nice, France (1988) 169 – 174.

93. J. Nerz, B. Kushner, and A. Rotolico. Effect of deposition methods on the physical properties of tungsten-carbide-12wt% cobalt thermal spray coatings. In: Protective Coatings: Processing and characterization (Ed) R.M Yaziei, MMM Soc. (1990).

94. J. Nerz, B. Kushner, and A. Rotolico. Characterization of tungsten carbide coatings as a function of powder manufacturing and deposition technologies, in High Performance Coatings: Processing and Characterization (Ed.) R.M Yazici, MMM Soc. (1990).

95. J. Nerz, B. Kushner, and A. Rotolico. Microstructural evaluation of tungsten carbide-cobalt coatings, Journal of Thermal Spray Technology, 1(2), (1992) 147 – 152.

96. D. Ghosh, D. Lamy, T. Sopkow and I. Smuga-Otto. The effect of spray parameters and atmosphere on the properties and microstructure of WC-Co coatings. In: Proc. 24th Int. SAMPLE Technical Conf. Oct. 20 – 22, T.S. Reinhart, M. Rosenow, Ray A. Cull and E. Struckholf (Eds.), (1992) T28 – 42.

97. B. Arsenault, J.G. Legoux, H. Hawthorne, J.P. Immarigeon, P. Gougeon, and C. Moreau. HVOF process optimization for the erosion resistance of WC-12Co and WC-10Co-4Cr coating. In: Thermal Spray 2001; New surface for a new millennium, CC Berndt, K.A Khor, and E.F Lugscheider (Eds), ASM Int. (Pub). Materials Park, Ohio-USA, (2001) 1051 – 1059.

98. H.L. de Villiers-Lovelock, and S. Luckyx. Preliminary investigation of the potential of VC-WC-Co HP/HVOF powders and coatings. In: Thermal Spray: Surface Engineering via Applied Research, Proc. 1st ITSC, Montreal, Canada, 8 – 11 May, C.C Berndt (Ed.) ASM Int. (2000) 647 – 656.

99. M. Factor and I. Roman. A critical evaluation of the employment of microhardness techniques for characterizing and optimizing thermal spray coating. In: Thermal spray; Surface Eng. via Applied Research. Proc. 1st

ITSC, Montreal, Canada, CC Berndt(Ed) ASM. Int. (Pub), Material Park, OH, USA, (2000) 1345 – 1354.

100. V. Rajinikanth and K. Venkateswarlu. An investigation of sliding wear behaviour of WC–Co coating. Tribology International, 44, (2011), 1711 – 1719.

101. Q. Yang, T. Senda, and A. Ohmori. Effect of carbide grain size on microstructure and sliding wear behavior of HVOF-sprayed WC–12% Co coatings. Wear, 254, (2003), 23 – 34.

102. P.H. Shipway, D.G. McCartney, and T. Sudaprasert. Sliding wear behaviour of conventional and nanostructured HVOF sprayed WC–Co coatings. Wear 259 (2005) 820 – 827.

103. T. Sudaprasert, P.H. Shipway, and D.G. McCartney. Sliding wear behaviour of HVOF sprayed WC–Co coatings deposited with both gas-fuelled and liquid-fuelled systems. Wear 255 (2003) 943 – 949.

104. Q. Yang, T. Senda, and A. Hirose. Sliding wear behavior of WC–12%Co coatings at elevated temperatures. Surface & Coatings Technology, 200 (2006) 4208 – 4212.

105. D.Z. Guo and L.J. Wang. Study of fracture and erosive wear of plasma sprayed coatings. Journal of Thermal Spray Technology, 2(3), (1993) 257 – 263.

106. A. Karimi, Ch. Verdon and G. Barbezat. Microstructure and hydroabrasive wear behaviour of high velocity oxy-fuel thermally sprayed WC-Co(Cr) coatings. Surface and Coatings Technology, 57, (1993) 81 – 89.

107. I. Finnie. Erosion of surfaces by solid particles, Wear, 3 (1960) 87 – 103.

108. G.I. Sheldon. Similarities and differences in the erosion behaviour of materials. Journal of Basic Engineering, Trans. ASME, (Sept. 1970) 619 – 626.

109. H.L. de Villiers-Lovelock. The effect of VC additions on the microstructure and wear resistance of WC-Co HP/HVOF thermal spray coatings, MSc dissertation, (2000) University of the Witwatersrand. Johannesburg.

110. K. Bonny, P. De Baets, J. Vleugels, S. Huang, O. Van der Biest, and B. Lauwers. Impact of Cr_3C_2/VC addition on the dry sliding friction and wear response of WC–Co cemented carbides, Wear, 267 (2009), 1642 – 1652.

111. C.N. Machio, G. Akdogan, M.J. Witcomb, and S. Luckyx. Performance of WC-VC-Co thermal spray coatings in abrasion and slurry erosion tests. Wear, 258, (2005) 434 – 442.

112. B. Bhushan, Introduction to Tribology, John Wiley & Sons Inc., (2002) New York.

113. I.M. Hutchings, Tribology: Friction and Wear of Engineering Materials, Edward Arnold, (1992) London.

114. H.D. Young, R.A. Freedman, T.R. Sandin, A. Lewis Ford, Sears and Zemansky's University Physics, 10th edition, (2000) Addison Wesley Longman Inc., San Francisco.

115. G.P. Tilly. Erosion caused by impact of solid particles. In: Treatise on Material Science and Technology, vol. 13, (1977). Academic Press.

116. J.A. Charles, F.A.A, Crane, and J.A.G. Furness. Selection and Use of Engineering Materials, 3rd Edn, (1997) Butterworth-Heinemann.

117. J.K. Lancaster. The influence of substrate hardness on the formation and endurance of molybdenum disulphide films. Wear, 10 (1967), 103 – 107.

118. M. Divakar, V.K. Agarwal, and S.N. Singh. Effect of the material surface hardness on the erosion of AISI 316. Wear, 259, (2005), 110 – 117.

119. J. Paulo Davim. Tribology for Engineer: A practical guide. Woodhead Publishing Limited, USA (2011).

120. N. Sacks and P.Shipway. Private communication, 2011.

121. Bruker AXS. TOPAS V4: General profile and structure analysis software for powder diffraction data. User's Manual, Bruker AXS, Karlsruhe, (2008), Germany..

122. R.W. Cheary, and A.A. Coelho. A fundamental parameters approach to X-ray line-profile fitting. - J. Appl. Cryst., 25 (1992), 109 – 121.

123. R.W. Cheary, A.A. Coelho and J.P. Cline. Fundamental Parameters Line Profile Fitting in Laboratory Diffractometers. J. Res. Natl. Inst. Stand. Technol., 109 (2004), 1 – 25.

124. A. Kern, A.A. Coelho, and R.W. Cheary. Convolution based profile fitting - Diffraction Analysis of the Microstructure of Materials, edited by Mittemeijer, E.J. & Scardi, P. Materials Science, Springer, ISBN 3-540-40510-4, (2004) 17 – 50.
125. A.A. Coelho. Indexing of powder diffraction patterns by iterative use of singular value decomposition. J. Appl. Cryst., 36 (2003), 86 – 95.
126. A.A. Coelho and A. Kern. Discussion of the indexing algorithms within TOPAS. - CPD Newsletter, 32 (2005), 43 – 45.
127. A.A. Coelho. Whole Profile Structure Solution from Powder Diffraction Data using Simulated Annealing. J. Appl. Cryst., 33 (2000), 899 – 908.
128. A.A. Coelho. A charge-flipping algorithm incorporating the tangent formula for solving difficult structures. Acta Cryst., A36 (2007), 400 – 406.
129. H E Exner and H P Hougardy (Ed). Quantitative Image Analysis of Microstructures, A practical guide to techniques, instrumentation and assessment of materials, DGM Informationsgesellschaft mbH (Pub.) (1988).
130. D.K. Shetty and I.G. Wright. On estimating fracture toughness of cemented carbides from Palmqvist crack. Journal of Materials Science Letters, 5, (1986), 365 – 368.
131. M. Mahmoodan, H. Aliakbarzadeh, R. Gholamipour. Microstructural and mechanical characterization of high energy ball milled and sintered WC–10wt%Co–xTaC nano powders, International Journal of Refractory Metals and Hard Materials, 27, (2009), 801 – 805.
132. E.J. Wentzel, and C. Allen. The erosion-corrosion resistance of tungsten-carbide hard metals. International Journal of Refractory Metals and Hard Materials, 15 (1997); 81 – 87.
133. J.B. Zu, I.M. Hutchings, and G.T. Burstein. Design of a slurry erosion test rig. Wear, 140 (1990); 331 – 344.
134. S. De Palo, M. Mohanty, H. Marc-Charles, and M. Dorfman. Fracture toughness of HVOF sprayed WC-Co coatings. In: Thermal Spray: Surface

Engineering via Applied Research, Proc. 1st ITSC, Montreal, Canada, 8 – 11th May, CC Berndt (Ed) AM Int., (Pub), (2000) 245 – 250.

135. L.M. Berger, M. Nebelung, P. Vuoristo and T. Mantyla. Development of TiC-Ni-based hardmetal compositions for thermal spraying. In: Proc. 14th Int. Plansee Seminar, G Kneringer, P. Rodhammer and P. Wilharitz (Eds) Plansee AG, Reutte, 2, (1997) 477 – 484.
136. H.E. Exner. Physical and chemical nature of cemented carbides. International Metals Review, 4, (1979), 149 – 173.
137. D.F. Carrol. Sintering and microstructural development in WC-Co based alloys made with superfine WC powder, International Journal of Refractory Metals and Hard Materials, 17, (1999), 13 – 132.
138. A. Love, S. Luyckx, and N. Sacks. Quantitative relationships between magnetic properties, microstructure and composition of WC–Co alloys. Journal of Alloys and Compounds, 489 (2010); (2), 465 – 468.
139. J. Pirso, M. Viljus, and S. Letunovitš. Friction and dry sliding wear behaviour of cermets, Wear, 260 (2006), 815 – 824.
140. Jorn Larsen-Basse. Binder extrusion in sliding wear of WC-Co alloys. Wear, 105 (1985), 247 – 256.
141. J.F. Shackelford and W. Alexander. CRC Materials Science and Engineering Handbook, 3rd edition (2001), CRC Press.
142. http://www.webelements.com/cobalt/physics.html - accessed 10/05/2013.
143. R. Warren. Microstructural development during the liquid phase sintering of VC-Co alloys. Journal of Materials Science, 7, (1972), 1434 – 1442.
144. A.S. Bolokang, C. Banganayi, S. Luyckx and D.G. Billing. Production by mechanical alloying and characterization of nano-size (W,V)C powder. Vanadium International Technical committee (Vanitec), 2007, www.vanitec.com. – Accessed 14/11/2012.
145. S. Luyckx, D. Whitefield, M. Witcomb and L. Cornish. The development of WC-VC-Co hard metal: A review of past work and new results. Intl. Conf. on Powder Metallurgy and Particulate Materials, Las Vegas, Nevada, USA. 1 (1998) 85 – 91.

146. J. Dusza, L. Parilak, and M. Slesar. Fracture characteristics of ceramic and cermet cutting tools. Ceramics International, 13, (3), (1987), 133 – 137.

147. Lardner, E., and Iggstrom, S. Proc. of 10th Int. Plansee Seminar, (H. M. Ortner, ed.), Vol. 1, Metallwerk Plansee, Reutte, p. 549 (1981).

APPENDICES

APPENDIX A: GENERAL DATA

Appendix A1: Calculation of the equivalence of weight percent and volume fractions of the starting powders

Assumptions

1. Chemical formula for VC was V_8C_7
2. VC dissolved WC to form WV_4C_5 (as shown from XRD analysis)
3. No W, V and C atoms went into solution in the Co.

The volume of each phase was calculated from the mass fractions of the respective phases. **Table A1.1** gives the relative molecular masses of the chemical species and the densities used to convert the phase mass into volume. While the densities of WC, V_8C_7 and Co are known and can be obtained from any book of Physical Properties of Materials, the density of WV_4C_5 was obtained from the XRD reference card. The amount of WC that went into solution in V_8C_7 was determined.

Table A1.1 Relative molecular masses of chemical species

Atomic species	Relative molecular mass (g/mol)	Phase density (g/cm^3)
W	183.85	-
C	12.01	-
V	50.94	-
WC	195.86	15.7
V_8C_7	491.61	5.7
WV_4C_5	447.67	8.038
Co	58.933	8.9

The procedure for calculating the volume fraction for one of the powders is as follows:

To calculate the volume fractions for WC-12Co-10VC powder, the composition (78wt%WC, 12wt%Co and 10wt%VC) implies that each 100 g of the powder contained 10 g of VC.

Step 1: To determine the amount of WV_4C_5 formed

$$\boldsymbol{Moles\ of\ V_8C_7\ in\ 10\ g} = \frac{mass\ of\ V_8C_7}{relative\ molecular\ mass\ of\ V_8C_7} = \frac{10}{491.61}$$
$$= 0.0203\ moles$$

This represents $8 \times 0.0203 = \mathbf{0.1624\ moles\ of\ V}$

$$Possible\ moles\ of\ WV_4C_5\ from\ 0.1624\ moles\ of\ V = \frac{0.1624}{4}$$
$$= \mathbf{0.0406\ moles}$$

0.0406 moles of WV_4C_5 contain 0.0406 moles of W (WV_4C_5)

Therefore,

$$The\ amount\ of\ WC\ that\ forms\ WV_4C_5 = 0.0406 \times 195.86 = \mathbf{7.9519\ g}$$

The mass of WC that does not go into solution $= 78 - 7.9519 = \mathbf{70.0481\ g}$

$$Total\ mass\ of\ WV_4C_5 = mass\ of\ V_8C_7 + mass\ of\ WC\ in\ solution$$
$$= 10 + 7.9519 = \mathbf{17.9159\ g}$$

Step 2: To determine the equivalent volume fraction of the phases

In order to determine the equivalent volume fraction of the individual phases, the procedure shown in **Table A1.2** was adopted.

Table A1.2 Calculation of volume fractions

	Phases		
	WC	**WV_4C_5**	**Co**
Mass (g)	70.0481	17.9159	12
Density (g/cm^3)	15.7	8.038	8.9
Volume (cm^3)	4.46	2.23	1.35
Total volume	4.46 + 2.23 + 1.35 = **8.04**		
Volume fraction	$\frac{4.46}{8.04} = 0.5547$	$\frac{2.23}{8.04} = 0.2774$	$\frac{1.35}{8.04} = 0.1679$
Volume fraction (%)	55.47	27.74	16.79

Appendix A2: Summary of the properties of the balls used in the friction and sliding wear test as supplied by the manufacturer

Table A2. 1 Properties of the balls

		Balls	
Properties	**Unit**	**WC-Co**	**100Cr steel**
Crystallization	-	Poly	Poly
Composition	wt. %	WC(6T10)	-
Purity	%	WC94+Co6	-
Density	g/cm^3	15	-
Hardness	HV	1400	600 -800
Compression strength	N/mm^2	5300	1000
Fracture toughness	$MPa.m^{0.5}$	-	30 – 80
Elasticity constant	GPa	610	200
Thermal expansion	$10^{-6}. K^{-1}$	5.5	10 - 12
Thermal conductivity	W/m.K	50	50

Appendix A3: Derivation of the formulae for the calculation of wear volume of the samples and the balls used in friction and sliding wear test.

The derivations of the equations used to determine the worn substrate and button volumes used in calculating the wear rates given in Section 3.2 by equations 3.10 and 3.11 respectively are given below.

Wear volume of samples, V_s

Assumptions

1. A perfect circle for the wear tracks which results in difference between two circles – inner and outer circles.
2. Worn section produced a maximum penetration depth, Pd_{max}.

$$Wear\ volume = difference\ in\ worn\ area\ \times maximum\ penetration\ depth$$

$$Area\ of\ circle = \pi r^2$$

Where r = radius of circle.

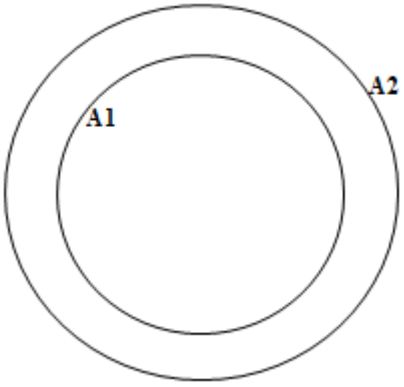


Figure A3. 1 Schematic plan view of the worn track of the samples

Hence, difference in area of the two circles with areas A1 and A2 with radii R1 and R2 respectively, becomes;

$$\Delta A = A_2 - A_1 = \pi R_2^2 - \pi R_1^2 = \pi(R_2^2 - R_1^2)$$

Therefore, the wear volume, V_s, at the maximum penetration depth, Pd_{max}, will be

$$V_s = \pi \times (R_2^2 - R_1^1) \times Pd_{max}$$

Wear volume of ball, V_b

The volume of a spherical segment is given by

$$V = \frac{1}{6} \times \pi \times h \times (3 \times a^2 + 3 \times b^2 + h^2) \qquad A3-1$$

Where a, b, and h are the lower base radius, the upper base radius and the segment height respectively, as shown in Figure A3-2.

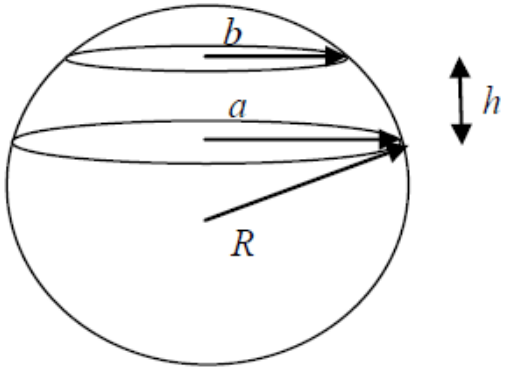


Figure A3. 2 Sketch showing parameters, a, b, h and R of a spherical segment

For a spherical cap, b = 0,

Hence, Equation A3-1 becomes

$$V = \frac{1}{6} \times \pi \times h \times (3 \times a^2 + h^2) \qquad A3-2$$

From Pythagora's theorem,

$$R^2 = a^2 + (R-h)^2 \qquad A3-3$$

$$a^2 = 2Rh - h^2 \qquad A3-4$$

Substituting A3 – 4 into A3 – 2, we have

$$V = \frac{1}{6} \times \pi \times h \times (3 \times (2Rh - h^2) + h^2) \qquad A3 - 5$$

$$V = \frac{1}{6} \times \pi \times h \times (6Rh - 2h^2) \qquad A3 - 6$$

And factorizing like terms,

$$V = \frac{1}{3} \times \pi \times h^2 \times (3R - h) \qquad A3 - 7$$

For the balls, R = Rb. Hence, the wear volume of the ball becomes,

$$V_b = \frac{1}{3} \times \pi \times h^2 \times (3 \times R_b - h) \qquad A3 - 8$$

APPENDIX B: HVOF THERMAL SPRAY COATINGS

Appendix B1: Friction responses

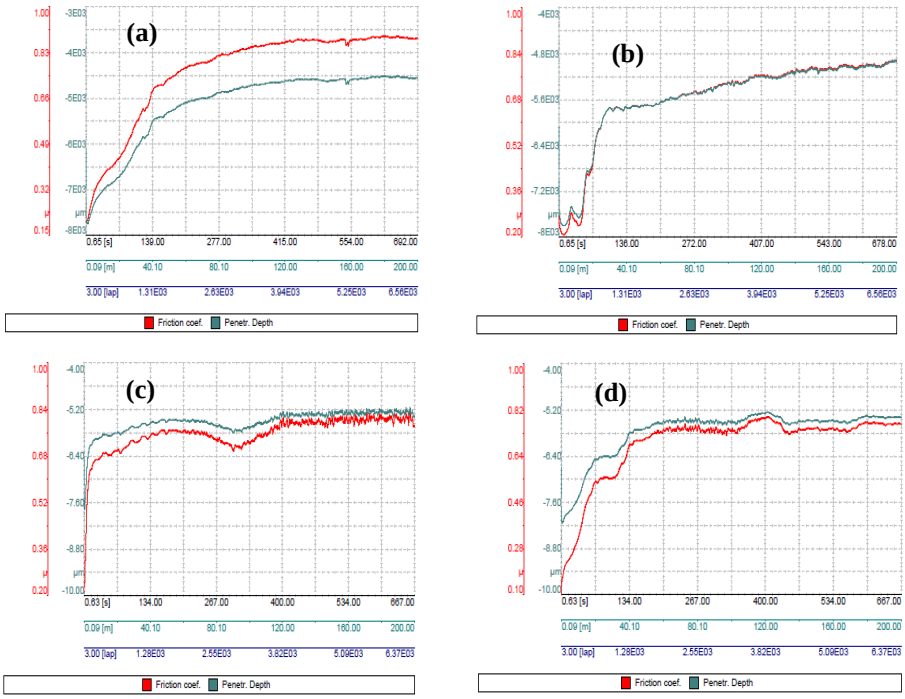


Figure B1. 1 Friction response against 100Cr steel ball against (a) WC-12wt%Co, (b) WC-12wt%Co-10wt%VC, (c) WC-17wt%Co-10wt%VC (Run 38), and (d) WC-17wt%Co-10wt%VC (Run 39) coatings.

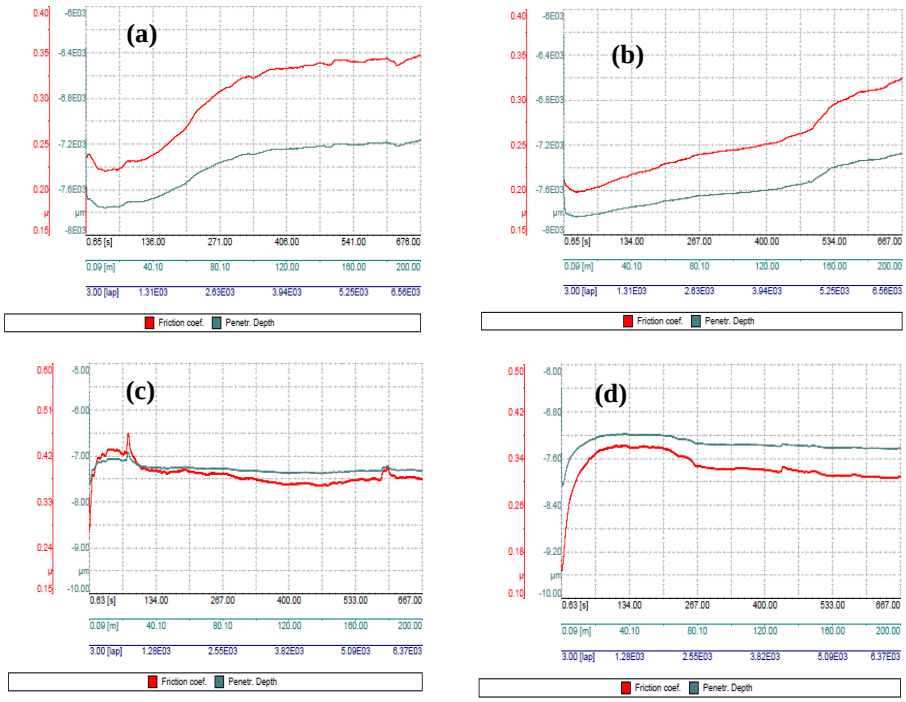


Figure B1. 2 Friction response against WC-Co ball against (a) WC-12wt%Co, (b) WC-12wt%Co-10wt%VC, (c) WC-17wt%Co-10wt%VC (Run 38), and (d) WC-17wt%Co-10wt%VC (Run 39) coatings.

Appendix B2: SEM images of the wear tracks

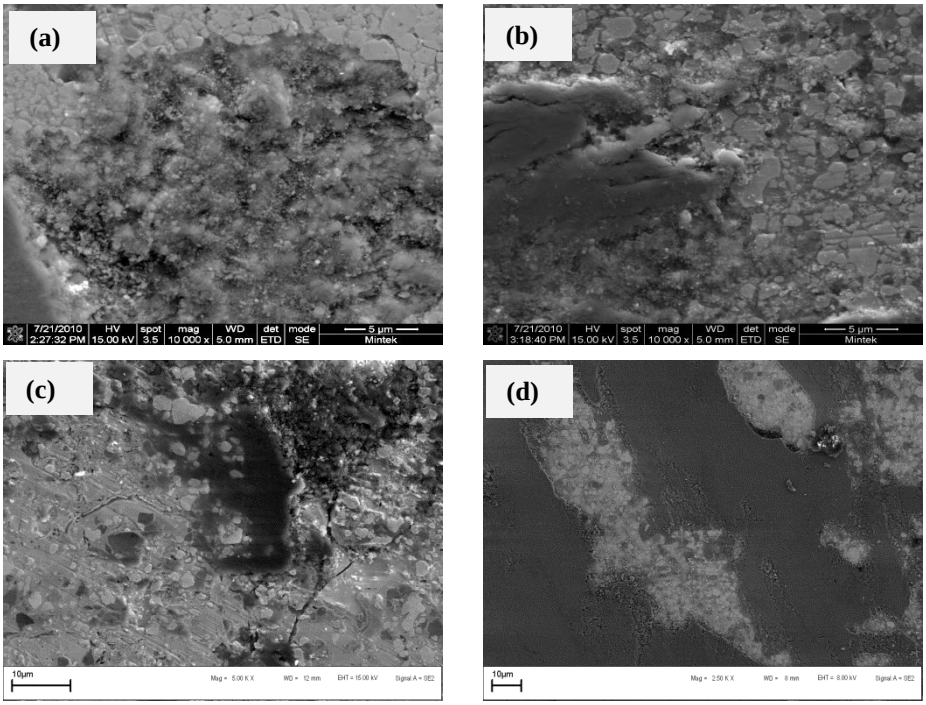
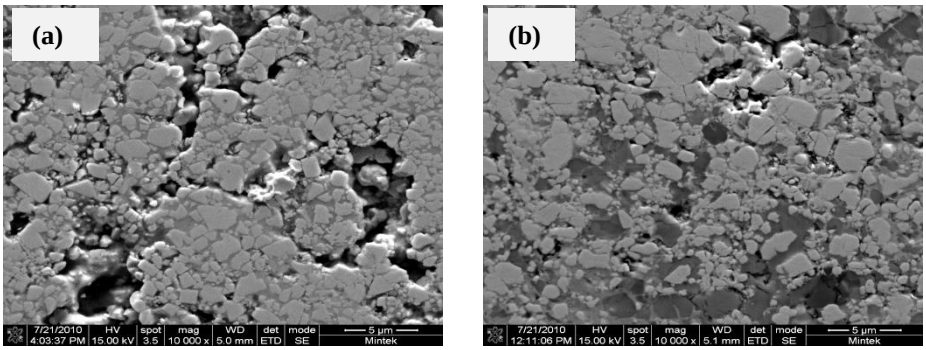


Figure B2. 1 High magnifications SEM images against the 100Cr steel ball on the wear tracks of (a) WC-12wt%Co, (b) WC-12wt%Co-10wt%VC, (c) WC-17wt%Co-10wt%VC (Run 38), and (d) WC-17wt%Co-10wt%VC (Run 39) coatings.



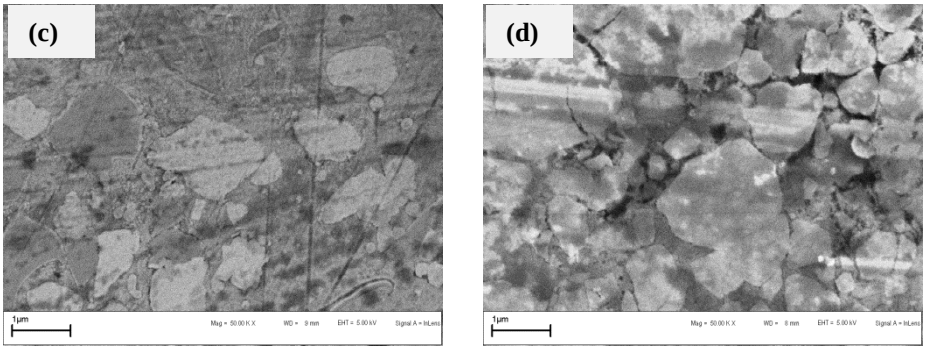


Figure B2. 2 High magnifications SEM images against the 100Cr steel ball on the wear tracks of (a) WC-12wt%Co, (b) WC-12wt%Co-10wt%VC, (c) WC-17wt%Co-10wt%VC (Run 38), and (d) WC-17wt%Co-10wt%VC (Run 39) coatings.

Appendix B3: XPS spectra on the worn tracks after sliding test.

Appendix B3A: Against 100Cr steel balls.

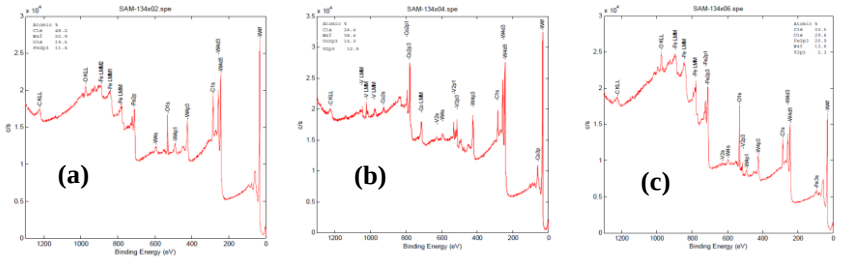


Figure B3A. 1 Wide XPS scan of the wear tracks on the (a) WC-12wt%Co, (b) WC-12wt%Co-10wt%VC and (c) WC-17wt%Co-10wt%VC coatings.

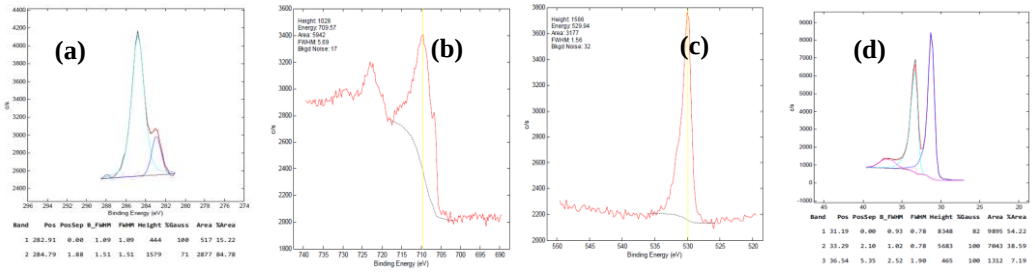


Figure B3A. 2 Narrow XPS scans of the wear track of the WC-12wt%Co coating showing (a) carbon (b) iron (c) oxygen and (d) tungsten peaks. The inserted tables show the de-convolution of peaks.

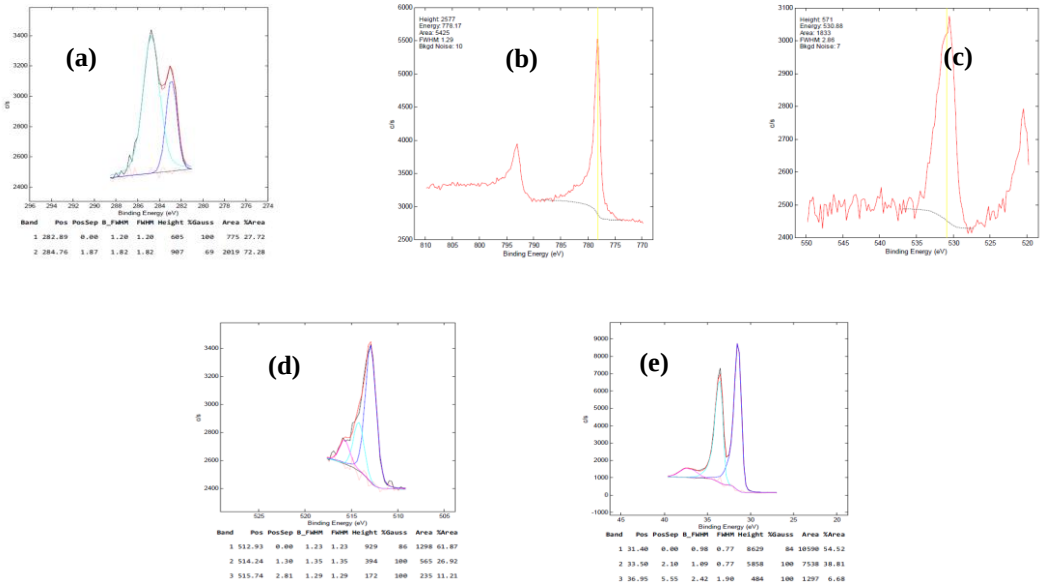


Figure B3A. 3 Narrow XPS of the worn track of the WC-12wt%Co-10wt%VC coating showing (a) carbon (b) cobalt (c) oxygen (d) vanadium and (e) tungsten peaks. The inserted tables show the de-convolution of peaks.

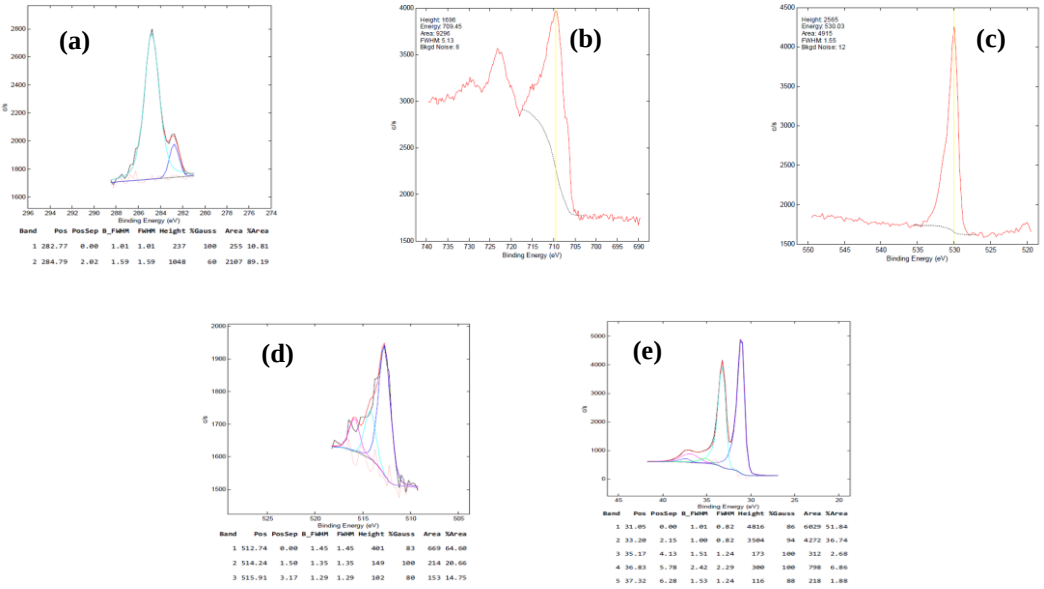


Figure B3A. 4 Narrow XPS of the worn track of the WC-12wt%Co-10wt%VC coating showing (a) carbon (b) cobalt (c) oxygen (d) vanadium and (e) tungsten peaks. The inserted tables show the de-convolution of peaks.

Appendix B3B: Against WC-Co balls.

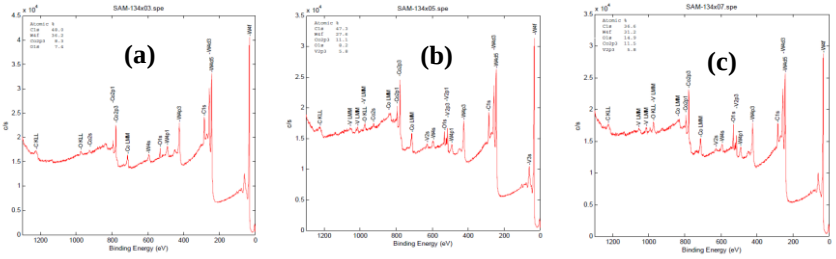


Figure B3B. 1 Wide XPS scan of the wear tracks on the (a) WC-12wt%Co, (b) WC-12wt%Co-10wt%10VC and (c) WC-17wt%Co-10wt%VC coatings

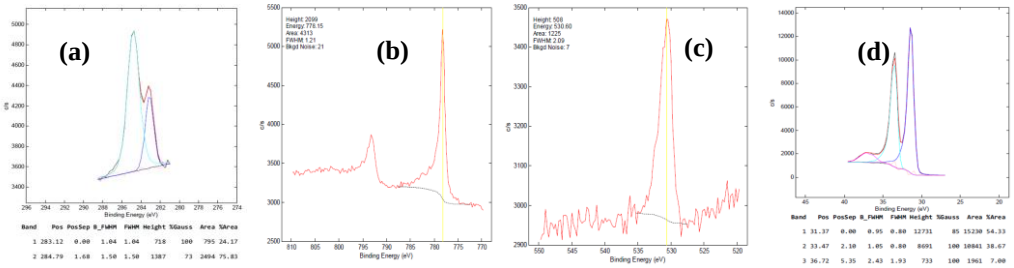


Figure B3B. 2 Narrow XPS scans of the wear track of the WC-12wt%Co coating showing (a) carbon (b) iron (c) oxygen and (d) tungsten peaks. The inserted tables show the de-convolution of peaks.

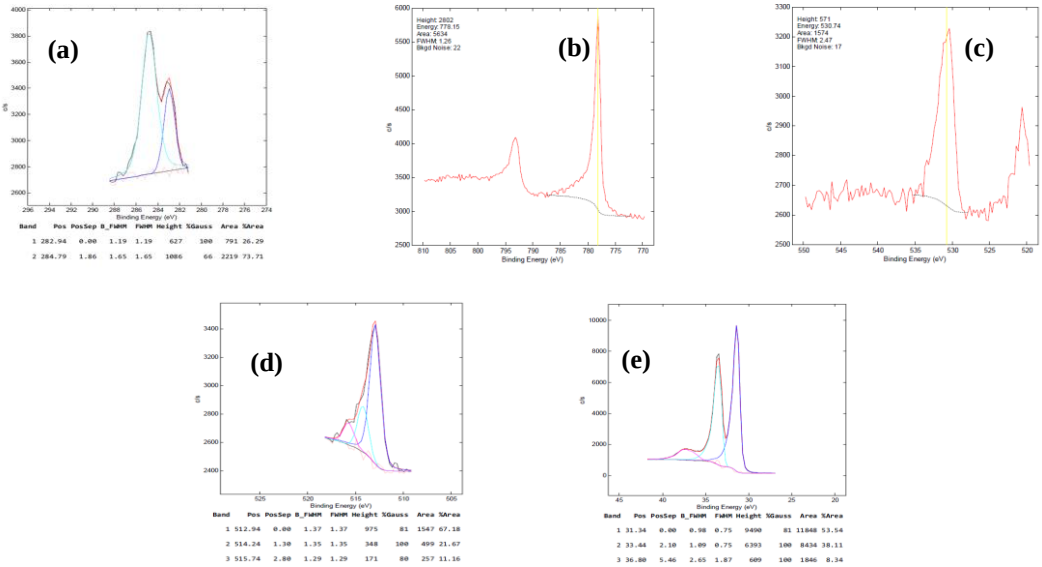


Figure B3B. 3 Narrow XPS scans of the wear track of the WC-12wt%Co-10wt%VC coating showing (a) carbon (b) iron (c) oxygen and (d) tungsten peaks. The inserted tables show the de-convolution of peaks.

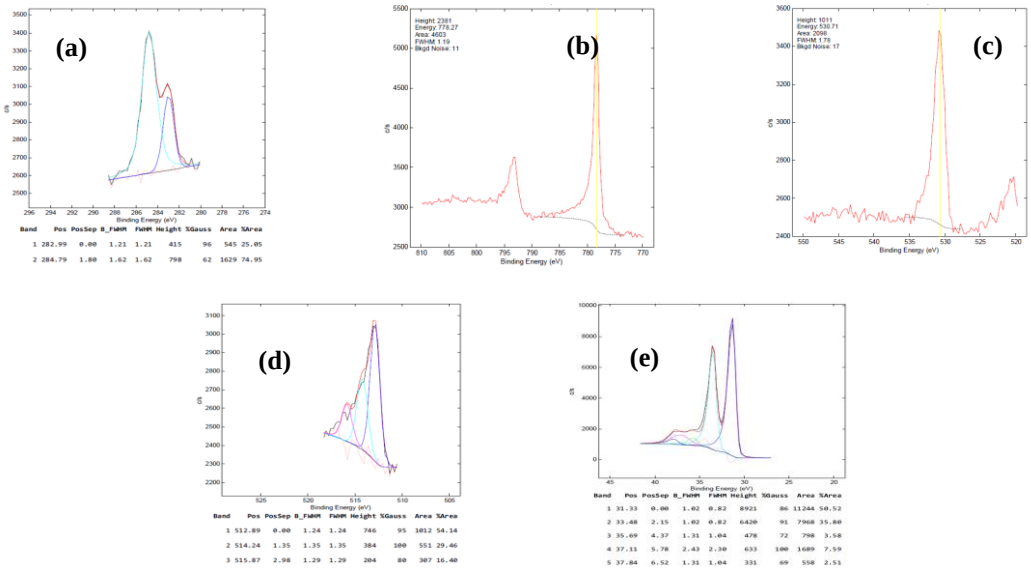


Figure B3B. 4 Narrow XPS scans of the wear track of the WC-17wt%Co-10wt%VC coating showing (a) carbon (b) iron (c) oxygen and (d) tungsten peaks. The inserted tables show the de-convolution of peaks.

Appendix B4: Slurry erosion wear data

Appendix B4A: Average mass loss and erosion rate against time curves

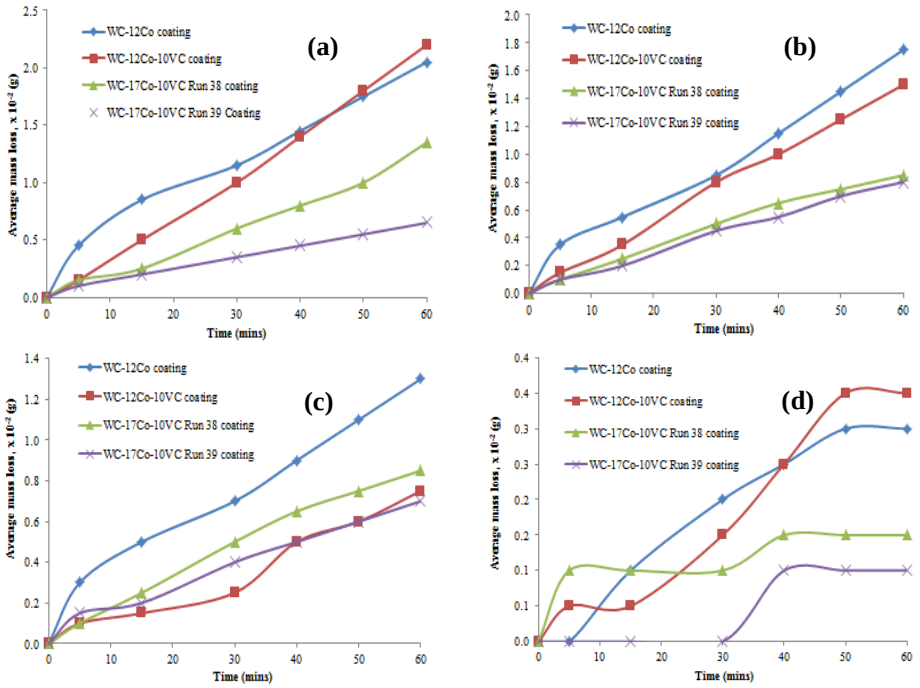


Figure B4A. 1 Average mass losses against time curves for (a) 90°, (b) 75°, (c) 60°, and (d) 45°.

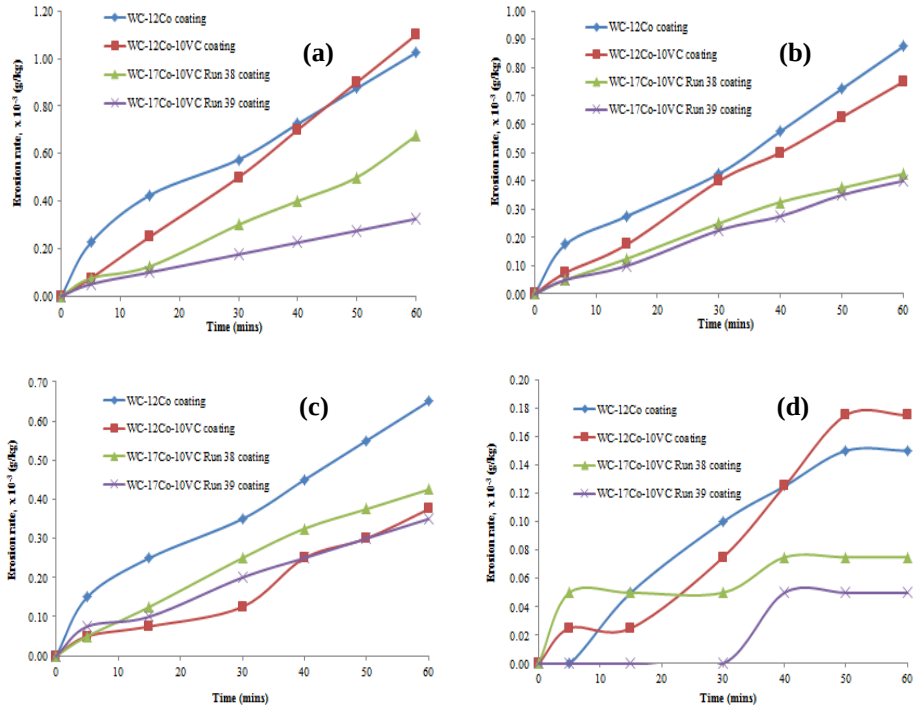


Figure B4A. 2 Average erosion rate against time curves for (a) 90°, (b) 75°, (c) 60°, and (d) 45°.

Appendix B4B: High magnification SEM images of the eroded surfaces

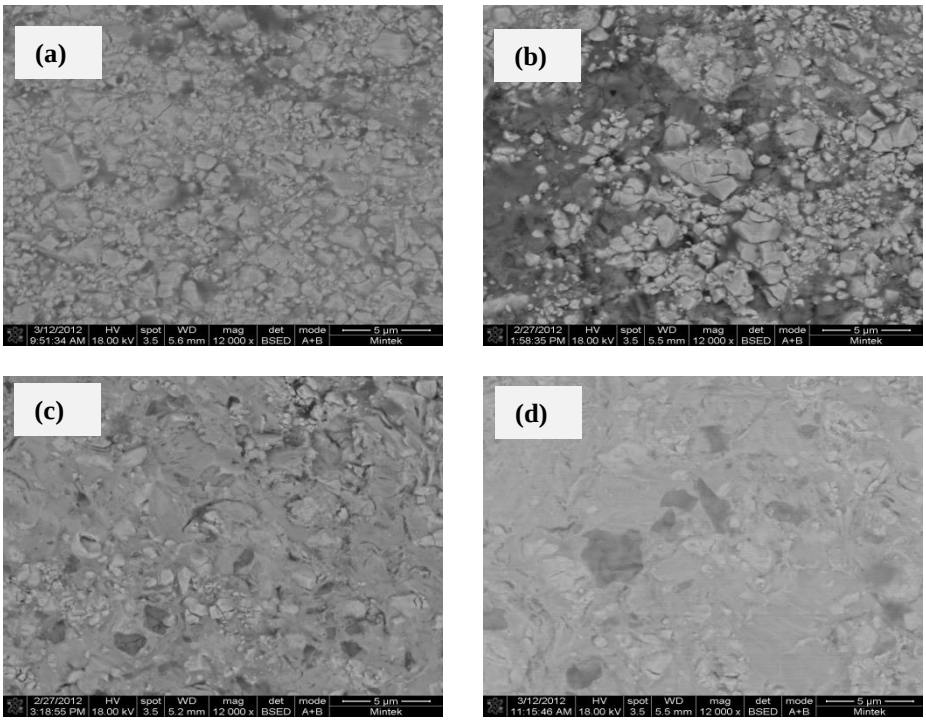


Figure B4B. 1 SEM images of the eroded surface of (a) WC-12wt%Co, (b) WC-12wt%Co-10wt%VC, (c) WC-17wt%Co-10wt%VC (Run 38), and WC-17wt%Co-10wt%VC (Run 39) coatings at 90°.

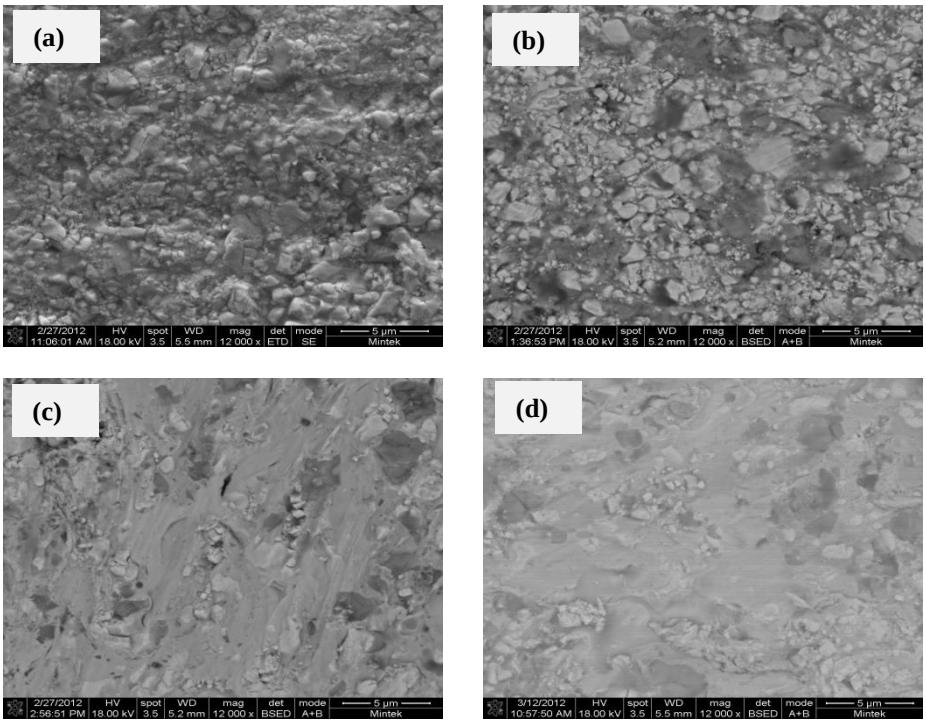


Figure B4B. 2 SEM images of the eroded surface of (a) WC-12wt%Co, (b) WC-12wt%Co-10wt%VC, (c) WC-17wt%Co-10wt%VC (Run 38), and WC-17wt%Co-10wt%VC (Run 39) coatings at 75°.

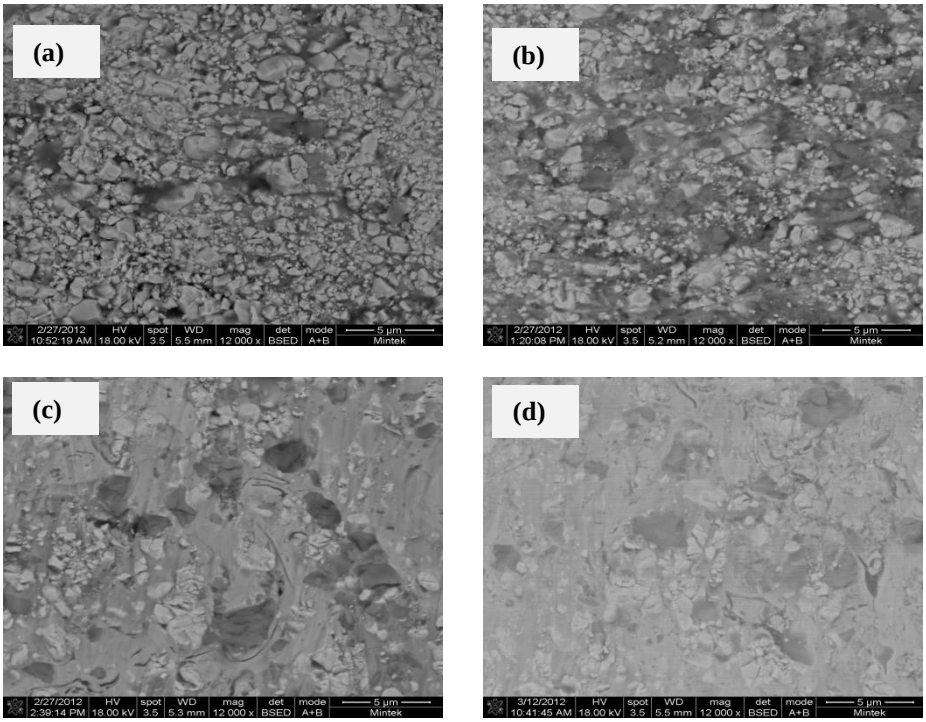


Figure B4B. 3 SEM images of the eroded surface of (a) WC-12wt%Co, (b) WC-12wt%Co-10wt%VC, (c) WC-17wt%Co-10wt%VC (Run 38), and WC-17wt%Co-10wt%VC (Run 39) coatings at 60°.

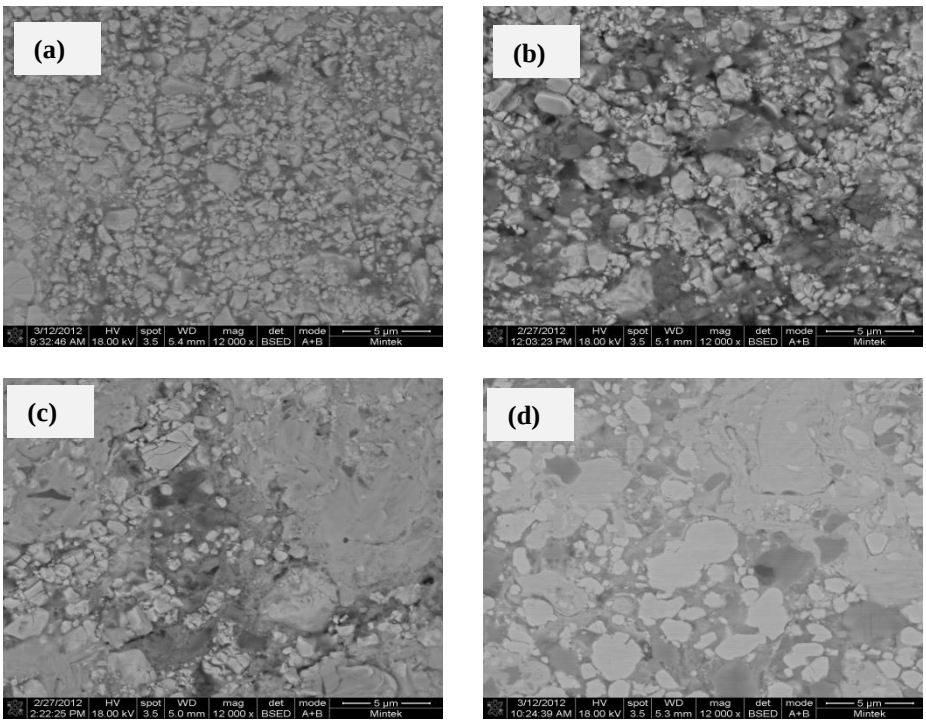


Figure B4B. 4 SEM images of the eroded surface of (a) WC-12wt%Co, (b) WC-12wt%Co-10wt%VC, (c) WC-17wt%Co-10wt%VC (Run 38), and WC-17wt%Co-10wt%VC (Run 39) coatings at 45°.

Appendix B5: EDAX mapping and EDX analyses on the eroded surface of WC-17wt%Co-10wt%VC coatings

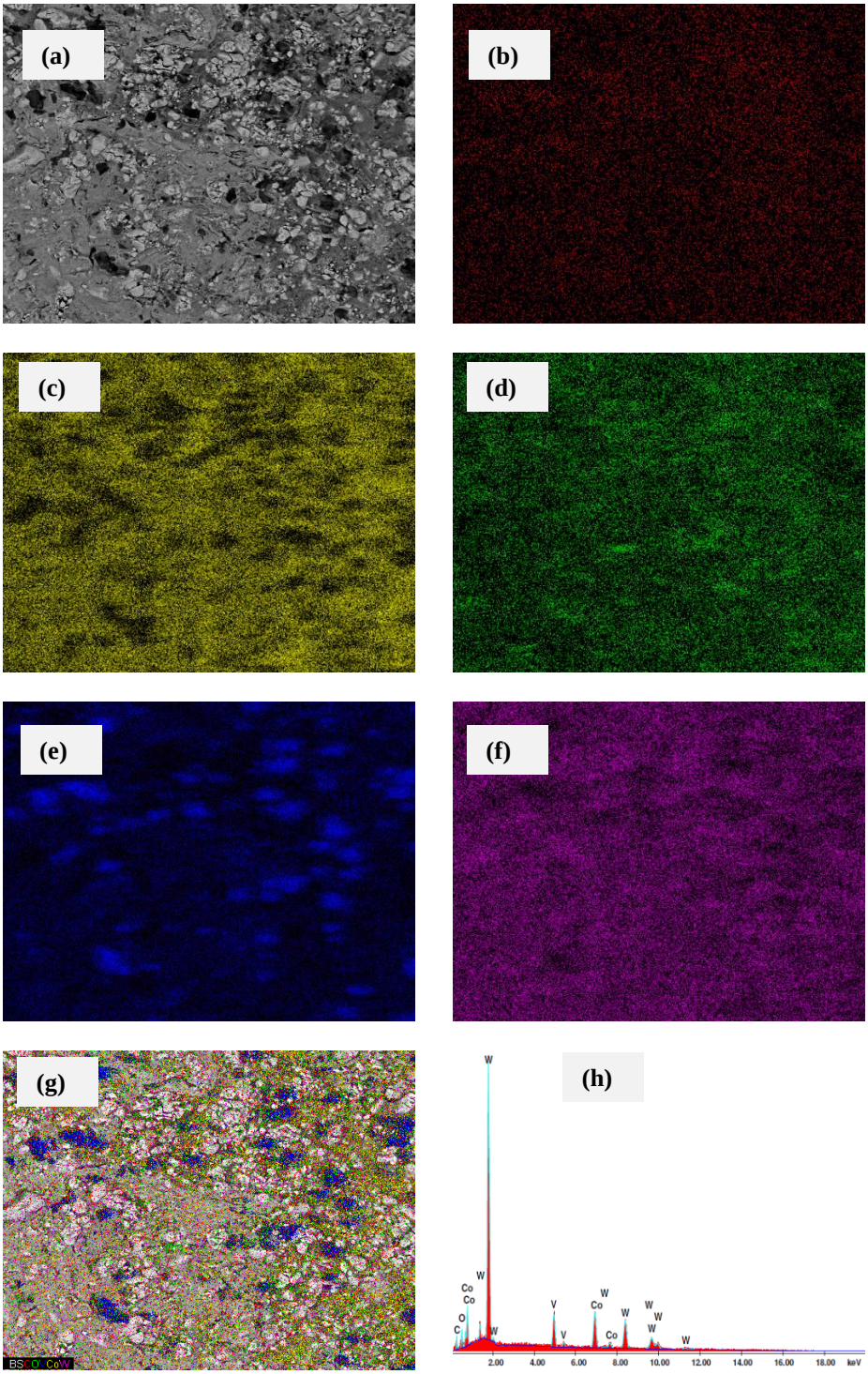


Figure B5. 1 EDAX maps showing the elemental distribution on the eroded surface of the WC-17wt%Co-10wt%VC Run 38 coating (a) BSE SEM image (b) carbon distribution, (c) cobalt distribution, (d) oxygen distribution, (e) vanadium distribution, (f) tungsten distribution, (g) the overlay, and (h) the EDX analysis.

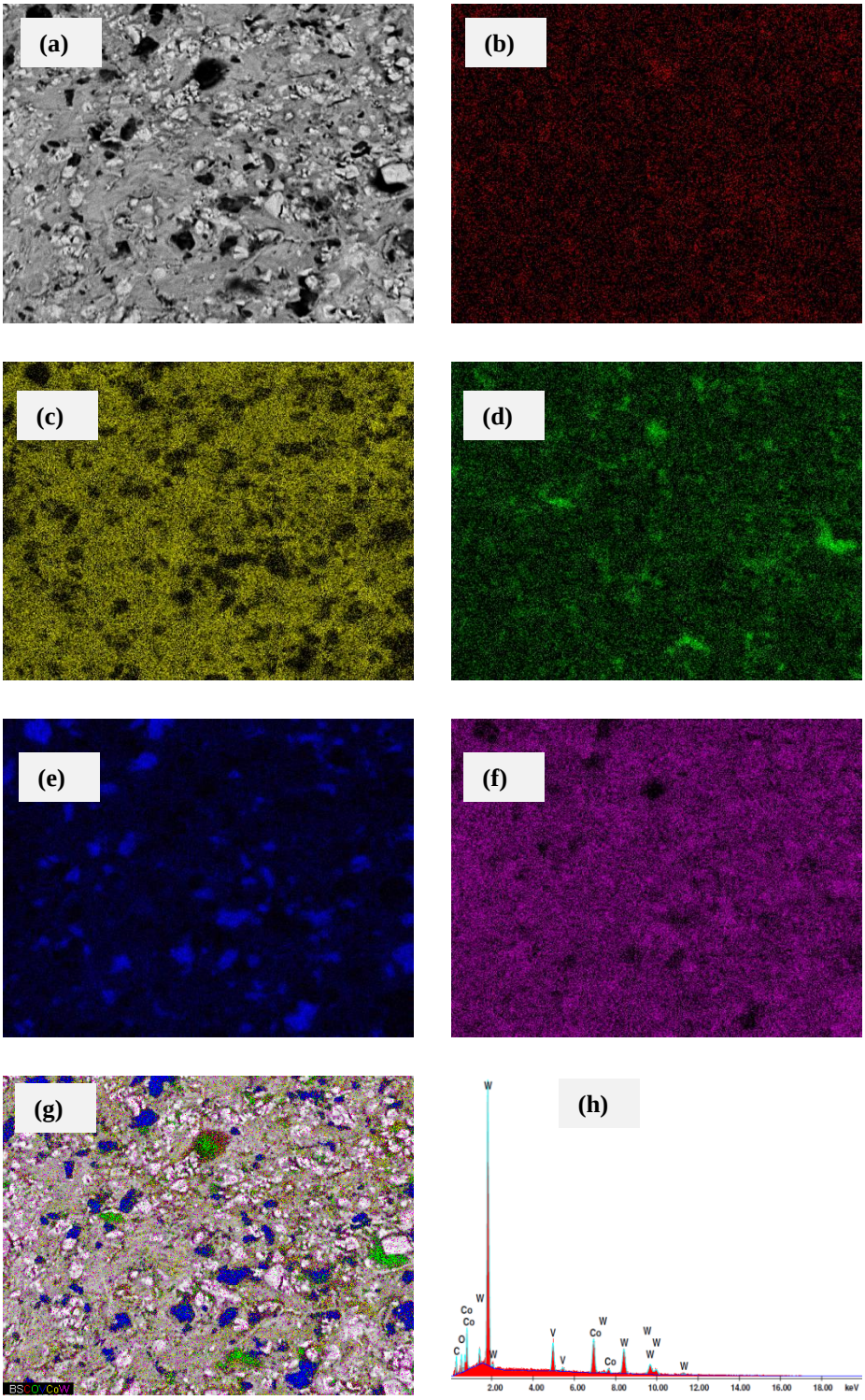


Figure B5. 2 EDAX maps showing the elemental distribution on the eroded surface of the WC-17wt%Co-10wt%VC Run 39 coating (a) BSE SEM image (b) carbon distribution, (c) cobalt distribution, (d) oxygen distribution, (e) vanadium distribution, (f) tungsten distribution, (g) the overlay, and (h) the EDX analysis.

APPENDIX C: CONVENTIONALLY SINTERED ALLOYS

Appendix C1: Friction responses

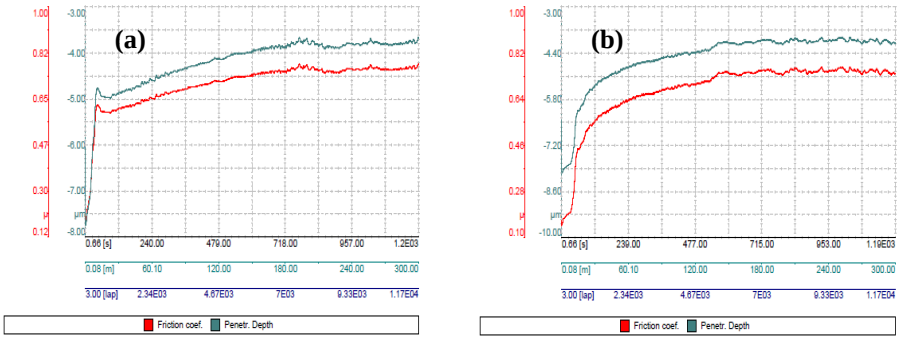


Figure C1. 1 Friction response against the 100Cr steel ball for (a) WC-12wt%Co, and (b) WC-12wt%Co-10wt%VC alloys

Appendix C2: SEM images of the wear surface after sliding

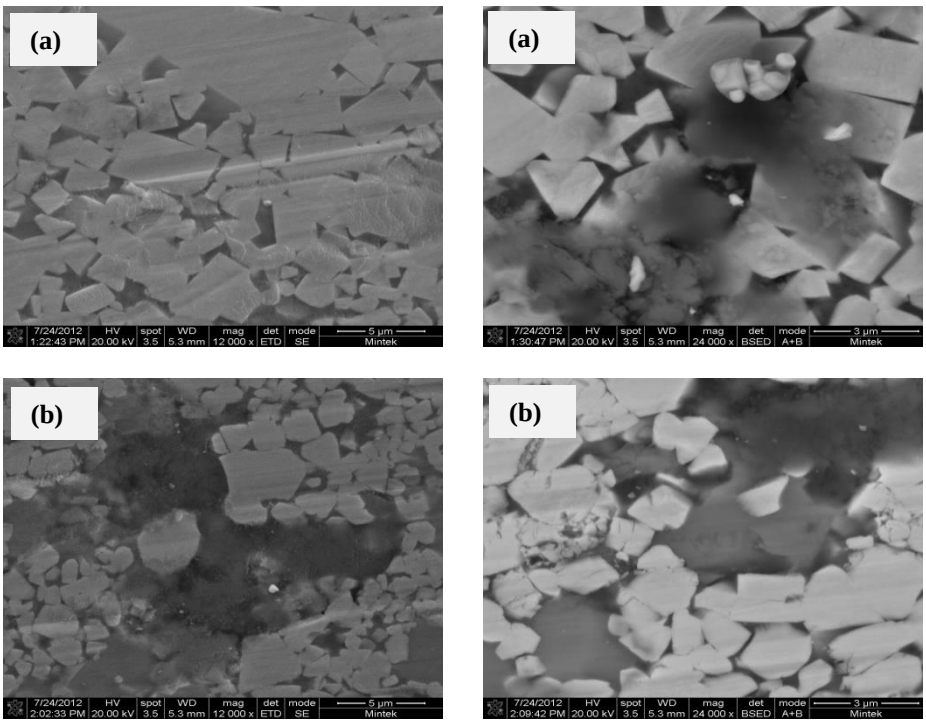


Figure C2. 1 High magnification SEM images of the wear surfaces after sliding against 100Cr steel ball for (a) WC-12wt%Co, and (b) WC-12wt%Co-10wt%VC alloys.

Appendix C3: Slurry erosion wear data

Appendix C3A: Average mass loss and erosion rate against time curves

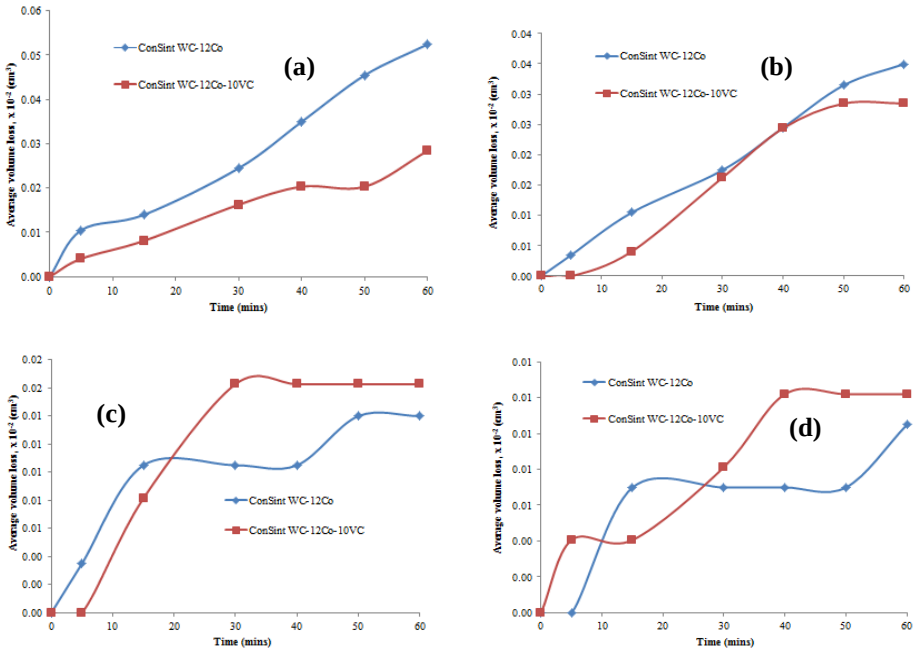


Figure C3A. 1 Average mass losses against time curves for (a) 90°, (b) 75°, (c) 60°, and (d) 45°.

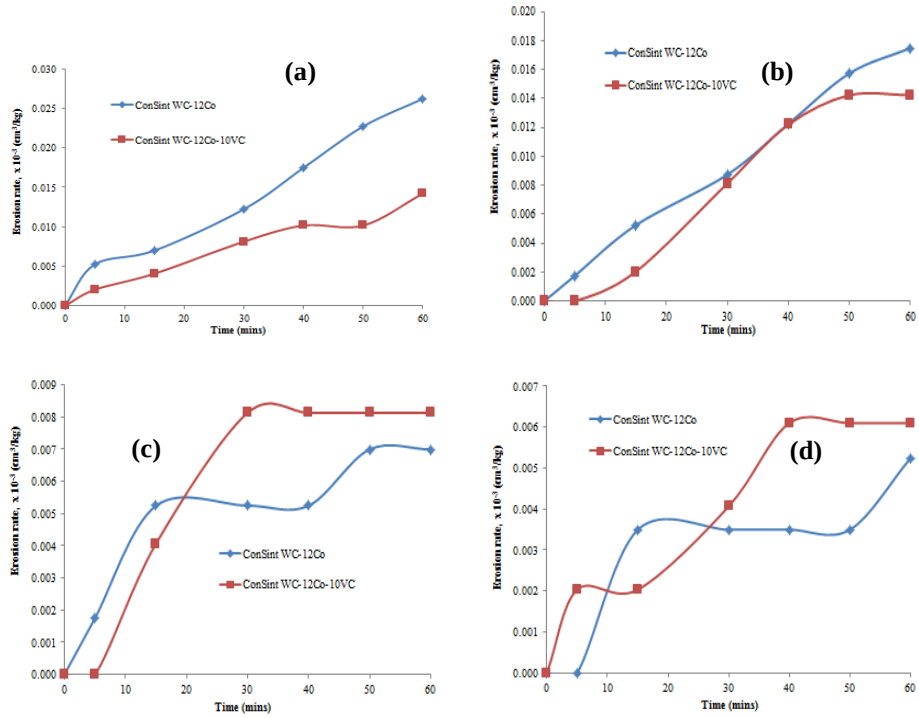


Figure C3A. 2 Average erosion rate against time curves for (a) 90°, (b) 75°, (c) 60°, and (d) 45°.

Appendix C3B: High magnification SEM images of the eroded surfaces

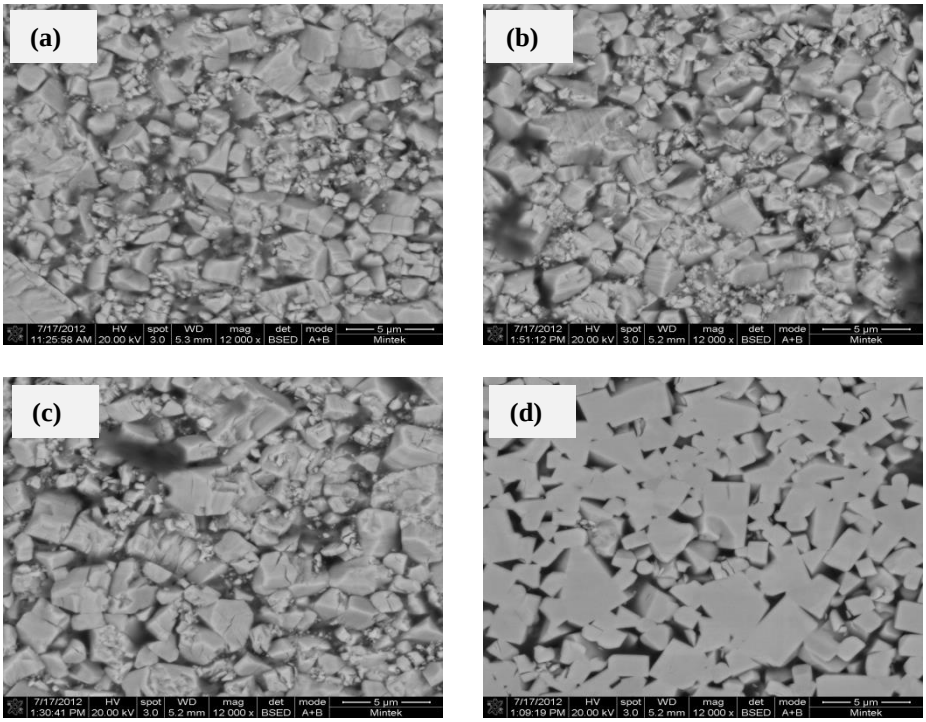


Figure C3B. 1 SEM images of the eroded surface of WC-12wt%Co alloy at (a) 90°, (b) 75°, (c) 60°, and (d) 45°.

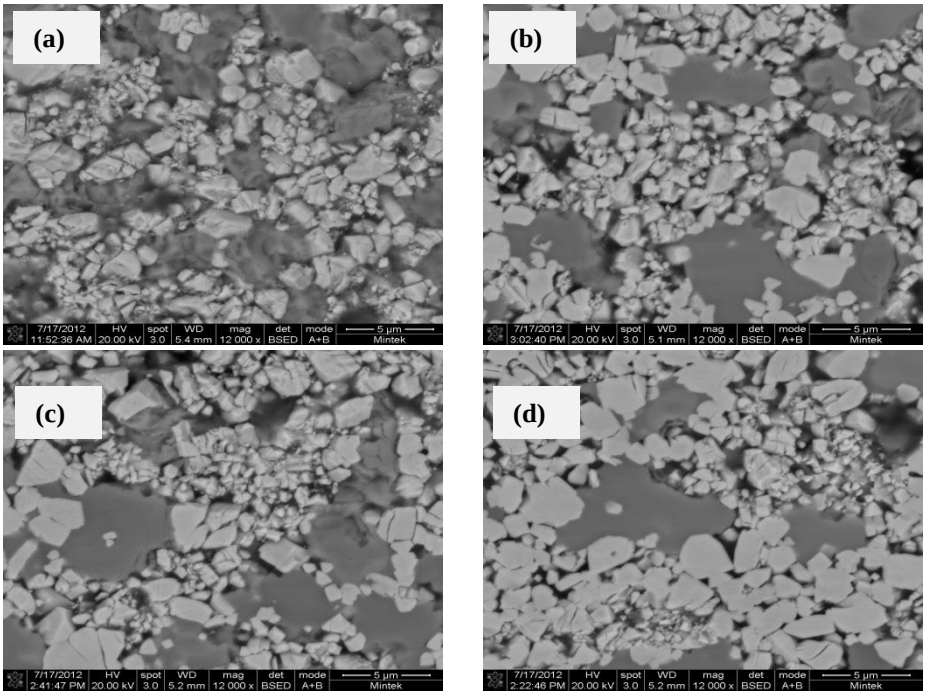


Figure C3B. 2 SEM images of the eroded surface of WC-12wt%Co-10wt%VC alloy at (a) 90°, (b) 75°, (c) 60°, and (d) 45°.

APPENDIX D: SPARK PLASMA SINTERED ALLOYS

Appendix D1: Friction responses

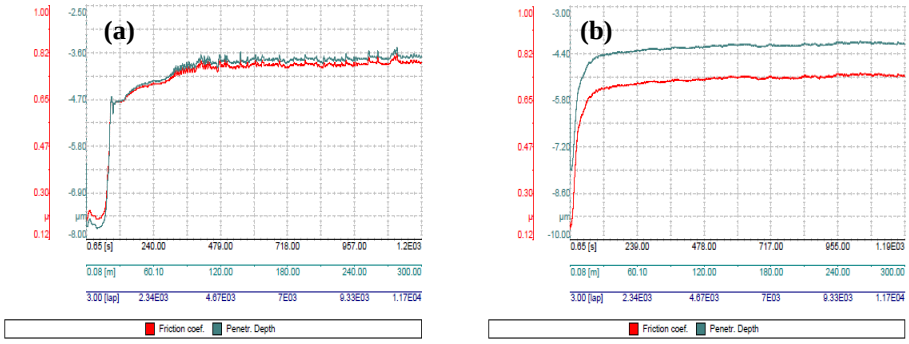


Figure D1. 1 Friction response against the 100Cr steel ball for (a) WC-12wt%Co, and (b) WC-12wt%Co-10wt%VC alloys.

Appendix D2: SEM images of the wear surface after sliding

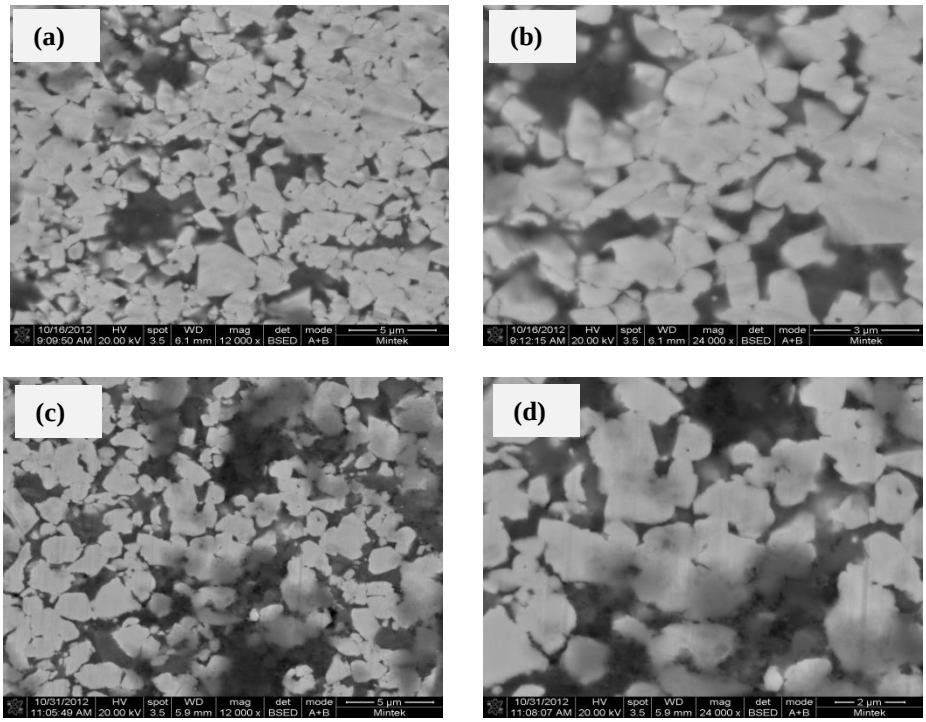


Figure D2. 1 High magnification SEM images of the wear surfaces after sliding against 100Cr steel ball for (a) WC-12wt%Co, and (b) WC-12wt%Co-10wt%VC alloys.

Appendix D3: Slurry erosion wear data

Appendix D3A: Average mass loss and erosion rate against time curves

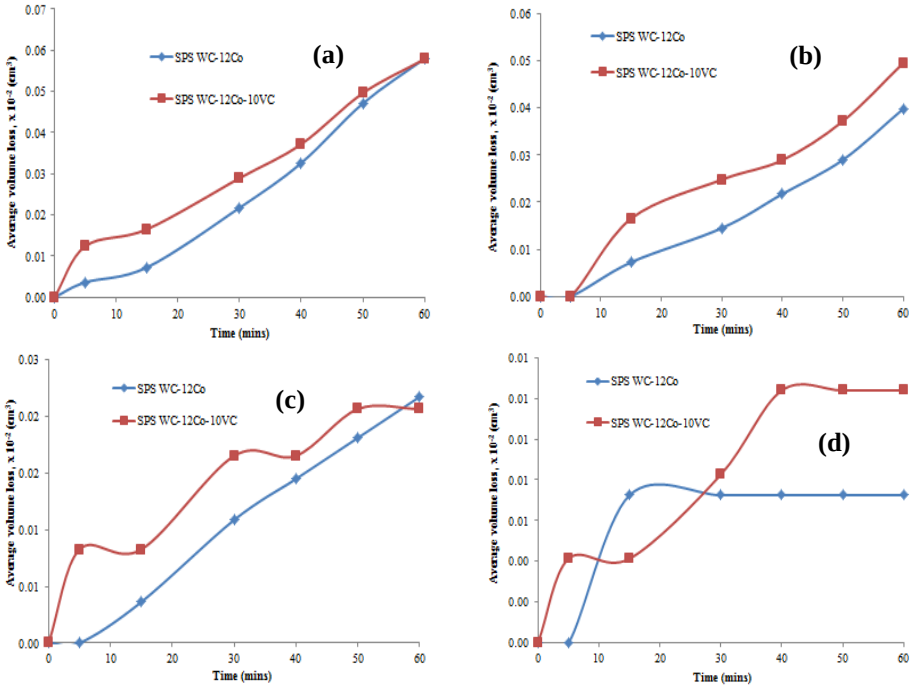


Figure D3A. 1 Average mass losses against time curves for (a) 90°, (b) 75°, (c) 60°, and (d) 45°.

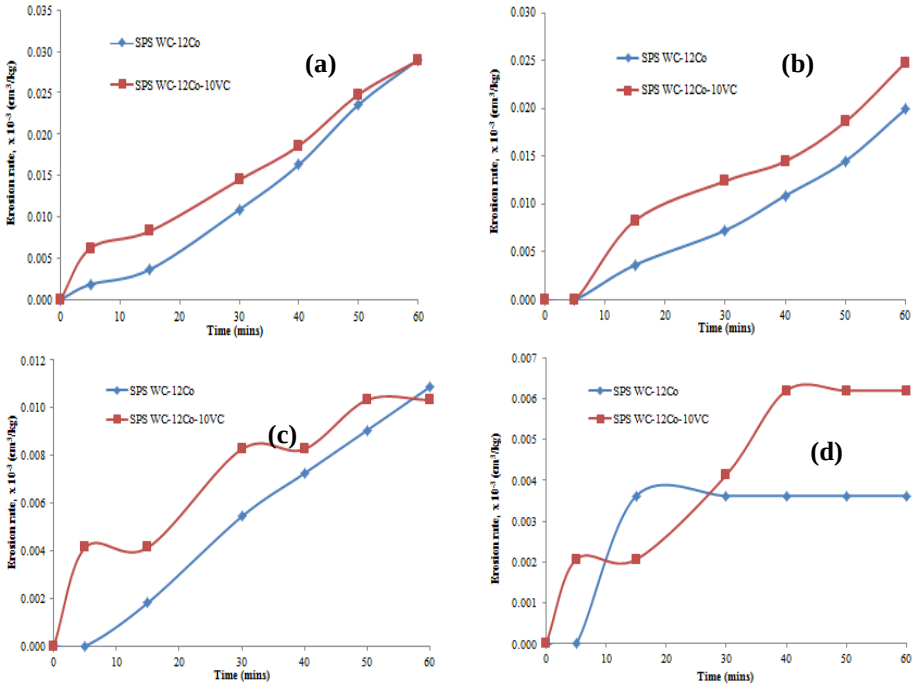


Figure D3A. 2 Average mass losses against time curves for (a) 90°, (b) 75°, (c) 60°, and (d) 45°.

Appendix D3B: High magnification SEM images of the eroded surfaces

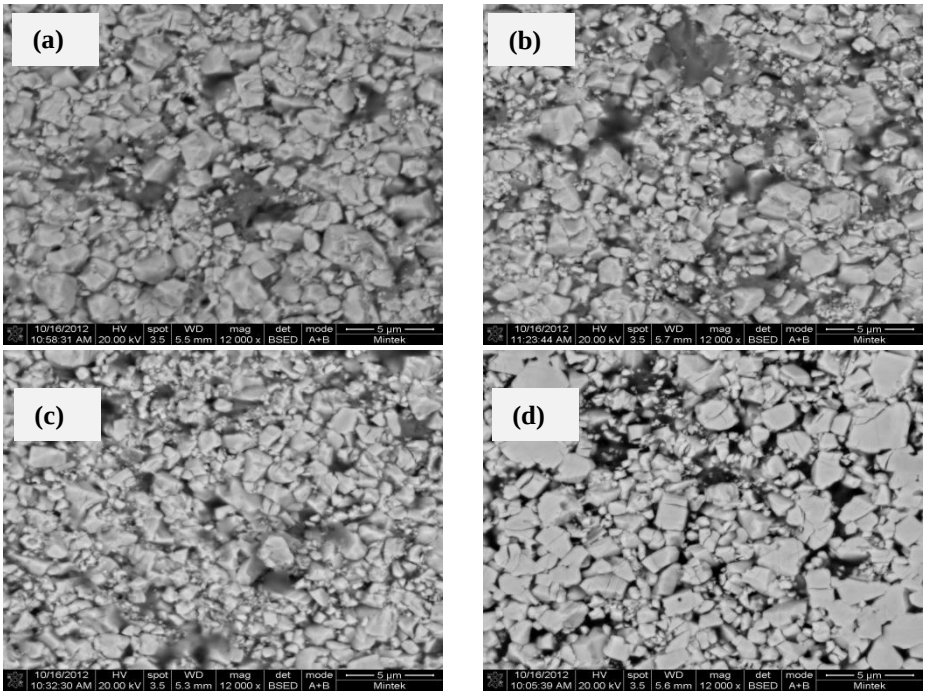


Figure D3B. 1 SEM images of the eroded surface of WC-12wt%Co alloy at (a) 90°, (b) 75°, (c) 60°, and (d) 45°.

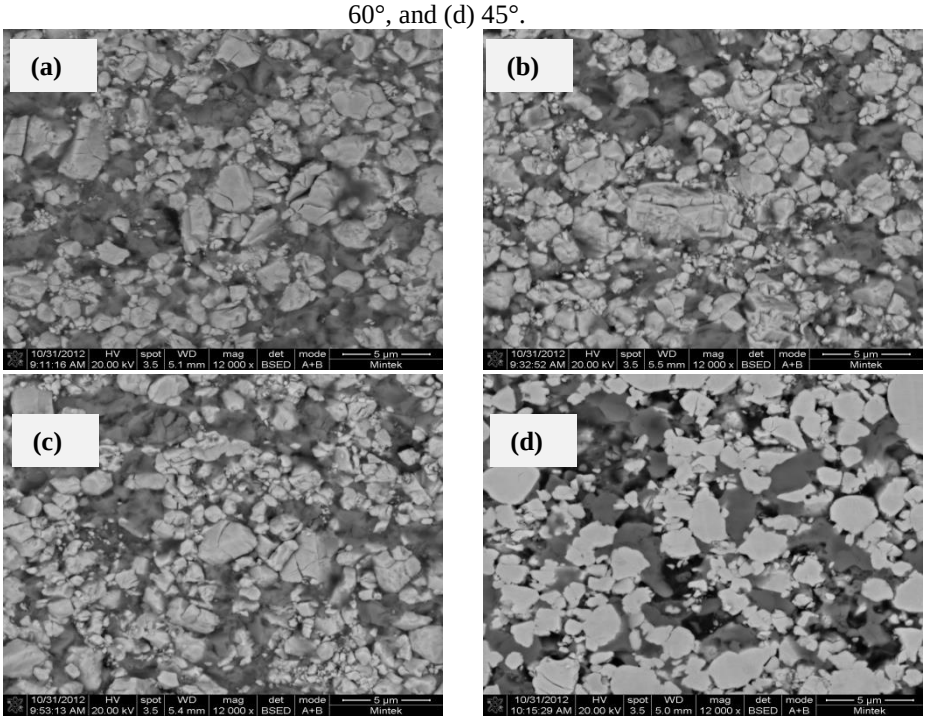


Figure D3B. 2 SEM images of the eroded surface of WC-12wt%Co 10wt%VC alloy at (a) 90°, (b) 75°, (c) 60°, and (d) 45°.